City Research Online

City St George's, University of London

Permanent repository link: https://openaccess.city.ac.uk/id/eprint/30837/

Enhancing Lift on a Three-Element High Lift Aerofoil System by Installing Air-Jet Vortex Generators

By

Neil Lewington

Thesis submitted as part of the requirements for the degree of Doctor of Philosophy

Centre for Aeronautics
School of Engineering
City University
Northampton Square
London EC1V OHB

November 2001

Abstract

In this research, an *interactive*, computational and experimental programme is presented that permits the rapid design of an optimum array of air-jet vortex generators (AJVGs) for use on an unswept, three-element high lift geometry in low speed flow. The interactive regime relies on the transfer of information between computational and experimental investigations, monitoring the flow field characteristics around the three-element high lift system, with the AJVGs active and quiescent. Careful definition of a 'local' flat plate AJVG computational model enables an assessment of the beneficial trends associated with the AJVG geometry and array configuration, prior to installation on the multi-component aerofoil system.

Two numerical approaches are employed to predict the flow field characteristics. The first combines a 2-D streamline based Euler solver coupled with an integral lag-entrainment boundary layer method (MSES of MIT). The second employs a finite volume block-structured, full Navier-Stokes (NS) flow solver, utilising the k-ε turbulence model with wall functions (CFX4 of AEA Technology). Computational studies of the flow field characteristics with the AJVGs active on the 'local' flat plate model and on the three-element high lift system utilise the NS solver only. Wind tunnel tests were conducted on the three-element high lift system for a range of angles of attack ($0°<\alpha<36°$) and jet blowing momentum coefficients ($0.0<C_\mu<0.12$) in City University's T2 low speed wind tunnel ($Re_c=1.37\times10^6$). The high lift system was configured with the slat and flap high lift devices in representative take-off settings with an array of 13 equi-spaced co-rotating AJVGs across the span of the wind tunnel model, located at x/c= 0.14c. The wind tunnel experiments involved measuring the chordwise surface static pressure and skin friction distributions and the wake profile downstream of the trailing edge.

The trends observed from the 2-D high lift system computations agreed with the experiments up to $\alpha\approx20°$, subsequent to which the CFX4 predictions deviated from the MSES and experimental findings. These differences result from neglecting the effects of boundary-layer transition; and the reliance on the law of the wall in the NS computations that is invalidated where flow separation is substantial. Improvements in the NS predictions can only be expected by making adequate provision for boundary-layer transition and by better modelling of the turbulence in the confluent boundary layers and near-wall flows above the wing component surfaces.

Computational models with the AJVGs active are able to represent the experimentally observed trends in flows where the adverse pressure gradient is weak. Using the 'local' AJVG model to identify beneficial trends in the flow field characteristics (filling out of the streamwise velocity profiles and enhanced skin friction), near-optimum air-jet spacings and flow features were determined. In stronger pressure gradient flows, however, more robust definition of the numerical boundary conditions either side of the air-jets is required, to facilitate adequate representation of the flow field downstream of the AJVG arrays.

Experimental results for the high lift system incorporating the AJVGs show it is possible to delay the onset of flow separation by up to 7° angle of attack, increase the maximum normal force generated by the high lift system by 25% and significantly delay drag rise. The greatest normal force enhancement $\Delta C_{Nmax}=0.6$, relative to the uncontrolled flow case, was determined with $C_\mu=0.057$ but useful flow control was achieved at values of C_μ as low as 0.014.

Contents

List of tables

List of figures

Nomenclature

AJVG	Air-jet vortex generator
b	Span of unswept high lift three component aerofoil system in wind tunnel (=740mm)
c	Retracted chord length of three component aerofoil system system in wind tunnel (=500mm)
C_{Dp}	Wake profile drag coefficient and constant in turbulence dissipation equation
C_f	Local surface skin friction coefficient in streamwise direction
ΔCf	Local surface skin friction relative to local background value, in streamwise direction
C_μ	AJVG jet blowing momentum coefficient ($= \dot{m}\,V_J / \frac{1}{2}\rho U_\infty^2 bc$) and constant in eddy viscosity equation
C'_μ	Constant in turbulent viscosity calculation
$C_M = \oint Cp \times d\left(\dfrac{x}{c}\right)$	Pitching moment coefficient about the leading-edge of the retracted chord aerofoil
$C_N = \oint Cp \, d\left(\dfrac{x}{c}\right)$	Normal force coefficient integrated from chordwise static pressure distribution on aerofoil model
$C_P = \dfrac{p - p_\infty}{\frac{1}{2}\rho U_\infty^2}$	Static pressure coefficient on wing surface(s)
D_H	Hydraulic diameter of AJVG
$H = \delta^*/\theta$	Boundary-layer shape parameter on model surfaces
$I\Delta C_f$	Integrated figure of merit for skin friction enhancement due to AJVGs
k	Kinetic energy of turbulence
K	Wind tunnel calibration constant in static pressure coefficient calculation

$\dot{m}$	AJVG mass flow rate obtained from orifice plate in blowing supply line to the wind tunnel model
M	Freestream Mach number
p	Local static pressure measured at aerofoil surface and in the high lift system wake, via static pressure orifices
Re_c	Reynolds number based on retracted aerofoil chord length and tunnel freestream conditions
s	Spanwise spacing between AJVGs
$S=s/c$	Non-dimensional spanwise spacing between AJVGs
u, v, w	Fluctuating velocity components in the (x, y, z) directions (u and x parallel to freestream)
U,V,W	Mean velocity components in the (x, y, z) directions
u*	Streamwise friction velocity
V_J	Velocity at jet exit
$V_R=V_J/U_\infty$	Jet to freestream velocity ratio
VVG	Vane vortex generator
x, y, z	Orthogonal coordinate directions, x-parallel to freestream C_μ direction
$y^+ = \dfrac{u^* y}{v}$	Dimensionless distance normal to wall
α	Angle of attack (incidence) measured in degrees wrt freestream direction
δ	Streamwise boundary layer thickness
δ^*	Streamwise boundary layer displacement thickness
ε	Turbulence dissipation rate
ϕ	AJVG pitch angle with respect to the local model surface tangent
γ	isentropic exponent
η, ξ, φ	Curvilinear coordinate system, η in freestream direction
μ	Dynamic molecular viscosity
$v=\mu/\rho$	Kinematic molecular viscosity
θ	Streamwise boundary-layer momentum thickness

ρ	Fluid density
τ_w	Wall shear stress in x- or streamwise direction
ψ	AJVG yaw (skew) angle with respect to the freestream direction

Subscripts

e	Boundary layer edge
∞	Freestream
le	Leading edge
te	Trailing edge

Superscripts

*	Initial guess of a property
'	Corrected value of a property
—	Mean value of a property

Declaration

I grant powers of discretion to the University Librarian to allow my thesis to be copied in whole or in part without further reference to the author. This permission covers only single copies made for study purposes, subject to normal conditions of acknowledgement.

Acknowledgements

This thesis is evidence of the support I have received from my family, friends and colleagues for the duration of this project.

I would especially like to thank my supervisors, Dr. Frank S. Henry and Prof. David J. Peake for their constant encouragement and invaluable guidance throughout my research and during the thesis write-up.

Thanks are due to BAE SYSTEMS and EPSRC for giving me the opportunity to realise this project and to Mr. Chris Barber, Mr. Mike Smith and Mr. Martin Young for their assistance in the wind tunnel laboratory at City University.

I am most grateful to my office colleagues Dr. Christoph Küpper, Mr. Saif Deen Akanni and Mr Chris Singh for the lively debate, on all matters, both in and out of office hours and to Mr. Dennis 'Putney' Witt for his computer services.

Above all, my heartfelt thanks go to my 'princess' and soul mate Miss Michele Brett, to whom I am eternally grateful and to whom this thesis is dedicated. Throughout my PhD., Michele's unbounded love, support and encouragement has provided the foundations upon which I have been able to achieve so much. I cherish the time we have and the future I know we will share.

1. Introduction

1.1 Problem definition

The demand for aircraft with greater manoeuvrability, high speed cruise and low speed landing and take-off capabilities, has directed much of the development of modern high lift systems. Considerable documentation is available for the optimal location of leading edge and trailing edge devices from collaborative research programmes between government and industry, such as the UK's "National High Lift Programme" of the 70s. However, further improvements in wing performance by means of 'active' or 'passive' flow separation control have been demonstrated for both simple geometries as well as complex systems. The current research is a continuation of a programme undertaken at City University [Innes (1995)], investigating the improvements in performance of an unswept aerofoil, representative of the inboard section of an Airbus-A320 high lift system, by the application of vane vortex generators (VVGs) and air-jet vortex generators (AJVGs). The work originated from an underlying interest within British Aerospace (BAe) to develop efficient low-speed high lift systems, in terms of lift and drag capabilities, as a design criterion, with structural considerations taking lesser priority.

Separation control and skin friction enhancement by means of vortex generators have been the goals of much of the research conducted at City University's Centre for Aeronautics over the last 10 years. Studies covering a variety of external and internal flows have indicated potentially useful skin friction enhancement with noticeable suppression of flow separation in both subsonic and transonic flows. Notably, the findings of Innes (1995), showed that employing VVGs and AJVGs considerably delayed the onset of flow separation and the level of pressure recovery at the trailing edge for a high lift system in the take-off configuration. With conventional VVGs, the onset of flow separation from the trailing edge of the flap was delayed by up to 5° angle of attack, generating an improvement in maximum total normal force (C_{Nmax}) 5% above that of the cleanfoil. Employing AJVGs at the same chordwise location and blowing with a stagnation pressure ratio of 1.6 delayed the onset of stall by up to 6°,

1

whilst generating a C_{Nmax} 22% (i.e., $\Delta C_N \approx 0.6$, $C_\mu \approx 0.1$) above that of the cleanfoil. The author concluded that the beneficial effects observed using AJVGs were far superior to those observed by employing conventional VVGs. Subsequent work, Innes (1996), also highlighted improvements in the drag characteristics of the high lift system in the landing configuration.

Part of the success of the research at City University is due to the coupling of computational and experimental techniques. As computing power has increased, the 'numerical experiment' plays an ever more significant role as a design tool. By validating numerical models in the digital wind tunnel with carefully contrived analogue wind tunnel experiments, interactive experimental and computational testing regime has been established. This facilitates sensitivity analysis of the flow separation control concept to be evaluated relatively quickly before implementation in more complex geometric systems.

This research focuses on an interactive computational and experimental testing regime to optimise the performance of a high lift system by employing arrays of AJVGs to delay the onset of flow separation.

An AJVG consists of a small jet emerging from an aerodynamic surface that is pitched and skewed relative to the oncoming freestream flow. The jet induces the local boundary layer and freestream flow to form well-organised, helical structures as the combined flow penetrates downstream. In contrast with conventional VVGs, AJVGs offer improved penetration of the vortices through severe pressure gradients by pumping excess momentum along the vortex cores with the advantage of virtually no parasitic drag when inactive [see Peake et al (1999)]. Arranging several AJVGs in an array has highlighted the potential for significant improvements in the aerodynamic characteristics of the high lift system. Further improvements in the array performance are expected by altering jet-to-freestream velocity ratio (V_R), spacing between adjacent AJVGs and rotational sense of the vortex arrays.

1.2 Goal and key specific objectives

The goal of this research is to design an interactive computational and experimental test regime to investigate and enhance the performance of a three-element high lift system, that is configured with an array of AJVGs. The key specific objectives are to determine optimal AJVG array installations by studying the sensitivity of the AJVG control process to jet to freestream velocity ratio (V_R), jet spacing (S), and whether co-rotational or counter-rotational vortex arrays offer better flow field enhancement. To achieve this goal, the manner in which the vortices transfer momentum from the high momentum to low momentum fluid regions, in the confluent boundary layer(s) above the multi-element aerofoil upper surface, needs to be established.

The interactive computational and experimental test regime will compare the results obtained with the finite volume Navier-Stokes flow solver CFX4 (of AEA Technology), the coupled viscous-inviscid 2-D flow solver MSES (of MIT) with those results of carefully contrived wind-tunnel experiments. CFX is chosen to analyse the flow around the multi-element aerofoil because of the past success of the software in predicting complex swirling flows at City University [see Henry & Pearcey (1994), Akanni & Henry (1995), Küpper (1999) and Lewington et al (2000)]. The MSES flow solver, a successful coupled Euler plus lag entrainment viscous flow computational tool Drela (1996) is used to compare and check-calibrate the performance of CFX4

The research is divided into the following sections:

- Design of a 2-D numerical model to analyse the flow around the high lift system, through a range of angles of attack up to C_{Nmax}.

- Develop a 'local' numerical AJVG model that reasonably reflects the physical conditions above the mainfoil of the high lift system.

- Assess, using the 'local' numerical model, the sensitivity of the AJVG control process to V_R, S and rotational sense of the vortex systems, in providing skin friction enhancement.

3

- Develop a numerical model that emulates the high lift system incorporating the optimised array of AJVGs.

- Investigate experimentally the high lift system in the take-off configuration, to extend the existing experimental database with wake profile drag and surface shear stress data over a range of angle of attack.

2. Literature review and state of the art

Much of the design and optimisation of high lift systems has been achieved by an iterative wind tunnel testing process coupled with relatively simple theoretical methods, the results of which are extrapolated to full-scale aircraft. As computing power has increased and flow physics improved in code development, designers are becoming more reliant on expeditious numerical techniques to analyse the flow field around complex aerofoil geometries before undertaking expensive production tests in large wind tunnels at high Reynolds numbers. Successfully coupling verified and validated computational methods with judicious experiments enables the rapid development of efficient and near-optimal high lift configurations. Indeed, the development of the A320 high lift system in terms of optimal leading-edge slat and trailing-edge flap locations and deflections was the direct result of one such interactive research project in the UK "National High Lift Programme" [summarised by Woodward & Lean (1993)]. By successfully combining extensive experimental data interactively with computational results, BAe developed the Weybridge conceived W6-4 wing. The wing has a simple but efficient near full span leading edge slat and a single component trailing-edge Fowler flap (see Fig. 2.1) continuous across its span with only two spanwise segments. The combination of this over wing slat with a single slotted flap incorporates physical simplicity with structural lightness, yielding fine aerodynamic characteristics capable of meeting stringent requirements on lift/drag ratio and airfield performance [see Back & Wedderspoon (1986)]. Further enhancement of this already capable high lift system performance is expected by employing carefully contrived interactive computational and experimental techniques to assess active viscous flow control with air-jet vortex generators [see, for example Innes (1995) and Lewington et al (2000)].

The following section summarises the principles of flow separation and stall on unswept aerofoils and some of the useful computational and experimental research to date covering high lift systems and viscous flow control with passive solid and active pneumatic vortex generators. An overview of those significant investigations that have set milestones, in the authors opinion, are outlined in Table 2.1 below.

Table 2.1: An overview of the current state of the art of high lift aerodynamics		
High Lift Systems		
Date, Author	**Application + Test conditions**	**Key findings**
1921, Handley-Page	Including transverse slots into an aerofoil profile to improve lift. U_∞=40-80ft/s, $0°<\alpha<80°$	Cutting transverse slots through the aerofoil profile increased the lift generated by up to 50% in some configurations. Utilising multiple slots on aerofoil configurations can increase lift by up to three times that of a single aerofoil.
1972, Smith	Analysis of multi-element aerofoils at high incidence and the principles behind high lift generation.	(i) Slat effect - Circulation around forward element reduces negative pressure peaks on downstream element. (ii) Circulation effect - Circulation around downstream elements reduces the negative camber effects on upstream element. (iii) Dumping effect - Trailing-edge of upstream element is in a region of high velocity relieving adverse pressure gradients effects on the boundary layer (iv) Off-surface pressure recovery - More effective deceleration of the wake occurs in a region of high velocity away from the wall. (v) Fresh boundary layer effect - Each element starts with fresh boundary layer more capable of withstanding adverse pressure gradients.
1972, Foster	Mechanisms of stall of wing sections with high lift devices in two-dimensional flow. Re_∞ of the order 10^6	A close analogy exists between the nature of stall on wings configured with and without a trailing edge flap. In some cases this analogy can be extended to wings configured with leading-edge and trailing-edge devices but the proximity of the slat plays a key role in the nature of stall.
Experimental examples		
1974, Ljungström	Experimental optimisation of multiple element airfoils. Low speed 2-D tests ($Re_\infty \approx 10^6$) Optimisation criteria on C_{Lmax}	Slat position has a substantial effect on the viscous flow over the flaps. Optimum slat/flap positions correspond to flow fields with little interaction between component wakes and downstream component boundary layers.

1989, Adair & Horne	Detailed measurements of the shear-layers on an aerofoil configured with a single slotted flap. $M=0.09$, $Re_\infty=1.8\times10^6$, $\alpha=8.2°$	The initially inviscid slot flow has a dominant effect on the near-wall and near wake flows. A log-linear region is identifiable in the flap boundary layer but the turbulence in the slot flow requires care to be taken when deducing the wall skin friction. The Reynolds normal stress gradient in the cross-stream momentum has significant implications on the near wall flow when the flow separates.
1990, Nakayama et al	Mean flow and turbulence measurements on an aerofoil configured with a slat and flap. $M=0.2$, $Re_\infty=3.0\times10^6$, $\alpha=10°$, $18°$	Even with no major separation recorded at the tested angles of attack, considerable thickening and pressure variation occurred across the shear flow regions above the flap and in the near wake. Wake curvature effects on turbulence observed in several regions of the flow field, prompt the idea that flow reversal could first occur in the wake. Turbulence in the slat wake significantly affects boundary-layer transition and growth on the mainfoil. Accurate theoretical methods will require very general methods to enable sufficient definition of the flow phenomena in the predictions
1994, Moir	Measurements on a two-dimensional high lift system with high lift devices at low speed. ($54ms^{-1}<U_\infty<67ms^{-1}$)	Quantifiably accurate experimental data for the global pressure distribution and momentum deficit in the wake downstream of the high lift system over a range of angles of attack up to stall. The accuracy of the data makes the wind tunnel tests an excellent validation tool for computational models.
2000, Thomas et al	LDV measurements of the confluent boundary layers on a three-element high lift system. Focuses on a case with strong and a case with weak boundary layer confluence. $Re_\infty=1.2\times10^6$	Early boundary-layer confluence results in increased mixing between the retarded wall flow and the slat wake, thus increasing the momentum defect near the wall, giving rise to a reduced level of suction on the element. The near wall flow region demonstrates a classical log-law region. The inner region of a confluent boundary layer behaves in a similar manner to a classic turbulent boundary layer in an adverse pressure gradient but instead of adjusting to the local inviscid freestream the mean flow properties adjust to the velocity imposed by the lower side of the slat wake.

Viscous/inviscid interaction flow prediction techniques		
1966, Hess & Smith	Potential flow solution method to predict the flow field around arbitrary shaped bodies.	The code can cope with irregular shapes and the interference effects generated by an ensemble of bodies, i.e., high lift systems. The potential flow field is simulated with a continuously varying vortex sheet around the surface of the body. A constant value of the singularity strength is assumed at the centre of the panel but may vary from one panel to the next. Tangential velocities and pressures can be determined at the centre of each panel. The code enables an estimate of the integrated lift and pitching moment.
1968, Cebeci & Smith	An algebraic method based on the eddy-viscosity concept to solve for the complete boundary layer with provision for transition and separation.	Adequate for predicting attached flows, the results achieved with this heavily simplified algebraic method become increasingly unsatisfactory as the flow on the aerofoil upper surface approaches separation. The algebraic method provides the wing designer with a relatively simple tool that can be readily implemented to analyse the flow field qualitatively.
1973, Green et al	A rapid method to predict the development of turbulent boundary layers. The method employs the momentum equation, the entrainment equation and the rate of change of entrainment coefficient (lag).	Including the 'lag' rate of change of entrainment equation provides a worthwhile improvement in predict capabilities with minimal increase in required CPU time. The 'lag' equation can be derived with little empiricism from the differential equation for shear stress. The method allows first order corrections for the effects curvature on turbulence to be implemented in a straight forward manner.
1987, Lock & Williams	A complete review of viscous/inviscid interactions in aerodynamics.	Employing viscous/inviscid interaction methods enables designers to predict the flow field phenomena rapidly and relatively simply. Improvements are expected if the methods can include the following: (i) The second order effects in the boundary layer equations and their influence on the inviscid flow field (ii) Possibly adopting local solutions for the Navier-Stokes equations in regions of significance [see Oskam (1983)].

8

Applications of viscous/inviscid techniques		
1974, Jacob & Steinbach	An integral method for predicting the lift generated by a multi-element aerofoil configuration.	Prediction of C_{Lmax} is possible by including the displacement effect of the separated wake. Although, complicated to program once done the code can be easily adapted to predict the flow around most arbitrary aerofoil geometries. Improvements should include provision for long separation bubbles and merging boundary layers over the multi-component systems.
1978, Brune & Manke	An upgraded viscous flow analysis of multi-element aerofoil configurations. M=0.15, $Re_c=3\times10^6$	The code includes representation of the displacement effects of the boundary layer and wake with Green's lag-entrainment method and boundary layer separation with the method of Nash and Hicks. Transition is also accounted for with the e^n method pioneered by Smith (1952). Reliability of the code is improved with the solution converging within a few iterations. Inclusion of the displacement effects of the boundary layer separation and wake characteristics much improve the predictive capabilities of the code particularly close to C_{Lmax}
1990, Drela & Giles	A streamline-based Euler discretisation and a two-equation integral boundary layer formulation that is coupled through the displacement thickness. Incompressible and compressible flow regimes for a range of angles of attack	Use of streamline-based Euler discretisation is effective at reducing the size of the numerical problem and enables the wake trajectories and separation zones to be captured. The multi-deck integral method for the confluent boundary layer allows representation of the asymmetric properties above the aerofoil and in the wake. The code provides an accurate and efficient method for predicting the flow field around multi-element aerofoils so that much of the preliminary design work can be conducted numerically.

6

Applications of RANS techniques		
1989, Bartsch et al	Navier-Stokes calculations of 2-D steady state turbulent flow around two high lift aerofoil configurations with the k-ε turbulence model on a lock-structured grid. $Re_c=1.8\times10^6$, $0°<\alpha<16°$	Good agreement between predicted and experimental results is demonstrated throughout the tested incidence range. The k-ε turbulence model is able to adequately predict the flow around multi-element aerofoil configurations although deficiencies in the predictive capabilities are evident. Improvements in the predictions are expected if detailed experimental data for the mean flow and fluctuating velocities, pressures and Reynolds stresses is obtained. That way an appropriate turbulence model can be selected to predict the flow field around multi-element aerofoils.
1992, Rogers et al	Simulation of incompressible flows around multi-element aerofoils with the one-equation Baldwin Barth and algebraic Baldwin Lomax turbulence models on block-structured and Chimera grids. $Re_c=1.5\times10^6$, $0°<\alpha<20°$	The one-equation Baldwin Barth model is robust and shown to be an efficient and accurate method of predicting maximum lift for two high lift aerofoil configurations. A common discrepancy between the experimental and predicted results is demonstrated when large regions of separated flow exist. Employing a Chimera grid approach is found to be easier to implement that the block-structured grid approach as it requires less grid points and less time to generate the grid.
1993, Anderson & Bonhaus	Computations of the flow field around multi-element aerofoils with the one equation Baldwin-Barth and Spalart-Allmaras models on unstructured grids. $Re_c=9\times10^6$, $0°<\alpha<25°$	The unstructured mesh technique enables grids to be readily generated for the complex multi-element aerofoil geometries. With relatively coarse grids adequate resolution for determining the pressure distribution is possible. To be able to resolve the velocity profile much finer grids are required, which results in an increased computation time for the solution.

High lift system CFD Workshops		
1996, Ying	Results from a CFD workshop to simulate the flow over a three-element aerofoil tested in the NASA Langley Research Center. Ten codes employing viscous/inviscid interaction (VII) and RANS methods coupled with block-structured, Chimera and unstructured grids were utilised. $M=0.2$, $Re_c=9\times10^6$	To enable CFD to be employed as an efficient design and production tool the paper identifies the following issues to be addressed. I) Development of efficient automated grid generation software. II) Improved compact schemes are required for unstructured approaches to reduce memory usage III) Multi-processor computing techniques should be utilised to reduce computing time. IV) Pre-conditioners for low Mach number flows to reduce convergence time V) Develop/improve simple and robust turbulence models to capture the essence of the flow physics. VI) Gain a better understanding of boundary-layer transition to enable identification of CFD correlations.
1997 Fejtek	A computer code validation exercise for predicting the flow field around a three-element aerofoil in the take-off configuration. Ten participants from industry and academia using VII and RANS techniques to predict lift, pitching moment and drag characteristics of the high lift system. $M=0.197$, $Re_c=2.52\times10^6$	The exercise echoes many of the findings from the CFD-Workshop identified by Ying above. To obtain adequate predictions of the high lift flow field the numerical method should account for: i) A suitable grid density ii) Far -field boundary corrections to eliminate the effects of close proximity of boundaries in the computations. iii) Accurate specification of transition locations iv) Employ at least a one-equation turbulence model v) Provision for compressibility effects at high αs. Considering the current state of the art for one- and two-equation turbulence models the author concludes that focusing on grid dependency and transition offers the best short term hope of being able to consistently predict the flow fields associated with high lift systems.

1999 Lindblad & De Cock	Prediction of maximum lift with VII and RANS CFD techniques for a multi-element aerofoil in the take-off configuration. $M=0.22$, $Re_c=4.5\times10^6$	Again the conclusions highlight the significance on the quality of the predictions of adequately modelling transition and turbulence The results show that with RANS as opposed to VII techniques it is possible to predict C_{Lmax} when it occurs due to wake boundary layer confluence prior to severe flow separation. Most significantly the authors conclude that coupling VII, RANS and experimental wind tunnel techniques enables solutions to many of the design problems to be resolved without the need for extensive and costly wind tunnel testing.
Vortex Generators		
1950, Bruynes & Taylor	Solid VVGs as fluid mixing devices.	Employing the devices resulted in useful suppression of boundary layer growth.
1960, Wallis	Circular AJVGs installed on an aerofoil, pitched and skewed to the oncoming freestream $Re_c=4\times10^6$, $D_{jet}=0.71$mm, $c=9.5$mm	Useful suppression of boundary layer separation and a performance comparable to VVGs with only low mass fluxes required to power the system.
1961, Pearcey	Solid VVGs and AJVGs installed on aerofoils to suppress shock-induced boundary layer separations. $M=1.0$ to 1.4	Spacing between the VVGs is a key factor in the ability of the vortices to convect low momentum fluid away from the aerodynamic surface. If the distance between the vanes (D) is below three times its height (h) the proximity of the adjacent vortices limits the effectiveness of the VVG array. At successive spacings above $D/h=3$ the decay in the performance of the array reduces slowly.
1991, Gad-el-Hak & Bushnell	A comprehensive review of the mechanisms associated with flow separation and its control with passive and active techniques.	Both passive and active separation control techniques enables the near wall velocity profiles to be modified to delay boundary-layer separation. Developments in flow prediction methods have transformed conventional flow separation control from an art to a science. The authors conclude that further research should include optimisation of AJVG arrays.

Experimental studies and Numerical studies		
1982, Shabaka et al	Single and multiple vortices embedded in turbulent boundary layers. $U_\infty=30ms^{-1}$, h O(δ), zpg	The eddy viscosity components identified from the Reynolds Stresses suggest that the simple empirical correlations employed are not adhered to. The use of simple turbulence models to predict vortical flow fields is therefore unlikely to yield sufficient detail for the complex flow field.
1987, Lindriat et al	VVG in a turbulent boundary layer on a flat plate. $U_\infty=30ms^{-1}$	Use of an algebraic turbulence model enables prediction of the flow field associated with single and a pair of vortices embedded in the turbulent b.l.
1987, Westphal et al	Co- and counter-rotating VVGs in turbulent boundary layers $U_\infty=27ms^{-1}$, h O(δ), zpg+apg	In adverse pressure gradients the vortex core grows considerably faster. As the diameter of the core grows to a sufficient fraction of the distance of the core from the wall the velocity contours become elliptical in their shape.
1988, Pauley & Eaton	Vortex pairs embedded in turbulent b.l.s (VVGs). $U_\infty=16ms^{-1}$, h O(δ), zpg	Potential flow theory can define the general motion of the vortex pairs with some modifications for the induced velocity effects. Proximity of the adjacent vortices affects the spreading of the vortex core.
1989, Johnston & Nishi	Vortex pairs embedded in turbulent b.l.s (AJVG). $U_\infty=15ms^{-1}$, h O(δ), zpg	Comparable performance to VVGs in terms of suppression of boundary layer separation demonstrated by AJVGs in the counter-rotating configuration with the flow between them towards the wall.
1990, Lin et al	AJVGs and tangential slot blowing to suppress turbulent b.l. separation ($R_\theta=9000$)	To obtain comparable performance in terms of boundary-layer separation control with tangential slot blowing requires C_Q an order of magnitude higher than $C_Q=0.03$ for the AJVGs.
1992, Compton & Johnston	Single AJVG in a turbulent b.l. $U_\infty=15ms^{-1}$, 0°<yaw<90°	Skin friction enhancement downstream of the AJVG array considerably influenced by the jet yaw angle. Best results for yaw>45°
1992, Selby et al	Controlling separation from a 25° inclined ramp. $U_\infty=40ms^{-1}$	Jet flux, skew angle and jet orientation are critical for AJVG performance. Tangential slot blowing requires a mass flux one order of magnitude greater than AJVGs to achieve equivalent flow separation control performance.
1994, Henry & Pearcey	AJVG in a turbulent boundary layer on a flat plate. $Re_\infty=5\times10^6$	Predictions with the k-ε turbulence model show significant thinning of the b.l. downstream of the AJVG array with a jet-to-freestream velocity ratio of 1
2000, Lewington et al	AJVG in a turbulent boundary layer on a flat plate. $U_\infty=35ms^{-1}$	Simple numerical models can be used to conduct sensitivity studies on the AJVG control process i.e., jet spacing, velocity ratio and array configuration

2.1 High lift systems

Developing aerofoils that are capable of generating high lift with efficient cruise characteristics still creates a dilemma for wing designers. The task requires generating maximum lift without causing the boundary layer on the surface of the wing to separate. Moving a wing through a fluid induces a local increase in the velocity around the upper surface followed by a corresponding decrease in velocity as the flow approaches the trailing edge. As the angle of attack of the wing increases, so do the induced velocities on the suction side ensuring a corresponding increase in the severity of the pressure gradient to decelerate the flow towards the trailing edge. In simple terms, it is the rate of deceleration as the flow approaches the trailing edge that determines whether separation of the upper surface viscous flow will occur.

Avoiding flow separation whilst maintaining the ability to generate lift on aerofoil sections can be achieved with relatively simple geometry changes. Improvements are made possible by altering three main parameters: (i) the chord, (ii) the camber, (iii) the growth of the boundary layer. Changes to the aerofoil geometry, i.e., leading edge radius, camber and variable camber leading edges, have demonstrated improved lifting characteristics but the greatest improvements in aerofoil performance result from deploying leading edge devices (slats) and trailing edge devices (flaps) together, to enhance the flow over the mainfoil. Some examples of leading-edge and trailing-edge devices are shown on Fig. 2.1 over the page. By making the slats and flaps retractable, designers can develop wings better equipped for improved airfield performance and high speed cruise.

Multi-element aerofoils are far from being a new concept with investigations dating back to Handley-Page (1921) and Lachmann (1921). Both authors appeared to recognise that by either placing two aerofoils close together or cutting a slot parallel to the leading edge, sloping upwards and rearwards, enabled up to 25% more lift to be generated by the aerofoil system. However, the fundamental physical principles governing the mechanism of lift enhancement were not identified until fifty years later.
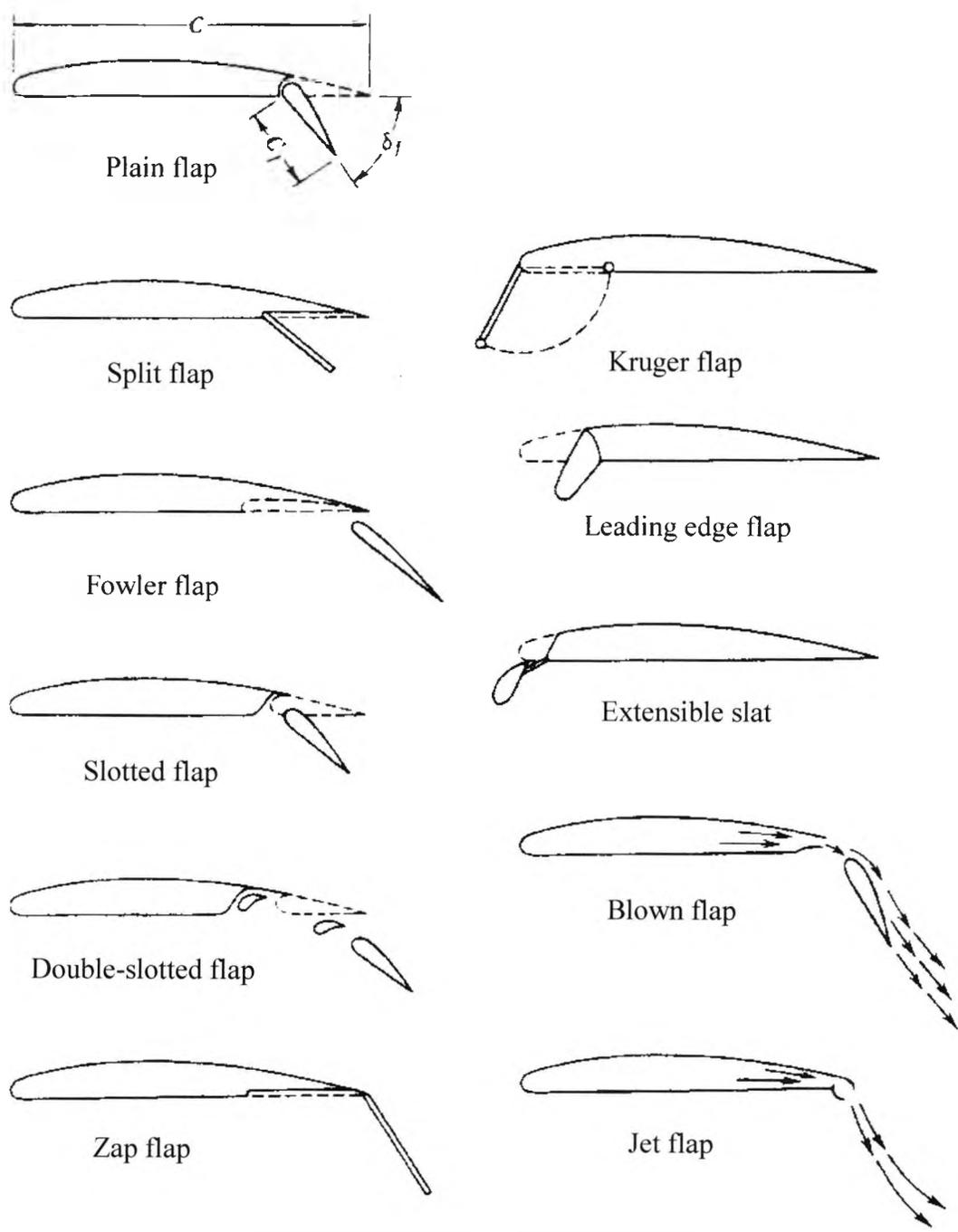
Figure 2.1: Examples of solid and pneumatic leading-edge-and-trailing edge high lift devices, from Shevell (1989)

Smith (1972) categorised the primary effects of properly designed aerodynamic slots on aerofoils. These effects were composed of:

(i) Slat effect - The circulation on the forward element runs counter to the circulation on the downstream element and reduces negative pressure peaks on the downstream element.

(ii) Circulation effect - In turn, the downstream element places the trailing edge of the adjacent upstream element in a region of high velocity, that is inclined to the mean camber line at the rear of this forward element. This flow inclination induces appreciably greater circulation on the forward element.

(iii) Dumping effect - Because the trailing edge of the forward element is in a region of appreciably higher velocity the boundary layer flow 'dumps' at a higher velocity. This higher discharge velocity relieves the pressure rise impressed on the boundary layer, so alleviating separation problems.

(iv) Off-the surface pressure recovery - The boundary layer from the forward element is dumped at velocities appreciably higher than freestream. The deceleration of the wake occurs away from the wall and is usually more effective that any deceleration occurring in contact with the wall.

(v) Fresh boundary-layer effect - Each new element starts out with a fresh boundary layer. Thin boundary layers are better equipped than thicker boundary layers to withstand severe adverse pressure gradients.

The above categories divide the problem of developing high lift into regions of the aerodynamics of the boundary layer and the aerodynamics of the essentially inviscid flow outside of the boundary layer. If wing design is to be successful, interaction between the viscous and inviscid regions of the flow field must be fully understood.

When the boundary layer is attached, viscous effects have only a small influence on the level of lift generated by the aerofoil. But, when a boundary layer separates from

16

the aerofoil surface, there can be catastrophic losses in lift accompanied by corresponding increases in drag. The process of conversion by viscosity of kinetic energy to pressure energy within the boundary layer can only continue to a limited extent within an adverse pressure gradient. On a two-dimensional aerofoil section at the separation point, the streamwise shear stress reaches zero. The streamlines near the surface behave in the manner depicted in Fig 2.2, significantly affecting the inviscid region of flow outside the boundary layer upstream and downstream of the separation point, Thwaites (1960). The physical mechanism of (nominally) two-dimensional separation is largely unsteady but gives the analogous mean flow streamlines for both laminar and turbulent flows except that turbulence is more effective than viscosity at transferring energy from the outer to the inner parts of the boundary layer, Schlichting (1979). Thus, in otherwise similar circumstances, turbulent boundary layers are capable of negotiating more severe adverse pressure gradients than laminar ones.
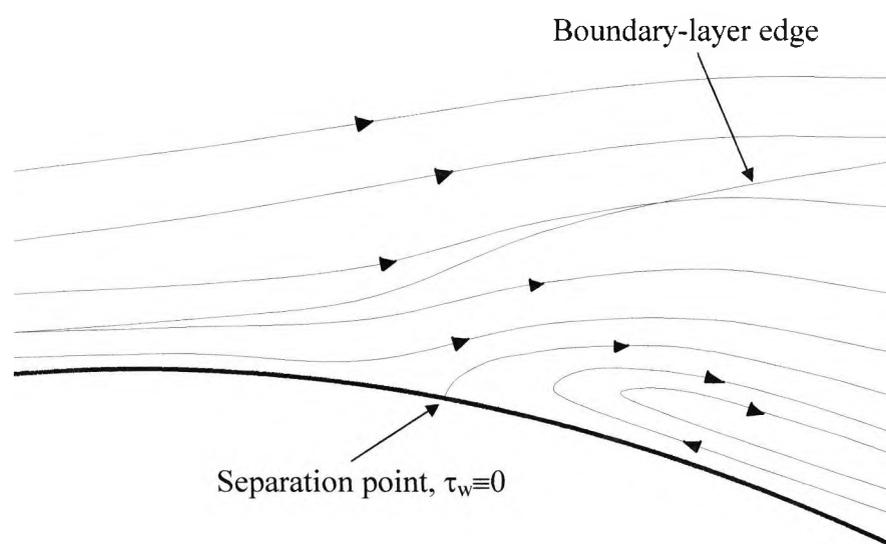
Figure 2.2: Mean streamlines approaching boundary-layer separation in nominally two-dimensional flow

To understand the effect of boundary-layer separation and thus the onset of stall on a two-dimensional high lift system, it is useful to look at the nature of stall itself. Foster (1972) illustrates the nature of two-dimensional stall for a range of single element and multi-element aerofoils in wind tunnel tests at Reynolds numbers based on the chord of the order 10^6 (see Fig 2.3 over the page). He defines three modes of stall on a single

aerofoil as the result of either separation from the trailing edge, separation from a long bubble from the leading edge or bursting of a short bubble near the leading edge. On relatively thick aerofoil sections (thickness chord ratio, t/c, >0.15) in moderate adverse pressure gradients, the turbulent boundary layer will separate near the aerofoil trailing edge. Stall on these thicker aerofoils usually occurs when the separation point moves forward from the trailing edge, on the aerofoil upper surface, as the severity of the adverse pressure gradient increases with increasing angle of attack. On thin aerofoil sections (t/c≈0.12), the laminar boundary layer may separate before transition to a turbulent boundary layer. Transition then occurs in the separated region until the turbulent boundary layer reattaches to form a long bubble. As the angle of attack of the aerofoil increases the length of the bubble extends towards and beyond the trailing edge. During this process the lift curve slope decreases steadily as it approaches maximum lift. Aerofoils with moderate sections (0.12<t/c<0.15) may also experience separation of the laminar boundary layer. However, a turbulent boundary layer reattaches quickly leaving only a short bubble. As the adverse pressure gradient on the aerofoil increases, the pressure in the bubble decreases until some critical value where it bursts, resulting in a catastrophic loss of lift. Foster (1972) observed that the presence of leading-edge separation bubbles reduced the level of suction generated by the favourable pressure gradient around the leading edge (see Fig. 2.3). In applications where high lift generation is an important design consideration, it is desirable to enforce stall to result from a gradual separation of the turbulent boundary layer from the aerofoil trailing edge.
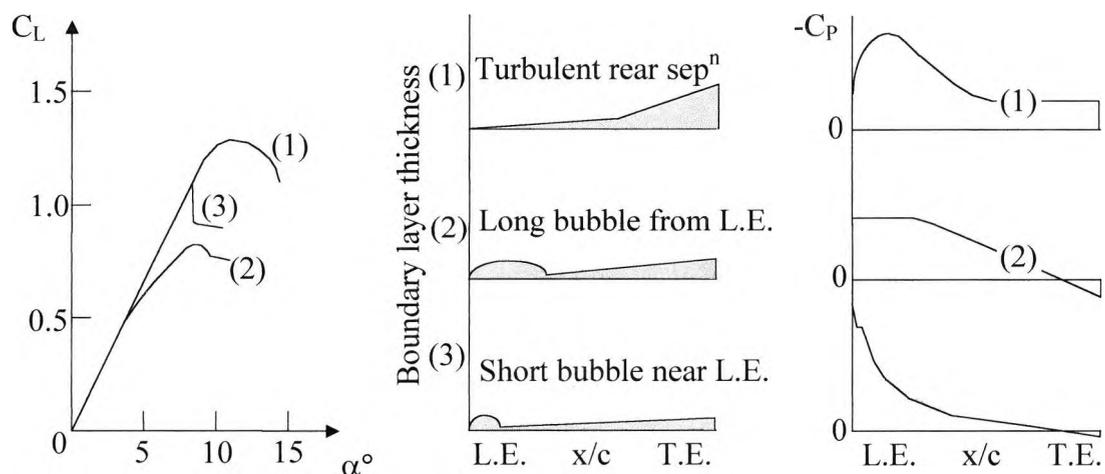
Figure 2.3: Stalling characteristics of single aerofoils, from Foster (1972)

Stall on a multi-component aerofoil may result from the breakdown of flow on either one or more of the upper surfaces of the high lift components or a breakdown of flow on the upper surface of the mainfoil. The surface on which the separation occurs depends greatly upon the location of the high lift device relative to the mainfoil. Investigations on aerofoils equipped with slotted flaps and set up for optimum aerodynamic performance have shown little interference between the mainfoil wake and the flap boundary layer [Foster et al (1970)]. Under these conditions of weak viscous layer interaction the position of separation on the flap component is expected to be invariant with angle of attack. Instead the maximum lift is dependent on the viscous flow over the mainfoil, on which there is a 'simple' boundary layer, and so the corresponding stall behaviour will be analogous to that discussed for a single aerofoil. Aerofoils set-up to generate maximum lift, equipped with both leading-edge and trailing-edge high lift devices, have exhibited extensive mixing between the wake from the slat and the viscous layers above the mainfoil, Foster (1971). The nature of stall for such a configuration is therefore highly dependent on slat position. Figure 2.4 shows the development of the viscous layers on a multi-element aerofoil configured with a leading-edge slat and a trailing-edge flap.
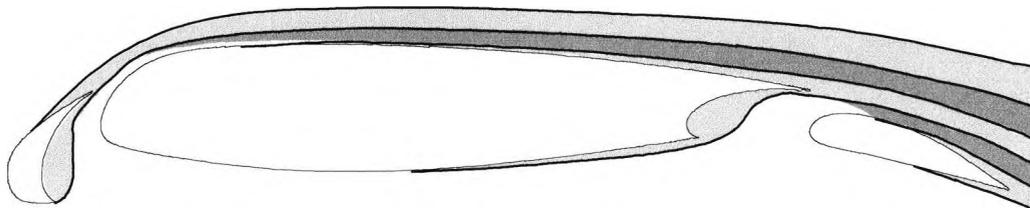
Figure 2.4: Development of viscous layers above multi-element aerofoils, from Foster (1972)

Foster (1972) observed that at low slat angles of attack the severity of the pressure gradient on the mainfoil is considerably less than that of the slat, so that separation usually occurs on the slat. As the slat angle is increased so does the severity of the adverse pressure gradient on the mainfoil, in which case, stall occurs on the mainfoil. Experiments [Foster (1971) and Ljungström (1974)] have highlighted that minimal interaction between the slat wake and the mainfoil boundary layer can induce early boundary-layer transition on the mainfoil, as a result of the presence of the turbulent

wake above the mainfoil boundary layer. This premature transition to a turbulent boundary layer on the mainfoil upper surface then reduces the likelihood of leading-edge stall occurring. Ljungström (1974) also concludes that the viscous flow control effects of increasing the slat gap are essentially the same as reducing the influence of the slat wake on the mainfoil boundary layer.

As the majority of the lift produced by the high lift system is carried by the mainfoil component, the slat and flap settings are often optimised to ensure that stall is the result of trailing edge separation on the mainfoil. Gaining a better understanding of the mechanisms of stall enables the development of efficient high lift systems that can be optimised to generate maximum lift.

Reducing the time required for designers to optimise multi-element aerofoil systems, in terms of leading-edge and trailing-edge device location, relies on the ability to successfully combine wind tunnel experiments and computational methods. However, development of sophisticated prediction techniques is dependent upon having accurate experimental data, on which to base the models of the flow field behaviour, particularly in the off-design scenarios close to stall. The following section details some of the important experimental studies and the computational techniques that have been employed to expedite the development of high lift aerofoil configurations.

2.1.1 Experimental and numerical analysis

Accurate prediction of the flow field around a high lift system still remains a challenging task for all of today's analytical techniques. Primarily, this is because the flow field around multi-element aerofoils contains several complex features, that are not associated with single element aerofoils, even in two-dimensions [as highlighted by King & Williams (1988)].

(a) As the flow field surrounding the multi-element aerofoil is multiply connected, the calculation of the inviscid flow is no longer a simple task.

(b) Wakes from upstream elements are able to merge with the boundary layers connected to downstream components.

(c) Initially, the wakes from upstream elements develop in the strong pressure gradients associated with the downstream components.

(d) Significant normal pressure gradients are generated over the flap due to the thickness and extreme curvature of the viscous flow above the flap.

(e) The curvature of the flow has a significant influence on the turbulence structure of the boundary layers.

(f) Constraints of high speed cruise dictate that the high lift devices must fit snugly around and into the mainfoil. As a result, regions of separated flow are generated in the slat and flap coves when the high lift devices are deployed.

(g) High lift coefficients generated by multi-element aerofoils may lead to regions of compressible/supersonic flow on the upper surface of the slat, even at freestream Mach numbers as low as 0.2.

(h) Extensive regions of separated flow may occur throughout the incidence range when large flap deflections are deployed at landing.

Complete solutions of the flow field are not and may never be possible due to the randomly time dependent nature of the flow in close proximity to the boundaries. Computational approaches, capable of adequately describing the flow field around a high lift system, have, therefore, been developed to hasten experimental optimisation of high lift configurations and shorten the design cycle. As previously discussed, high lift aerodynamics can be separated into that of the boundary layer and that of the essentially inviscid flow outside of the boundary layer. Solving the inviscid Euler equations or employing panel methods enables the flow outside of the boundary layer(s) to be defined relatively simply and accurately. The question of the flow within the boundary layer requires a more sophisticated approach. With multi-element

aerofoils operating at high Reynolds numbers (Re>10^6) transition from laminar to turbulent flow is inevitable. Some form of turbulence modelling is essential if the boundary layer is to be accurately represented.

Solving the Reynolds Averaged Navier-Stokes (RANS) equations coupled with suitably sophisticated turbulence models yields sufficient information to adequately describe the flow field around high lift system geometries. However, up until the last 20 years such techniques have been prohibitively expensive in terms of computer CPU time and storage required for complex geometries. Restrictions imposed by insufficient computing power and inadequate turbulence models meant much of the early theoretical research into wing design relied upon coupled viscous-inviscid interaction approaches to satisfy the tight schedule demands of industry.

The performance of any computational technique can only be assessed upon comparison with reliable experimental data, for which a good degree of accuracy and repeatability of the results has been demonstrated. A dominant factor influencing the performance of high lift systems results from the transport of energy and momentum by turbulence within the boundary layers and wakes. An understanding of the relationships between these phenomena within the boundary layer is essential if computational techniques are to be advanced. Further development of computational techniques requires accurate measurement of the mean velocity profiles, boundary layer transition and fluctuating velocities within the turbulent boundary layers and wakes. Armed with the information from these studies it should then be possible to develop numerical techniques that will account for the current shortcomings of computational methods.

Experimental considerations and examples

If experimental wind tunnel methods are to be successfully utilised interactively with computational methods to optimise the performance of high lift system geometries, it is essential to minimise uncertainties that are inherent in wind tunnel experiments. Discrepancies in experimental results can arise from a number of sources, such as imperfections on the experimental high lift system geometry and instrumentation uncertainty. In tests on unswept aerofoil systems the need to ensure nominal two-

dimensionality of the wind tunnel test flow is of greatest significance. The most common approach to achieve a good degree of two-dimensionality of the wind tunnel flow field is to control the premature separation of the merging boundary layers at the junction of the aerofoil and wind tunnel wall. Failure to do so will result in a region of separated flow spreading in a triangular wedge across the upper surface of the aerofoil system. This introduces a spanwise pumping effect on the separating boundary layer, giving rise to an oscillatory, highly three-dimensional, breakdown of the aerofoil flow field.

As part of the UK National High Lift Programme during the 1970s tests were designed to provide a large degree of accurate two-dimensional data from wind tunnel tests on multi-component aerofoil systems for comparison with computational methods. Moir (1994) details one such set of experiments conducted on a two-dimensional multi-element aerofoil ($Re_c=3\times10^6$). Two-dimensionality of the wind tunnel flow was ensured with local suction at the aerofoil/wind tunnel wall junctions. The two-dimensionality of the flow was checked by comparing the surface pressure distributions monitored at two spanwise locations (0.4% variation of flow uniformity along the chord and insignificant variation across the span) and monitoring tufts on the multi-element aerofoil component surfaces. Measurements were made of the surface pressures on each of the aerofoil system components and pitot traverse methods were employed to determine momentum deficit in the shear layers above the aerofoil and in the wake downstream of the trailing edge. Subsequent integration of these surface pressure measurements enabled the determination of the overall integrated lift, drag and pitching moment coefficients.

The tests described by Moir (1994) and other similar tests Foster et al (1971) provided a valuable source of data for comparing the predictive capabilities of the current computational methods. However, further development of the more sophisticated computational techniques required measurements of the fluctuating velocities within the viscous flow region. Obtaining data of this nature is by no means trivial, as the flow variables are highly sensitive to disturbances in the flow field caused by the measuring devices. Only with the advent of hot wire probes and laser Doppler velocimetry techniques, has it been possible to make accurate detailed measurements

of the shear flows, in order to guide computational code developers as to which flow features should be modelled.

Adair & Horne (1989) made detailed measurements of the flow field around and downstream of a NACA 4412 aerofoil equipped with a trailing-edge flap. Low speed (U_∞=30ms^{-1}) tests were conducted in a closed circuit wind tunnel with the aerofoil at an incidence of 8.2° at a chord Reynolds number of 1.8×10^6. Uniform transition to turbulent flow on the suction and pressure side of the mainfoil and the suction side of the flap was ensured with boundary layer trips. Static pressure taps recorded the pressure distribution around the high lift system and a sting mounted pitot-static tube recorded the freestream and wall boundary layer wind tunnel properties. Upstream of the separation on the flap and throughout most of the wake a stationary hot-wire anemometer was employed to measure the turbulence intensity. In the regions of reversed flow and high turbulence intensity a laser velocimeter was used to capture the flow field characteristics. The results show that the inviscid jet through the slot between the mainfoil and the flap has a dominant effect on the near wall flow over the flap and in the wake. A linear-log region is apparent in the flap boundary layer except in the region of reversed flow. In particular, these experiments highlighted the relationships between the Reynolds normal and shear stresses in the near wall, wake and flap gap flows on the two-element aerofoil.

A similar set of experiments was conducted by Nakayama et al (1990) on a three-element high lift system at two angles of attack. Tests were conducted in the NASA Langley Research Center's Low Turbulence Pressure Tunnel at a nominal Mach number of 0.2 and a chord Reynolds number of 3×10^6. Side-wall blowing was employed to suppress aerofoil wind tunnel wall boundary layer interactions. Two-dimensionality of the flow field was assessed by monitoring the aerofoil surface flow with minitufts and measurements of spanwise pressure distribution at the mainfoil and flap trailing edges. Generally the indications from monitoring the mini-tufts were that the flow directions on the aerofoil surfaces did not vary in the spanwise direction except at the model/wind tunnel wall junctions. However, these results were not identified as being conclusive in regions where the local flow speed and skin friction were very small.

Even with no major separation recorded at the tested angles of attack, considerable thickening and pressure variation occurred across the shear flow regions above the flap and in the near wake. Evidence of wake curvature effects on turbulence were also observed in several regions of the flow field, prompting the idea that flow reversal could first occur in the wake rather than on the aerofoil surface. Turbulence in the slat wake is shown to significantly affect the laminar-to-turbulent transition and boundary layer growth on the mainfoil. Accurate theoretical methods will, therefore, have to include very general methods to be able to adequately predict all of these complexities in the viscous flow regions.

More recently the experiments of Thomas et al (2000) study the development of streamwise boundary layer confluence and its effects on the lift produced by a high lift system. Their results show that the optimal lift performance is achieved when the boundary layer confluence is delayed to the most aft location on the mainfoil. Early confluence results in increased mixing between the retarded wall flow and the slat wake, thus increasing the momentum defect near the wall. As a result, the displacement thickness and momentum thickness grow more rapidly on the mainfoil giving rise to a reduced level of suction on the element.

Detailed analysis of the flow in the near wall region on the mainfoil demonstrates that a classical log-law region exists. Despite the profile differences between a confluent boundary layer and a conventional turbulent boundary layer Thomas et al (2000) demonstrate that the mean velocity profiles can be well represented with algebraic expressions. They show that the inner region of a confluent boundary layer behaves in much the same way as a classic turbulent boundary layer in an adverse pressure gradient but instead of adjusting to the local inviscid freestream the mean flow properties adjust to the velocity imposed by the lower side of the slat wake as the effective 'new' freestream.

Results from these tests have defined the key challenges for CFD code development. Extensive databases of experimental data now exist for two-dimensional tests on high lift aerofoil configurations at low Reynolds numbers ($Re_c < 9 \times 10^6$). However, future

progress in predictive techniques requires similar data to that discussed above for full scale Reynolds numbers tests, as well as, the effects of three-dimensionality on high lift configurations.

Viscous/inviscid flow field solution techniques

The success of coupled viscous/inviscid approaches has been governed by the fact that, throughout the majority of the aerofoil incidence range at high Reynolds numbers, the effects of viscosity and turbulence are confined to relatively thin shear layers in the immediate neighbourhood of the wetted surfaces of the multi-element aerofoil components.

Development of the 'Douglas-Neumann' method by Hess & Smith (1966) permitted, for the first time, the calculation of the inviscid potential flow around arbitrary shaped bodies. A special characteristic of the code was its ability to cope with irregular shapes and the interference effects generated by an ensemble of bodies. Employing this method enabled the determination, for the first time, of inviscid flow fields associated with high lift systems. The potential flow field is simulated by a continuously varying vortex sheet around the surface of the body. The vortex sheet consists of a series of N straight-line segments (panels), tangential to the body surface, at the centre of which the source and vortex strength is defined. A constant value of the singularity strength is assumed at the centre of the panel but may vary from one panel to the next. Defining the circulation as the sum of all the vortex strengths yields N simultaneous equations. To obtain a square system of N+1 equations, the Kutta condition is imposed at the aerofoil trailing edge, that equates both of the tangential velocity components on the upper and lower surfaces of the aerofoil. Solving the set of N+1 simultaneous equations then enables the determination of the aerofoil surface tangential velocities and pressures centre of each panel. By assuming that the pressure on each panel remains constant, integrated lift and pitching moment can be estimated.

The complexities of multi-element aerofoil geometry and the often neglected effects of compressibility has resulted in a wide use of relatively simple approaches such as the 'Douglas-Neumann' method described above, to predict the behaviour of the

inviscid flow field. Field methods are available but often require extensive work to generate suitable meshes on which to discretise the full Euler equations. Such methods require a grid of points surrounding the aerofoil system with very fine meshes in regions where the flow velocity and pressure change rapidly. To accurately derive the numerical boundary, it is advantageous to ensure that the mesh conforms to the high lift system solid surface(s). This becomes exceptionally difficult when the slat and flap gaps are small. Hall & Suddhoo (1984) employed a finite difference method to solve compressible potential equations on a two-component aerofoil. The grid is produced by conformally mapping the regions exterior to two aerofoils to the annular region between two concentric circles. Clarke et al (1985) solve the Euler equations on a Cartesian grid that does not conform with the aerofoil surface. In this case, an approximation is used to replace the boundary condition. Other approaches such as Oskam (1983), employ a field method in the regions where compressibility effects are likely to occur and utilise surface-singularity techniques elsewhere. Patches of boundary-conforming grids are generated in the regions where compressibility effects are significant. The full potential equations are solved with a fully-conservative finite-volume method. On three sides of the mesh the boundary conditions are imposed by surface singularity methods whilst the fourth is represented as the aerofoil surface. Each of the field methods described above demonstrated the ability to represent the flow field characteristics around multi-element aerofoils. However, they were limited by the need to know the locations where compressibility effects were important and the difficulties of defining grids when the slat and flap gaps are small. These problems are relatively simple to deal with in two-dimensional flows but were far more difficult to estimate on three-dimensional configurations.

Contained within the two-dimensional incompressible turbulent boundary layer equations are terms representing the fluctuating velocity components (Reynolds stress terms). The relationships between these terms and the mean velocity distribution within the boundary are complex and difficult to define. In the past, treatment of the viscous side of the problem employed the basic assumption of 'classical' boundary layer theory, i.e., there is no variation in pressure across the boundary layer, only the normal derivatives of shear stress are important and the Reynolds normal stresses can be neglected. A relatively simple method (integral methods) to predict physically

relevant flow fields was achieved by integrating the shear layer properties with empirical relationships for the higher-order viscous effects, such as streamline curvature effects on the level of turbulence within the boundary layer.

A variety of these 'integral' methods have been produced with work dating back to Thwaites (1960) one-equation method for the laminar boundary layer. This method fails in regions of separated flow, as it links the shape parameter H to the local pressure gradient that is a non-unique relationship when separation is present. Better agreement with experiments, by employing predictive methods that are capable of dealing with thin separated regions, have been demonstrated by utilising two-equation integral formulations based on dissipation closure. Most notably the work of Stevens et al (1971), Brune and Manke (1978), Whitfield (1978) and Le Balleur (1981) have highlighted the ability of the two-equation integral approach to predict the flow field around aerofoils at off-design angles of attack. Two-equation integral methods rely on solving the integral momentum and kinetic energy shape parameter equations around the aerofoil surface as shown in equations (2.1) and (2.2) respectively.

$$\frac{d\theta}{d\zeta} + \left(2 + H - M_e^2\right)\frac{\theta}{u_e}\frac{du_e}{d\zeta} = \frac{C_f}{2} \tag{2.1}$$

$$\theta\frac{dH^*}{d\zeta} + \left[2H^{**} + H^*(1-H)\right]\frac{\theta}{u_e}\frac{du_e}{d\zeta} = 2C_D - H^*\frac{C_f}{2} \tag{2.2}$$

Closure of the integral boundary layer equations is then achieved by defining functional dependencies for the velocity profile shape upon the dissipation coefficient (C_D), the shear stress coefficient (C_f), the kinetic energy shape parameter (H^*) and the density shape parameter (H^{**}). This provides the designer with a quick, simple and accurate method of predicting the aerofoil flow field characteristics, even up to stall.

Better estimates of the higher-order viscous effects, such as boundary layer/wake and wake/wake confluence, which are approximated with empirical relations in the integral methods, are possible by solving some form of the (time-averaged) Navier-Stokes equations within the viscous region. To alleviate some of the shortcomings

28

associated with integral methods, 'differential' methods that solve the full partial-differential equations describing the flow in the viscous region were developed. Solutions for the viscous layers are obtained by adequately defining the change in the Reynolds stresses with the mean velocity distribution. Cebeci & Smith (1968) describe a method based on the eddy-viscosity concept to solve for the complete boundary-layer characteristics, including transition and separation points. Although adequate for predicting attached flows, the results achieved with this simplified algebraic method become increasingly unsatisfactory as the flow on the aerofoil upper surface approaches separation. However, the algebraic method of Cebeci & Smith (1968) does provide the wing designer with a relatively simple tool that can be readily implemented to analyse the flow field qualitatively.

Complete analysis of the boundary layer associated with low Reynolds number flows ($Re_c \approx 10^6$) requires some representation of laminar to turbulent transition. A common approach is to employ the spatial amplification theory of Orr-Sommerfield that is essentially the e^9 method pioneered by Smith (1956). The method assumes that transition occurs when the most unstable of the Tollmien-Schlichting (T-S) waves has grown by a factor of approximately e^9. This correlation is arrived at by studying the maximum amplification ratio of the T-S waves for a number of aerodynamic flows. In all, 28 different body shapes were examined in 9 different test environments, including bodies of revolution, convex plates in channels, aerofoils in flight and aerofoils in wind tunnels. Calculation of the amplification factor requires the disturbance growth rate to be related to the local boundary layer parameters (the local skin friction, the turbulence structure and the amplification factor). One method is to use the Falkner-Skan profile family Falkner & Skan (1931) to solve the Orr-Sommerfield equations for a range of shape parameters and unstable frequencies. Employing this technique, Gleyzes et al (1985) have shown an approximation for the integrated rates of the amplification factor as:

$$n = \frac{dn}{d\,Re_\theta}(H_k)[Re_\theta - Re_{\theta 0}(H_k)] \tag{2.3}$$

where $\dfrac{dn}{d\,\mathrm{Re}_\theta}$ and $\mathrm{Re}_{\theta0}$ are the amplification theory slope and critical Reynolds number based on empirical relationships and H_k is the kinematic shape parameter. The advantage of this approach is that the location of transition can be directly related to the streamwise co-ordinate along the aerofoil surface, and so can be specified or determined within the boundary layer formulation. Although, no more accurate than other methods of predicting transition (see Arnal 1997) the above approach enables the user to account for boundary-layer transition at any location on the aerofoil surface.

Once a technique is established that is capable of adequately representing the viscous and inviscid regions of the desired flow configuration, the next step is to couple both solutions via a boundary condition on a matching surface. Perhaps the most obvious position for the matching surface is the outer edge of the shear layer on the aerofoil surfaces. Employing this common technique ensures no overlapping of the inviscid and viscous solutions and minimises the number of calculations required for the inviscid region, irrespective of whether panel or field methods are being employed. There are, however, two main disadvantages associated with defining the matching surface between the viscous and inviscid regions as being the shear layer edge. Firstly, neither the location of the shear layer edge and the velocity distribution normal to the matching surface are known prior to calculation, and therefore an iterative method is required to define the surface. Secondly, in flows where shock boundary-layer interactions are significant, it is impossible to represent the pressure variations across the boundary layer at the foot of the shock with this choice of matching surface. Le Balleur (1981-83) showed that the failure of the approach at higher Mach numbers was entirely due to a mathematical characteristic of the interactive scheme and its inability to represent all the pressure variations across the boundary layer near the shock. What is more significant is that Le Balleur showed it was possible to delay these difficulties to higher Mach numbers by making the matching surface at the displacement thickness; but he also shows that the problems could be completely eliminated if the matching surface is integrated up to the 'wall' itself. This latter approach (known as the surface transpiration technique) has now formed the basis for the majority of integral boundary layer methods as it forms the basic framework for

the numerical solutions. Definition of a fixed surface that couples the two solutions then enables a solid boundary condition on which to define the source distribution in the panel method solutions and the numerical grids for the field methods.

The marriage of viscous/inviscid solutions is often highly dependent on the level of interaction between the two flows, i.e., whether the flow is attached, separating or separated. For weak interactions, converged solutions are possible by solving the inviscid flow to provide the boundary conditions for the viscous region via an iterative process. Beyond separation some form of inverse method is required as the viscous layer has a significant influence on the inviscid flow behaviour. To obtain a converged solution near separation, where neither inviscid nor viscous flows dominate, the simultaneous solution of both regions may be preferred. In recent years these three main approaches have been identified as the 'direct', 'semi-inverse' and 'quasi-simultaneous' methods. The reader is referred to <u>Lock & Williams (1987)</u> for a comprehensive view of coupling techniques.

Applications of viscous/inviscid techniques

Callaghan & Beatty (1972) show significant improvements in the potential flow predictions of the flow field around both single and multi-element aerofoils by the inclusion of the viscous flow. They employed the 'Douglas-Neumann' potential code for the inviscid flow with the differential method of <u>Cebeci & Smith (1968)</u> and the transition correlations of Smith (1956). Predictions were compared with results from the McDonnell-Douglas two-dimensional high lift development experimental programme. Low speed tests were conducted on a typical transport high-lift planform with a 27 inch chord. The large amount of flow separation and steep adverse pressure gradients associated with high lift systems often induces premature separation near the wind tunnel walls by increasing the interaction between the model and wind tunnel wall boundary layers. Side wall suction was employed here to limit the endwall boundary layer growth and thus reduce three-dimensional effects. While potential flow predictions qualitatively represented the flow field, it generally over-predicted the total lift force. Callaghan & Beatty (1972) showed that by inclusion of the differential method to model the viscous effects, lift coefficient predictions were

reduced from 30% to 3% above that of the experiment including flows where some flow separation was observed on the mainfoil upper surface.

Bhateley and Bradley (1972) employed a similar surface singularity method to Callaghan & Beatty (1972) for the inviscid flow coupled with differential boundary method as discussed above. However, estimates for an entire angle of attack sweep were investigated by making provision for the effects of boundary-layer separation on the multi-element aerofoil system components. Transitional effects were studied by relating the momentum thickness Reynolds number with a criterion for analysing the effects of laminar separation bubbles and their behaviour. Separated flow regions were approximated by assuming that the equivalent body contour follows a separating streamline that emanated from a separation point, as indicated by the boundary layer calculations. Attempts were also made to approximate, analytically, the nature of the separating streamline by flow visualisation techniques in experiments. Experiments were conducted as part of the high lift system research and development programme at the National Research Council, Ottawa, Canada, with a 2-foot-chord model, a nominal Mach number of 0.2 and a chord Reynolds number of 2.5 million. Nominally two-dimensional flow was imposed throughout the incidence range by employing endwall blowing to eliminate wall/model boundary-layer interference. Comparisons of predicted pressure distributions with the experimental data show the model is capable of reasonably representing the flow near stall with only minor discrepancies near the trailing edge, that increase with increasing trailing edge stall. These discrepancies are the result of the inability of the differential model to represent pressure conditions in the separated wake.

An example of an integral boundary layer method that does not requires the definition of a grid around the aerofoil surface is demonstrated in the work of Jacob & Steinbach (1974). They employ a surface singularity method for the potential flow coupled with an integral dissipation method described by Rotta (1968) for the viscous calculations. The code makes provision for separation and transition by taking into account the Reynolds number of the flow based on the chord length. Below $Re \approx 5 \times 10^4$ a calculated laminar separation point is enforced with no turbulent reattachment. Above $Re \approx 1 \times 10^5$, turbulent separation and transition are either defined from experimental

results or defined at the point of laminar separation. These constraints ensure the highly unpredictable effects resulting from the formation of laminar separation bubbles and sudden bursting of these bubbles are neglected. Stall is always assumed therefore to be a consequence of trailing-edge separation. Definition of a separation point also allows the calculation of the potential flow along a separating streamline. Results for the multi-element aerofoil are compared with the $C_L(\alpha)$-curve from the experiments of Foster et al (1970). Good agreement between predicted and experimental results is obtained for several multi-element configurations in terms of maximum lift and stall angle prediction. The authors conclude that, although, relatively difficult to program once the method is established it can easily be applied to a number of alternative configurations. Suggested improvements in the code's capabilities require a method of accounting for the effect of the merging shear layers and wakes from the high lift system components.

One method that accounts for the confluent boundary layers above the multi-element aerofoil surface is described by Brune & Manke (1978). The code is essentially a modified version of the viscous flow solver of Stevens et al (1971). There are four main modifications to the aerodynamic model to account for some of the more complex features associated with multi-element aerofoil flow fields. These modifications include; (i) representation of the aerofoil surface boundary layer and aerofoil component wake displacement effects with the surface transpiration technique, (ii) the prediction of wake parameters with the lag-entrainment method of Green et al (1973), (iii) provision for turbulent boundary layer separation with the method of Nash & Hicks (1968) and (iv), estimation of the onset of confluent boundary layer separation with the method of Goradia & Lyman (1974). A surface-singularity method is employed for the inviscid flow that permits the inclusion of the viscous flow displacement effects by utilising the surface transpiration technique, over the aerofoil surface and wake centreline. Here the source strength (Λ) on the displaced surface is defined as being proportional to:

$$\Lambda = \frac{d}{ds}\left(\delta^* U\right) \qquad (2.4)$$

where δ^* denotes the displacement thickness and U represents the local velocity of the inviscid flow. Representation of the wake centreline is achieved by extending the stagnation streamline from the trailing edges of the high lift system components. The laminar boundary layer is determined with a compressible method and provision for a specified or calculated transition location is included. Use is made of two integral methods to calculate the turbulent boundary layer. The incompressible method of Truckenbrodt (1955) based on the energy and momentum integral equations, during the iterative cycle and the method of Stevens & Goradia (1971) that avoids failure of the boundary layer method as separation is approached. Turbulent boundary layer separation is taken into account by studying the upstream effects of turbulent shear stress with the method of Nash and Hicks (1968) at the end of the iterative solution procedure. The properties of the wake are analysed with the lag-entrainment method of <u>Green et al (1973)</u> which enables calculation of the profile drag of the high lift system. Confluence of the upstream wakes and boundary layers is accounted for by assuming a composite profile boundary layer merging with one wake and special treatments for the channel like flows between aerofoil elements. The code is validated by comparing predictions to a host of experimental data for single and multi-element aerofoils: most notably, the comparisons with the unpublished results on a four element high lift aerofoil system conducted in the Boeing Research wind tunnel. Tests were conducted on the 2-foot un-extended chord model with a 5-foot span at a chord Reynolds number of approximately 2 million. Endwall blowing was utilised to closely approximate two-dimensional flow conditions across the complete span, at least up to stall. Good agreement between theory and experiment for the chordwise surface pressure distribution and integrated normal force below the onset of trailing edge stall is shown for both single and multi-element aerofoil configurations. Results show the quality of the predictions deteriorate rapidly with the increasing degree of separation at the trailing edge and in the cove regions. Drag predictions are less encouraging though with notable discrepancies between theory and experiment for all of the aerofoil configurations. The discrepancies between theory and experiment cannot be solely attributed to the chosen viscous/inviscid technique. The presence of large regions of separated flow in the experiment questions the validity of assuming a two-dimensional flow field in which to determine the profile drag. The authors conclude that the best agreement between the predictions and the experiment were

34

demonstrated for flow fields where the flow is mainly attached. For this reason further tests are required in the off-design aerofoil configurations to adequately test the flow field for the entire flight envelope.

Field methods have also highlighted their potential for reasonably accurate prediction of the chordwise pressure distribution and profile drag downstream of the high lift system. Drela (1990) employed a streamline based Euler discretisation coupled with a two-equation boundary-layer integral formulation, via the displacement thickness, to analyse the flow field associated with a 4 element high lift system. The flow solver calculates the inviscid stream lines around the multi-element aerofoil using a surface singularity method. The numerical grid is then generated across these streamlines by defining normal streamlines that are orthogonal to the multi-element component surfaces. One advantage of this solution technique is that the field mesh can be continually updated during the solution process, to account for the displacement effects of the surface boundary layers and multi-element aerofoil component wakes. The computational method also demonstrates that once a converged solution for a single angle of attack has been obtained only a few more iterations are required to calculate the flow fields at alternative angles of attack. Code validation was assessed using data from the experiments of Brune & Sikavi (1983), in which detailed measurements of the surface pressure distribution, velocity profile and wake profile drag were made. Good agreement is shown throughout the majority of the polar sweep for both integrated lift and drag characteristics. There is slight over-prediction of the maximum lift that the authors attribute to the absence of boundary-layer confluence effects in the calculation. The experiment clearly shows the slat wake and mainfoil boundary layer merging as the combined system flows downstream. As the merged wake enters the strong pressure gradients associated with the aft flap elements, there is a tendency for flow reversal to occur in the wake, limiting the maximum lift that can be generated. The slat wake confluence, therefore, has significant implications on the multi-element aerofoil lift performance. Drela's method enables reasonably accurate, rapid calculations for the two-dimensional flow fields associated with multi-element aerofoils, throughout the majority of the angle of attack sweep. The code provides a good platform to guide sophisticated RANS solutions for two- and three-dimensional flow fields.

While some impressive results have been demonstrated employing viscous/inviscid techniques, many of the essential flow field parameters still require an accurate solution of the time-averaged Navier-Stokes equations. The advent of increased computing power and storage has focussed recent research towards utilising and developing RANS methods. In regions where the effects of viscosity are small, solutions for the flow field variables can be readily obtained with simple finite volume methods. However, in the majority of multi-element high lift aerofoil applications there is transition of the boundary layer from laminar to turbulent flow. To ensure that RANS techniques can adequately represent the flow field, some method of predicting transition and turbulence quantities within the viscous flow field is necessary. The following discussion outlines the procedure for RANS methods when predicting multi-element aerofoil flows and some most common turbulence modelling techniques utilised in these solutions. The reader is also referred to Table 2.1 for the key milestones in high lift system flow field prediction with RANS techniques.

Reynolds averaged Navier-Stokes methods

The complex nature of the flow field and geometry of high lift systems requires large numbers of grid nodes to resolve the steep variations of the dependent variables in the numerical solution. As single structured body-conforming grids cannot be generated for most practical geometries, suitable flow field discretisation methods have been developed to enable solutions of the RANS equations to be obtained. The most popular methods currently employed use either structured multi-block grids, Chimera based overlapping grids or unstructured meshes to adequately discretise the solution domain [see Jasper et al (1993) for a comparison]. Multi-block structured approaches require the computational domain to be subdivided into regions in which the control volumes with the region have one-to-one point connectivity. This method requires slightly larger meshes to ensure adequate grid resolution but enables easier implementation of the numerical flow solver. Examples of the applicability of multi-block methods to multi-element high lift flows are shown in the work of Bartsch et al (1989), Rogers et al (1992) and Godin et al (1997). A Chimera overlaid grid approach enables independent generation of structured meshes around the high lift system that do not need to match at the block boundaries. As a result, the quality of the mesh on

the aerofoil surface is not compromised by the dependency on the grid in the outer zones of the computational domain. Rogers et al (1992) conclude a Chimera over-laid grid approach enables detailed flow characteristics to be captured with much less effort required for grid generation. Unstructured meshes lend themselves most readily to the complex geometries associated with high lift systems, due to the relative ease with which a computational mesh can be generated for the complex high lift system geometry, as reported in the work of Anderson & Bonhaus (1993) and Valarezo & Mavriplis (1993). Definition of point clouds for the tetrahedral cells in the regions of greatest significance within the flow field allows the flow characteristics to be accurately represented. However, unstructured flow solvers suffer mainly from two pitfalls. Firstly, highly stretched cells at the wall boundaries can introduce inaccuracies into the flow solutions, as relevant flow variable gradients are approximated with linear methods across the cell boundaries. Secondly, each tetrahedral cell in an unstructured mesh requires its own local co-ordinate system, which results in an increase in the required computer storage and CPU time to achieve a solution.

Upon adequate discretisation of the computational domain, successful analysis of the flow field around a multi-element aerofoil is dependent on the application of a suitable turbulence model to adequately define the behaviour of the flow within the viscous shear layers. Unfortunately, the question of modelling the turbulence still remains a major stumbling block. Turbulence models that are simple enough for practical application are often over-simplified and thus incapable of accurately describing all the features of the flow. In particular, the effects of streamline curvature on wakes [Bradshaw (1973)], transition and boundary layer confluence [Ying et al (1998)], all of which have a significant effect on the lift and drag characteristics of high lift systems, are often neglected. Sophisticated turbulence models are available, that approximate the higher-order effects of modelling the Reynolds stresses. However, the more sophisticated turbulence modelling techniques often require a level of empirical data, to achieve a converged solution, that can only be obtained from extensive wind tunnel tests. As a result, the reliance of sophisticated turbulence models on empirical data, limits their ability to be used as effective design tools. The

three most common turbulence modelling approaches are introduced below, but for a more sophisticated discussion of turbulence modelling techniques see Section 3.5.

In laminar flows, energy dissipation and transport of mass, momentum and energy normal to the streamlines are governed by the viscosity of the fluid. The relationship between the fluid properties and viscosity lead to the assumption that turbulence could be represented as an increase in viscosity (the eddy viscosity). Early attempts to predict turbulent flows (that is zero-equation models) define the eddy-viscosity by relating the turbulent kinetic energy, or a velocity scale to a length scale [see Cebeci & Smith (1968) and Baldwin & Lomax (1978)]. Although adequate for attached flow scenarios, the models have difficulty describing the confluent boundary layers and flow behaviour when separation is present. More accurate and robust solutions have been demonstrated by employing one-equation models of Baldwin & Barth (1991), (B-B) and Spalart & Allmaras (1992), (S-A). The B-B and S-A models are versions of the two-equation k-ε turbulence model that are simplified to solve only one transport equation to determine the eddy viscosity. The final commonly employed approach is to use two-equation turbulence models calculating the distribution of the length scale of the turbulent vortical structures and the turbulent kinetic energy. Examples of two-equation models frequently employed for aerodynamic flows are modifications of the k-ε model of Launder & Spalding (1974) and the k-ω model of Wilcox (1988). The following section highlights some of the studies the author believes indicates the ability of the turbulence models to adequately represent the flow fields about multi-element high lift systems.

Applications of RANS techniques

Bartsch et al (1989) employ a conservative finite volume approach to solve the full Navier-Stokes equations coupled with the k-ε turbulence model on a general non-orthogonal multi-block structured grid around two separate multi-element high lift systems. Wall functions are employed within the flow field solutions to describe the rapidly varying turbulence parameters close to the aerofoil surface. No provision for laminar-to-turbulent transition is made, thus, the flow is assumed to be fully turbulent throughout the tested angle of attack range. In order to reduce the computer storage space required to obtain solutions for the flow field, all dependent variables were

stored at the centre of the control volume, as opposed to utilising a staggered grid arrangement. Central differences were employed to discretise the diffusive fluxes and a combination of central and upwind differences to discretise the convective fluxes. With no explicit equation for pressure in the incompressible formulation of the Navier-Stokes equations the SIMPLE algorithm of Patanker & Spalding (1972) is employed to link the pressures to the velocities. This computational technique offers a relatively 'inexpensive' method of adequately simulating the flow field around both two-dimensional and three-dimensional multi-element aerofoil configurations without the need to resolve for flow field variables in the near wall region. Predicted results for the surface pressure distributions, mean velocities and Reynolds stresses are compared with the experiments of Adair & Horne (1989). Relatively good agreement between predicted and experimental results is shown for the surface pressure distributions. The flow solver constantly under-predicts the peak suction on each component of both high lift systems and fails to predict separation at the trailing edge. Significant deviations from the experiment are shown in the mean velocity and Reynolds shear stress profiles as the computed wakes appear to spread more rapidly than those in the experiment. Nevertheless, the computational technique is capable of identifying experimental trends observed in the flow field around complex multi-element high lift configurations. As a result, the technique readily lends itself to an interactive computational/experimental high lift design optimisation method for both two- and three-dimensional flow fields.

Investigations by Rogers et al (1992), Jasper et al (1993) and Nelson et al (1999) studying the flow fields associated with a range of single and multi-element aerofoils highlight the robustness and superiority of the B-B method over the earlier zero-equation models to predict multi-element flows. The multi-block structured and Chimera grid generation approaches were coupled with the ARC2D, CFL3D, INS2D and PEGSUS incompressible flow solvers to discretise the solution domain. An incompressible approach was deemed valid as the effects of compressibility should be confined to relatively small regions near the leading edge with the aerofoil in the take-off and landing configurations. Transition in the computations is modelled by setting the respective production and eddy-viscosity terms in the Baldwin-Barth (B-B) model and Baldwin-Lomax (B-L) model to zero upstream of the defined transition location.

Computed results for the NACA 4412 aerofoil equipped with a trailing-edge flap were compared with the experiments of Adair & Horne (1989). The computational results led to each of the groups of authors concluding that the B-B turbulence model performs significantly better than the B-L turbulence model for multi-element flows. Very good agreement is shown between computed results and the experiment for the surface pressure distribution with some discrepancy when flow separation is present. Notable difficulties are apparent when the flow solvers encounter laminar separation bubbles, multiple regions of separated flow and unsteady wake flow. Better agreement between the mean velocity profiles and Reynolds shear stress profiles is also demonstrated using the B-B model when compared with the previous findings of Bartsch et al (1989) for the NACA 4412 aerofoil equipped with a trailing-edge flap. Further improvements in predictive capabilities are expected if the turbulence models can be modified to better represent the experimentally demonstrated non-linearities of the pressure gradients in the near wall and near wake regions of the high lift system flow field. However, the constraints of increased computer storage and CPU time to solve the modified turbulence models may limit the effectiveness of the methods as design tools.

Modified versions of the k-ε turbulence model either employing wall functions or integrating up to the wall have indicated the potential for improved predictions of the turbulent wake structure. Valarezo & Mavriplis (1993), Rogers et al (1994) and Nelson et al (1999) all employ the k-ω Shear Stress Transport (k-ω SST) model of Menter (1992) to predict the flow field around a range of multi-element aerofoils. The k-ω SST model eliminates the sensitivity of ω in the free shear layer flows by switching to an alternative form of the k-ε turbulence model away from the near wall region. In most cases, the laminar-to-turbulent boundary layer transition is modelled by switching off the production terms. Although switching off the production terms in the turbulence models accounts for some laminar flow over the aerofoil surfaces, the method is crude and has no physical meaning. Little variation in the predicted surface pressure distributions is apparent in the results obtained with each of the tested turbulence models when the majority of the flow is attached on the high lift system components. However, when flow separation is substantially established, results

obtained with the two-equation k-ω SST turbulence model have demonstrated much better agreement between predicted and experimental maximum lift characteristics. The superior performance of the k-ω SST turbulence model is primarily due to the fact that it accounts for the transport of the principal turbulent shear stresses in adverse pressure gradient flows. Analysis of the mean velocity profiles show differences between each of the computations and the experiment, particularly with respect to the predicted boundary layer confluence and the velocity deficits from upstream wakes. Results obtained with the S-A turbulence model exhibit better agreement with experimentally determined mean velocity profiles, in flows where separation is negligible. When separation is dominant, the k-ω SST model again yields better agreement between the computational and experimentally determined trends.

Difficulties experienced in accurately computing maximum lift for multi-element flows has prompted a number of CFD workshops to discuss the further development of more advanced numerical techniques. In separate studies initiated by the CFD Society of Canada [Fejtek (1997)], the NASA CFD Challenge Workshop [Ying (1996)] and the GATEUR high lift programme [Lindblad & De Cock (1999) and Lorentzen & Lindblad (1999)] state of the art numerical techniques have been employed in an attempt to predict the complex flow fields associated with multi-element high lift systems.

Fejtek (1997) summarises the results of the computer code validation exercise instigated by the CFD Society of Canada. Numerical results were validated with the experimental data described by Moir (1994) covering a series of AGARD sponsored wind tunnel tests specifically designed for CFD validation purposes. The choice of experimental data for validation reflects the acknowledged high degree of accuracy and repeatability reported in the wind tunnel tests. Experiments were conducted on a three element high lift system in the take-off configuration with respective slat and flap deflections of 25° and 20°, at a Mach number of 0.197 and a chord Reynolds number just above 3 million. Reliable two-dimensional surface pressure distribution, pitching moment, drag and velocity profile experimental data were available for an angle-of-attack range 0° through 23°. Laminar-to-turbulent boundary layer transition

41

was fixed at 12.5% of the chord on the upper and lower surfaces of the mainfoil with natural transition occurring on the slat and flap components. Fixing transition ensured that stall of the multi-element high lift system resulted from trailing-edge boundary layer separation on the mainfoil component. As a result, the difficulties associated with predicting the highly non-linear effects on the flow variables that exist in laminar separation bubbles were eliminated.

Ten participants in the CFD code validation exercise, employing both viscous/inviscid and RANS approaches to analyse the flow field characteristics, obtained results for the surface pressure distributions around the multi-element high lift system and mean velocity profiles above the mainfoil and flap elements. Seven participants employed block-structured or overlaid meshes, two utilising an unstructured mesh and one requiring no field mesh. Both incompressible and compressible flow equations were solved on two-dimensional and three-dimensional meshes coupled with either integral boundary-layer methods or one/two-equation turbulence models. The two viscous/inviscid approaches employed the lag-entrainment method of Green et al (1973) for the turbulent boundary layer coupled with, for the inviscid flow, a full potential flow equation method on a Cartesian mesh and a surface-singularity distribution method. RANS solutions were obtained with the one-equation S-A and two-equation k-ω SST and k-g turbulence models. Transition predictions are included in some of the calculations with the e^9 method Smith (1956), the Boeing transition model, or setting the turbulence transport equations to zero upstream of the transition strip on the experimental model.

Predicted results of the lift, drag and pitching moment highlight the inability of the viscous/inviscid techniques to model the flow field as viscous effects become significant and the boundary layers separate. Deviations from the experimental trends are demonstrated to be significantly reduced by employing RANS methods. At higher angles of attack, results obtained with the incompressible flow solvers are incapable of describing the lift, drag and pitching moment characteristics due to compressibility effects on the variation of the pressure field. The findings presented by Fejtek (1997) are echoed in all three CFD validation exercises mentioned above. Each author concludes that to be able to predict the flow field accurately around a multi-element

42

high lift system, the designer must ensure that within the computations the following issues are addressed:

- The grid density around the multi-element high lift configuration must be suitably fine to capture all of the relevant turbulent flow physics.
- The location and method of predicting boundary-layer transition is sophisticated enough to mirror the experimentally observed findings.
- The RANS method must employ, at least, a one-equation turbulence model to define the fluctuating flow field characteristics in the near wall and near wake regions.
- The effects of compressibility on the flow field variables are modelled so that the confluent boundary layers above the high lift system are adequately defined.

Although good agreement between computational and experimental data has been demonstrated for two-dimensional multi-element aerofoils by employing both viscous/inviscid and RANS computational techniques, the development of these techniques is demonstrated to be highly dependent upon the availability of accurate and reliable experimental data, to identify the turbulent flow physics and to benchmark the numerical techniques against. The difficulties associated with predicting multi-element high lift flows demonstrate that the current state of the art of CFD techniques does not eradicate the need for wind tunnel experiments. However, CFD techniques can expedite the optimisation of multi-element high lift systems by enabling designers to identify beneficial trends associated with component profile modifications and lap and gap settings without the need for extensive wind tunnel testing. CFD therefore has a significant role in the development of optimum high lift configurations in both two-dimensions and on a three-dimensional wing.

Enhancements in high lift system capabilities have been demonstrated by gaining a better understanding of the flow field and by the ability to engineer variable wing geometries. However, further improvements in the lift and drag characteristics have been demonstrated by the implementation of 'passive' or 'active' boundary layer control. Innes et al (1995) show that employing vane and air-jet vortex generators on a three component high lift system enabled considerable extension of the angle of attack range, whilst increasing the maximum generated lift by up to 30%. It follows that

43

coupling a suitable CFD technique with high lift and flow control technologies will permit the design of improved high lift configurations. The following section details some of the most significant computational and experimental investigations of passive and active flow control techniques to date.

2.2 Passive and active flow control with vortex generators

The purpose of any flow control device is to enhance the momentum transfer within the boundary layer to delay the onset of flow separation. By far the most popular method currently employed to delay boundary-layer separation in a variety of external and internal aerodynamic flows is the installation of protuberance-type vortex generators (VGs). These devices work by inducing the local boundary-layer and freestream flow to form well-organised vortical structures, as the combined flow penetrates downstream. Increased mixing is promoted as high momentum fluid from the freestream is swept along a helical path towards the surface. Likewise, the low momentum fluid is rapidly convected away from the surface by the vortical motion. As a result, the mean streamwise momentum of the fluid within the boundary layer is increased and flow separation is delayed. VGs provide a continual source of re-energisation for the retarded flows within the boundary layer countering the growth caused by adverse pressure gradients and reducing skin friction. Steeper adverse pressure gradients and stronger shock waves can then be adequately negotiated by viscous flows on aerodynamic surfaces suitably configured with vortex generators. Useful drag reductions may also result from properly employing VGs, as the persistent effects of the vortical motion are able to limit the growth of the wake downstream of the trailing-edge, even when there has been flow departure from the surface.

A range of 'passive' solid vortex generator devices exists which protrude from the aerodynamic surface to influence the flow field either within or exterior to the boundary layer, as shown in (see Figure 2.5 over the page).
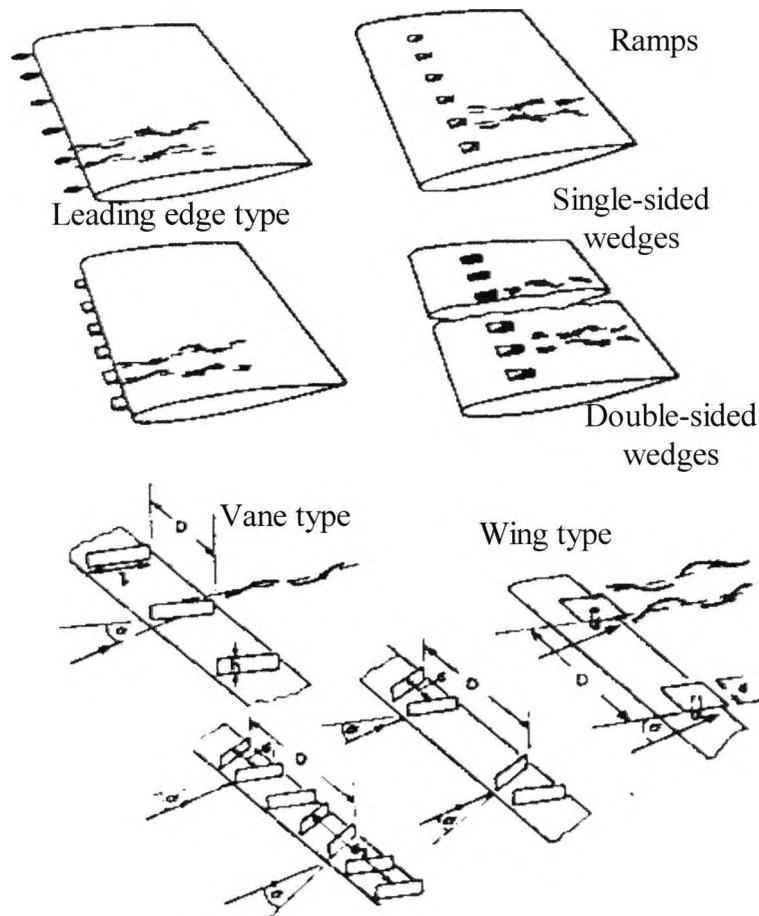
Figure 2.5: Examples of solid vortex generators, from Pearcey (1961)

The most commonly-employed types are those of the solid Vane Vortex Generator (VVG). Bruynes and Taylor of the United Aircraft Corporation first introduced VVGs in the mid forties [Bruynes & Taylor (1950)]. They consist of arrays of small plates mounted normal to the aerodynamic surface that are of the order δ in height but, are set yawed to the oncoming flow to generate a matrix of parallel longitudinal vortices. Setting each VVG to the same height and yaw angle across the surface enables the generation of a set of co-rotating identical vortices. Alternatively, the devices can be arranged at alternate positive and negative yaw angles to generate a counter-rotational vortex system [Pearcey (1961)].

A disadvantage of deploying such devices is the additive parasite and induced drag on the body due, in part, to local boundary layer thickening around the vortex generator. The penalties are more than offset by the improvements in the lifting and pitching moment characteristics of the aerofoil and the ability of the devices to delay shock-

45

induced boundary-layer separation in cruise. Nevertheless, modifications primarily concerned with reducing the surface area of the VVGs, has enabled some reduction of the additive parasitic drag. Lin et al (1990) demonstrate the employment of submerged vane vortex generators with a height of approximately 20% of the local boundary-layer thickness that adequately suppress flow separation. For a more extensive review of the use of solid vane vortex generators to control flow separation, the reader is referred to Gad-el-Hak & Bushnell (1991).

Elimination of the installed drag effects of the flow control devices themselves leads to the idea of 'active' devices that can be stowed or de-activated when not required. It is here that the potential for pneumatic flow control devices may be exploited; by injecting excess momentum into the retarded flows, or by limiting the growth of the retarded flows by wall suction schemes. A promising application of a pneumatic device to increase the momentum transfer within the turbulent boundary layer was demonstrated by Wallis (1952) with air jet vortex generators (AJVGs). Each AJVG consists of a jet of air squirting from the aerodynamic surface, to interact with and mix with the oncoming freestream and viscous flows. Initial tests conducted with the air jets exiting perpendicular to the surface in a cross-flow indicated the presence of a counter-rotating vortex pair acting as a flow spoiler. In subsequent investigations, Wallis (1960) revealed that yawing and pitching the jet system relative to the freestream direction significantly enhanced the strength of one of the vortex pair while weakening the influence of the other, as shown in Figure 2.6. Even with low jet mass fluxes, a dominant vortex like those produced by VVGs could be generated. Two main advantages result from employing AJVGs on aerodynamic systems as opposed to conventional solid VVGs. The first is that when not required, the AJVGs can be de-activated eliminating the additive drag penalty associated with the solid vanes. Secondly, the mass flux of the exiting jets serves to power the vortex cores as the helical structures migrate downstream, offering improved penetration of the combined flow system through the adverse pressure gradient regions.
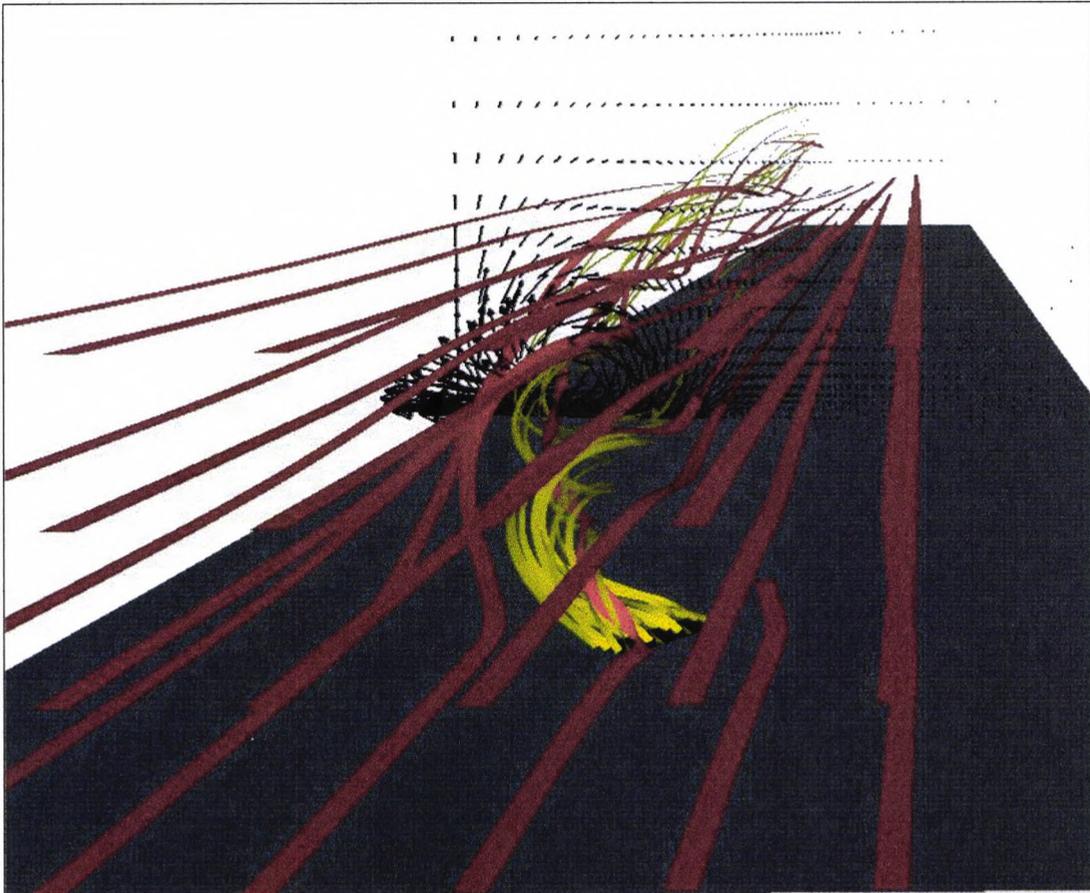
Figure 2.6: Vortex formation developed by yawed and pitched air jets, from
Lewington et al (2000)

Performance of the vortex systems whether co-rotational or counter-rotational is
dependent upon the spacing between the vortices. The spacing between the VGs must
be sufficiently large to ensure that the low momentum fluid is convected away from
the surface and not swept back towards the surface by the adjacent vortex. In the co-
rotating vortex configuration (see Figure 2.7 below) the velocity contours demonstrate
the effects of VVG spacing on the development of the vortex array.
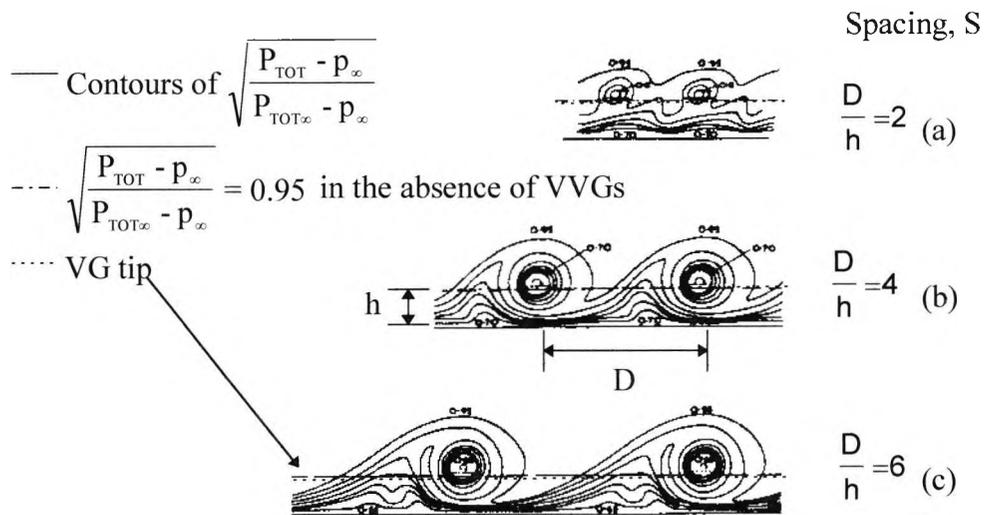
Figure 2.7: Co-rotating vortex arrays from equi-spaced vortex generators indicated by contours of velocity, from Pearcey (1961)

Below D/h=4, the low momentum fluid that is being swept away from the surface by one vortex is forced back to the surface by the adjacent vortex. In this case, the beneficial effects induced by the vortices on the momentum transfer within the boundary layer are damped by the proximity of the adjacent VVG. Above a spacing of D/h=4, there is little interference between the adjacent vortices and a stable array of useful vortices is generated for purposes of flow control.

In the counter-rotating vortex configuration, the spacing and rotational sense of the vortices has a significant influence on the subsequent momentum transfer within the boundary layer (Figure 2.8). When the induced flow between the adjacent vortex pairs is towards the surface (common flow down), effective skin friction enhancement is achieved by impinging a region of high energy fluid along the surface. The opposite is true when the induced flow between adjacent vortices is away from the surface (common flow up).

$$\frac{x}{D} = 1.6 \ (a)$$

$$\frac{x}{D} = 3.2 \ (b)$$

$$\frac{x}{D} = 6.4 \ (c)$$

Contours of $\sqrt{\dfrac{P_{TOT} - p_\infty}{P_{TOT\infty} - p_\infty}}$

$\sqrt{\dfrac{P_{TOT} - p_\infty}{P_{TOT\infty} - p_\infty}} = 0.95$

in the absence of VGs

VG axis

$$\frac{x}{D} = 12.8 \ (d)$$
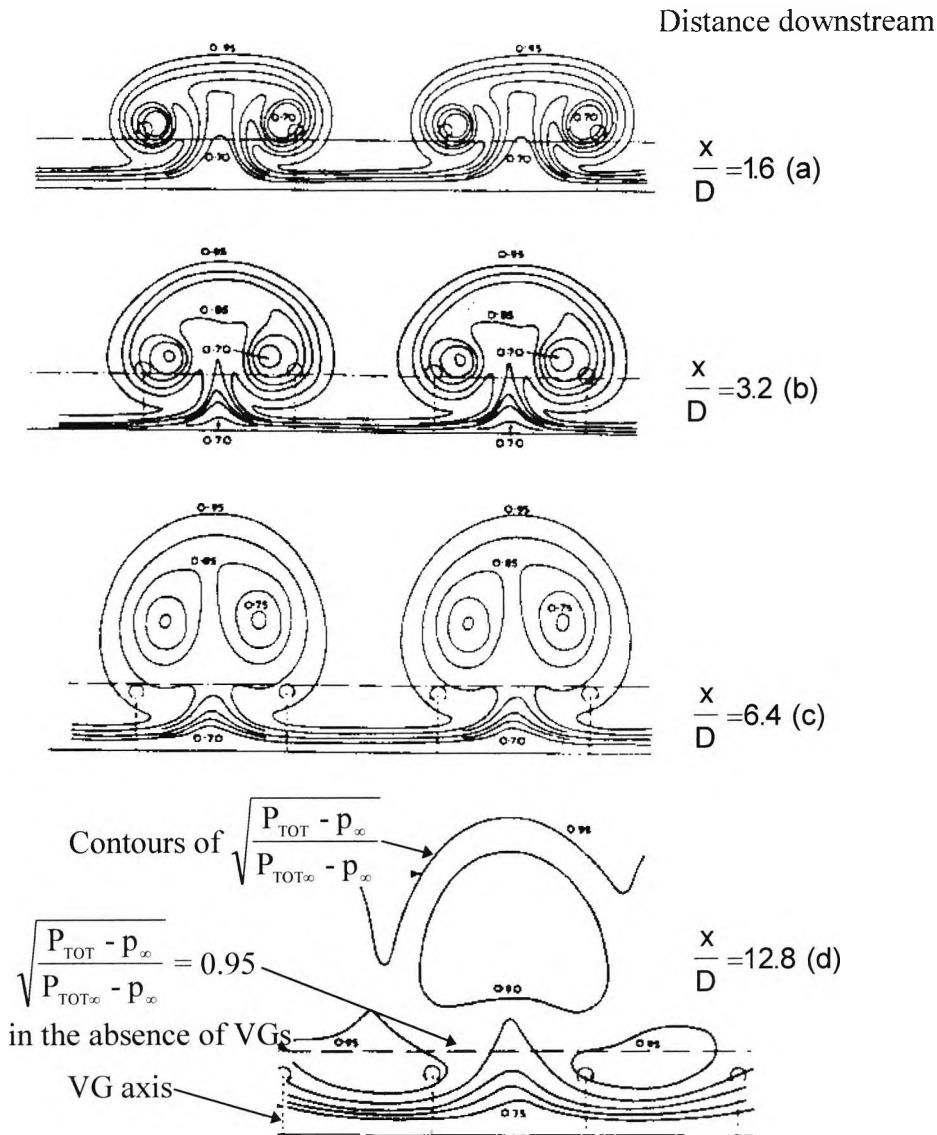
Figure 2.8: Counter rotating vortex arrays from equi-spaced vortex generators indicated by axial velocity contours, from Pearcey (1961)

When arrays of vortex generators are to be installed to suppress flow separation on an aerodynamic surface, an understanding is required of the way in which the adjacent vortices in the array are affected by the induced velocities from neighbours. When considering an array of equi-spaced co-rotating VGs, it is possible to see that the induced velocities on any one vortex by its neighbours, perpendicular to the wall, are equal and opposite (see Figure 2.9). As a result, the induced velocities between each vortex pair do not influence the height of the vortex array above the surface as it flows downstream. However, the induced velocities in the crossflow direction, parallel to the wall, are equal in magnitude and direction to those of the image vortices in the

surface. As a result, the vortex array is displaced laterally in the direction of the velocity induced by the image vortices as it flows downstream.
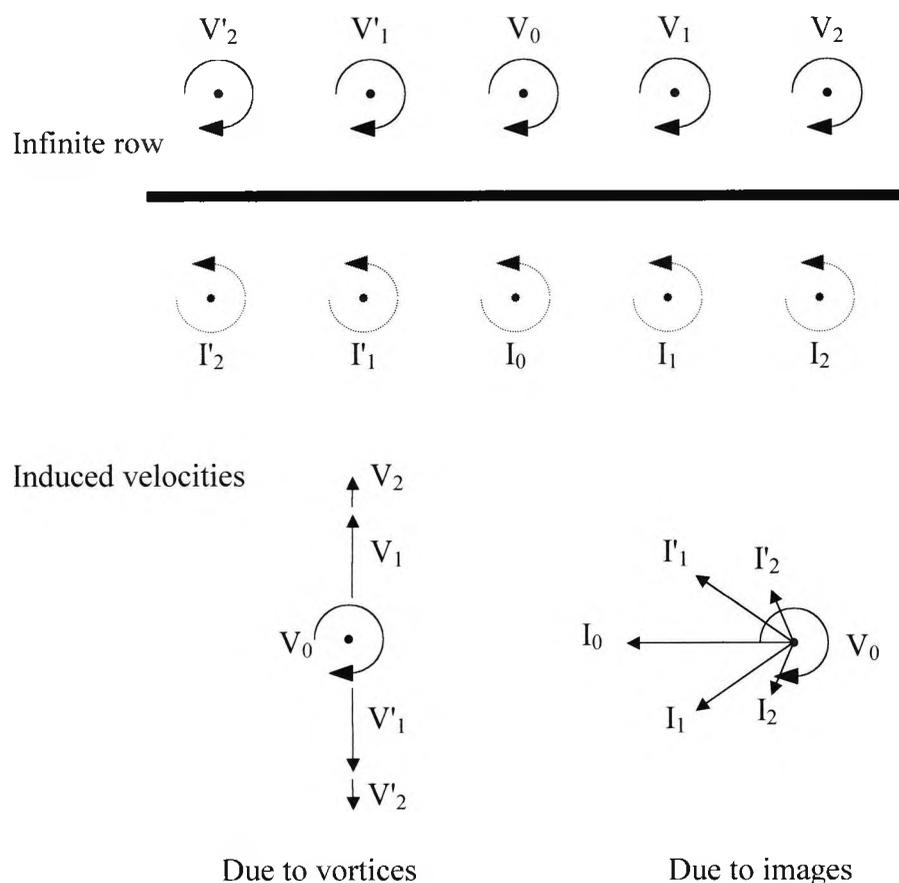
Figure 2.9: Velocities induced by an infinite co-rotating vortex array, from <u>Pearcey (1961)</u>

<u>Pearcey (1961)</u> demonstrates, that provided the spacing between the adjacent vortices is sufficient (>D/h=4) in the co-rotating configuration it is possible to promote the momentum transfer within the boundary layer over a significant portion of the chord of the aerodynamic surface (lengths of up to 100 VVG heights).

When a counter-rotating array of vortices is generated, the interaction between the adjacent vortices significantly influences the path of the vortex array as it progresses downstream. When the counter-rotating VGs are equi-spaced, the induced velocities on the vortices will be as depicted on Figure 2.10.
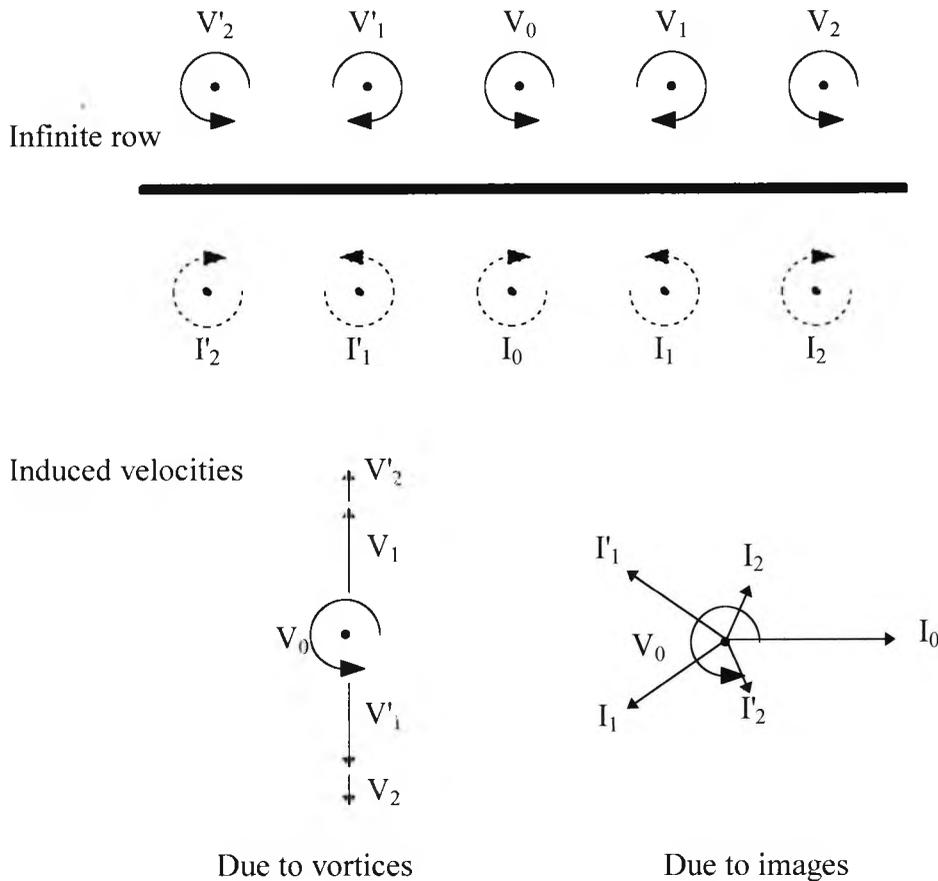
Figure 2.10: Velocities induced by an infinite counter-rotating vortex array

Figure 2.10 demonstrates that the induced velocity on each vortex forces it to move laterally in the direction of its rotation. However, as each vortex moves within the array the interaction between it and the adjacent vortices changes. As the vortex approaches its nearest neighbour the induced velocities between the vortices increase. The end result is that as the array progresses downstream the adjacent vortices move together in pairs. Once pairing of the vortices is initiated the induced velocities between the adjacent pair rapidly convects the vortices away from the surface. The convection of the vortex array away from the surface then reduces the array's ability to transfer momentum between the freestream and the retarded near wall flow (to approximately 20 VVG heights). However, convection of the vortex array away from the surface does enable enhanced mixing in the turbulent wakes above the multi-element high lift system mainfoil top surface. The effects of vortex pairing on the flow field enhancement as the array is convected away from the surface are demonstrated on Figure 2.8.

51

The choice of VG array configuration is therefore dependent upon the flow field that the designer intends to control. If the desired effect is to suppress boundary layer growth over the majority of the aerodynamic surface then the designer would be best advised to employ a co-rotating configuration for the vortex generators. However, if the desired result is suppression of boundary-layer growth over a short section of the aerodynamic surface then a counter-rotating VG configuration should yield the greatest skin friction enhancement.

2.2.1 Experimental and numerical techniques

Vane vortex generators

Since the mid forties, vortex generators have been applied to a wide range of both internal and external aerodynamic flows. Studies have monitored the effects of VVGs on delaying buffet onset, stall progression and shock induced boundary-layer separations on wings, to controlling the flow distortion in aircraft intake ducts. As a consequence, there is an extensive experimental and more recent computational database depicting the nature of the flow field about aerodynamic systems configured with VVGs.

An extensive review by Pearcey (1961) summarised the effects of vortex generator types in arrays, for which an empirical set of rules for the design and installation of the flow control devices was stipulated. By tracking the locations of the vortices and monitoring their effect on the problem boundary layer, the nature of the interactions between adjacent vortices was explored. In particular, attention was paid to the effect of the spacing between the VVGs. For a VVG co-rotating vortex array, Pearcey showed that above a spacing of $D/h \approx 4$ (where D is the distance between the VVGs and h is the height of the vane) useful surface skin friction enhancement on the aerodynamic surface could be achieved up to $100\delta_{VG}$ downstream of the array. Even greater skin friction enhancement was demonstrated by employing counter-rotating VVG arrays to suppress boundary layer separation on aerodynamic systems. However, the vortex pairing characteristics described above, limit beneficial effects of the counter-rotating vortex array downstream of the VVGs to about $20\delta_{VG}$.

The development of numerical techniques to analyse the complex flow interactions between vortices, and between them and the boundary layer, echoes the development of predictive techniques employed to analyse the flow field around multi-element high lift geometries. Accurate measurement of the experimental mean and fluctuating velocity components within the vortical flow field may permit the identification of relationships between turbulence model hypotheses such as eddy-viscosity and eddy-diffusivity. Armed with the information from detailed vortical flow field analysis it may then possible for designers to employ suitably sophisticated turbulence models that can account for some of the higher-order viscous effects, such as turbulence transport, in complex vortical flows.

One batch of experiments designed to identify the behaviour of the eddy viscosities in vortical flows is described in the work of Shabaka et al (1982) and Metha et al (1982 and 1983) describe a batch of wind tunnel experiments on one or more vortices embedded in a turbulent boundary layer, in a nominally zero pressure gradient flow, at low Reynolds numbers ($Re_c \approx 5 \times 10^6$). They showed the terms in the Reynolds-stress transport equations (notably those affecting turbulent diffusion) do not obey simple algebraic relationships, as the turbulence is appreciably far from isotropic. Some comparative tests to characterise the vortex properties in terms of core location and Reynolds stress distribution within the vortex core were conducted by Westphal et al (1987), on a single vortex embedded in a turbulent boundary layer, subjected to a moderate adverse pressure gradient. They demonstrated that when the turbulent boundary layer and embedded vortex are subjected to a moderate adverse pressure gradient there is appreciably accelerated vortex core growth, a more pronounced elliptical nature to the streamwise vorticity contours and greater distortion of the Reynolds stresses within the vortex core. This increased distortion of the Reynolds stresses within the vortex core signals that there will be modelling difficulties when attempting to predict real-world vortical flows with standard turbulence models. Pauley & Eaton (1988) extended the investigations of Westphal et al (1987) to multiple co-rotating and counter-rotating vortex pairs and their effect on the vorticity and circulation at several streamwise locations, in a low speed wind tunnel tests ($R_\theta = 1700$ at the VVG). The vortices were generated by half-delta vanes positioned downstream of the boundary layer trip so that the height of the VVGs was of the order

53

of the boundary layer thickness. The authors demonstrated that the interaction between vortex pairs embedded in otherwise two-dimensional boundary layers behave in qualitatively the same manner as would be defined by potential flow theory with some allowance for the presence of induced vortices. More importantly, they identified that the proximity of the adjacent vortices does not promote the loss of vortex circulation but it does affect the spreading of the vorticity. The direction and extent of this vortex spreading is controlled by the strength and proximity of the adjacent vortices, but the rate at which vortex circulation decreases is proportional to the distance from the wall.

To simulate a single vortex and a vortex pair embedded in a turbulent boundary layer, Liandrat et al (1987), solved a reduced set of Navier-Stokes equations, with a finite-volume approach, neglecting longitudinal diffusion. The flow field turbulence quantities were modelled with two separate techniques. The first utilised the two-equation k-ε model based on the Boussinesq hypothesis [Boussinesq (1877)] that connects the turbulence length scale to the mean flow properties. The second employs second-moment closures to model the Reynolds stresses in the transverse flow directions [Launder et al (1975)]. Computational results were compared to the experiments of Shabaka et al (1982) analysing the flow fields associated with a single vortex and a 'common flow up' vortex pair. Solutions obtained by employing the k-ε turbulence model demonstrated the ability of the technique to represent the turbulence quantities in the region affected by the single vortex/boundary layer interactions. However, the reliance on the Boussinesq hypothesis causes the technique to partly fail in multiple vortex scenarios. Better estimates of the secondary motion and longitudinal vorticity were achieved by employing second-moment closures to model the Reynolds stresses in the single vortex case. However, employing second-moment closures requires extensive empirical data that is flow configuration specific and time-consuming to measure. As a result, higher-order accurate turbulence models are often prohibitively expensive, in terms of computing time and model set-up, so do not lend themselves to trend analysis for vortical flow fields. Lindriat's work highlights two important factors. Firstly, to be able to accurately predict vortex/boundary layer interactions there is a need for sophisticated modelling techniques, i.e., employing second-moment closures to model the Reynolds stresses. Secondly, he demonstrates

that relatively simple techniques can be employed to qualitatively represent the vortical flow fields, i.e., techniques based on simpler algebraic relationships. With this in mind it was now possible for designers to make use of these simpler numerical approaches to expedite the development of flow control devices.

Air-jet vortex generators

Wallis (1952) showed that by directing a jet of air normal to the surface into an approaching flow it was possible to generate a pair of weak counter-rotating vortices. However, the effect of the vortex pair was not sufficient to delay separation of the boundary layer over an extensive region. By pitching and yawing the jets to the oncoming freestream Wallis (1960) produced a strong streamwise vortex that was capable of delaying boundary-layer separation. Later tests by Pearcey (1961) and Rao (1988) examined the ability of AJVGs to alleviate separation caused by shock wave/boundary-layer interactions. Comparable results to those found with VVGs were demonstrated in the level of pressure recovery measured at the trailing edge, when employing an array of rectangular AJVGs. Freestone (1985) compared the performance of a tapered VVG with both a circular and a rectangular AJVGs. He showed that for respective pitch and skew angles of 30° and 60°, it was possible to match and supersede the magnitude of the vorticity downstream of the VVGs and circular AJVGs with rectangular AJVGs. This work highlighted the need for a greater understanding of the mechanisms behind vortex generation with these devices.

Johnston & Nishi (1989) also highlight the potential for employing pitched and skewed circular AJVGs as a means of 'passive' and 'active' flow control in strong adverse pressure gradients low speed flows (Re≈10^6). A number of co-rotating and counter-rotating AJVG vortex arrays were investigated by pitching at 45° and skewing to the freestream flow by ±90°. Johnston & Nishi (1989) show that for jet-to-freestream velocity ratios (V_R) greater than 0.8 the vortices generated are capable of reducing, if not eliminating boundary-layer separation. Comparisons with the experiments of Pauley & Eaton (1988) revealed that the performance of an AJVG vortex array is at least comparable if not better than a VVG array in terms of skin friction enhancement and vorticity measured downstream of the devices.

A detailed comparison between the vortices produced by AJVGs and solid VVGs, approximately 1.5 times the boundary-layer height, is discussed by Compton & Johnston (1992). Results for the AJVGs are obtained with the jets pitched at 45°, skewed at 0°, 45° 90, 135° and 180° to the freestream direction, for jet velocity ratios ranging between 0.7 and 1.3. They conclude that the rate of decay of transverse peak vorticity and circulation of the AJVG vortices is much less when compared to that of the solid VVGs. The vorticity and circulation in the transverse planes downstream of the vortex arrays are shown to be highly dependent upon V_R and skew angle, with an optimal value for the skew angle suggested to lie between 45° and 90°.

AJVGs were competed against tangential blowing in a parametric study by Selby et al (1992) to control the flow over a two-dimensional rearward facing ramp in low speed wind tunnel tests ($R_\theta \approx 9000$). The parameter studies included the variation of the jet orifice diameter (D_0), jet orientation (ϕ and ψ), total flow coefficient (C_Q) and longitudinal jet orifice location (L/δ) as outlined in Table 2.2.

Test flow conditions:

$U_\infty = 40 ms^{-1}$, δ (at sep^n point) = 33mm, θ (at sep^n point) = 3.3mm

Table 2.2: Details of AJVG parameter study conducted by Selby et al (1992)

Jet orifice diameter (D_0/θ)	Jet Pitch wrt surface (ϕ)	Jet Skew wrt freestream (ψ)	Jet total flow coefficient ($C_Q = Q/\lambda\delta U_\infty$)	Jet location ahead of sep^n (L/δ)
$0.24 < D_0/\theta < 1.45$	$15° < \phi < 90°$	$0° < \psi < 90°$	$0.013 < C_Q < 0.052$	$3\delta < L/\delta < 40\delta$

The performance of the AJVGs and tangential blowing techniques were assessed by monitoring the level of pressure recovery downstream of the two-dimensional ramp. By altering the jet parameters separately the authors concluded: (i) decreasing the orifice diameter improved the performance by increasing V_R; (ii) increasing the jet flux improved the AJVG performance by increasing V_R; (iii) reducing the pitch angle

improved performance by ensuring the momentum transfer occurs nearer to the model wall; (iv) increasing skew angles up to values of 60° and 90° improved the performance by increasing the strength of the dominant vortex; (v) reducing the distance between the AJVG array and the separation line generally improves the performance of the array, although, the effects of the vortex arrays can be persistent with the AJVGs located 40 boundary layer heights upstream of the separation point; (vi) Jets orientated to produce counter-rotating arrays are not as effective as co-rotating and exhibit a lower level of spanwise uniformity in the streamwise pressure distribution; (vii) the performance of co-rotating arrays of AJVGs offers a greater spanwise extent of pressure recovery at much lower total flow coefficients than with tangential slot blowing. In order to obtain the same level of pressure recovery with tangential slot blowing, Selby et al (1992) concluded that the mass flux coefficient C_μ, would have to be an order of magnitude greater than those mass flows used with the AJVGs.

The AJVG investigations described above highlight the potential for a low cost flow control device, in terms of power requirements, capable of suppressing boundary-layer separation. In some cases, AJVGs have been shown to out-perform existing techniques, with the added advantage of a reduced parasitic drag contribution when quiescent.

Research at City University has concentrated upon the application of AJVGs to single and multi-element aerofoil configurations either to alleviate shock-induced boundary-layer separations or to improve lift/drag performance [see Rao (1988), Pearcey et al (1993), Innes (1995) & Lewington et al (2000)]. Substantial improvements in the lift and drag performance of a high lift system (representative of the inboard section of an Airbus A320 three element wing) employing AJVGs is published by Innes et al (1995). Low speed wind-tunnel tests were conducted with the high lift system in the take-off mode configured separately with either co-rotating arrays of VVGs or AJVGs. Employing AJVGs resulted in an extension of both the usable angle-of-attack range (approximately 6°) and a 30% increase in the normal force coefficient C_{Nmax}. Velocity profiles measured over the mainfoil with the AJVGs active indicate that the level of mixing between the freestream and the confluent boundary layers is enhanced,

resulting in a reduced momentum defect within the confluent boundary layer and thus an inferred reduction in the profile drag.

Recent numerical studies at City [Henry & Pearcey (1994) and Akanni & Henry (1995)] have shown that it is possible to simulate the complex three-dimensional flow field associated with single and multiple arrays of AJVGs in zero and adverse pressure gradients. They employed a finite-volume approach to solve the full Navier-Stokes equations on a single block-structured grid coupled with a k-ε turbulence model. A number of jet pitch and skew angle configurations was tested with the pitch varied between 15° and 90° and the skew varied between 60° and 90°. The performance of the AJVG arrays was assessed by monitoring the axial skin friction and the maximum vorticity decay across the solution domain span at two locations downstream of the air jets. Predictions were verified with the published experimental data of Compton & Johnston (1992). Employing the AJVGs was shown to elevate the mean axial skin friction downstream of the AJVG array by up to 60% above the undisturbed value (C_f=0.003) in both the zero and adverse pressure gradient flows. Although notable differences between the predicted and experimental data points were apparent, the computational approach identified the underlying trends associated with the peak vorticity decay. The success of the City University research has given rise to a simple method of performing sensitivity studies on the AJVG control process in physically relevant flow fields (zero and adverse pressure gradient) without the need for extensive wind tunnel experimentation. With this in mind it will be possible to study and optimise the effectiveness of AJVG arrays prior to installation on complex geometries.

2.3 Summary of the current state of the art for high lift system optimisation

Wind tunnel testing

Initial progress in high lift system design has relied upon iterative wind tunnel testing to optimise the performance of the two-dimensional multi-element aerofoil configurations, with the results then being extrapolated to model three-dimensional wing, and hence to full scale applications. Although successful, iterative wind tunnel testing is both time consuming and may be expensive, depending on model scale and wind tunnel size. It is often the case that many prototypes are required before an optimal multi-element aerofoil configuration is reached. Hastening of the design process resulted from a better understanding of the flow physics associated with multi-element aerofoil configurations [as outlined in the work of <u>Smith (1972)</u> and <u>Foster et al (1972)</u>]. Subsequent to these investigations, the existing fluid flow prediction techniques could be adapted to deal with multi-element aerofoil configurations, with the knowledge-base-experiments used to verify and validate code development.

As computing power increased, it was possible to utilise and develop more sophisticated numerical approaches to predict the flow field associated with high lift system geometries. Improvements in the predictive capabilities of a numerical approach required the effects of turbulence, wake/boundary-layer interactions and (ideally) boundary-layer transition to be accounted for in code formulation. Once again, the development of numerical techniques capable of representing these flow field phenomena relied on a better understanding of the physical processes involved. By making use of hot-wire and Laser-Doppler measuring techniques, it was possible to extensively measure the mean and fluctuating viscous flow field around multi-element aerofoil geometries in wind tunnel tests [see <u>Adair & Horne (1989)</u>, <u>Nakayama (1990)</u> and <u>Moir (1994)</u>]. The results of these types of test provided code developers with a suitable experimental database with which to validate numerical models.

59

Viscous/inviscid interaction computational approaches

Early approaches at predicting multi-element aerofoil flow fields employed a viscous/inviscid interaction (VII) approach that separates the flow field around the aerofoil into two parts. The first is the essentially inviscid flow in the freestream and the second the viscous flow close to the surface and in the wakes of the multi-element aerofoil components [see Lock & Williams (1987) for a comprehensive review]. In the main VII approaches were successful as they provided good approximations of lift and drag characteristics of the high lift system with only limited knowledge of the freestream flow conditions and the multi-element aerofoil geometry. However, the methods often failed to predict maximum lift coefficient (C_{Lmax}) and stall angle (α_{STALL}) as they could not account for the effects of increasing confluency of the boundary layer with increasing angle of attack. Better representation of C_{Lmax} and α_{STALL} with numerical techniques required solving the governing flow equations (the Navier-Stokes equations) with suitably sophisticated models to account for turbulence. However, solving the Navier-Stokes equations required considerably more computer storage space and often prohibitive CPU time to calculate the flow field around the high lift system (especially on a three-dimensional wing).

Navier-Stokes computational approaches

The advent of supercomputers permitted, for the first time, solutions of the Navier-Stokes equations for the entire high lift system flow field. Early predictions made use of relatively simple and computationally efficient algebraic models to predict the eddy-viscosity within the turbulent boundary layers and wakes [see Cebeci & Smith (1968)]. Reasonable agreement with wind tunnel results was demonstrated with this algebraic approach, but off-design flow field predictions (close to stall) remained beyond the capability of this numerical technique [see Brune & Manke (1978)]. The availability of accurate experimental data provided the inspiration for a series of CFD workshops [see Ying (1996), Fejtek (1997) and Linblad & Cock (1999)]. Good agreement between the experimentally determined and predicted C_{Lmax} and α_{STALL} was demonstrated with some of the numerical approaches (within 5% C_{Lmax} and 1° to 2° α_{STALL}). The findings of these workshops established the salient requirements, within the numerical techniques, to enable reasonably accurate prediction of the off-

design high lift system flow field characteristics. Primarily, the authors concluded that the numerical method should include at least a two-equation turbulence model and that some provision for laminar to turbulent boundary layer transition must be made.

Flow control with vortex generators

Improving the lift and drag performance of multi-element aerofoil configurations has relied mainly upon altering the geometry and location of the various leading-edge and trailing-edge high lift devices. The current state of the art, with regard to high lift devices, indicates that little improvement in the performance of the high lift system can be expected by further modifying the device geometry and location. Flow control, whether utilising passive or active devices, has been demonstrated to improve high lift system performance characteristics [see Innes (1995)]. The most common form of flow control device is the 'passive' solid vane vortex generator (VVGs) of Bruynes and Taylor (1950). Generating vortices from solid vanes that protrude from the aerodynamic surface enhances mixing between the retarded flow in the viscous shear layers and the high momentum fluid in the freestream. As a result, the momentum deficit in the boundary layer is reduced, as is the likelihood of boundary-layer separation. Improvements in the performance of a three-element high lift system of up to 15% C_{Lmax} and 3° α_{max} have been demonstrated when utilising VVGs designed with the set of empirical rules devised by Pearcey (1961).

Employing VVGs however is not without cost, as the devices protrude from the aerodynamic surface generating additional parasitic drag. In an attempt to reduce the adverse effects of parasitic drag, pneumatic devices that could be de-activated when not required were studied [see Wallis (1960), Gad-el-Hak & Bushnell (1991) and Selby et al (1992)]. The simplest approach was to employ tangential slot blowing along the aerodynamic surface to inject momentum into the boundary layer. Although successful, the power requirements of the system make it an unsuitable option for many aerofoil applications (but see Blackburn Buccaneer). By blowing through discrete jets, that are pitched and skewed to the oncoming freestream flow, Wallis (1956) demonstrated it was possible to significantly enhance the axial skin friction on the aerodynamic surface, thereby reducing the potential of boundary layer separation across the span, downstream of the air-jet vortex generators (AJVGs). Employing

relatively low mass momentum fluxes to power the system ($C_\mu \approx 0.01$), it was possible to match and in some cases outperform the conventional VVGs when employing AJVGs [see Rao (1988), Johnston & Nishi (1989) and Innes (1995)].

Computational techniques have also been employed to predict the complex flow fields associated with vortices [see Lindriat et al (1987)]. Once again, with improved computer technology, these computational techniques have been subsequently employed to model the vortex generators themselves. In particular, the work of Henry & Pearcey (1994), Akanni & Henry (1995) and Küpper (1999) demonstrated the ability of numerical methods to adequately predict the flow field local to vortex generators in both zero and adverse pressure gradient flows.

In order to optimise the performance of flow control devices, it is logical to adopt the successful interactive computational/experimental approach outlined in the development of efficient high lift systems in Section 2.1.1. Much of the early work into flow control has focussed on the effectiveness of the devices and whether or not computational methods are capable of predicting the flow field. The intent of this study is to analyse the sensitivity of the AJVG control process to jet spacing, jet-to-freestream velocity ratio and rotational sense of the vortex array numerically, prior to installation on a complex three-element aerofoil geometry. By validating numerical studies with some carefully contrived experiments [see Lewington et al (2000)] it will be possible to develop a near optimum array of AJVGs for installation into the high lift system, without the need for extensive wind tunnel testing.

3. Numerical methods

3.1. Introduction

Any fluid flow is governed by the fundamental physical principles of mass conservation, energy conservation and Newton's second law. It is possible to express these principles in terms of mathematical equations that generally take a partial differential (or integral) form. A non-linear, coupled system of partial differential equations is difficult to solve analytically and there is no general closed-form solutions to these equations. Analysis of a flow field requires approximations to partial differential equations via algebraic expressions at discrete points throughout the solution domain. Solving the algebraic expressions at sufficient points in the flow field then enables numerical values to be determined for the basic mean flow properties (anywhere in the solution domain, i.e., pressure, velocity, temperature, shear stress,....etc.). This particular approach to numerical fluid flow analysis is known as Computational Fluid Dynamics (CFD) and has been demonstrated as an effective design and development tool for many engineering applications.

A large number of commercially available CFD codes exist, often complete with a suite of tools capable of simulating a wide range of fluid flow problems. A summary of the performance of several commercial codes applied to five benchmark simulations of varying complexity is described by Freitas (1995). The purpose of the study was to identify a common reference point to evaluate commercially available codes. The true potential of this benchmarking process, however, was not realised as not all of the code vendors provided solutions to all of the benchmark problems. In particular, the results highlighted the pit falls associated with employing over simplified turbulence models to predict relatively complex flow fields. Freitas (1995) concludes that to obtain adequate flow field predictions the code user must balance grid resolution and discretisation accuracy with an appropriate closure model.

The most common form of commercial code solves the governing flow equations using a finite-volume method on body-fitted grids. Numerical results in this project were obtained by employing a finite-volume, block-structured viscous flow solver,

CFX (AEA Technology). CFX was chosen to analyse the flow field around the high lift system in this project because of its success in predicting the complex swirling flows associated with Vortex Generators (see Henry & Pearcey (1994), Akanni & Henry (1995), Küpper (1999) and Lewington et al (2000)). At present the author is unaware of published data demonstrating the ability of CFX to predict the complex flow field associated with a high lift geometry. To assess the CFX predictions, comparisons will be made with wind tunnel experiments conducted at City University and the results obtained using MSES, a fast viscous/inviscid interaction flow solver. MSES has been specifically designed to predict the two-dimensional flow field around multi-element aerofoil geometries. It is successful and has been suitably validated with experimental results [see Drela (1990)].

The majority of commercial flow solvers contain pre- and post-processing facilities that enable the user to generate numerical grids and analyse the results of the numerical simulation within the one software package. However, the in-built pre- and post-processing packages are often not sophisticated enough, to set-up and analyse the problem within acceptable time limits, when the flow field solution domain is geometrically complex, like that of a multi-element high lift system. Specialist software packages are available that provide more 'user-friendly' approaches to grid generation and data analysis. In this project, extensive use is made of the grid generation package ICEM-CFD (ICEM Technologies) and the post-processing package Ensight [Computational Engineering International (CEI)], coupled with the numerical flow solver CFX.

3.2 Governing equations of fluid motion

The governing integral or partial differential equations of fluid flow, in either 'conservative' or 'nonconservative' form [see Anderson (1995)], are obtained by considering the motion of the fluid with one of two approaches. 'Conservative' forms of the flow equations are obtained by considering a fixed volume in space with the fluid flowing into it and out of it. 'Nonconservative' forms of the flow equations arise from considering a fixed mass of fluid moving along a streamline with the fluid. In most aerodynamic applications the form of the flow equations that are solved does not

significantly affect the progress of the solution. However, for highly transient problems the stability of the numerical solution is sometimes dependent upon the form of the governing flow equations that are solved.

Both numerical methods utilised in this project employ a finite-volume approach to solve the 'conservative' form of the partial differential flow equations, as expressed below. CFX solutions were obtained with the code tailored to assume a fully turbulent, steady-state and incompressible flow regime. MSES employed the compressible Euler equations, for the inviscid part of the multi-component flow field, coupled with an integral boundary layer solution. Note that the wind tunnel test flow in this study is steady-state and incompressible ($M_\infty \approx 0.12$, $Re_\infty = 1.3 \times 10^6$), although some effects of compressibility may exist around the slat leading-edge at high α and near the jet orifice at high jet momentum coefficients. These effects, are usually small enough to be neglected at the freestream Mach number, $M_\infty = 0.12$, investigated here.

Full derivations of both 'conservative' and 'nonconservative' forms of the governing flow equations are described in Anderson (1995).

Conservation of mass via the continuity equation:

$$\frac{\partial \rho}{\partial t} + \nabla.(\rho V) = 0 \qquad\qquad (3.1)$$

Where:

ρ = Density in fluid flow

V = Velocity vector

Newton's Second Law, F=ma (the momentum equations per unit volume):

$$\frac{\partial(\rho\phi)}{\partial t} + \nabla(\rho V \phi) = -\frac{\partial p}{\partial x} + \frac{\partial \tau_{xx}}{\partial x} + \frac{\partial \tau_{yx}}{\partial y} + \frac{\partial \tau_{zx}}{\partial z} + \rho f_x \qquad (3.2a)$$

$$\frac{\partial(\rho\phi)}{\partial t} + \nabla(\rho V \phi) = -\frac{\partial p}{\partial y} + \frac{\partial \tau_{xy}}{\partial x} + \frac{\partial \tau_{yy}}{\partial y} + \frac{\partial \tau_{zy}}{\partial z} + \rho f_y \qquad (3.2b)$$

$$\frac{\partial(\rho\phi)}{\partial t} + \nabla(\rho V \phi) = -\frac{\partial p}{\partial z} + \frac{\partial \tau_{xz}}{\partial x} + \frac{\partial \tau_{yz}}{\partial y} + \frac{\partial \tau_{zz}}{\partial z} + \rho f_z \qquad (3.2c)$$

Inertia Forces   Viscous forces

Pressure forces   Body forces
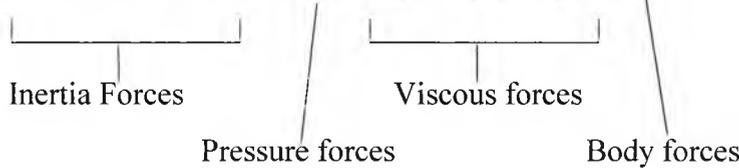
where: ρ = density in fluid flow

        V = velocity vector

        ϕ = the general variables (u, v, w)

        τ = viscous stresses in fluid

        f = force per unit mass

Note: The inviscid Euler form of the momentum equations is obtained by omitting the viscous terms.

3.3 Grid generation

Any finite-difference or finite-volume method requires the generation of a suitable grid of discrete nodes on which to solve the algebraic form of the governing flow equations. To ensure suitable discretisation of the flow domain associated with complex geometries, the majority of numerical methods utilise non-uniform body fitted grids. Within the context of finite differencing, it is not possible to obtain solutions of the flow equations on non-uniform grids. A transformation of the curvilinear co-ordinate, body-fitted grids (Figure 3.1a), is therefore required to provide a uniform computational domain (Figure 3.1b). The governing flow equations are then

solved on the computational domain and the results translated back into the physical domain.
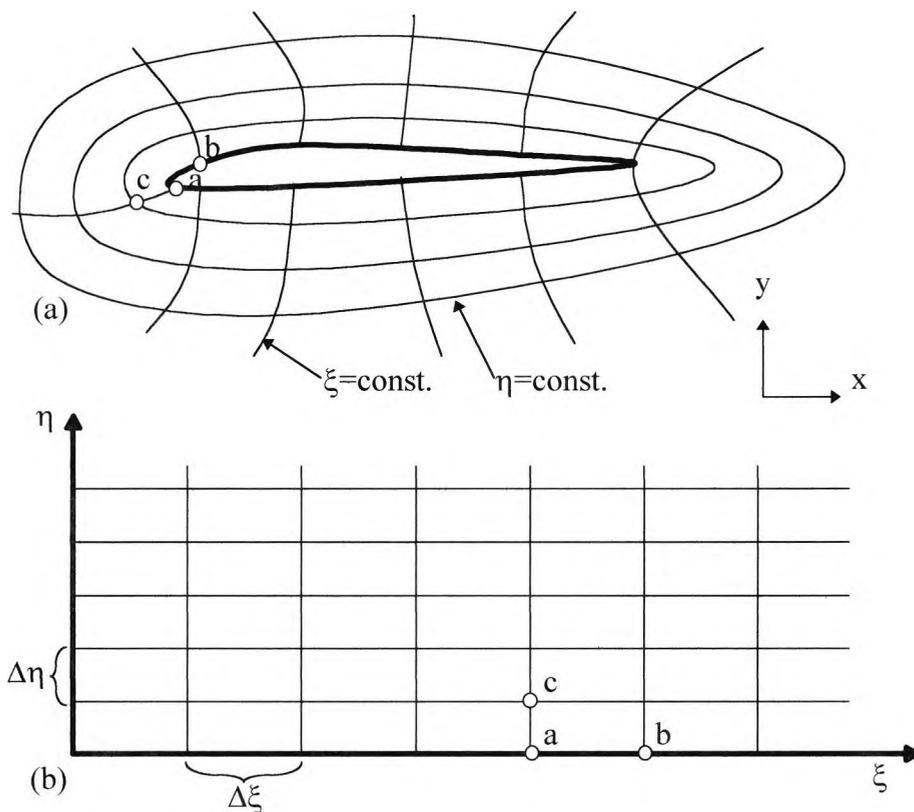
Figure 3.1: Schematic of body fitted grid co-ordinate system (a) Physical domain; (b) Computational domain

The partial differential flow equations must also be transformed from general curvilinear (ξ, η, φ) co-ordinates to the computational Cartesian co-ordinates (x, y, z), where:

$$\xi = x(x, y, z) \tag{3.3a}$$

$$\eta = \eta(x, y, z) \tag{3.3b}$$

$$\varphi = \varphi(x, y, z) \tag{3.3c}$$

For simplicity, if we consider a transformation for a two-dimensional steady-state problem, then the co-ordinate transformation for the partial derivatives in the governing flow equations is described by equations 3.3a and 3.3b.

The derivative transforms can be expressed in nonconservative form, using the general parameter ϕ $(= u, v)$ as:

$$\frac{\partial \phi}{\partial x} = \frac{\partial \xi}{\partial x}\frac{\partial \phi}{\partial \xi} + \frac{\partial \eta}{\partial x}\frac{\partial \phi}{\partial \eta} \qquad (3.4a)$$

$$\frac{\partial \phi}{\partial y} = \frac{\partial \xi}{\partial y}\frac{\partial \phi}{\partial \xi} + \frac{\partial \eta}{\partial y}\frac{\partial \phi}{\partial \eta} \qquad (3.4b)$$

where $\dfrac{\partial \xi}{\partial x}, \dfrac{\partial \xi}{\partial y}, \dfrac{\partial \eta}{\partial x}$ and $\dfrac{\partial \eta}{\partial y}$ are called the metrics of the transformation.

For the majority of applications, it is useful to have the transformations in the inverse form, as we need the geometry co-ordinates in a curvilinear form. This is achieved by defining the Jacobi matrix as:

$$J \equiv \frac{\partial(x,y)}{\partial(\xi,\eta)} = \begin{vmatrix} \dfrac{\partial x}{\partial \xi} & \dfrac{\partial x}{\partial \eta} \\ \dfrac{\partial y}{\partial \xi} & \dfrac{\partial y}{\partial \eta} \end{vmatrix} = \frac{\partial x}{\partial \xi}\frac{\partial y}{\partial \eta} - \frac{\partial x}{\partial \eta}\frac{\partial y}{\partial \xi} \qquad (3.5)$$

The resulting expressions for the inverse metrics can then be expressed as:

$$\frac{\partial \xi}{\partial x} = \frac{1}{J}\frac{\partial y}{\partial \eta} \qquad (3.6a)$$

$$\frac{\partial \eta}{\partial x} = -\frac{1}{J}\frac{\partial y}{\partial \xi} \qquad (3.6b)$$

$$\frac{\partial \xi}{\partial y} = -\frac{1}{J}\frac{\partial x}{\partial \eta} \qquad (3.6c)$$

$$\frac{\partial \eta}{\partial y} = \frac{1}{J}\frac{\partial x}{\partial \xi} \qquad (3.6d)$$

The derivative transforms (Eqns. 3.4a & b) can then be expressed in inverse conservative form as:

$$\frac{\partial \phi}{\partial x} = \frac{1}{J} \left[\frac{\partial}{\partial \xi} \left(\frac{\partial y}{\partial \eta} \phi \right) - \frac{\partial}{\partial \eta} \left(\frac{\partial y}{\partial \xi} \phi \right) \right] \tag{3.7a}$$

$$\frac{\partial \phi}{\partial y} = \frac{1}{J} \left[\frac{\partial}{\partial \eta} \left(\frac{\partial x}{\partial \xi} \phi \right) - \frac{\partial}{\partial \xi} \left(\frac{\partial x}{\partial \eta} \phi \right) \right] \tag{3.7b}$$

Consequently, a transformed version of the governing flow equations in two-dimensions can be expressed as:

Continuity:

$$\frac{\partial}{\partial \xi} G_1 + \frac{\partial}{\partial \eta} G_2 = 0 \tag{3.8}$$

where:

$$G_1 = \frac{\partial y}{\partial \eta} u - \frac{\partial x}{\partial \eta} v, \quad G_2 = \frac{\partial x}{\partial \xi} v - \frac{\partial y}{\partial \xi} u \tag{3.9}$$

x-momentum:

$$\frac{\partial}{\partial \xi} (G_1 u) + \frac{\partial}{\partial \eta} G_2 u = -\frac{\partial}{\partial \xi} \left(\frac{\partial y}{\partial \eta} p \right) + \frac{\partial}{\partial \eta} \left(\frac{\partial y}{\partial \xi} p \right) + \frac{\partial}{\partial \xi} \left(\frac{\partial y}{\partial \eta} \tau_{xx} \right) - \frac{\partial}{\partial \eta} \left(\frac{\partial y}{\partial \xi} \tau_{xx} \right)$$
$$+ \frac{\partial}{\partial \eta} \left(\frac{\partial x}{\partial \xi} \tau_{yx} \right) - \frac{\partial}{\partial \xi} \left(\frac{\partial x}{\partial \eta} \tau_{yx} \right) + J\rho f_x \tag{3.10a}$$

y-momentum

$$\frac{\partial}{\partial \xi} (G_1 v) + \frac{\partial}{\partial \eta} (G_2 v) = -\frac{\partial}{\partial \eta} \left(\frac{\partial x}{\partial \xi} p \right) + \frac{\partial}{\partial \xi} \left(\frac{\partial x}{\partial \eta} p \right) + \frac{\partial}{\partial \xi} \left(\frac{\partial y}{\partial \eta} \tau_{xy} \right) - \frac{\partial}{\partial \eta} \left(\frac{\partial y}{\partial \xi} \tau_{xy} \right)$$
$$+ \frac{\partial}{\partial \eta} \left(\frac{\partial x}{\partial \xi} \tau_{yy} \right) - \frac{\partial}{\partial \xi} \left(\frac{\partial x}{\partial \eta} \tau_{yy} \right) + J\rho f_y \tag{3.10b}$$

3.3.1 Grid topology

A major difficulty associated with the computational analysis of high lift systems lies with the ability to generate a suitable grid, capable of capturing the relevant flow phenomena. Three commonly employed techniques are reported in the literature to deal with the high lift geometries. These are, the block-structured approach, overlapping grid approach and unstructured grid approach (see Ying (1996) for a review of the commonly employed grid generation techniques for multi-element aerofoils).

Block-structured

The simplest form of a block-structured grid is the single block surrounding the geometry as shown in Figure 3.1. Unfortunately, as the complexity of the geometry increases, the applicability of a single block-structured grid diminishes. Single block-structured grids generated for multi-element geometries often require distorting some of the grid cells to a point where the accuracy of the numerical solution is compromised. Employing a multi-block structured approach as shown on Figure 3.2, on the other hand, enables the complex geometry to be subdivided into several individual blocks that transfer information across their common boundaries. Difficulties still remain in close proximity to the surface of the high lift system, as the individual blocks are required to match at the inter-block boundaries.
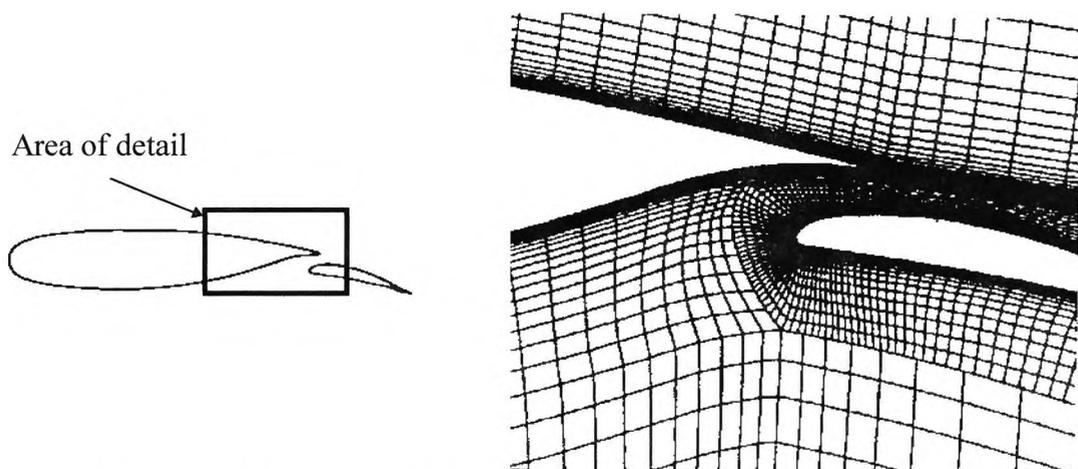
Figure 3.2: Example of a multi-block structured grid in the region of the flap nose

Overlapping grids (Chimera grids)

The overlapping grid technique is similar to the block-structured approach except that structured grids within the blocks are not required to match at the block boundaries (Figure 3.3). As a result, the block structure around the high lift system geometry can be generated independently of the outer flow regions without compromising the accuracy of the solution. Some extra computational effort is necessary to interpolate between the boundaries of the overlapping grid sections before coupling the grid with the flow solver.
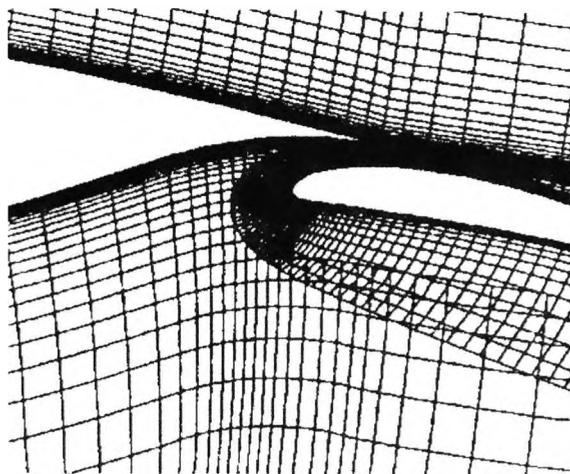
Figure 3.3: Example of an overlapping grid in the region of the flap nose

Unstructured grids

An unstructured approach readily permits the generation of grids for complex geometries by subdividing the solution domain into a number of triangular or tetrahedral cells (Figure 3.4). There are a number of disadvantages associated with employing an unstructured approach. As there is no regularity to the cell distribution, there are no co-ordinate lines that correspond to ξ, η and ζ and an individual local co-ordinate system is required for each element. Considerably more computer storage is, therefore, required for unstructured approaches when compared with multi-block methods. A further drawback, particularly with reference to high lift systems, is that the accuracy of the solution may be affected due to highly stretched cells at the aerofoil boundaries.
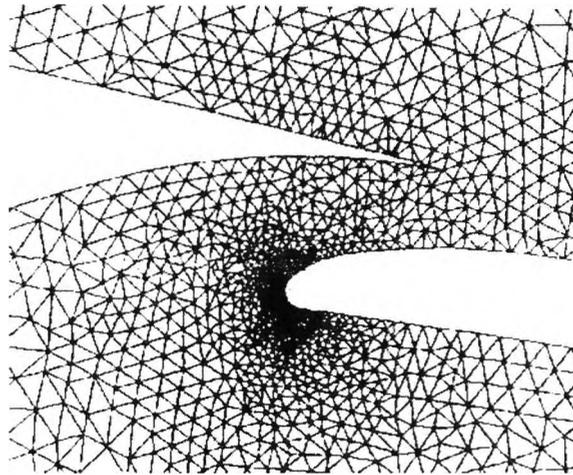
Figure 3.4: Example of an unstructured grid in the region of the flap nose

3.3.2 Grid generation

In this project, two techniques are utilised to subdivide the solution domain for the respective potential flow and finite-volume flow solvers. A streamline-based partial differential elliptic method [Drela & Giles (1987)] is employed to create grids for the two-dimensional inviscid/viscous flow solutions. Grids for the finite-volume solutions were constructed by employing ICEM-CFD, a Graphic User Interface (GUI) based pre-processing package [ICEM-CFD User manual (1999)]. ICEM-CFD permits the generation of block-structured and unstructured grids that can be translated into a format suitable for a number of commercially available flow solvers.

Grid generation technique for the CFX4 computations

Generation of both structured and unstructured grids with ICEM-CFD requires the use of four separate modules (detailed descriptions of the four modules are given in the ICEM-CFD user manual). These modules cover surface generation, grid generation, grid analysis and translation of the grid into a suitable format for the flow solver. Initially the model surface geometry is imported or created within the CAD style DDN module. The surface geometry is then coupled with one of the three grid generation packages P-Cube (Structured), Hexa (structured) and Tetra (Unstructured). Throughout this project, grids for the finite-volume code CFX4 were constructed with the block-structured module P-Cube as opposed to the HEXA module. P-Cube was preferred in this case because the module enables the user to have much greater

control of the grid features, particularly in close proximity to the aerofoil surfaces. The quality of the generated grid (cell skewness, aspect ratio and determinants) is checked with the grid analysis module Leo. Completed grids are then converted into a readable format for the relevant flow solver.

The CAD based package, DDN, enables definition of digital geometry upon which to affix the computational grid. In this project, surface locations coincident with the experimental model for the multi-element aerofoil, were read into the CAD package. Non-uniform rational B-splines (NURBS) were then created through these points to properly describe the two-dimensional high lift system and ensure its suitability for comparison with the experimental model. Projecting the NURBS in the third dimension then enabled the creation of B-spline surfaces to describe a solid section of the multi-element aerofoil. Upper and lower surface boundaries were defined at the wind tunnel walls to enable accurate comparison with experiments. Inlet and Outlet boundaries for the solution domain were defined 18 chord lengths upstream and downstream of the high lift system to minimise the influence of these boundaries on the flow field around the multi-element aerofoil.

Reading the surface geometry into the grid generation module P-Cube enables definition of the block structure and the grid for the computational domain. P-Cube works on the following hierarchy system; vertices, edges, faces and blocks. The user defines a grid by firstly subdividing the solution domain into blocks that are mapped to the surface geometry. Secondly, the cell distribution is set by controlling the edge bunching or distribution of the cell vertices along the edge, to ensure a grid resolution capable of capturing the flow phenomena in the regions of greatest significance (see Figure 3.5 over the page).
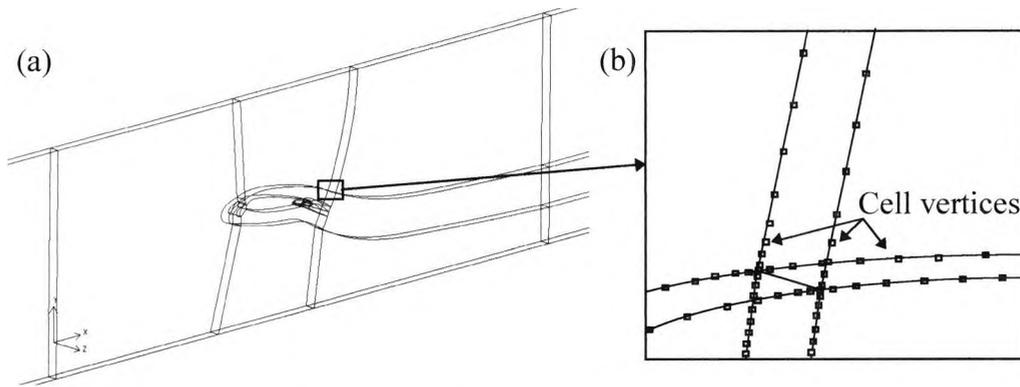
Figure 3.5: Examples of (a) High lift system block structure and (b) Edge bunching

ICEM-CFD then generates the interior cell vertices with a facial interpolation scheme from the block edges across the coupled blocks. Accuracy of the numerical solution is often highly dependent upon the orthogonality of the cells, particularly at the block boundaries. One approach that ensures near monotonic transfer of information across the cell boundaries is to use blending schemes in conjunction with the grid generation technique. The most common blending schemes (and the one employed in this project) utilise the respective transfinite interpolation methods proposed by Gordon & Hall (1973) and Eriksson (1982) in two- and three-dimensions. These schemes employ arc length based interpolants to define the interior nodes between the block faces and only require information for the vertex locations on the block boundaries.

Transfinite interpolation requires the definition of a number of blending functions for all three global coordinate axes to be able to compute the locations of the inner vertices between the user-defined vertex locations on the block edges, as shown on Figure 3.6.
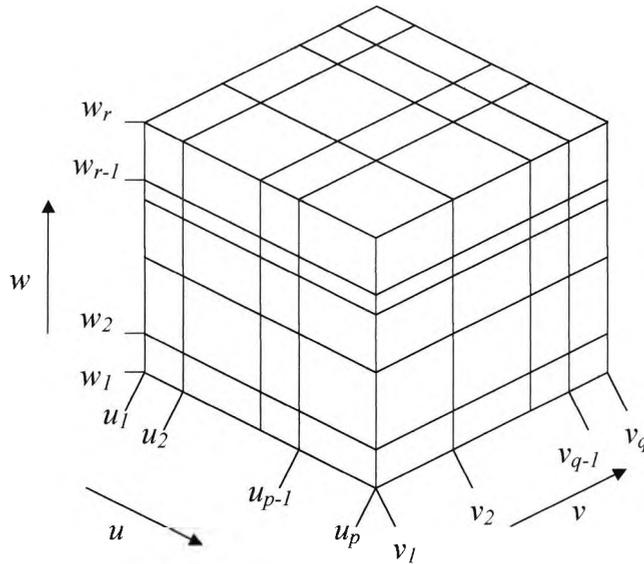
Figure 3.6: An example solution domain specified on planes of u, v, or w

Let $f(u,v,w) = [x(u,v,w), y(u,v,w), z(u,v,w)]$ where $u_1 \leq u \leq u_p$, $v_1 \leq v \leq v_q$ and $w_1 \leq w \leq w_r$. These functions are not known throughout the domain but only along certain planes:

$f(u_k,v,w) = a_k(v,w);$ $k=1,2,....,p$

$f(u,v_k,w) = b_k(u,w);$ $k=1,2,....,q$

$f(u,v,w_k) = c_k(u,v);$ $k=1,2,....,r$

Interpolation between these planes requires the definition of a set of univariate blending functions below:

$\alpha_k(u);$ $k=1,2,....,p$

$\beta_k(v);$ $k=1,2,$ $,q$

$\gamma_k(w);$ $k=1,2,$ $,r$

which only have to satisfy the following conditions:

$\alpha_k(u_l)=\delta_{kl};$ $\beta_k(v_l)=\delta_{kl};$ $\gamma_k(w_l)=\delta_{kl}$

where: $\delta_{kl}=0;$ $k\neq l$ $\delta_{kl}=1;$ $k=l$

The interpolated function $f(u,v,w)$ is then defined by the recursive algorithm:

$$
\left.
\begin{aligned}
f_1 &= \sum_{k=1}^{p} \alpha_k(u) a_k(v,w) \\
\\
f_2(u,v,w) &= f_1(u,v,w) + \sum_{k=1}^{q} \beta_k(v)[b_k(u,w) - f_1(u,v_k,w)] \\
\\
f(u,v,w) &= f_2(u,v,w) + \sum_{k=1}^{r} \gamma_k(w)[c_k(u,v) - f_2(u,v,w_k)]
\end{aligned}
\right\}
\qquad (3.11)
$$

Boundary types for the solution domain can also be defined on blocks or faces, within the P-Cube module, namely Inlet planes, Outlet planes, Pressure Boundaries, Symmetry planes and Walls. More sophisticated boundary type definition such as periodic boundaries, however, require modifications to the grid geometry file (see Section 3.4.2).

Grid generation technique for the MSES computations

Grid generation for the MSES viscous/inviscid code is enveloped completely within the flow solver. Initially, a potential flow solution is obtained to enable generation of a set of streamlines about the multi-element aerofoil. Setting the vertex distribution on the aerofoil surfaces then permits definition of the normal grid lines across the streamlines. Grid orthogonality at the aerofoil surface and across the streamlines is ensured by means of elliptic smoothing. Figure 3.7 represents a typical grid for the high lift system produced by the MSES flow solver.
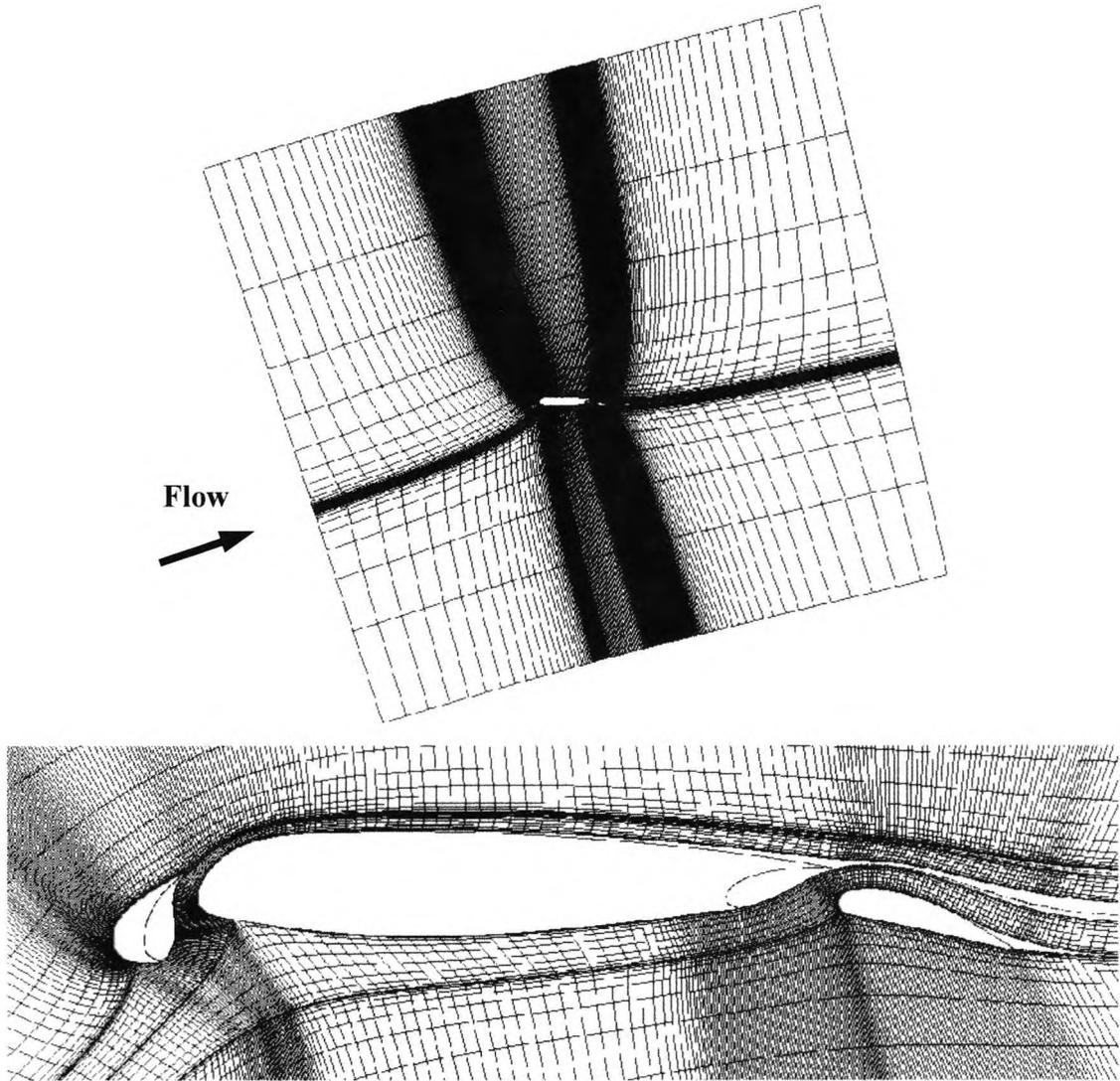
Flow

Figure 3.7: Grid topology generated by the MSES flow solver

3.4 Solving the incompressible three-dimensional Navier-Stokes equations

In general, analytical expressions for flows governed by the Navier-Stokes equations, as a function of location (x, y, z), are not available to permit determination of the basic variables u, v, w, p. CFD approaches to solve the Navier-Stokes equations replace the partial derivatives with approximate algebraic difference quotients defined at discrete points within the solution domain. The most common discretisation methods are encompassed within Finite-Volume Methods (FVM) or Finite Element Methods (FEM): see Ying (1996). Although utilised extensively in structural analysis, FEM techniques have lent themselves to aeronautical studies with the development of

unstructured gridding techniques. However, the large computer storage requirements and more generalised FVM gridding techniques have resulted in the majority of flow solvers utilising FVMs.

3.4.1 Finite-volume method

FVMs require the solution domain to be divided into a number of control volumes (CVs) by a grid that defines the control volume boundaries (Figure 3.8). This enables simple profile variation assumptions (e.g. linear) to be made for the dependent variables across adjacent CVs. The integral conservation equations are approximated over the CV so that algebraic expressions for the dependent variables can then be defined at discrete points throughout the solution domain. Errors in the approximation are related to the number of CVs within the solution domain. As the number of CVs approaches infinity the magnitude of the error tends to zero. Further improvements in the solution accuracy also arise from better approximations of the flow variable profile variations across the CVs.
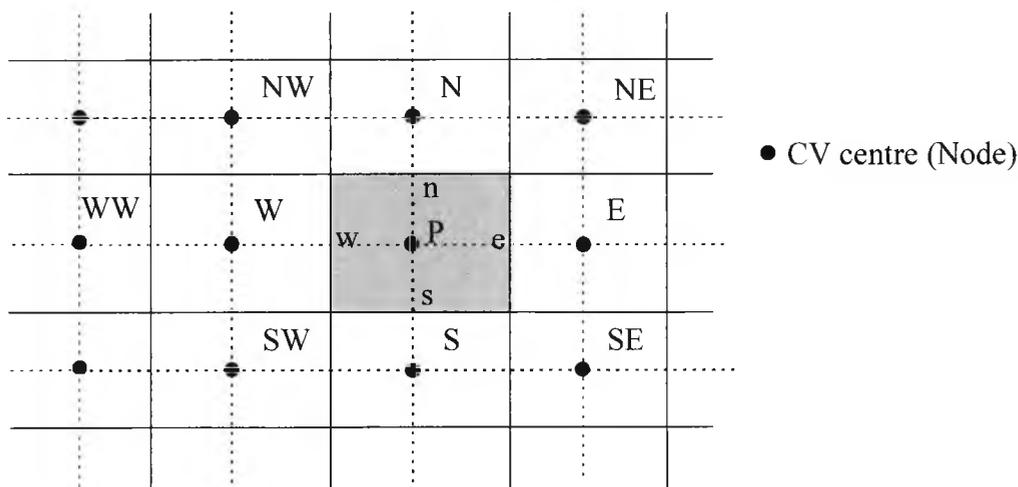
Figure 3.8: Finite volume discretisation of a solution domain

Calculation of the surface integral for the dependent variable over the entire CV requires knowledge of the variation of the dependent variable over each of the CV surfaces. Two levels of approximation are introduced. Firstly, the surface integral must be expressed as a function of the variable values across the cell faces. Secondly, the variable values have to be expressed as a function of the nodal values.

The simplest form of integral approximation is based on the midpoint rule, where the integrand is defined as a mean variable value, at the face centre, multiplied by the face area (see the following example for discretising the advection term in the momentum equation in one-dimension). As the variables cannot be determined exactly, they are expressed via interpolation methods from the values at the surrounding nodes. The accuracy of the solution is highly dependent upon the sophistication of the interpolation method. Unfortunately, the convergence and stability of a numerical solution are also dependent upon the chosen interpolation scheme. It is often the case that more accurate interpolation schemes diverge as they are more sensitive to the direction of the flow.

Example: Approximation of the advection term across the CV, with the midpoint rule, in one-dimension (see Figure 3.8)

Advection term:

$$\rho \int_{w}^{e} \frac{\partial (u\phi)}{\partial x} dx \approx \rho u \left[\phi_e - \phi_w \right] \tag{3.12}$$

where:

$$\phi_e = \frac{1}{2} \left(\phi_P + \phi_E \right), \quad \phi_w = \frac{1}{2} \left(\phi_P + \phi_W \right)$$

so that Eqn. (3.12) becomes:

$$\rho \int_{w}^{e} \frac{\partial (u\phi)}{\partial x} dx = \frac{\rho u}{2} \left[\phi_E - \phi_W \right] \tag{3.13}$$

Interpolation schemes to calculate the dependent variables, with a finite volume technique at the nodes, are known as differencing schemes. This definition arises because employing finite differencing methods to approximate partial differentials yield the same expressions. CFX4 permits the user to employ one of seven differencing schemes of varying degrees of complexity.

The resulting algebraic expressions for the dependent variables are then solved with iterative methods until a pre-defined convergence criterion is achieved. In CFX, the linearised difference equations for each variable in each CV are solved with simultaneous linear equation solvers. In contrast, MSES employs a Newton solution procedure to obtain simultaneous solutions of the inviscid and viscous flow with the flow equations discretised on an intrinsic grid.

In the following section, the various differencing schemes are demonstrated for the advection terms by considering the CV shown on Figure 3.8. Before elaborating on the various differencing schemes, it is useful to introduce the concepts of numerical dissipation and numerical dispersion. Finite differencing methods for the flow variables include some round-off or truncation errors. When included in the governing flow equations, the truncation errors can tend to smooth out sharp gradients (dissipation) or manifest themselves as non-physical oscillations (dispersion). This effect is purely a consequence of numerical differencing and so has no physical significance to the solution. In general, if the lowest order term in the truncation error contains an even derivative (e.g. $\partial^2 u/\partial x^2$) then the solution will tend to exhibit dissipative errors. On the other hand, if the lowest order term in the truncation error is odd (e.g. $\partial^3 u/\partial x^3$) then the solution will tend to exhibit dispersive errors, as shown in Figure 3.9. The dichotomy associated with the above discussion is, that more often than not, some numerical dissipation is required to ensure a 'stable' solution.

(a) Exact solution   (b) dissipative error   (c) dispersive error
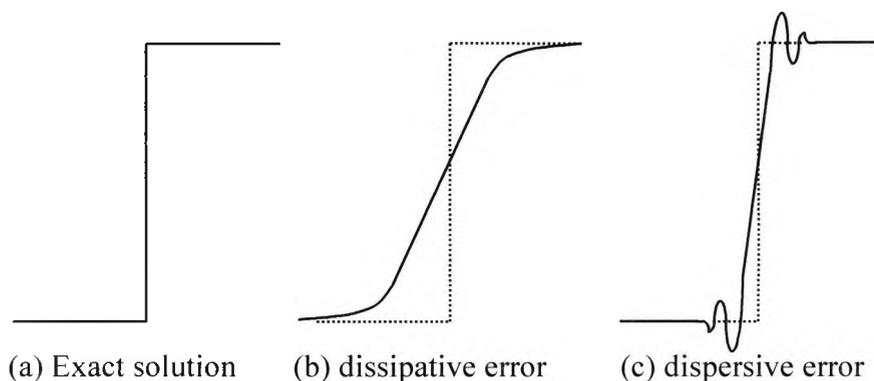
Figure 3.9: Numerical dissipation and dispersion effects on computed 'sharp' gradients

Upwind differencing (UDS)

The quantity of the dependent variable ϕ is set equal to the adjacent upstream value, i.e., on the west face depending on the flow direction:

$$\phi_w = \begin{cases} \phi_W, & \text{if } u_w > 0 \\ \phi_P, & \text{if } u_w < 0 \end{cases} \qquad (3.14)$$

This scheme is first-order accurate and unconditionally stable but introduces numerical dissipation that distorts the numerical solution.

Central differencing (CDS)

The dependent variable is determined as the mean value of the two adjacent nodal values, i.e.,

$$\phi_w = \frac{1}{2}\left(\phi_W + \phi_P\right) \qquad (3.15)$$

Although CDS is a second-order accurate scheme, its stability is dependent upon the magnitude of the cell Reynolds number (the ratio of convective to diffusive fluxes at the cell face) defined as:

$$\text{Re}_c = \frac{u\Delta x}{v} \equiv \frac{\text{Convection}}{\text{Diffusion}} \quad \Rightarrow \quad \text{Unstable if } |\text{Re}_c| > 2$$

where Δx is the distance between the cell faces

Hybrid differencing (HDS)

An HDS scheme eliminates the stability problems of CDS by switching between UDS and CDS depending on the cell Reynolds number. As a result, the HDS can only be considered first order accurate.

If $|\text{Re}_c| \geq 2$ Convection is dominant and diffusion is ignored, $\therefore$ UDS is employed

If $|\text{Re}_c| < 2$ Convection and diffusion are equally important, $\therefore$ CDS is employed

Higher order upwind differencing (HUW)

HUW is a second-order accurate upwind scheme that extrapolates to the CV face from two upstream nodal points (see CFX solver manual).

$$\phi_w = \begin{cases} \dfrac{3}{2}\phi_W + \dfrac{1}{2}\phi_{WW}, \text{ if } u_w > 0 \\ \dfrac{3}{2}\phi_P + \dfrac{1}{2}\phi_E, \text{ if } u_w < 0 \end{cases}$$

(3.16)

Quadratic upwind differencing (QUICK)

A third-order accurate scheme for the advection terms that employs two upstream points as well as one downstream, proposed by Leonard (1979) is:

$$\phi_w = \begin{cases} \dfrac{3}{8}\phi_P + \dfrac{3}{4}\phi_W - \dfrac{1}{8}\phi_{WW}, \text{ if } u_w > 0 \\ \dfrac{3}{8}\phi_W + \dfrac{3}{4}\phi_P - \dfrac{1}{8}\phi_E, \text{ if } u_w < 0 \end{cases}$$

(3.17)

This scheme is somewhat unstable due to the inclusion of the downstream variable.

Curvature Compensated Conjective Transport (CCCT)

The higher-order schemes often suffer from non-physical overshoots in the solution. CCCT is a modified bounded version of QUICK that is designed to eliminate the overshoots.

$$\phi_w = \begin{cases} \left(\dfrac{3}{8}-\alpha\right)\phi_P + \left(\dfrac{3}{4}+2\alpha\right)\phi_W - \left(\dfrac{1}{8}+\alpha\right)\phi_{WW}, \text{ if } u_w > 0 \\ \left(\dfrac{3}{8}-\alpha\right)\phi_W + \left(\dfrac{3}{4}+2\alpha\right)\phi_P - \left(\dfrac{1}{8}+\alpha\right)\phi_E, \text{ if } u_w > 0 \end{cases}$$

(3.18)

where α depends on the curvature of the variable ϕ. Further details of the advection scheme are given in Alderton & Wilkes (1988).

CONDIF

The CONDIF advection scheme was developed to eliminate the difficulties associated with CDS and the matrix coefficients. In the CONDIF scheme, the matrix coefficients are written so as to be diagonally dominant and upwind differencing is employed if non-physical overshoots occur (see Alderton & Wilkes (1988)).

Pressure velocity correction

Upon discretisation of the momentum equations, no determination of the pressure and no independent use of continuity have been made. This is because pressure does not feature explicitly in the continuity equation and so can only be considered as a constraint in the momentum equations. A commonly-employed approach in the majority of finite volume flow solvers is the SIMPLE scheme (Semi Implicit Method for Pressure Linked Equations). The scheme uses a pressure correction rather than the pressure itself to correct the velocities determined from the momentum equations. A guess for the pressure (p^*) is employed to determine the velocity components (u_i^*), which can be substituted into the continuity equation. If continuity is not satisfied the velocities (and subsequently the pressure) can be updated with correction values (u_i', p'). The process is then repeated, as outlined below, until convergence is achieved.

The velocity and pressure correlations are:

$$u_i = u_i^* + u_i', \text{ and } p = p^* + p' \tag{3.19}$$

The continuity equation is:

$$\frac{\partial u_i^*}{\partial x_i} + \frac{\partial u_i'}{\partial x_i} = 0 \tag{3.20}$$

The linearised momentum equations are:

$$A_P^{u_j} u_{i,P}^* - \sum_k A_k^{u_j} u_{i,k}^* = S_{u_i}^* - \left(\frac{\partial p^*}{\partial x_i} \right)_P \qquad (3.21a)$$

$$A_P^{u_i} u_{i,P} - \sum_k A_k^{u_i} u_{i,k} = S_{u_i} - \left(\frac{\partial p}{\partial x_i} \right)_P \qquad (3.21b)$$

Subtracting Eqn. (3.21a) from a similar expression for u_i, [Eqn. (3.21b)] and dividing by $A_P^{u_i}$ and using Eqn. (3.19), yields an expression that relates the velocity and pressure corrections.

$$u_{i,P}' = \widetilde{u}_{i,P}' - \frac{1}{A_P^{u_i}} \left(\frac{\delta p'}{\delta x_i} \right) \qquad (3.22)$$

where

$$\widetilde{u}_{i,P}' = - \frac{\sum_k A_k^{u_i} u_{i,k}'}{A_P^{u_i}} \qquad (3.23)$$

Taking the divergence of Eqn. (3.19) and satisfying continuity gives:

$$\frac{\partial u_i^*}{\partial x_i} + \frac{\partial u_i'}{\partial x_i} = 0 \qquad (3.24)$$

Utilising Eqn. (3.22) to eliminate the u_i' yields the pressure-correction equation:

$$\frac{\partial}{\partial x_i} \left[\frac{1}{A_P^{u_i}} \left(\frac{\partial p'}{\partial x_i} \right) \right]_P = \left[\frac{\partial u_i^*}{\partial x_i} \right]_P + \left[\frac{\partial \widetilde{u}_i'}{\partial x_i} \right]_P \qquad (3.25)$$

As the value of the velocity correction $\widetilde{u}_i'$ is unknown, the term is usually dropped yielding the pressure-correction equation of Patankar & Spalding (1972). Once the pressure-correction equation has been solved, the velocities are updated using Eqns. (3.19) and (3.22). The method is limited, however, as it has a tendency to converge

84

relatively slowly due to the $\widetilde{u}_i'$ being neglected. Improved convergence has been demonstrated with the SIMPLEC method proposed by Van Doormal & Raithby (1984). Here the velocity correction $\widetilde{u}_i'$ is approximated by a weighted mean of its neighbour's values giving:

$$\widetilde{u}_{i,P}' \approx -u_{i,P}' \frac{\sum_k A_k^{u_i}}{A_P^{u_i}}$$

(3.26)

Substituting Eqn. (3.26) into Eqn. (3.22) gives the following approximate relationship between u_i' and p':

$$u_{i,P}' \approx -\frac{1}{A_P^{u_i} + \sum_k A_k^{u_i}} \left(\frac{\partial p'}{\partial x_i} \right)$$

(3.27)

A further constraint is that the pressure source term in the momentum equation is solved with central differencing and only alternate computational nodes are involved in the pressure force calculation. As a result, oscillatory or checkerboard pressure fields can develop (Figure 3.10) that are interpreted as 'uniform' by the momentum equations.
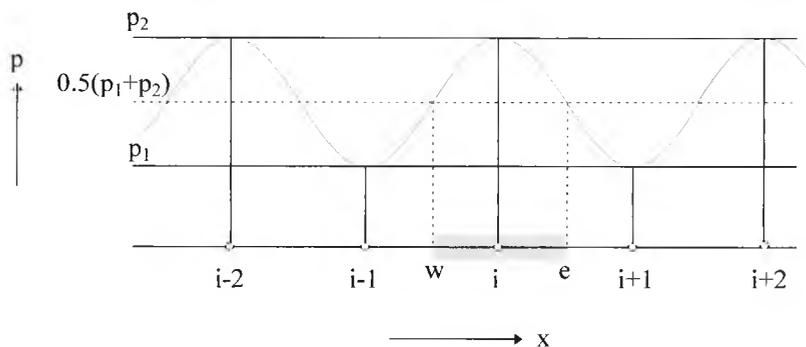
Figure 3.10: Checkerboard pressure field arising from central differencing

One approach to eliminating the effects of checkerboarding was to employ staggered grids so that the pressures and velocities are solved at different locations. However, for complex geometries, storage requirements often prohibit the use of staggered grids. This disadvantage was overcome by employing the algorithm of Rhie & Chow (1983) that enabled the results to be stored in a collocated arrangement at one location

in the CV with the pressures being determined at the CV faces. The algorithm contains an artificial pressure dissipation that mimics staggered grid behaviour and has been shown to improve convergence on non-orthogonal grids. Applying the algorithm to the 'guessed' velocities on the cell faces yields the following expression at the east face:

$$u_{x,e}^* = -\overline{\left(u_x^*\right)}_e - \overline{\left(\frac{1}{A_P}\right)}_e \left[\left(\frac{\partial p^*}{\partial x}\right)_e - \overline{\left(\frac{\partial p^*}{\partial x}\right)}_e \right] \qquad (3.28)$$

where:

$$\overline{\left(u_x^*\right)}_e = \frac{1}{2}\left[\left(u_x^*\right)_E + \left(u_x^*\right)_P\right], \quad \overline{\left(\frac{1}{A_P}\right)}_e = \frac{1}{2}\left(\frac{1}{\left(A_P\right)_E} + \frac{1}{\left(A_P\right)_P}\right),$$

$$\overline{\left(\frac{\partial p^*}{\partial x}\right)}_e = \frac{1}{2}\left[\left(\frac{\partial p^*}{\partial x}\right)_E + \left(\frac{\partial p^*}{\partial x}\right)_P\right], \quad \left(\frac{\partial p^*}{\partial x}\right)_e = \frac{p_E^* - p_P^*}{\Delta x_e}$$

Similar arguments can be used to determine expressions for the remaining four cell faces.

3.4.2 Boundary condition implementation

A well-posed numerical solution requires the correct implementation of physically relevant boundary conditions. Failure to do so can only result in a non-physical solution that does not pertain to a real life flow situation. Solution domain boundary conditions can take one of two forms or a mixture of the pair [see p118 Anderson (1995)]. The Dirichlet form relies on specifying the dependent variables (u, v, w, p) along the boundary; whereas Neumann boundary conditions rely on specifying the derivatives of the dependent variables along the boundary.

CFX4 boundary condition implementation

Boundary conditions on the grids for CFX4 are defined on the faces at the block boundaries. In this project, use is made of the following boundary condition types:

Inlet boundary - In the standard form, inlets describe the velocity components and turbulence properties across the face at the cell centres. By default, the flow solver employs the velocity vectors stated in the command language file and bases the turbulence parameters on empirical relationships between Reynolds stress and kinetic energy. More advanced inlet profiles for all parameters can be defined by making use of FORTRAN user routines (USRBCS) that interface with the flow solver.

Pressure boundary - For incompressible flow, the pressure is set to a constant value as defined in the command language file. Once again making use of the USRBCS routine enables the definition of a variable pressure profile if required.

Symmetry plane - Here the velocity normal to the plane and the gradients of all other quantities are set to zero. The boundary condition therefore acts as a slipping wall through which the flow cannot pass.

Periodic boundary - These ensure that all variables, and hence coefficients, have the same value either side of the computational or physical domain.

Inter-block boundary - A generalisation of the periodic boundary condition. At inter-block boundaries all variables and coefficients have identical values on the common face between adjacent blocks.

Wall boundary - The no-slip condition is enforced at a wall i.e. u, v, and w are equal to zero. Turbulent properties may be determined with a number of techniques but for this project a logarithmic law of the wall profile is utilised [see p58 Thwaites (1960)].

MSES boundary condition implementation

For the inviscid region, the aerofoil surface boundary conditions are simply defined by the adjacent streamlines that are displaced from the surface by the calculated displacement thickness. The pressure here is a result of the calculation and no extrapolation to the aerofoil surface is required. Far-field boundary conditions are imposed from the pressure corresponding to a uniform freestream plus a far-field circulation, source strength and two doublet components. The far field circulation is calculated from trailing edge Kutta condition in the same manner as a potential flow solver. The advantage of such an approach is to permit the boundary to be placed only a few chords away from the aerofoil, significantly reducing the number of unknowns in the numerical solution. At the inlet and outlet faces, the streamline corresponding to the flow angle from the freestream vortex, source, and doublet combination is specified at each streamline as shown on Figure 3.11.

$$q_\infty = \frac{1}{2}\rho U_\infty^2$$
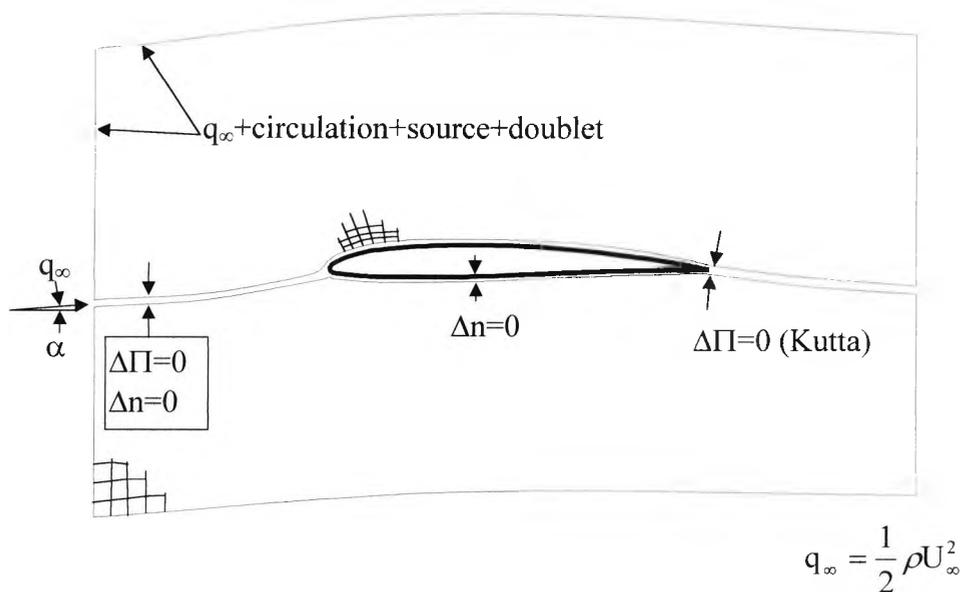
Figure 3.11: Boundary conditions for the MSES flow solver, from Drela (1990)

3.4.3 CFX4: - Code overview

CFX4 is a finite-volume based numerical flow solver using a structured and patched, nonorthogonal, curvilinear co-ordinate grid with a collocated variable arrangement. The code has the ability to predict wholly laminar, wholly turbulent but not transitional flows. Heat transfer flows that can be coupled with a variety of models (multi-phase, spray, explosion,...etc.)to simulate more advanced flow situations. The complete software package consists of a pre-processing module, a front-end module, a solver module and a post-processing module.

The pre-processing modules (CFX-Build and CFX-Meshbuild) enable the user to define the geometrical solution domain and the finite difference grid in an interactive manner. CFX-Meshimport is a finite element to multi-block grid converter that outputs optimal block structures in a readable format for CFX processing. Input specifications for the flow solution are defined with the front-end module in the form of a command language file. Within this command language file the boundary conditions and fluid properties are specified.

The solution module solves the discretised form of the flow and 'dumps' the results to disc files. Information is received in a form that permits calculation of the solution on a variety of computer platforms including parallel processors.

Finally, the results of the flow solution can be graphically visualised with the post-processing module. Alternatively, interfaces for other specialised graphics packages may be utilised.

3.4.4 MSES: - Code overview

MSES is a two-dimensional coupled viscous/inviscid flow solver capable of dealing with multi-element aerofoil flows. The code combines a streamline-based Euler discretisation and a two-equation integral boundary layer formulation coupled through the displacement thickness. MSES solves the laminar portion of the boundary layer with the method of Thwaites (1960) and the turbulent portion with the entrainment

method of Green et al (1973). Both laminar and turbulent boundary layer methods are coupled by employing a two-equation dissipation-type closure with the lag equation added to the turbulent formulation. Laminar to turbulent boundary-layer transition is accounted for with the e^n method as described in Chapter 2. A multi-deck shear layer approach is utilised to enable calculation of the asymmetric wakes and the confluent boundary layers above the aerofoil surfaces.

The inclusion of Green's lag-entrainment method in the MSES formulation offers a worthwhile improvement in accuracy of the predictions without significantly increasing CPU time. This is because the 'lag' equation for the entrainment coefficient is developed from the differential equation for shear stress derived by Bradshaw et al (1967), with empiricism required to account for the non-uniform pressure distributions exerted externally to the boundary layer in most engineering flows. As a result, the lag-entrainment method permits a straightforward way of assessing at least first-order corrections for the influences of longitudinal surface curvature on the turbulence structure.

Pre-processing, problem definition, problem solution and post-processing modules are all contained within one interactive front-end. The user defines the basic aerofoil geometry and boundary conditions in data files that are then utilised by the flow solver module.

3.5 Turbulence modelling techniques

Turbulence is defined as a flow in which the flow quantities vary randomly with time and space, enabling statistically independent average variables to be computed. As turbulence is not an equilibrium phenomenon, it requires some external energy to produce it (either mean flow or pressure gradient) without which viscous forces will cause it to decay. When no preferred direction for the fluctuations occurs and the flow is in complete disorder, the turbulence is said to be 'isotropic'. This condition is somewhat hypothetical as no real flows exist that are completely isotropic; but isotropic turbulence is the simplest to model and forms the fundamental basis for 'anisotropic' flows. In most cases, anisotropic turbulent flows do exhibit a significant

degree of isotropy in the fine structure and hence are defined as 'locally isotropic'. By assuming local isotropy in the controlling fine structure of the turbulence it is possible to adequately approximate the behaviour of anisotropic flows.

A turbulent flow has a swirling motion of vortices (or eddies) of varying size and fluctuating frequency produced by the external agent, i.e. a mean flow or a pressure gradient. The energy of these eddies is cascaded down from the large-scale vortices to increasingly smaller scales, until viscosity can dissipate their energy into the internal energy of the fluid. Throughout this cascade, the rate at which the energy is transferred to smaller scales is equal to the rate it is dissipated at the smallest scale; i.e., production is in near balance with dissipation.

Two distinct kinds of turbulence have been identified depending on the way in which the irregular motion is induced. Turbulence generated by frictional forces on walls is defined as 'wall turbulence' and turbulence resulting from differences of velocity in the free shear layers is defined as 'free turbulence'. Flows associated with high lift systems are a complex mixture of both types.

Numerical prediction of the nature of turbulent flow has given rise to two main approaches. The first, Direct Numerical Simulation (DNS), relies on solving the unsteady Navier-Stokes equations for every perturbation in the flow. As a result, an immense number of calculations is required making the approach prohibitively expensive for the majority of flow situations. The second is the Reynolds Averaged Navier-Stokes (RANS) method in which the dependent variables in the Navier-Stokes equations are replaced with mean and fluctuating components and a time average taken (see Figure 3.12).

Dependent variable
$$U_i = \overline{U}_i + u_i$$
where
$$\overline{u_i} = 0, \ \overline{u_i^2} \neq 0, \ \overline{u_i u_j} \neq 0$$

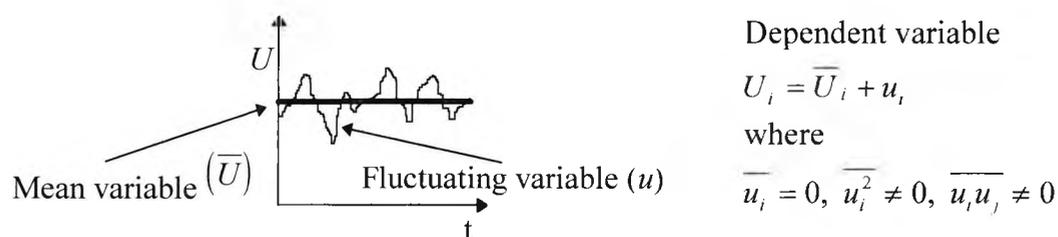Mean variable $\left(\overline{U}\right)$ Fluctuating variable (u)

Figure 3.12: Reynolds averaging applied to the flow field velocity components

This resultant form of the Navier-Stokes equations contains six unknown stress terms that are the product of the fluctuating velocities, $\overline{\rho u^2}$, $\overline{\rho uv}$, $\overline{\rho uw}$, $\overline{\rho v^2}$, $\overline{\rho vw}$ and $\overline{\rho w^2}$. These stress terms are known as the turbulent stresses or Reynolds stresses on account of the fact that Reynolds was the first to give the turbulent flow equations in this form, as shown below for incompressible steady flow:

$$\nabla(\rho U \phi) = -\frac{\partial p}{\partial x} + \mu \nabla^2 U + \left[-\frac{\partial(\overline{\rho u^2})}{\partial x} - \frac{\partial(\overline{\rho uv})}{\partial y} - \frac{\partial(\overline{\rho uw})}{\partial z} \right] + S_x \qquad (3.29a)$$

$$\nabla(\rho U \phi) = -\frac{\partial p}{\partial y} + \mu \nabla^2 U + \left[-\frac{\partial(\overline{\rho uv})}{\partial x} - \frac{\partial(\overline{\rho v^2})}{\partial y} - \frac{\partial(\overline{\rho vw})}{\partial z} \right] + S_y \qquad (3.29b)$$

$$\nabla(\rho U \phi) = -\frac{\partial p}{\partial z} + \mu \nabla^2 U + \left[-\frac{\partial(\overline{\rho uw})}{\partial x} - \frac{\partial(\overline{\rho vw})}{\partial y} - \frac{\partial(\overline{\rho w^2})}{\partial z} \right] + S_z \qquad (3.29c)$$

Closure of these RANS equations requires a turbulence model to approximate the turbulent stresses. For most practical flow situations, it is not advisable to employ higher-order turbulence models. Firstly, higher-order models involve solving more complex differential equations, so require greater computer storage. Secondly, the equations corresponding to the higher-order approaches are more sensitive to the starting procedure and require additional boundary condition treatments.

Several methods have been developed to predict turbulent flows with varying degrees of accuracy. In laminar flows, energy dissipation and transport of mass and momentum are brought about by viscosity. Boussinesq suggested in 1877 that the effects of turbulence may be represented as an increase in viscosity, leading to the well known 'eddy-viscosity model'.

$$-\overline{u_i u_j} = -\frac{2}{3} k \delta_{ij} + v_T \left[\frac{\partial U_i}{\partial x_j} + \frac{\partial U_j}{\partial x_i} \right] \qquad (3.30)$$

where v_T is the eddy viscosity and δ_{ij} is the Kronecker delta, and k is the turbulence kinetic energy , $k = \dfrac{\overline{u_i u_j}}{2}$.

In its simplest form (the zero-equation model) the turbulence is characterised by its kinetic energy or a velocity scale and a length scale for the energy cascade. Prandtl suggested a 'mixing length model' that relates the velocity scale to the mean velocity field:

$$v_T = C'_\mu \sqrt{k} L \qquad (3.31)$$

where C'_μ is a constant and L is the length scale for the energy cascade.

Although applicable to flows with curvature and pressure gradients, the definition of the energy cascade length scale for complex geometries is difficult. As a result, the zero equation approach is incapable of adequately representing the flow fields associated with complex geometries. Examples of zero-equation models include those of Cebeci-Smith (1968) and Baldwin-Lomax (1978). More sophisticated approaches employed a transport equation for the turbulent kinetic energy or a transport equation for the eddy-viscosity in order to account for the geometry effects on the flow field, i.e. the one-equation models of Bradshaw et al (1967), Baldwin-Barth (1991) and Spalart-Allmaras (1992). A significant level of success has also been achieved for a number of applications with two-equation turbulence models such as the k-ε model employed for this research. Two-equation approaches retain the Boussinesq eddy viscosity concept and employ transport equations for the turbulent kinetic energy and the distribution of the length scale. A fundamental principle of the two-equation turbulence models is that the flow is 'locally isotropic' so that production and dissipation are in near balance. The following relationship between rate of turbulence dissipation, length scale and turbulent kinetic energy is utilised in this project:

$$\varepsilon = C_D \frac{k^{\frac{3}{2}}}{L} \qquad (3.32)$$

where C_D is a constant

By combining Eqns. (3.31) and (3.32) the eddy viscosity can be determined via a relationship between k and ε without the need to define a length scale:

$$v_T = C'_\mu C_D \frac{k^2}{\varepsilon} \Rightarrow v_T = C_\mu \frac{k^2}{\varepsilon} \tag{3.33}$$

A transport equation for the dissipation can be derived exactly from the Navier-Stokes equations that has a form similar to that of the energy equation. The complexity of the equation however requires a large degree of modelling. Substitution of the complex terms in the dissipation equations with the modelled correlation's for the convection, diffusion and generation of vorticity, results in the following transport equations that constitute the k-ε model:

$$\frac{\partial k}{\partial t} + U_i \frac{\partial k}{\partial x_i} = \frac{\partial}{\partial x_i}\left(\frac{v_T}{\sigma_k}\frac{\partial k}{\partial x_i}\right) - \underbrace{v_T\left(\frac{\partial U_i}{\partial x_j} + \frac{\partial U_j}{\partial x_i}\right)\frac{\partial U_i}{\partial x_j}}_{P} - \varepsilon \tag{3.34}$$

$$\frac{\partial \varepsilon}{\partial t} + U_i \frac{\partial \varepsilon}{\partial x_i} = \frac{\partial}{\partial x_i}\left(\frac{v_T}{\sigma_\varepsilon}\frac{\partial \varepsilon}{\partial x_i}\right) + c_{1\varepsilon}\frac{\varepsilon}{k}P - c_{2\varepsilon}\frac{\varepsilon^2}{k} \tag{3.35}$$

where:

Table 3.1: Standard empirical constants as defined by Launder and Spalding (1974)

C_μ	$c_{1\varepsilon}$	$c_{2\varepsilon}$	σ_k	σ_ε
0.09	1.44	1.92	1.0	1.3

With only a few exceptions it is not possible to apply two-equation RANS models to the near wall region without some modification to the k and ε turbulence transport equations due to the anisotropy of the turbulence. The turbulent profile can however be subdivided into separate regions [see Figure 3.13 below taken from Thwaites (1960)].
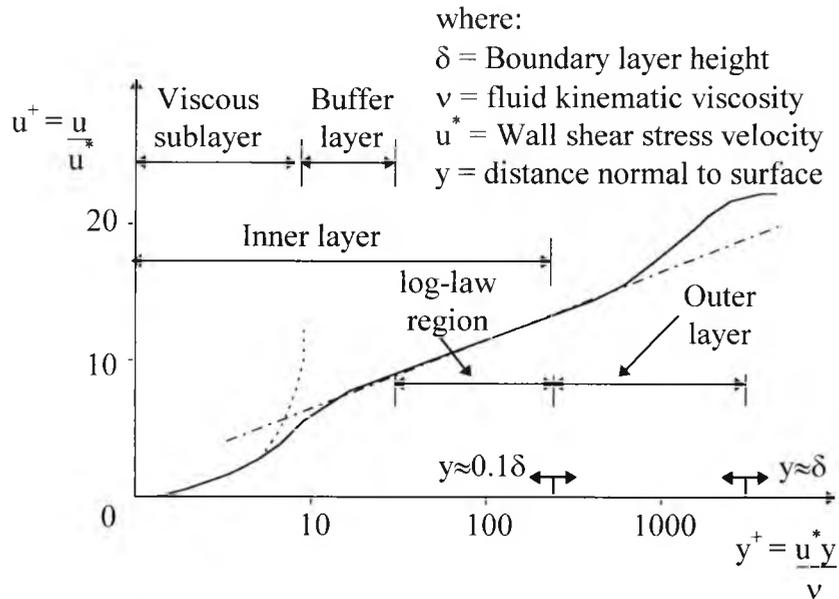
Figure 3.13: Fully turbulent boundary layer on a flat plate, from Thwaites (1960)

Coincident with the wall is the 'viscous sublayer' where viscous forces dominate over the turbulent fluctuations. Above the viscous sublayer, the viscous effects decrease with increasing distance from the wall in the 'buffer region' until finally we enter the 'fully turbulent log law region' where the turbulent fluctuations dominate. To accommodate the rapidly changing turbulence parameters in the near wall region, a common approach is to employ wall functions to act as a boundary condition on the 'no-slip' surface. This removes the need for excessively fine grids at the solid surface without necessarily detracting from the accuracy of the solution (at least in flows where the log-law holds). The method does require that the first grid point is located in the fully turbulent log law region. A number of definitions are available for the law of the wall region where the range of $20 \leq y^+ \leq 400$ for flat plate flow is widely accepted [Thwaites (1960)]. The boundary condition for the velocity component parallel to the wall (U) is:

$$\frac{U}{U^*} = \frac{1}{\kappa} \ln\left(y^+ E\right)$$ (3.36)

where: $y^+ = \dfrac{yU^*}{\nu}$, $U^* = \sqrt{\dfrac{\tau_W}{\rho}}$

E = roughness factor (typically 9 for smooth walls), and κ = Von Karman constant (0.41).

95

Assessment of the wall shear stress, τ_W, requires the k equation to be solved at the grid node adjacent to the wall, by employing the following boundary conditions for k and ε at the model surface:

$$\frac{k}{U^{*\,2}} = \frac{1}{\sqrt{C_\mu}} \qquad\qquad (3.37)$$

$$\varepsilon = \frac{C_\mu^{3/2} k^{3/2}}{\kappa y} \qquad\qquad (3.38)$$

3.6 Numerical models

3.6.1 Introduction

Three computational models have been utilised in an attempt to predict and estimate the sensitivities of parameters affecting the flow field of the high lift system incorporating an array of AJVGs. Precise calculation of flows around high lift geometries in two-dimensions is a challenging task, as discussed in Chapter 2. The inclusion of a flow control device requires a certain degree of simplification of the numerical model. This project utilises three models of varying complexity to analyse the flow field associated with a two-dimensional high lift geometry: an AJVG installed on a flat plate in a zero and a favourable/adverse pressure gradients; and a three-dimensional slice of a high lift geometry incorporating an AJVG. The computational solution process is outlined below in Figure 3.14.
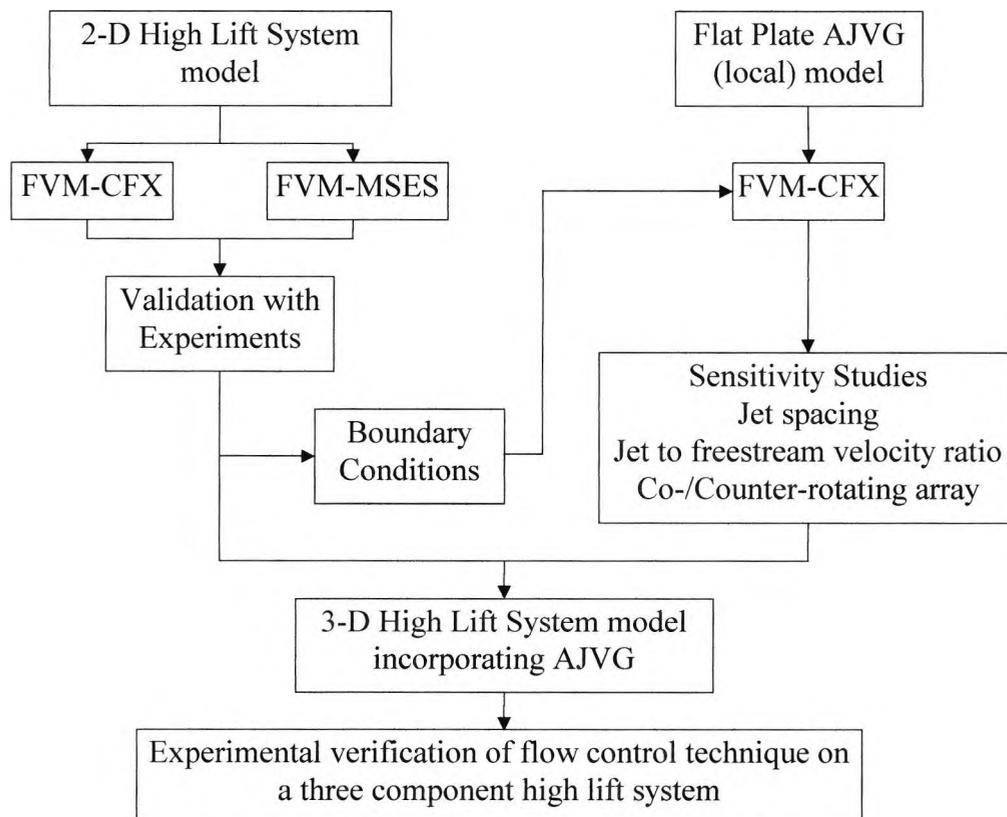

Figure 3.14: Computational solution procedure

3.6.2 Two-dimensional high lift system computations

Computational results for the flow field around the high lift system are compared and validated with the experiments conducted by Innes (1995) and the author. In the finite volume method, the freestream flow and model boundary conditions for the computational domain were made coincident with those in the wind tunnel experiments. The assumption of incompressible flow has implications on the location of the inlet and outlet flow boundaries. To limit the effects on the flow field around the high lift system, these boundaries were located at a distance of 18 chord lengths up and downstream of the multi-element configuration. As a result, the computational solution domain takes the form represented on Figures 3.15-3.18. Suitable discretisation of the flow domain was achieved by subdividing the domain into 17 blocks with approximately 50,000 control volumes. Upon interfacing the grid with CFX-Meshimport, the problem is reduced to 13 grid blocks.

Wall-boundary conditions are defined on the aerofoil surfaces and the wind tunnel walls for the preliminary two-dimensional high lift system flow field analysis. However, tests showed little difference between results obtained when employing wall or alternatively symmetry boundary conditions at the wind tunnel wall boundaries. As a result, subsequent tests employed symmetry boundaries to represent the wind tunnel walls, as this required less grid refinement to resolve the boundary layers growing on the wind tunnel wall above and below the high lift system. Inlet flow conditions are defined with a 'plug' U-velocity profile equivalent to that measured in the experiments ($U_\infty=40ms^{-1}$). The outlet boundary condition is represented by a constant value for the freestream static pressure, i.e., $p_\infty= 1bar$.
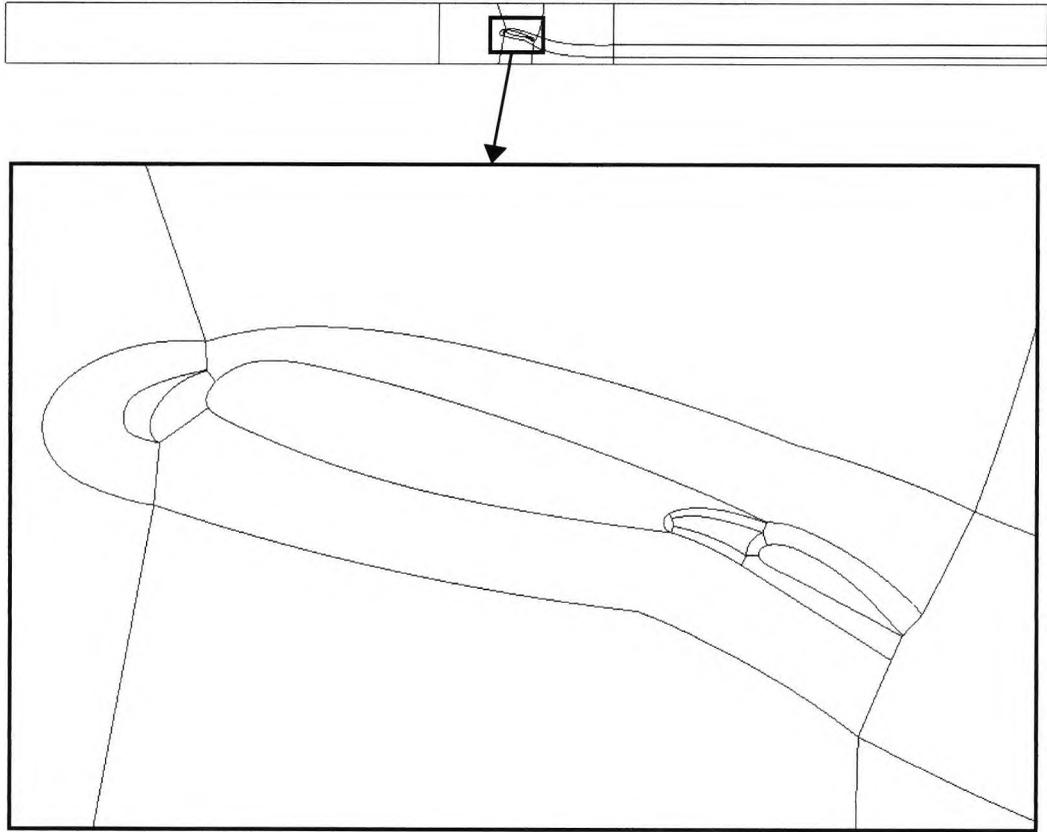
Figure 3.15: Block-structure for the 2-D high lift system model
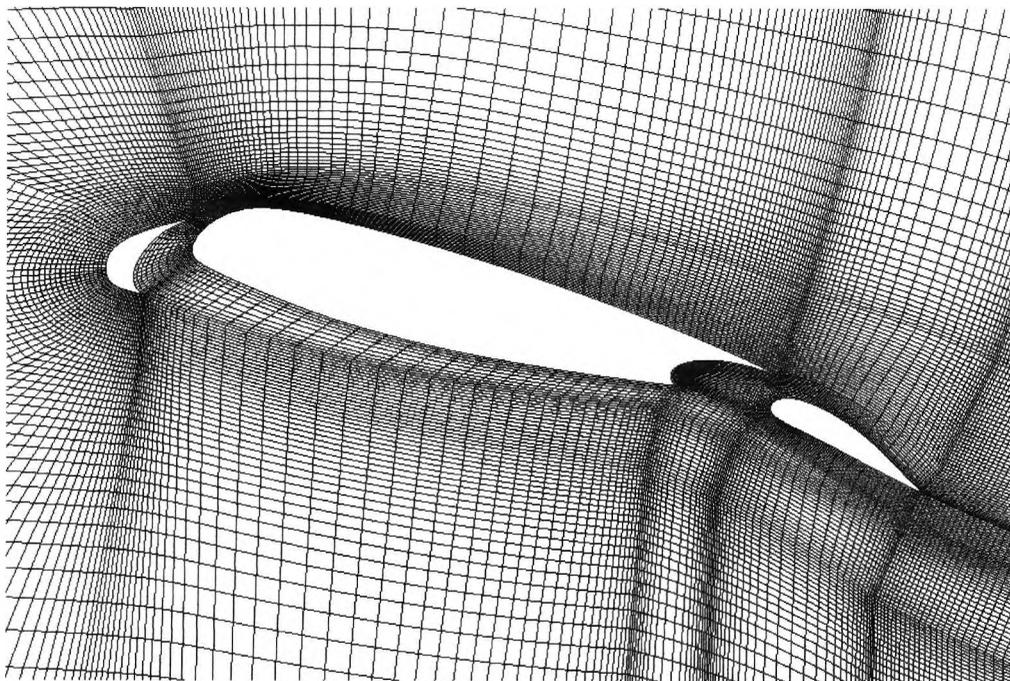

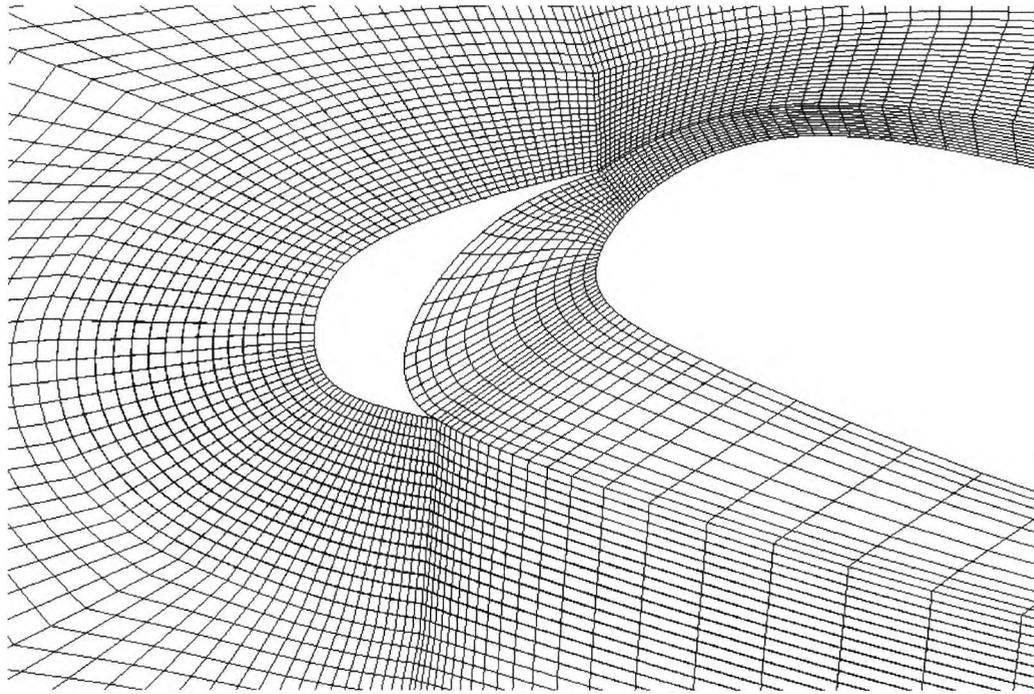Figure 3.16: Computational grid around the high lift system

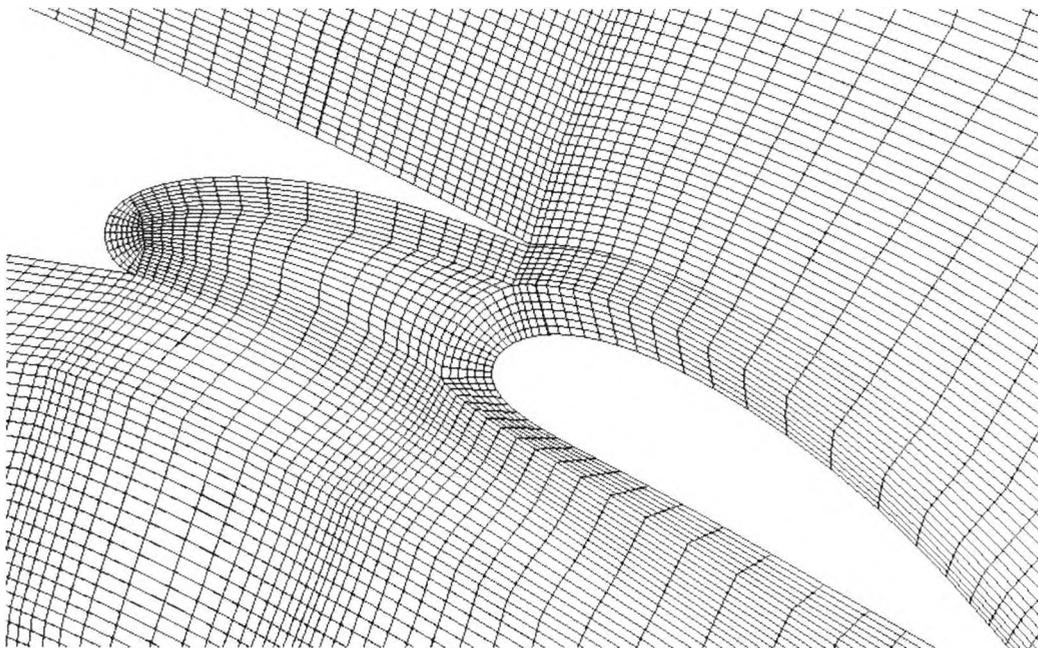Figure 3.17: Computational grid around the high lift system slat

Figure 3.18: Computational grid around the high lift system flap

Viscous/inviscid calculations were conducted with the high lift system assumed to be in free air, due to convergence difficulties experienced when employing wall boundary conditions.

3.6.3 Three-dimensional flat plate air-jet vortex generator model computations

The increased complexity analytically of incorporating an AJVG into a high lift system limits the ability of employing the computational models as an optimisation tool. Sensitivity studies investigating the effect of jet spacing S, jet to freestream velocity ratio V_R and whether co- or counter-rotating arrays offer improved performance, are conducted on simple flat plate models. The applicability of this approach to more complex systems relies on the ability to carefully define representative boundary conditions on the local model. In this project, attempts were made to simulate the effects of the strong pressure gradients observed on the high lift system by imposing analogous favourable/adverse pressure gradients on the surface of the flat plate geometry. Employing a performance enhancement criterion such as a given degree of wall shear stress enhancement then enables determination of optimum AJVG arrays. Extrapolation of these results to the more complex multi-element aerofoil geometry permits the assessment of the flow control technique in the digital wind tunnel before undertaking experiments in the analogue wind tunnel.

The local AJVG model is set up to represent an air-jet installed on the upper surface of the mainfoil on the multi-element aerofoil at a chordwise location of x/c=0.14. The rectangular air-jet geometry includes respective pitch and skew angles of 45° and 60°. The measured boundary-layer heights with the AJVGs quiescent at this location are approximately 10mm throughout the incidence range tested. To match this undisturbed boundary-layer height, the distance from the flow inlet in the computation domain to the AJVG was calculated using the theoretical boundary-layer correlations of Schlichting (1979), pp.658. The outlet flow boundary of the local model is then set far enough away from the AJVG to limit its 'non-physical' influence on the flow field. The resultant local model solution domain corresponds to three retracted chord lengths of the complete high lift system geometry (1500mm), with the middle section simulating the upper surface of the mainfoil (see Figure 3.19). This enables a pressure gradient representative of an aerofoil close to stall to be imposed on the "equivalent" flat plate surface, without generating a non-physical flow field solution. On either side of the AJVG, periodic or symmetric boundary conditions can be imposed to simulate infinite arrays of either co- or counter-rotating AJVGs respectively. A jet inlet with a

'plug' velocity profile, that is pitched and skewed to the oncoming freestream, is defined for the AJVG with a Fortran user routine in CFX.
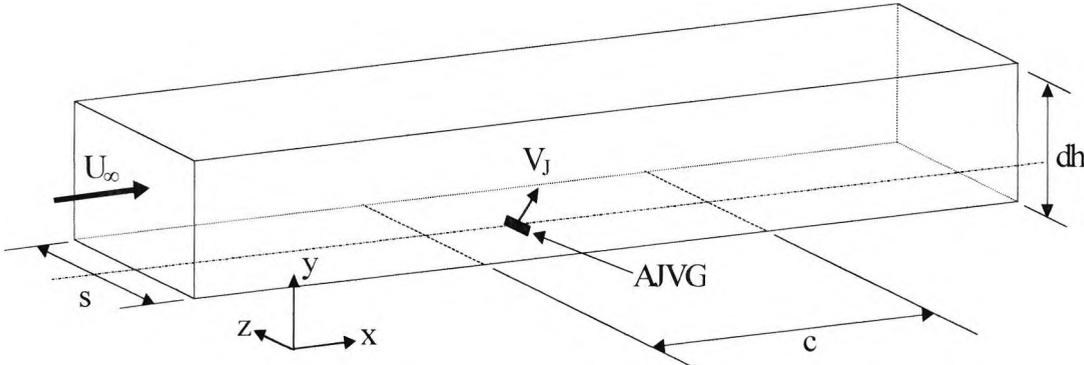

Figure 3.19: Flat plate model incorporating AJVG

A typical computational grid representing the AJVG on a flat plate, employing a jet spacing, s=0.102c, is shown on Figure 3.20.
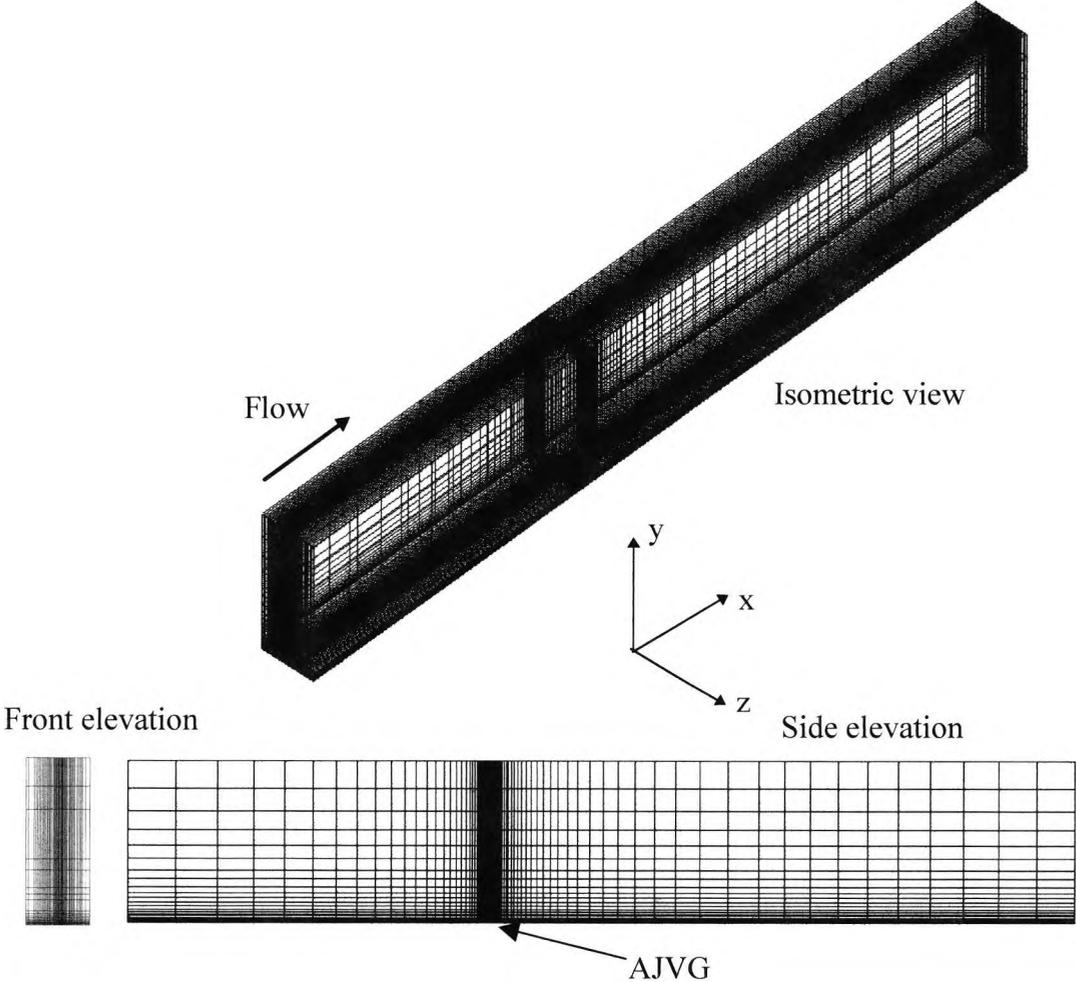
Figure 3.20: Computational grid for the flat plate geometry incorporating an AJVG

The grid consists of a single-block with approximately 60,000 control volumes. When the jet spacing is altered, the grid density in the z-direction is adjusted to maintain the control volume aspect ratio for which the grid independent solutions are obtained.

3.6.4 High lift system incorporating an array of air-jet vortex generators

Construction of the high lift system numerical model incorporating the AJVG utilises the results of the 2-D high lift system and local AJVG model tests. The optimum jet spacing and grid refinement around the AJVG from the local model tests are combined with the block structure of the 2-D high lift system grid. Some local grid refinement is required to accommodate the AJVG at the surface of the aerofoil. CFX requires one control volume in the third dimension to perform a two-dimensional calculation. Extension to a three-dimensional grid simply requires the suitable definition of the control volume distribution in the z-direction. Re-definition of the block face on the aerofoil surface enables specification of the AJVG location on the mainfoil surface. Figure 3.21 shows the surface grid distribution on the 3-D high lift system incorporating the AJVG.

Figure 3.21: Surface grid distribution for the 3-D high lift system incorporating the AJVG

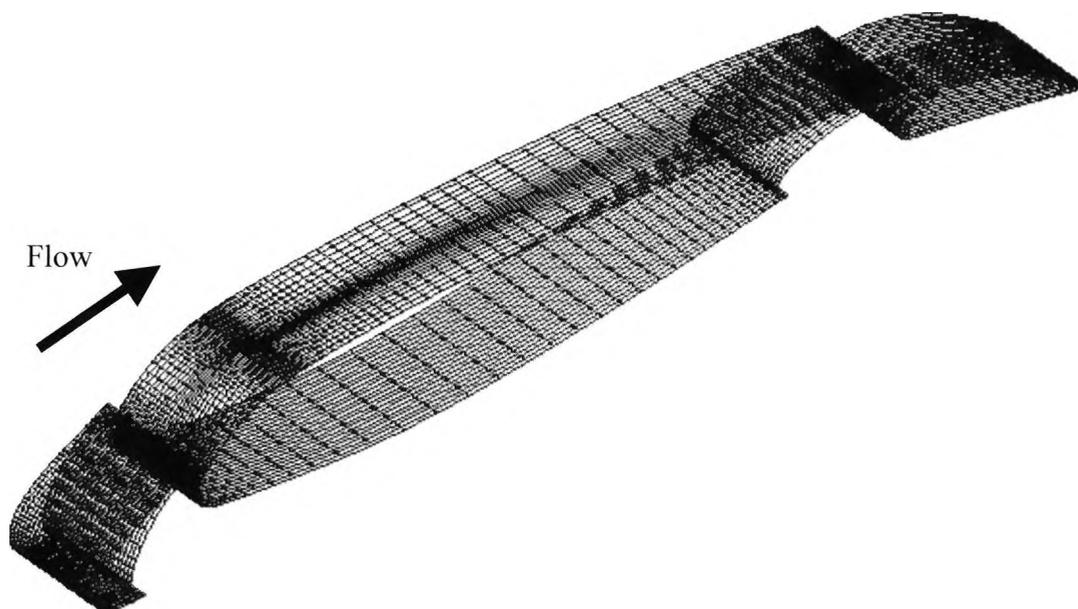### 3.6.5 Summary of the numerical computational models

A set of numerical experiments has been devised to evaluate and optimise the performance of an array of AJVGs on a three-element high lift system. Combining the results of flow solutions achieved with relatively simple numerical models enables sensitivity studies on the AJVGs to be conducted before installing in multi-component aerofoil systems. The following table details the numerical models and the flow properties:

Table 3.2: Computational model properties

Numerical Model	2-D High Lift System		Flat plate AJVG	3-D High Lift System
Flow Solver	MSES	CFX4.2	CFX4.2	CFX4.2
Chord, c (mm)	500	500	500	500
Flow Reynolds number (Re_c)	1.1×10^6	1.1×10^6	1.1×10^6	1.1×10^6
Domain height (mm)	-	1120	260	1120
Non-dim. domain width S=s/c	-	-	0.051<S<0.203	0.102
AJVG Geometry	-	-	Rectangular	Rectangular
AJVG D_H (mm)	-	-	4.18	4.18
AJVG pitch angle AJVG skew angle	-	–	$\phi=45°$ $\Psi=60°$	$\phi=45°$ $\Psi=60°$
AJVG array configuration	-	-	Co-rotating Counter-rotating	Co-rotating Counter-rotating
Jet to freesteam velocity ratio (V_R)	-	-	$0.5<V_R<4$	$1.5<V_R<4$
Incidence range	$5°<\alpha<27°$	$5°<\alpha<31°$	-	$5°<\alpha<25°$
Pressure gradient	Aerofoil	Aerofoil	zpg. & fav/apg	Aerofoil

Note: The CFX4 predictions assume the flow is fully turbulent and MSES predictions assume the flow is laminar/transitional/turbulent.

104

4. Experimental approaches

4.1 Wind tunnel set-up

Experiments were conducted in City University's T2 low speed wind tunnel at a Reynolds number of 1.37×10^6, based on the retracted chord and freestream conditions. T2 is a closed vertical circuit wind tunnel consisting of a working section of width 810mm, height 1120mm and length 1680mm, with corner fillets. The working section exit is vented to atmosphere and the turbulence level is below 0.7%. The unswept model is mounted vertically in the wind tunnel as shown on the schematic Figure 4.1.

The retracted and extended chord lengths of the high lift system are 500mm and 608.9mm respectively. The test Reynolds number of $Re_c = 1.3\times10^6$ is determined with the retracted chord length.
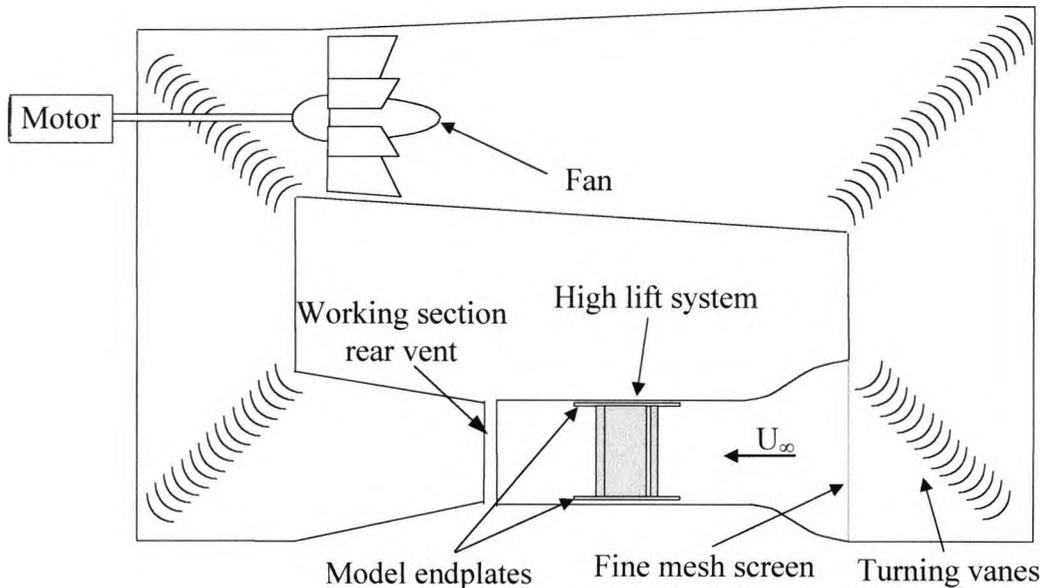
Figure 4.1: Schematic of T2 low speed wind tunnel

Nominally two-dimensional flow in the experiments is established by employing tangential blowing to control the boundary layers on two perspex endplates, between which the three-component high lift system is mounted. Adequacy of nominal two-dimensional flow was verified by monitoring the parallelism of minitufts in the endplate/aerofoil junctions at all angle of attack settings.

105

The high lift system is fitted with two separate arrays of 13 co-rotating rectangular AJVGs respectively located at 0.14c and 0.62c on the mainfoil top surface and spaced 51mm apart across the span. The rectangular air-jet slots are milled into a circular wooden plug 25mm in diameter and 14mm thick (see Figure 4.2) that are glued into recesses across the span of the mainfoil upper surface.
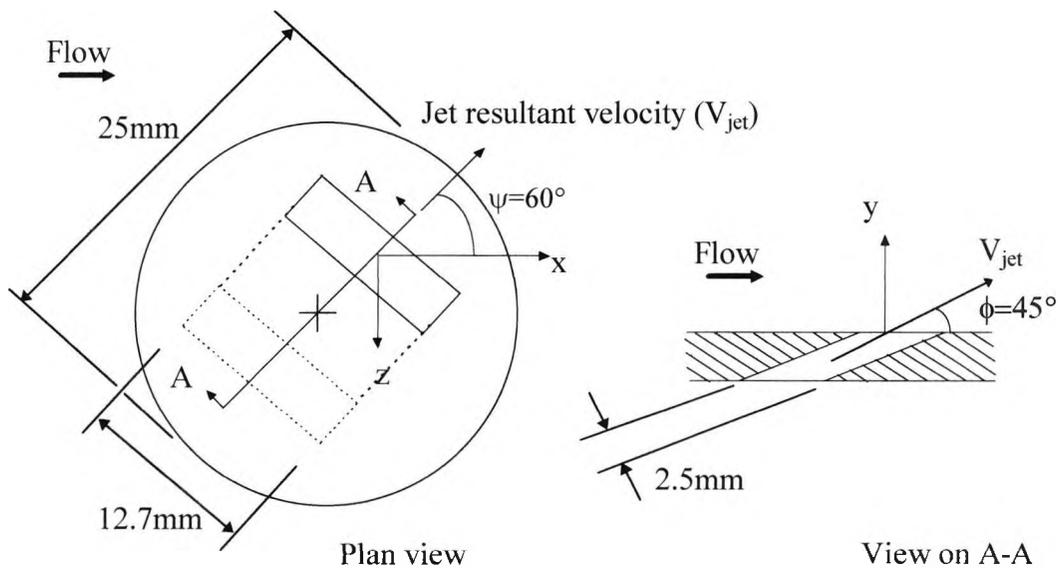
Note: y = direction normal to the aerofoil surface
z = spanwise direction

Figure 4.2: Air-jet slot configuration

Each AJVG array is supplied by a pressure regulated plenum chamber located within the mainfoil. Air is supplied to the AJVGs and endplate boundary layer control systems via a reservoir with a capacity to provide $15.2m^3$ of dry air at a maximum pressure of 45 bar. The reservoir is connected to the high lift system with high-pressure reinforced vinyl tubing that is ducted through two large steel plenum chambers. Flow to the individual control systems is regulated by lever-operated ball valves within the pressure lines.

Aerodynamic loads on the high lift system are carried via two 40mm diameter aluminium spindles mounted through the mainfoil element and perspex endplates at each spanwise extremity. The desired angle of attack is set by rotating the high lift system about the spindle axis on two sets of thrust roller bearings and locking the

model into position. Tests were conducted for an angle of attack range $0°<\alpha<36°$ with the AJVGs both active and quiescent.

4.2 Three-element high lift system with unswept leading- and trailing-edge

The three-element aerofoil system consists of a leading-edge slat, a main wing element and a trailing-edge flap. The mainfoil and trailing-edge flap are constructed from laminated mahogany joined with low moisture content. High loading on the leading-edge device, especially at high angles of attack, required the slat to be machined from solid aluminium alloy. The chordwise profile of the high lift system in the take-off configuration is shown below on Figure 4.3 (see Appendix D for the coordinates of the pressure taps on the high lift system).
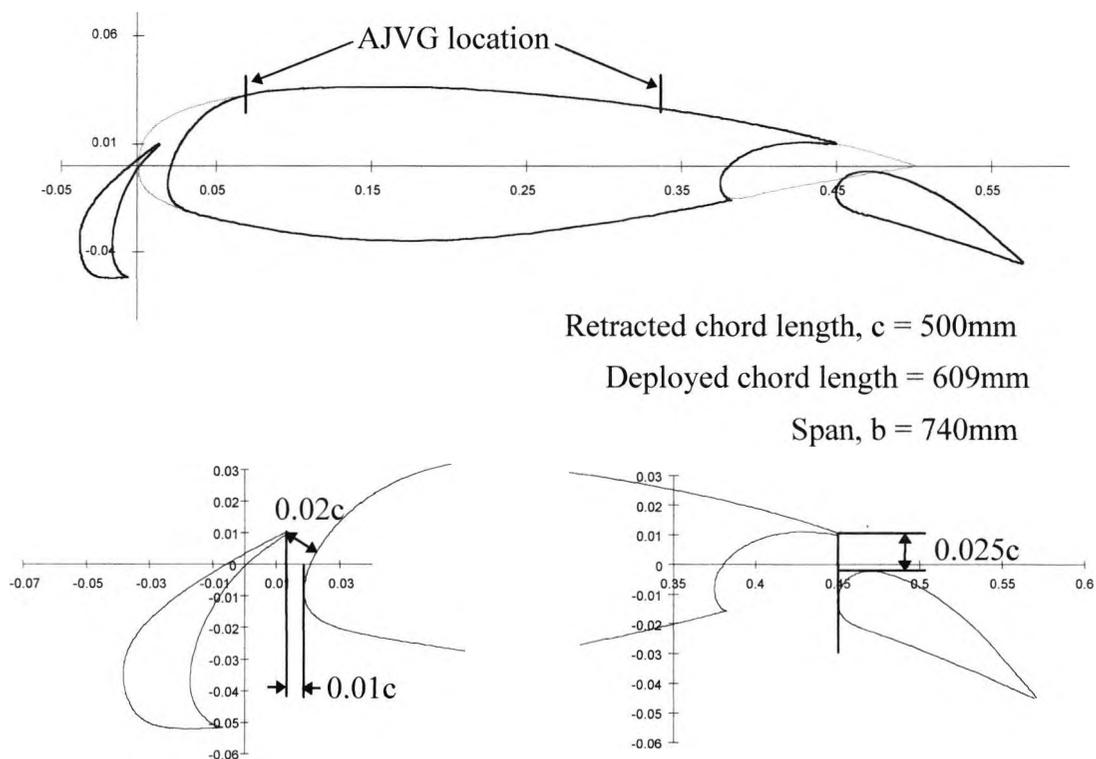

Figure 4.3: High lift system chordwise profile with lap and gap settings

The slat and mainfoil elements are connected to the endplates with harpoon bolts, while the flap element is affixed to two moveable aluminium plates at each end of the flap chord that are recessed into the perspex endplate. Rotateable endplates permit

testing over a range of flap angles and lap (and gap) settings. In this project, the slat and flap elements are both deflected at 20°, and fixed throughout the tests, to represent the multi-element aerofoil system in the take-off configuration.

Static pressure measurements were made via pressure tappings at mid-span of the slat, mainfoil and flap elements from which the integrated normal force coefficients were determined. The x/c locations for the pressure taps were defined with reference to the retracted chord length of 0.5m. Two pressure tappings located within the mainfoil plenum chambers to measure the stagnation pressure of the jet air, permit assessment of the jet momentum blowing coefficient (see section 4.3.2).

Air-jet vortex generator design

Installation of the AJVGs into the high lift system was intended to be determined from the results of the computational sensitivity study conducted using the three-dimensional local AJVG model as outlined in Section 3.6.3. However, the results demonstrated that the optimum AJVG spacing was close to the earlier recommendations of Pearcey (1961), Freestone (1985) and Rao (1988) of approximately 4δ. As a result, the existing AJVG array, utilising a jet spacing of 53mm, in the experimental high lift system model was not changed.

A distance of approximately 4 times the undisturbed boundary layer height (δ=13.25mm) between the AJVGs was utilised to minimise the adverse effects on the convection of the low momentum fluid away from the surface by the downwash side of the adjacent vortices. The jet slot passage and exit has a rectangular geometry with a slot aspect ratio of approximately 5 that is skewed and pitched at 60° and 45° respectively (see Figure 4.2).

4.3 Data measurement and analysis

The validity of experimental findings relies on the ability to minimise variances and errors associated with the method of data measurement and collection. The chordwise location of the static pressure tappings and the specified model dimensions were verified with a Vernier travelling microscope. The respective variances are 0.01mm and 0.5mm. With time, movement of the wood used to construct the mainfoil and flap, causes the brass tappings to protrude by up to ±0.1mm from the aerofoil surface. The surface of the model was checked frequently and re-finishing done when needed.

There are two methods (coarse and fine) to measure the angle of attack of the model in the wind tunnel relative to the tunnel centreline. The first (coarse) uses a brass arc (radius 325mm) with an inscribed scale between 0° and 45° that is embedded into the wind tunnel floor. A scored line through the reference chord, over the entire length of the perspex endplate, could then be aligned with the brass arc to measure the angle of attack to within ± 0.125°. The fine measurement involves a second pointer, attached to one of the 40mm diameter spindles about which the model was rotated. The pointer (radius 412mm) moved over a second scale permitting measurement of the angle of attack to within ± 0.06°.

The pressure measurement test procedure involved running the wind tunnel up to speed with the aerofoil at 0° incidence and the flow control devices activated if required. Once a uniform test flow field is established the desired angle of attack is set and the measurements taken. This procedure minimises the effects of hysteresis on the experimental results and ensures that when the AJVGs are employed they are influencing boundary-layer growth prior to reaching the cleanfoil stall angle of attack; rather than employing the AJVGs to restore attached flow after cleanfoil stall has occurred.

4.3.1 Pressure measurement on the wing and in the wake

Measurement of the chordwise static pressure distributions and shear layer plus wake properties were taken via pressure transducers connected to a CED 1401 data acquisition system. The 1401 is a multi-tasking system that can communicate with a PC using a DOS operating system on which the experimental data are stored. For a full explanation of the data acquisition system and software, see Innes (1995). An outline of the experimental data measurement procedure is shown on Figure 4.4.
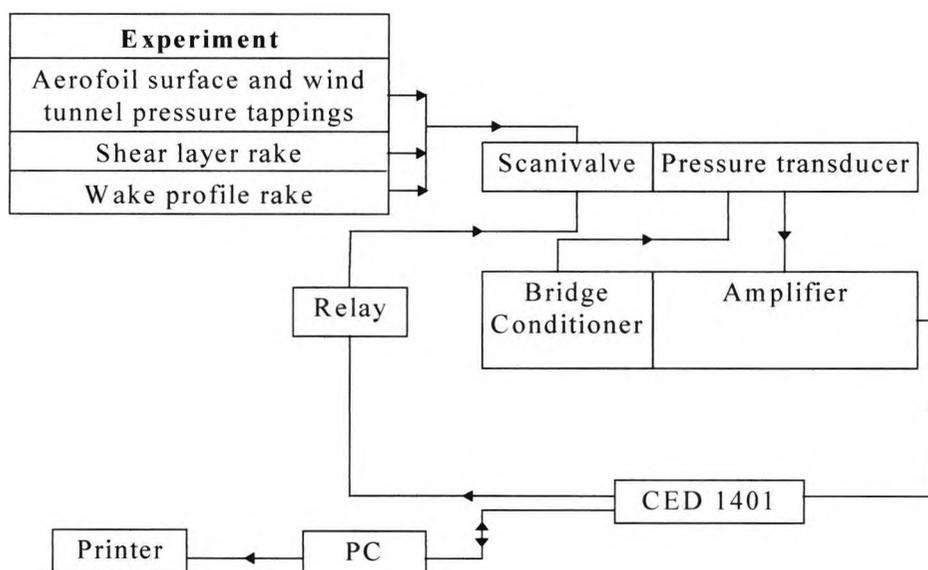

Figure 4.4: Experimental data measurement procedure

Chordwise static pressure distribution

The static pressure coefficients (C_{PS}) around the chord of the high lift system were measured by connecting the aerofoil surface pressure tappings (and the tunnel reference pressure tappings) to pressure transducers via 48 port scanivalves. Inclusion of the tunnel reference pressure tappings on the scanivalve enables calculation of the C_{PS} directly from the transducer output voltages, without the need for an absolute calibration; provided the pressure outputs are proportional to their inputs. Assigning port 0 as the atmospheric pressure reference and ports 24 and 25 as the tunnel contraction static pressures Innes (1995) outlines the following calculation procedure for the experimental C_{PS}:

110

Using:

$$C_P = \frac{p - p_\infty}{\frac{1}{2} \rho U_\infty^2} \Rightarrow \frac{(p - p_a) - (p_\infty - p_a)}{\frac{1}{2} \rho U_\infty^2} \qquad (4.1)$$

where:

p = static pressure on the aerofoil surface

p_a = atmospheric pressure

p_∞ = static pressure in the freestream

U_∞ = freestream velocity

Assuming:

$$\left. \begin{array}{l} \frac{1}{2} \rho U_\infty^2 = K_1(p_1 - p_2) \\[6pt] (p_1 - p_3) = K_2(p_1 - p_2) \\[6pt] (p_2 - p_3) = K_3(p_1 - p_2) \end{array} \right\} \qquad (4.2)$$

where:

$(p_1 - p_2)$ is static pressure drop along the tunnel contraction, and p_3 is the averaged static pressure measured along the wind tunnel working section centreline:

Substituting these relationships into Eqn. (4.1) gives:

$$C_P = \frac{(p - p_a) - (p_2 - p_a)}{K_1(p_1 - p_2)} + \frac{K_3}{K_1} \qquad (4.3)$$

Calibrating the wind tunnel prior to installing the high lift system yielded the following values for the K_1, K_2 and K_3 constants 1.0134, 0.9839 and 0.0161, respectively.

111

Shear-layer profile measurements

Confluent shear layers above a multi-element aerofoil can be expected to have thicknesses in excess of 0.15c at certain chord locations, Ying (1996). The shear layer rakes are constructed with a sufficient number of pitot tubes to capture the flow phenomena over the expected height. Two pitot rakes were constructed to measure the total pressure in the boundary layer (see Figure 4.5) at the five chordwise locations depicted on Figure 5.5. The largest rake contained 45 tubes equally spaced at 1.9mm and is used to measure the confluent boundary layers at high angles of attack, $\alpha > 25°$. The smallest rake contained 37 tubes spaced 1.5mm apart and proved sufficient for measuring the flow properties at lower angles of attack, $\alpha \leq 25°$. Both rakes were constructed from stainless steel tubes with respective inner and outer diameters of 0.711mm and 0.406mm. The rakes were then connected to the scanivalves with vinyl tubing. Shear layer explorations were recorded at 0.142c, 0.25c, 0.6c, 0.9c and 1.0c.

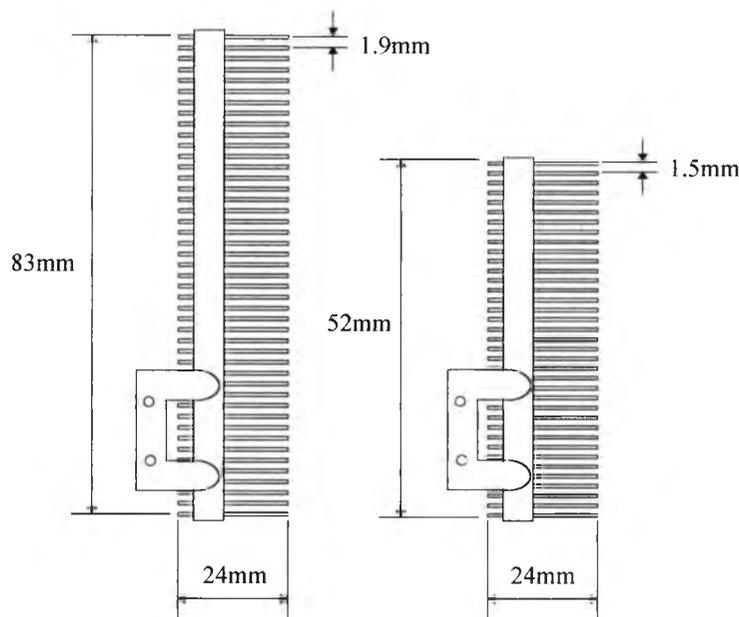Figure 4.5: Shear layer rake configurations

Wake profile measurements

The momentum deficit in the wake was measured, at one chord length downstream of the high lift system, with a 39 pitot tube and 5 pitot static tube wake rake using the pitot traverse method of B.M.Jones (1936). By measuring the static and pitot pressures across the wake, the following expression is used to evaluate wake profile drag.

$$C_{Dp} = 2 \int_{Wake} \sqrt{\frac{H_1 - p_1}{H_\infty - p_\infty}} \left(1 - \sqrt{\frac{H_1 - p_\infty}{H_\infty - p_\infty}} \right) d\left(\frac{y}{c} \right) \qquad (4.4)$$

where:

H_∞ = total head in the freestream

p_∞ = static pressure in the freestream

H_1 = local total head one chord length downstream of the high lift system

p_1 = local static pressure across the wake

y = distance normal to the aerofoil surface

The wake rake consists of 39 pitot tubes set at 5mm intervals in the centre and at 10mm intervals towards each spanwise extremity (see Figure 4.6). The total span is 240mm. Five static tubes are also included to measure the static pressure gradient across the wake.
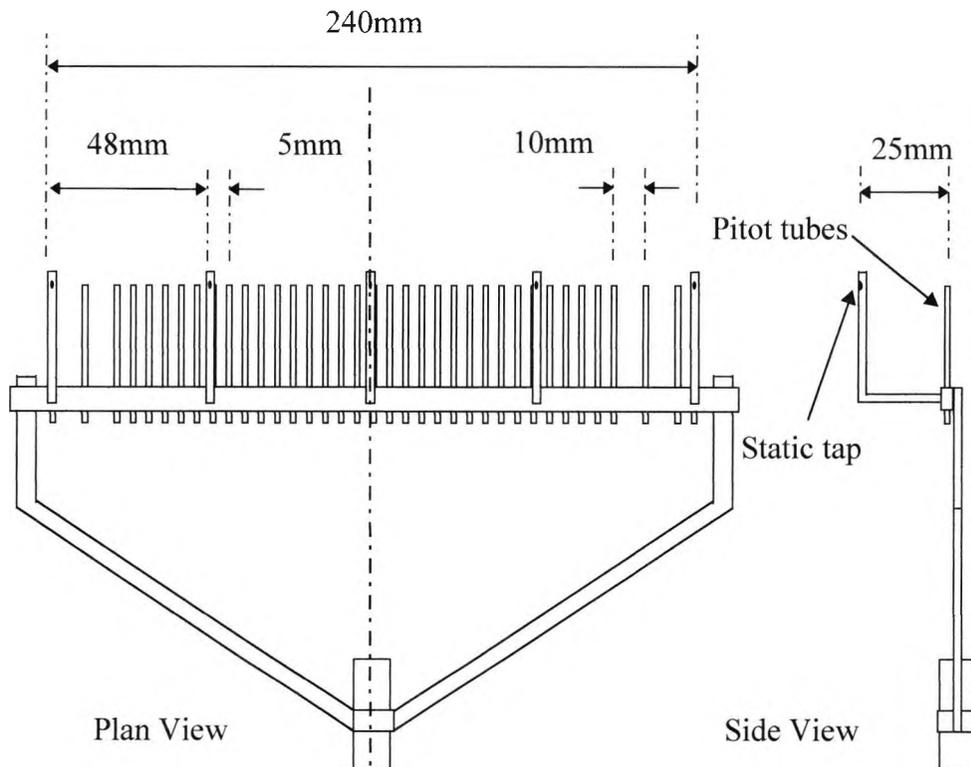

Figure 4.6: Wake rake configuration, symmetric about centreline

The accuracy of the measured C_{PS}, shear layer and wake profile properties is dependent upon the resolution of the data channels in the CED 1401 data acquisition

113

system. The voltage signals from the pressure transducers (±5 volt range) were handled with 12 bit accuracy, i.e., 2.4mV. At a constant tunnel speed of 40ms^{-1} where $(p_1 - p_2)$ = 950mV a resolution better than ±0.25% can be achieved in determining C_P.

Turbulent skin friction measurement

Direct measurement of the turbulent skin friction on an aerodynamic surface remains a challenge for experimenters. The most popular approaches measure the turbulent skin friction indirectly by separating and stagnating the flow at the aerofoil surface. Provided the device used lies within the log-law region of the boundary layer the pressure rise can be related to the local skin friction by 'wall similarity' variables. One geometrically simple device that has been calibrated for both incompressible and compressible flows, that is analogous to the Preston tube, is the cuboid obstacle block (see Figure 4.7). These devices have been calibrated for a family of shapes and offer a geometrically and practically simple method of measuring the turbulent skin friction. The block is attached with precision to the aerodynamic surface by abutting the block against a drill installed in the local static pressure orifice on the wing surface. The pressure measured without the block in place is subtracted from the pressure measured with the block in place and is related to the wall shear stress using the following expression derived by Nituch (1972):

$$Y = C_1 + C_2 X \qquad (4.5)$$

where:

$Y = \log_{10}\left[\dfrac{\rho_w \tau_w h^2}{\mu_w^2}\right]$, $X = \log_{10}\left[\dfrac{\rho_w \Delta p h^2}{\mu_w^2}\right]$ and C_1 and C_2 are constants dependent upon the obstacle block geometry and freestream flow conditions.
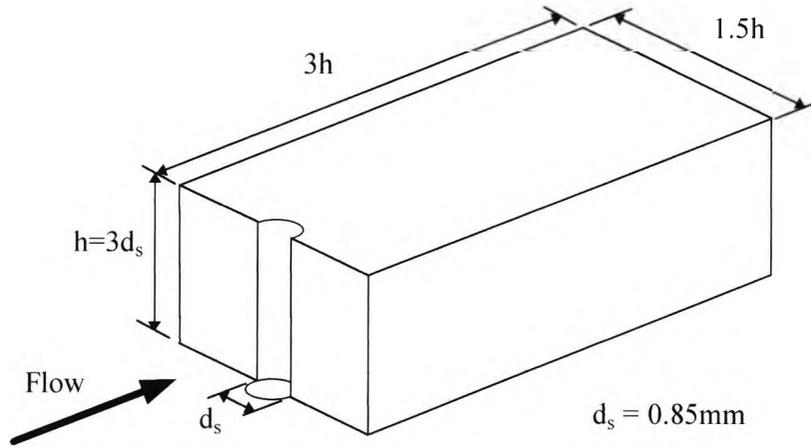
Figure 4.7: Obstacle block geometry shown abutting the local static pressure orifice, from Nituch (1972)

Rearranging Eqn. 4.5 and dividing through by the dynamic head yields the following expression for the wall shear stress based upon the pressure rise:

$$C_f = 10^{C_1} 2^{(1-C_2)} \, \text{Re}_{OB}^{2(C_2-1)} \, C_{P_{OB}}^{C_2} \qquad (4.6)$$

where:

Re_{OB} = Reynolds number based on block height, h, i.e. $\text{Re}_{OB} = \dfrac{\rho_\infty U_\infty h}{\mu_\infty}$

C_P = obstacle block pressure coefficient, i.e. $C_P = \dfrac{\Delta p_{OB}}{\frac{1}{2}\rho_\infty U_\infty^2}$

Δp_{OB} = pressure at the orifice with the block in place minus the local static pressure without the block in place.

For low speed, incompressible flows the respective values for the constants C_1 and C_2 are -1.254 and 0.875 as derived by Nituch (1972).

Employing solid obstacles to determine the turbulent skin friction is not without difficulty as the blocks induce a small separated region of flow in front of the block. This separation results in an unsteady pressure signal that has a characteristic frequency of oscillation. The experimental sampling rate must therefore be large enough to ensure measurement of a suitable mean level. Obstacle blocks also

115

influence downstream measurements of the wall shear stress due to a vortex generator effect. A study by Elfstrom et al (1982) indicates suitable assumptions for the required sampling rates and block spacings. For subsonic tests, a sampling rate of at least 1 second is required and a spacing of at least 200h is necessary along any one chordwise static pressure line, to ensure interference-free data downstream of a given obstacle block.

4.3.2 Orifice plate flow measurement installation

Assessment of the energy required to power the AJVG system in terms of added momentum is achieved by defining a jet momentum coefficient (C_μ) for the air-jet emerging from the wing surface:

$$C_\mu = \frac{\dot{m}(V_J - U_\infty)}{\frac{1}{2}\rho U_\infty^2 Sc} \tag{4.7}$$

where:

$\dot{m}$ = total mass flow rate through the AJVG system

V_J = air-jet velocity calculated from the compressible equation

Assuming isentropic flow in the blown system and in the freestream, yields the following expression:

$$\frac{\gamma}{\gamma-1}\frac{p_\infty}{\rho_\infty} + \frac{1}{2}V_J^2 = \frac{a_p^2}{\gamma-1} \tag{4.8}$$

where:

$$\left(\frac{\rho_J}{\rho_p}\right)^\gamma = \frac{p_\infty}{p_p} \tag{4.9}$$

$a_p = \sqrt{\gamma R T_{TOT}}$ the speed of sound in the AJVG plenum chamber, R = gas constant and T_{TOT} = is the temperature measured in the air supply system

The 'effective' drag of the high lift system with AJVGs operating can then be expressed as the sum of the measured wake profile drag and the energy supplied to the AJVG system:

$$C_{De} = C_{Dp} + C_{\mu} \qquad (4.10)$$

The mass flow rate through the AJVG system was measured using an orifice plate in the supply pipeline. The device was manufactured and installed in accordance with BS ISO 5167(1). The technique is an iterative method that yields a value for C_{μ} accurate to within ±3%. Readings were taken of the static pressure upstream of the orifice plate, the static pressure drop across the plate and the total temperature in the blowing supply line. A discharge coefficient D_c, for the plate is then given by Stolz's equation:

$$D_c = 0.5959 + 0.0312\beta^{2.1} - 0.184\beta^8 + 0.0029\beta^{2.5}\left(\frac{10}{Re}\right) + \frac{0.09L_1\beta^4}{\left(1-\beta^4\right)} \\ - 0.0337L_2\beta^3 \qquad (4.11)$$

where:

β = ratio of the orifice diameter to the pipe diameter

L_1 = the quotient of the distance of the upstream tapping from the upstream face of the plate and the pipe diameter (=1)

L_2 = the quotient of the distance of the downstream tapping from the downstream face of the plate and the pipe diameter (=0.47)

Calculation of the mass flow rate is then achieved using:

$$\dot{m} = \frac{D_c}{\left(1-\beta^4\right)^{0.5}} e_1 \frac{\pi}{4} d^2 \sqrt{2\Delta p} \qquad (4.12)$$

where:

d = internal pipe diameter upstream of the orifice plate (0.054m), e_1=1-$(0.41+0.35\beta^4)\Delta p/kp1$, k = pipe relative roughness (0.075) and Δp is the pressure drop between the plenum chamber and the local static pressure on the aerofoil surface at the air-jet exit, i.e., (p_p-p).

5. Two-dimensional high lift system

5.1 Initial prediction of the high lift system flow field

All numerical solutions of fluid flows contain errors that must be minimised, where possible, if the solutions are to be useful in the design process. These errors can be categorised into three main errors: *modelling*, *discretisation* and iteration or *convergence errors*.

Although the Navier-Stokes equations exactly describe fluid flows, solving them for most engineering applications of interest is currently impossible. *Modelling errors* are therefore introduced as the complex flow physics is simplified to facilitate a solution, with empirically based models. These errors are further compounded as initial boundary conditions that are unknown prior to testing or difficult to specify are simplified. The complexity of the test geometry can also influence a solution depending on the grid generation method employed to discretise the solution domain. In this project, a multi-block structured grid is utilised to discretise the solution domain. As a result, the inter-connectivity of the adjacent blocks in the mesh dictates the node distribution in some areas of the solution domain, particularly in the slat and flap coves. The combination of the above *modelling errors* can account for some of the variance between the measured flow physics and the approximate solution of the governing equations.

When using a finite-volume method, the definition of surface and volume integrals and variable values at intermediate locations gives rise to *discretisation errors* (A more detailed explanation of the influence of these errors is given in Chapter 3). Assessment of *discretisation error* requires solutions to be obtained on grids of increasing density until a grid independent solution is obtained.

Upon discretisation of the governing flow equations, the resulting linearised algebraic equations so formed are usually solved by an iterative method. A suitable convergence criterion must be defined as an adequate point to stop the iteration process. In general, this point is when the relative accuracy of the chosen flow parameter, compared to a

reference value, has reached a suitable limit. As a rule of thumb, Ferziger & Peric (1996) suggest the iteration errors should be reduced by at least one order of magnitude less than the discretisation error. For most engineering applications, this reduction of the *convergence error* corresponds to a three to four orders of magnitude reduction in the chosen flow parameter.

5.1.1 Convergence

CFX4 Solutions

The convergence criterion for the Navier-Stokes solutions is based upon the mass flow rate through the solution domain. By summing and averaging the net mass fluxes through each control volume in the solution domain (mass source residual) the error in continuity is determined. That is, as the mass source residual approaches zero: continuity is satisfied. Results are obtained on grids of varying density from 49000 to 65000 control volumes with the mass source residual non-dimensionalised by the inlet mass flow rate. Figure 5.1 is indicative of the behaviour of the CFX4 solutions for the 2-D high lift system at two angles of attack, $\alpha=10°$ and $\alpha=25°$.
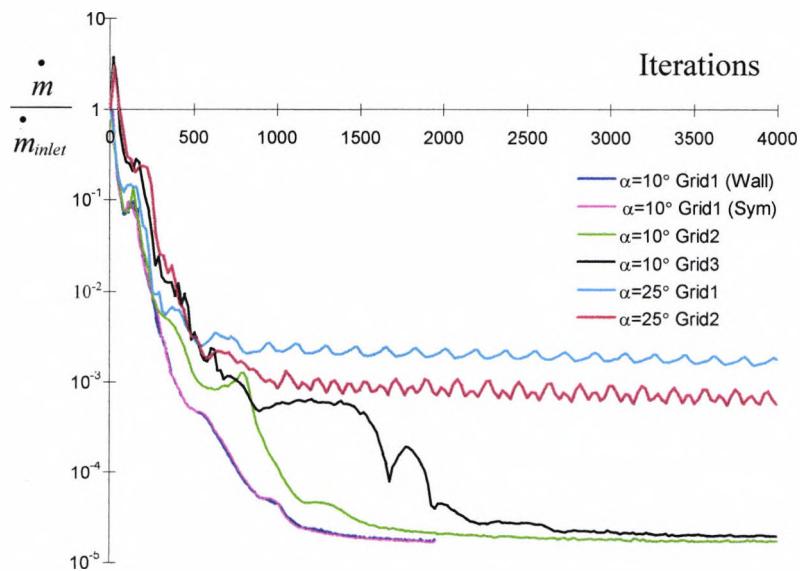

Figure 5.1: Convergence history of the 2-D high lift system CFX4 solutions at respective angles of attack of 10° and 25°

The reduction of the mass source residual depicted on Figure 5.1 for both angles of attack is indicative of convergence histories observed over the entire angle of attack range of the high lift system. The curves indicate that above 2000 iterations no further reduction of the mass source residual can be expected. At an angle of attack of 10°, the mass source residual converges to a value five orders of magnitude lower than that of the mass flow at inlet. This level of convergence is reduced as α increases. The reduction in the level of convergence is attributable to three assumptions: the use of pressure-velocity coupling equations (Eqns 3.25), the non-orthogonality of the grid at high angles of attack ($\alpha > 20°$) and the implementation of the law of the wall at the aerofoil surface for all angle of attack settings.

The pressure-velocity coupling algorithm of Rhie and Chow (1983) neglects the influence of the control volumes that are not directly adjacent to the cell in question, i.e., the NE, SE, SW and NW nodes depicted on Figure 3.8. Neglecting the influence of the diagonal control volumes is valid when the physical grid is orthogonal, as their influence is negligible when compared with the influence of the control volumes that are normal to the cell faces. As α increases, the numerical grid around the high lift system becomes more skewed and so the influence of these diagonal control volumes increases on the parameters at the node in question. When coupled with the fact that the flow field around the high lift system is highly curved with a complex turbulence structure at high α, neglecting the diagonal control volumes results in the omission of flow field information that significantly affects the calculated variables at the node of interest.

The assumption that the law of the wall region exists adjacent to the aerofoil surface at all angles of attack in the CFX4 solutions further influences the level of convergence. With increasing α, there is a growing region of separated flow on the upper surface of the mainfoil, through which the law of the wall region is invalid (as shown by the skin friction coefficient approaching zero on Figures 5.3, Section 5.1.2).

MSES solutions

As MSES can both predict the flow pattern around an aerofoil geometry and design an aerofoil geometry from a specified flow condition, the convergence criterion is often dependent upon the way in which the code is to be utilised. In this project, the high lift system is set at a specified angle of attack and the flow field around the geometry is calculated. Monitoring the generated lift and drag coefficients at each angle of attack assesses the convergence of the solution, as these coefficients are directly related to the flow field around the high lift system geometry. When the lift and drag coefficients become unchanged, the solution is adjudged to have converged. A solution, obtained with the high lift system set at an angle of attack 10°, requires approximately 15 iterations before the lift and drag coefficients become unchanged.

At the start of each iteration, MSES re-calculates the mesh around the high lift system geometry to take into account the displacement effects on the inviscid freestream of the viscous shear layers. Once convergence is achieved for a set angle of attack there is only a need for minor modifications to the grid to enable calculation of a nearby angle of attack. As a result, subsequent angles of attack can then be determined using the α=10° solution as its starting condition and only require a few more iterations to obtain a converged solution.

5.1.2 Grid dependence

Grid dependence studies were conducted with the high lift system at angles of attack of 10° and 25°. At both angles, three grid densities are tested with solution domains containing 48,976 (Grid1), 57,646 (Grid2), and 64,220 (Grid3) control volumes. The influence of the upper and lower solution domain boundary conditions was also investigated with the high lift system at α=10°. Initially the boundary conditions above and below the high lift system were defined as equivalent to the wind tunnel walls in the experiment. As a result, the computational grid at these walls had to be suitably fine to capture the flow physics within the boundary layers. To eliminate the need for grid refinement at the wind tunnel walls and hence reduce the size of the numerical grids required, tests were conducted with the upper and lower wall boundary conditions replaced by symmetry planes.

Figures 5.2 and 5.3 show the effects of the grid dependence studies on the chordwise surface pressure and tangential skin friction distributions around the high lift system at α=10° and α=25°, for both representations: the solid wall of the wind tunnel and symmetry planes.
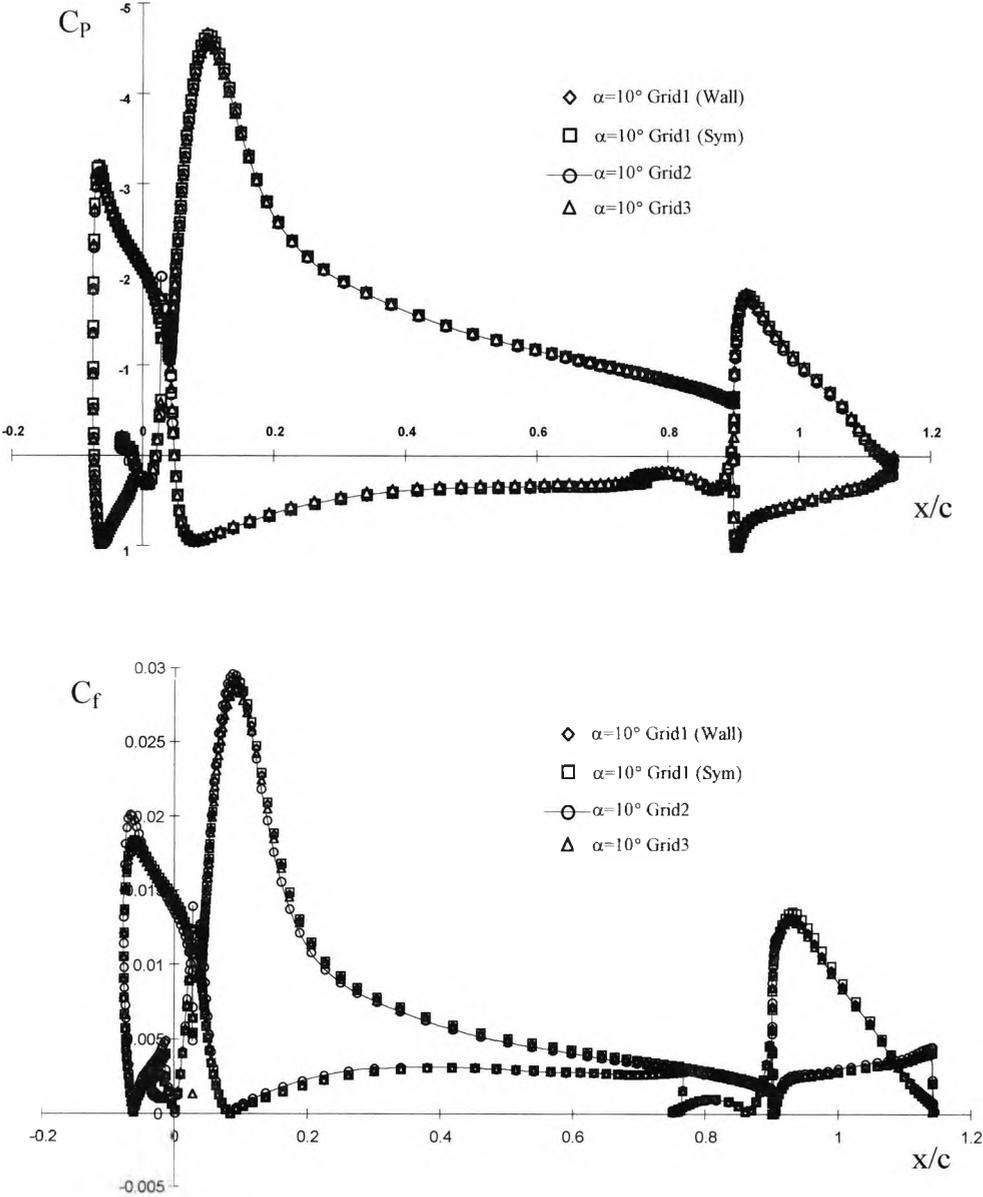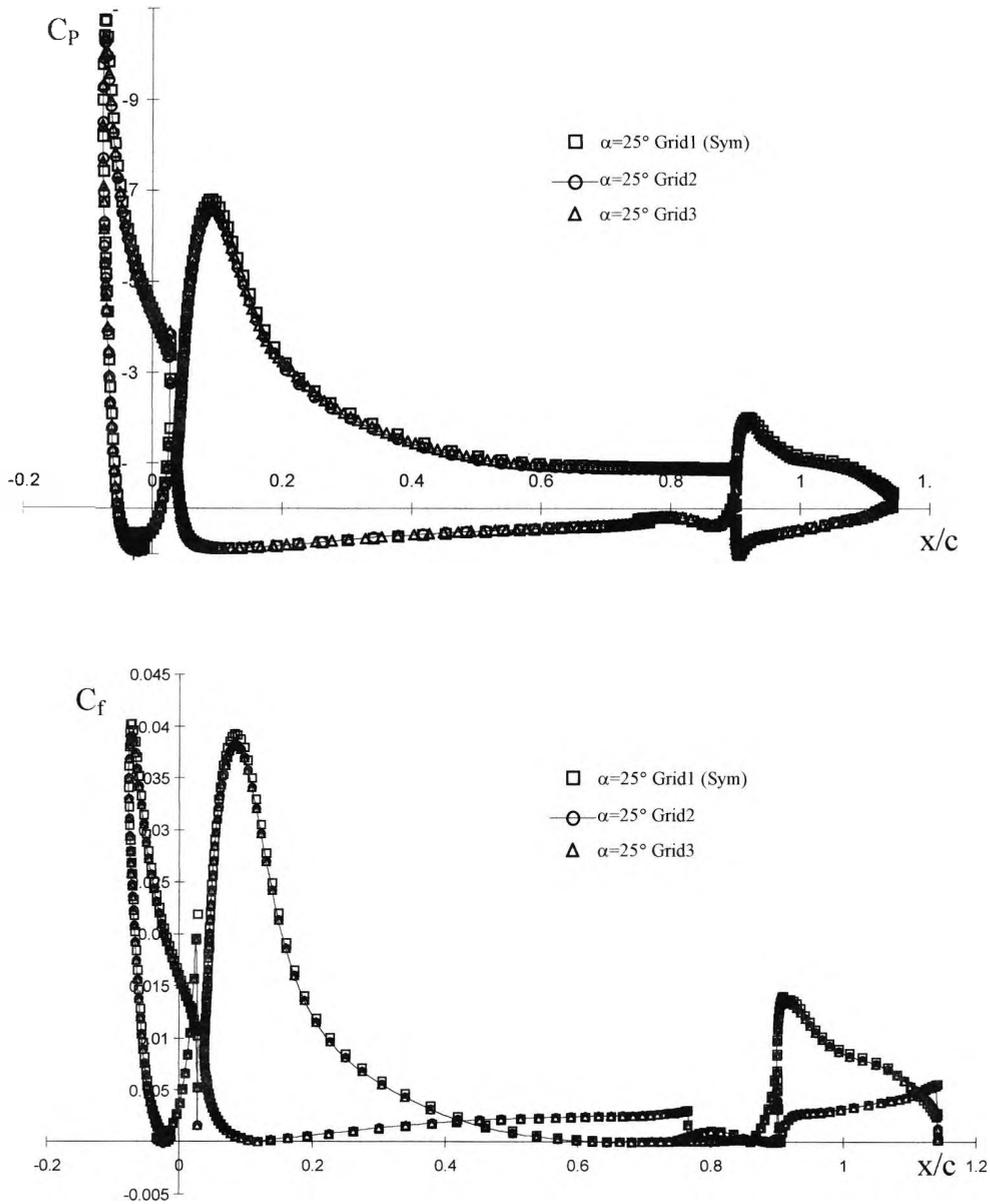

Figure 5.2: Predicted chordwise surface pressure and skin friction distributions around the high lift system on numerical grids of increasing density at α=10°, $Re_c=1.37\times10^6$, $M_\infty=0.13$

Figure 5.3: Predicted chordwise surface pressure and skin friction distributions around the high lift system on numerical grids of increasing density at $\alpha=25°$, $Re_c=1.37\times10^6$, $M_\infty=0.13$

At both angles of attack, the node distribution around the aerofoil surfaces remains relatively unchanged as the greatest influence on the solution is dependent upon the node distribution normal to the aerofoil surface. It should be noted that the cell distribution normal to the aerofoil surface is governed by the height of the cell at the

aerofoil boundary because of the assumption that the law of the wall region exists in the turbulence model formulation. Employing the law of the wall dictates that the first nodal point adjacent to the aerofoil surface lies outside of the boundary layer viscous sublayer and within the log-law region, i.e., $30 < y^+ < 150$ [see Thwaites (1960), pp 58].

Assessment of the effects of grid refinement was achieved by monitoring the changes on the high lift system surface pressure and skin friction distributions in much the same way as the study conducted by Jameson & Martinelli (1998). At both angles of attack, there is only small difference between the predicted chordwise surface pressure and skin friction distributions, irrespective of the numerical grid used. Increasing the grid density from Grid1 to Grid2 results in a slight reduction of predicted peak suction pressures around the leading edge of the high lift system components as the velocity gradients in the shear layers are better resolved. From Grid2 to Grid3 there is no discernible difference between both the predicted surface static pressure and skin friction distributions. No change in the predicted flow characteristics indicates the further refinement of the computational grid will not achieve a more accurate solution. Instead, further grid refinement will just increase the cost of calculating the high lift system flow field. Additional tests were then conducted using the numerical Grid2 density of 57,646 control volumes. It should be noted that as the angle of attack of the high lift system is increased, some local grid refinement was required to maintain the grid orthogonality and to ensure a converged solution was reached.

5.1.3 Advection term modelling

Five advection schemes were used to assess the influence of the discretisation error on the CFX4 flow field solutions (as discussed in Section 3.4). The computations indicate the flow field around the high lift system is dominated by the convective fluxes when the flow is attached. As a result, the cell Reynolds number (see Section 3.4) in the majority of the control volumes was greater than 2. This results in the solutions with the Hybrid advection scheme only being first-order accurate as the majority of the dependent variables within the solution domain are calculated using upwind differencing. Figure 5.4 shows the effect of advection term modelling on the

predicted chordwise pressure distribution around the high lift system; and the momentum deficit in the wake one chord length downstream of the wing trailing-edge. These results are obtained with the high lift system at an angle of attack of 10° and $Re_c = 1.37 \times 10^6$.
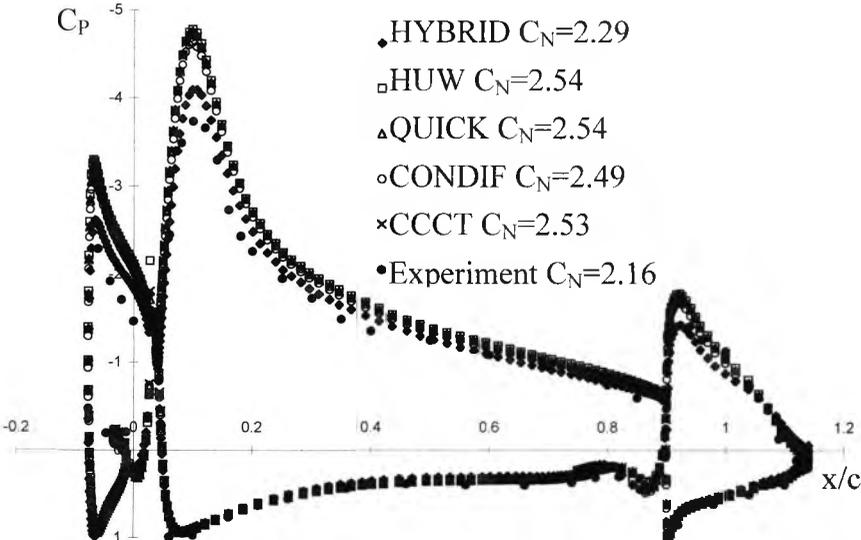
(a) Chordwise pressure distribution around the high lift system
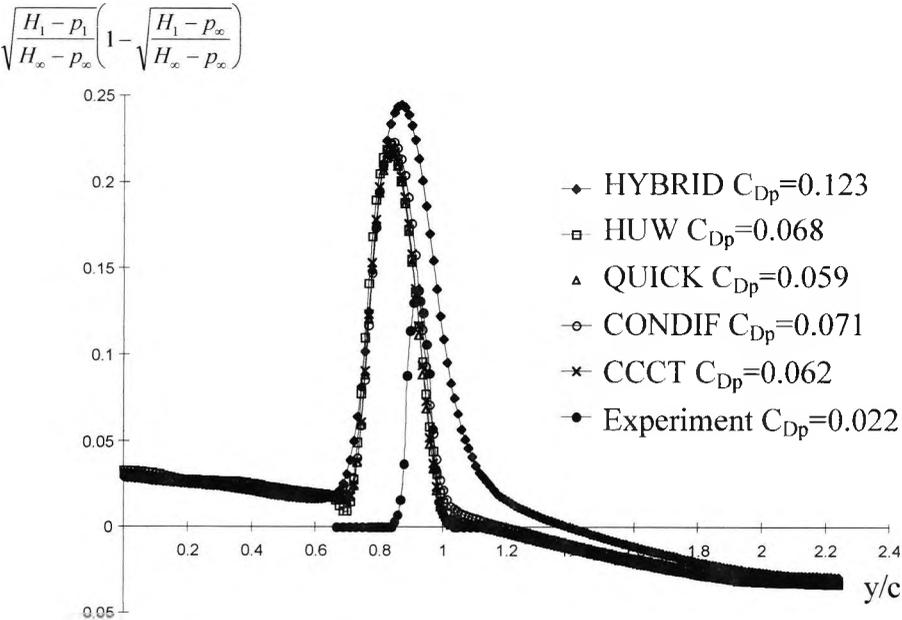
(b) Wake profile one chord length downstream of the high lift system

Figure 5.4: Influence of advection scheme on the chordwise surface pressure distribution and the downstream wake profile, $\alpha=10°$, $Rec=1.37 \times 10^6$, $M_\infty=0.13$

Reasonable agreement between the predictions and the experiment is demonstrated on the pressure side of the high lift system with larger variances on the suction side. Discussion of the flow physics behind the observed variances will be covered in the following section; for the moment, the focus remains on the differences in the numerical methods.

Results obtained employing the Hybrid advection scheme appear to agree best with the wind tunnel results yielding a predicted C_N 6% above the experiment. Increasing the order of accuracy of the advection scheme results in over-prediction of the peak suction pressures on all of the high lift system components. Consequently, the predicted normal force coefficients increase to approximately 18% larger than that determined from the experiment.

Conversely, predictions of the momentum deficit in the wake highlight substantial variances between the predictions and the wind-tunnel experiment. Employing the Hybrid advection scheme yields a wake profile drag coefficient six times larger than that measured in the experiment! The variance is reduced as the order of accuracy of the advection scheme increases. Reasonable agreement is shown for the predicted wake location and deficit on the pressure side of the high lift flow field. Notwithstanding, the magnitude of the momentum deficit on the suction side of the high lift system is grossly over-predicted with C_{Dp} still more than double the experimentally determined value.

At first glance, it may seem that the first-order accurate Hybrid differencing scheme out-performs the higher-order accurate schemes. The results for the momentum deficit in the wake clearly show that this is not case. The lower suction peaks on the pressure distribution plots and the increased momentum deficit in the wake with the Hybrid advection scheme is largely due to the round-off error in the differencing scheme formulation. The lowest order term in the truncation error of the Hybrid differencing equation is of second order, i.e., $\partial^2 u/\partial x^2$, and has a similar effect to adding viscosity to the solution. As a result, the viscous shear layers in the computations employing first-order accurate schemes grow considerably larger, demonstrated by the over-prediction of the momentum deficit in the wake. In turn, this results in the presence of a thicker

boundary layer at the flap trailing-edge that can increase the negative camber effects of the aerofoil and reduce the level of suction on the high lift system components.

Increasing the order of accuracy of the advection scheme dramatically alters the predicted surface pressure distribution around the high lift system and reduces the momentum deficit in the wake. Notably, little difference is apparent between the predictions obtained using the higher-order advection schemes. This is because for advection schemes of second-order accurate, or higher, the influence of the truncation error is significantly reduced.

The best agreement is achieved by employing the higher-order accurate QUICK and CCCT advection schemes that take into account the influence of a greater number of adjacent control volumes. Although these advection schemes account for the influence of more control volumes, they are somewhat unstable, which results in convergence difficulties at higher angles of attack. Additional numerical testing was conducted employing the HUW second-order accurate advection scheme (see Section 3.4) as it offers the best compromise between stability and accuracy.

5.2 Results and discussion of two-dimensional high lift system predictions

Computational and experimental tests on the high lift system with the AJVGs inactive (cleanfoil) involved measuring and predicting the following parameters at the locations depicted on Figure 5.5:

- Chordwise surface pressure and shear stress distributions at the centre span of each element of the high lift system.

- Shear layer profiles at four chordwise locations above the mainfoil and one location above the flap.

- The momentum deficit in the wake one chord length downstream of the high lift system.
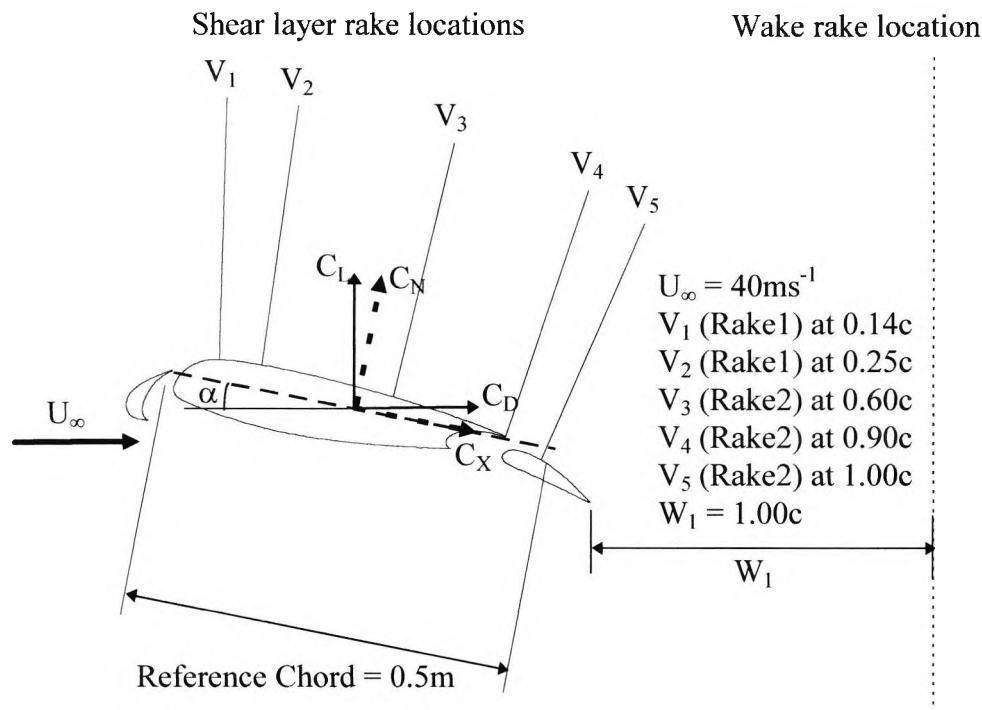
Figure 5.5: Unblown high lift system data measurement locations

The predictions are validated with experiments conducted on the high lift system by the author and previously by Innes (1995). Nominally two-dimensional flow around the high lift system wind tunnel model is established by employing endwall slot blowing, so that early separation originating from the model/endplate junction is

avoided. By monitoring the effects of endwall slot blowing pressure on measured C_{Nmax}, Innes (1995) demonstrates that the flow field around the high lift system is relatively insensitive to increasing the endwall slot blowing pressure much above the minimum value of 3psig. Consequently, Innes (1995) employs a slot blowing pressure of 4psig throughout the wind tunnel test regime. To ensure repeatability with the tests of Innes (1995), the author also employed a tangential slot blowing pressure of 4psig to re-energise the endplate/model junction boundary layer. Repeatability of the experiment of Innes (1995) was confirmed by evaluating the surface pressure distribution for a full angle of attack sweep with the AJVGs quiescent. Figure 5.6 shows a comparison of the normal force coefficients as determined by both experimenters from circuit integration of the wing C_{PS}. Some variance in C_N is evident but with the measured variance no less than 5% of the value obtained by Innes (1995). Close to stall, no discernible differences in the integrated normal force coefficients are apparent.
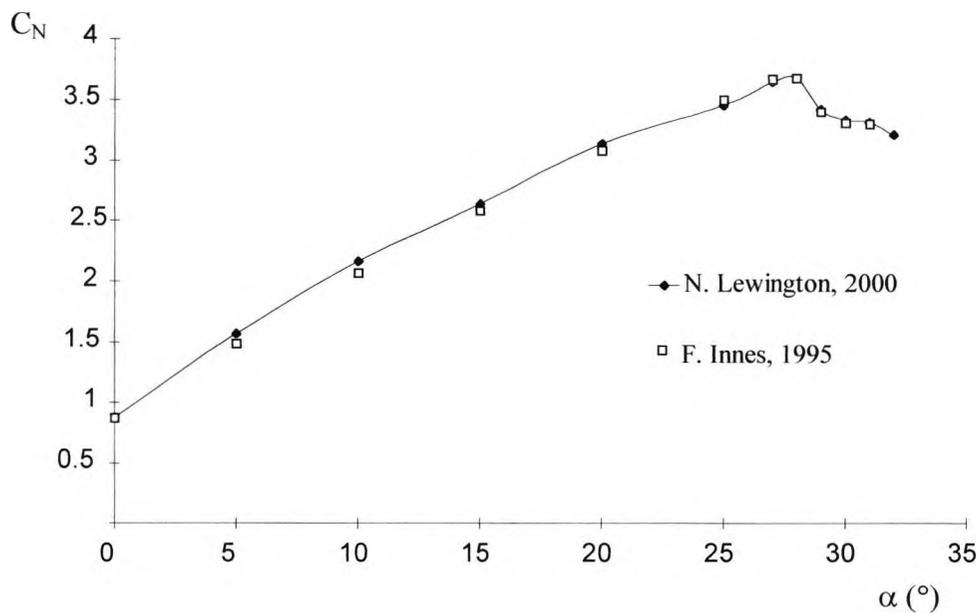
Figure 5.6: Repeatability between normal force coefficients of Lewington (2000) and Innes (1995) with angle of attack, C_μ=0, Re_c=1.37×10^6, M=0.13

Throughout this project, the lift force normal to the chord (C_N) is evaluated, as opposed to the conventional lift force that is relative to the freestream flow (C_L). C_N is the preferred force coefficient as there are insufficient pressure tapping orifices,

around the leading edges of the high lift system components, to enable accurate resolution of the chordwise forces (C_x), and hence wind axis resolved C_L and C_D.

Surface pressure and skin friction measurements (Figures 5.7-5.13)

Comparisons between the chordwise surface pressure distributions for the three-component high lift system are shown on Figures 5.7 to 5.9, for respective angles of attack of 10°, 15° and 25°. Note that the CFX predictions are obtained assuming fully turbulent flow, modelled with the standard k-ε turbulence model with wall functions, and by employing the HUW advection scheme.

At α=10° and 15°, there is reasonable agreement between the predicted and experimental results obtained with both CFX and MSES. However, CFX over-predicts to a greater extent the level of suction on each component of the high lift system, particularly around the slat and mainfoil leading edges.

The author believes that the increased level of suction predicted by CFX on the multi-element aerofoil components, is attributable to an over-prediction of the slat gap flow. This over-prediction yields increased flow velocities above the mainfoil upper surface and places the trailing-edge of the upstream slat component in a region of appreciably higher velocity, so that it benefits from the increased circulation effect outlined by Smith (1972). The over-prediction is felt to arise from a limitation, outlined below, with the HUW advection scheme that is employed to approximate the basic flow field variables (u, v, w and p).

The majority of the advection schemes employed by CFX are based upon upwind differencing, and so do not include any influence from the downstream control volumes. Extrapolation of the results at the control volume utilising the upstream nodes is therefore unbounded, and there is no guarantee that, even though the solution converges, the computational method will converge to a solution that represents the experimental flow field. Those schemes that do make provision for the influence of the downstream nodes (Central differencing, CCCT, CONDIF and QUICK) have been shown to be somewhat unstable and are heavily reliant on the grid density. In order to make use of advection schemes that account for both upstream and downstream

130

influence on the control volumes, the grid density would need to be extremely fine. Such grid densities are prohibitively expensive in terms of computer storage and CPU time and are beyond the capabilities of this project.

Better agreement between predictive and experimental measurements of the chordwise pressure distributions is demonstrated by the MSES calculations. There still remains some over-prediction of the peak suction levels, near the high lift system component leading edges. It is felt that the over-prediction of the suction levels around the high lift system component leading-edges in the MSES calculations result from inadequate definition of the slat and flap gap flows and an inability, within the code formulation, to account for the merging wake and boundary layer interactions.

The inadequate slat and mainfoil gap flow definitions are due to the displacement body model MSES employs to account for the viscous flow region; that displaces the inviscid streamline adjacent to the model surface by the displacement thickness. In attached flow situations the displacement body model ensures that the inviscid streamline closest to the surface accurately models the free shear layer, provided the predictions of the displacement thickness are correct. In regions of massive separation, such as the slat and mainfoil coves, the off-surface displacement vector is somewhat ambiguously defined, which can result in an unrealistic displacement of the inviscid flow field [see Drela (1990)].

Brune & Sikavi (1983) have demonstrated that slat wake/mainfoil boundary layer confluence can significantly limit the maximum lift capabilities of a multi-component high lift system. By monitoring velocity profiles above the flap component in their experiment they conclude that there is a tendency for flow reversal to occur in the merged slat wake/mainfoil boundary layer as it enters the strong pressure field above the aft flap element. In the current application, failure to account for the confluent slat wake/mainfoil boundary layer flows results in MSES predicting a higher degree of pressure recovery at the flap trailing edge; and hence an inferred increase in the circulation around the entire three-element high lift system (see Figure 5.13).

131

The MSES predictions indicate 'bumps' in the surface pressure distributions at respective chordwise locations of x/c ≈ -0.05, 0.1 and 0.95 (see Figure 5.9 for best effect). These 'bumps' correspond with laminar-to-turbulent transition separation bubbles, as indicated by the regions of negative shear stress on the surface skin friction distribution plots (Figures 5.10 to 5.12). The only evidence of such a 'bump' in the experiment is demonstrated on the upper surface pressure distribution of the flap at x/c ≈ 1.0. However, as no tests were conducted to assess boundary layer transition locations in the experiment, it is impossible to determine whether the measured 'bump' in the surface pressure distribution corresponds to boundary layer transition on the flap upper surface.

Above α=25°, the CFX predictions no longer adequately compare with the experimental trends. Examining Figure 5.13, the predicted CFX trailing-edge pressure coefficients on the mainfoil and flap rapidly diverge from experiments and MSES results, above α=15°. The flap trailing-edge pressure coefficient, as it becomes more positive, is indicative of the presence of flow separation at the flap trailing edge as the Kutta condition is no longer satisfied. Failure to satisfy the Kutta condition at the flap trailing-edge infers a reduction in the circulation and hence an associated reduction in the total normal force generated by the multi-component high lift system. The normal force coefficient plots on Figure 5.14 demonstrate that as the flap trailing-edge pressure diverges, above angles of attack of 20°, the total normal force carried by the high lift system is no longer linearly proportional to the angle of attack.

At α=25°, MSES surface C_P predictions still agree adequately with experimental results and, in particular, on the pressure side of the high lift system components. Again, some over-prediction of the peak suction is evident in close proximity to the leading edge of the mainfoil and slat. Once again this over-prediction of the level of suction is due to the inability of the method to account for boundary layer confluence, which becomes increasingly significant as the angle of attack increases.

Figures 5.10 to 5.12 show the chordwise surface skin friction distributions at respective angles of attack of 10°, 15° and 25°. At each presented α, moderate

agreement is demonstrated between the CFX predictions and the experiment on the pressure side of the high lift system. On the suction side, however, the CFX predictions differ increasingly from the experiment with increasing angle of attack. Most notably, there is a reduction in the magnitude of the wall shear stress in the CFX results close to the mainfoil trailing edge. By $\alpha=25°$ (Figure 5.12) there is evidence of the flow approaching separation at approximately 0.55c, as the wall shear stress tends to zero. The variance between the CFX predictions and the experiment is a result of the over-prediction of the momentum deficit within the shear layers, as shown on Figures 5.19 to 5.25 (see later discussion). Again, better agreement with the experiment is demonstrated with the MSES predictions.

At each angle of attack, MSES fails to adequately represent the surface skin friction distribution close to the component leading edge on the pressure side of the high lift system (see Figures 5.10-5.12). Improvements in the MSES skin friction predictions near the mainfoil and flap leading-edges require better definition of the slat and flap cove flows. Additionally, in real flows it is possible for the turbulence intensity in the cove regions to be convected to the downstream wakes, Ying (1996). However, in the MSES predictions, the flow in the coves is modelled by defining a fairing to account for the re-circulation regions. To improve MSES predictions in the cove regions, Drela (1990) suggests that a less arbitrary approach to defining the displacement body within the cove is achieved by constraining each displacement vector from the aerofoil surface to bisect the surface and the inviscid streamline at equal angles. As yet, no evidence of the success of this approach has been demonstrated.

Integrated normal force, wake profile drag and leading edge pitching moment coefficients (Figures 5.14-5.17)

Figure 5.14 shows the behaviour of the predicted and experimental integrated normal force, wake profile drag and leading-edge pitching moment coefficients for the three-component high lift system, with increasing angle of attack. To ensure appropriate comparison between the measured and computed data for C_N and C_{Mle}, the computed pressure coefficients are determined at the same pressure tap locations as in the experiment. Below $\alpha=20°$, predictions of integrated C_N and C_{Mle} agree moderately well with the experiment. Both CFX and MSES slightly over-predict the total normal

force on the high lift system, but yield values of $dC_N/d\alpha$ close to that measured in the experiment. Above $\alpha=20°$, both CFX and MSES do not predict the experimentally determined C_{Nmax} and the corresponding stall angle. However, the plots demonstrate that MSES is far more capable of representing the experimentally determined normal force characteristics, over a larger proportion of the tested angle of attack range.

MSES yields a value of C_{Nmax} 6% less than the experiment occurring at an angle of attack approximately 3° before the measured stall. CFX predictions above $\alpha=20°$ show differing trends with increasing α to those observed in the experiment, yielding a C_{Nmax} 25% less than the experiment occurring between $\alpha=25°$ and $\alpha=27°$. The loss of normal force on the high lift system is coincident with the divergence of the flap trailing edge pressure coefficient shown on Figure 5.13. Figure 5.15 shows the normal force coefficient variation with angle of attack for each component of the high lift system. Below $\alpha=15°$ there is good agreement between the CFX predictions and the experiment for the normal force carried by the slat. Above $\alpha=20°$, the CFX predictions indicate that the loss in total normal force generated by the multi-component high lift system is almost entirely due to the loss of lift on the mainfoil component. The flow breakdown on the mainfoil has little influence on the normal force carried by the flap in the CFX predictions. This is because the mainfoil slot flow re-energises the flap boundary layer, minimising the influence of the separated slat and mainfoil wake on the flow over the flap upper surface.

MSES predictions for the normal force carried by the mainfoil and flap are in good agreement with the experiment up until $\alpha=27°$. Beyond this angle of attack it was not possible to obtain a solution for the flow field with MSES. This is because the equations employed by MSES become singular when large regions of flow separation exist and can only be represented if the user inputs the point of origin and nature of the separating streamline.

Both computational techniques over-predict the momentum deficit in the wake downstream of the high lift system as depicted by the curves of C_{Dp} vs α (Figure 5.14). However, the variance observed between the predictions and the experiment is

much greater in the results obtained with CFX. At the experimental α_{max}, CFX predicts a wake profile drag five times larger than the experimentally determined value. The massive over-prediction of the momentum deficit by CFX is largely due to the inability of the k-ε turbulence model to account for the effects of streamline curvature on the eddy viscosity and mixing length within the turbulent wakes and boundary layers. The k-ε turbulence model relies on the assumption that turbulence production and dissipation are in near balance throughout the entire flow field. Tennekes & Lumley (1972) show that in high curvature flows production rates of the Reynolds stresses increase leading to anisotropic turbulence for which the eddy-viscosity hypothesis is invalid. Smits et al (1978) have also demonstrated that in highly curved flows the turbulence in the outer layer can be almost obliterated in positive camber bends, significantly reducing the boundary layer thickness. Finally, Menter (1992) demonstrates that the k-ε model predicts very high turbulence levels upstream of the stagnation points, which are subsequently transported around the entire geometry. This results in the over-prediction of turbulence levels within the boundary layers and wakes that dampen the mean flow velocities; leading to early boundary layer confluence and subsequent wake thickening.

Another reason for CFX over-predicting the momentum deficit in the wake is due to the assumption that the component viscous flows are fully turbulent. The MSES predictions, utilising the empirical e^n method, indicate that transition does not occur until 15% of the retracted chord on the mainfoil upper surface and 95% of the retracted chord on the flap upper surface (Figures 5.10-5.12). Not providing for laminar-to-turbulent transition is a substantial weakness of the CFX computations and therefore results in an increased growth of the momentum and displacement thicknesses, when compared with those predicted by MSES, and those measured in the experiment.

The excessive growth of the momentum deficit in the wake is forcefully represented on the C_N/C_{Dp} and C_{Dp} polars on Figure 5.16. At lower angles of attack, the normal force on the high lift system predicted by CFX is approximately 35 times the drag force. CFX predictions suggest that as the angle of attack increases, the corresponding drag increases exponentially, significantly reducing the range of the C_N/C_{Dp} envelope.

MSES predictions on Figure 5.16 also show a substantial reduction of the C_N/C_{Dp} envelope relative to the wind tunnel results. The optimum C_N/C_{Dp} performance occurs at the same point as that measured in the experiment (close to $C_N \approx 2.5$, $\alpha \approx 15°$).

The predicted and experimental trends for the pitching moment coefficient around the leading-edge of the retracted chord are depicted on Figure 5.17. Below $\alpha=20°$ ($C_N \approx 2.6$), both sets of predictions agree with the experiment in terms of the slope of the curves. Above $C_N \approx 2.6$, the variance between the CFX predictions and the experimentally determined trends becomes more evident once again. Initially, the leading-edge pitching moment plateaus at approximately $C_{Mle}=-1.05$, which corresponds to the reduced suction force on the mainfoil of the high lift system (see Figure 5.15). At even higher angles of attack, where the loss of lift increases on the slat and mainfoil in the CFX predictions, it may be inferred that the normal force generated by the flap serves to increase stability; by reducing the leading-edge pitching moment coefficient.

The MSES pitching moment slope predictions are in better agreement with the experimental findings, due to the ability of the code to better represent the pressure distribution around the high lift system throughout the angle of attack sweep. MSES matches the experimental trends throughout the majority of the angle of attack sweep but is shifted upwards by approximately $C_{Mle} \approx 0.05$. The upwards shift is attributable to the over-prediction of the normal force on the slat, that serves to increase the angle of attack round the leading edge of the retracted aerofoil, giving rise to a more positive pitching moment.

Shear layer profiles and integrated boundary layer properties (Figures 5.18-5.25)
Comparisons between the experimental and CFX predicted chordwise shear layer profiles, at respective angles of attack of 10°, 15° and 25°, are shown on Figures 5.18-5.20. The streamwise velocities are non-dimensionalised with the equivalent velocity at the shear layer edge (U_e) and the boundary-layer height (δ) is determined at the point where $u/U_e=0.99$.

A significant flow phenomenon that is evident on these plots and is inherent to multi-component high lift system aerodynamics is the presence of multiple viscous-layer interactions above the elements downstream of the leading edge slat. These multiple viscous-layer interactions, or confluent boundary layers, occur as the fresh boundary layer on the downstream high lift system components grow and eventually merge with the turbulent wakes that are shed from the upstream elements and the essentially inviscid cove/gap flows. The result of these multiple viscous-layer interactions is a highly complex mean velocity profile that is extremely difficult to predict. For a detailed analysis on the measurement and prediction of confluent boundary layers the reader is directed to Ying et al (1998).

At $\alpha=10°$, the CFX-predicted and experimentally measured shear layer profiles are quite different. Results obtained with CFX demonstrate significantly higher slat gap flow that results in a thinner boundary layer at $x/c=0.14$. However, under the influence of the adverse pressure gradient between 0.14c and 0.25c the CFX predictions indicate that the boundary layer grows at a considerably faster rate than that measured in the experiment. The accelerated growth of the mainfoil boundary layer in the CFX predictions is attributed to the over-prediction of the level of turbulence by the k-ε turbulence model in adverse pressure gradients and the inability to account for boundary layer transition in the CFX approach, as discussed above.

In Figure 5.19, $\alpha=15°$, both predicted and experimental results indicate the presence of the slat wake, evident as a velocity deficit in the shear layer profile above the mainfoil at approximately $y/c=0.02$, at a chordwise location of $x/c=0.14$. Further downstream at $x/c=0.25$, the experimental results show that mainfoil boundary layer has grown under the influence of the adverse pressure and begins to merge with the slat wake. However, in the CFX predictions the over-predicted level of turbulence in the slat wake and mainfoil boundary layers results in a much higher degree interaction between the viscous shear layers, to point where the slat wake and mainfoil boundary layer are almost completely merged (confluent). Similar trends are demonstrated for the predicted and measured shear layer profiles at $\alpha=25°$, Figure 5.20. However, in the CFX predictions the over-prediction of the mainfoil boundary layer growth and slat wake spreading results in shear flow reversal at the mainfoil trailing edge.

Experimental and predicted velocity profiles at the chordwise distance 1.0c on the flap upper surface show traits not unlike those demonstrated on the mainfoil (Figure 5.21). In the experiment the results demonstrate that at each angle of attack the confluent wake leaving the mainfoil trailing edge is separated from the boundary layer on the flap upper surface by the high momentum flap gap flow. However, in the CFX-predictions the high momentum flow through the flap cove is not sufficient to significantly limit the confluent slat/mainfoil wake merging with the flap boundary layer. There is also evidence of the shear reversal, in the confluent slat/mainfoil wake above the flap upper surface at $\alpha=25°$, in CFX predictions (Figure 5.21a).

The boundary layer integral properties, displacement thickness δ^*, momentum thickness θ and the shape parameter $H=\delta^*/\theta$ are plotted on Figures 5.22-5.25. These plots further highlight the inability of the CFX predictions to adequately track the complex shear layer development over the multi-component high lift system. At each angle of attack, CFX predicts a much faster growth rate for the displacement and momentum thicknesses (Figure 5.22). On the other hand, the MSES predictions (once downstream of the leading edge transitional bubble) the rates of growth of δ^* and θ follow closely the experimental measurements with some discrepancy at $\alpha=25°$ (Figure 5.24).

Figure 5.25 shows the most sensitive of the integral parameters: the shape parameter H, on the mainfoil of the high lift system at respective angles of attack of 10°, 15° and 25°. Close to the mainfoil leading edge, at x/c=0.18, both CFX and MSES predictions show a marked reduction in H as a result of the favourable pressure gradient acting on the boundary layer as peak suction is approached. Here the velocity profile has filled out close to the surface, so that δ^* is considerably reduced, but the velocity within the boundary layer is increased, so that H rapidly decreases. At $\alpha=10°$ and $\alpha=15°$, both CFX and MSES show that the proportionate increase in δ^* and θ is much the same as that measured in the experiment. However, at $\alpha=25°$, the gross over-prediction of δ^* in the CFX computations (Figure 5.24) results in the flow approaching separation at $H\rightarrow2.5$, Schlichting (1979).

Again the differences between both the CFX and MSES predictions and the experimental results are attributable to the modelling of the flow physics. Predicting the viscous flows with the k-ε approach, in the CFX predictions, relies on fact that the boundary layers on the multi-element high lift system components are only subjected to relatively weak pressure gradients. Under these weak pressure gradients flow conditions the turbulence within the viscous shear layers can be assumed to be 'locally isotropic' and H can be assumed to roughly constant. However, Smits et al (1978), Tennekes & Lumley (1972) and Menter (1992) have all demonstrated that this is not the case in strong pressure gradient flows. The k-ε approach is therefore limited when the multi-component high lift system is at higher angles of attack, where the adverse pressure gradients are significant. On the other hand, the lag-entrainment method is still physically meaningful at α=25°. This is because the lag-entrainment method takes in account the effects of changing pressure gradient on the rate of entrainment of momentum into (and hence the turbulence development within) the viscous shear layers. As a result, the MSES predictions map the experimental variation of H not unreasonably.

5.3 Summary of the two-dimensional high lift system results

The discussion in Section 5.2 details the predicted and experimentally-determined flow field characteristics around a representative two-dimensional, three-element, high lift system. Results were obtained for the chordwise surface pressure and skin friction distributions and shear layer profile development and hence, the corresponding properties: C_N, C_{Dp}, C_{Mle}, δ^*, θ and H. Predictions were obtained utilising two numerical flow solvers employing a finite volume block-structured approach (CFX) and a coupled viscous/inviscid approach (MSES). CFX predictions utilised the k-ε turbulence model [Launder and Spalding (1974)] to predict the flow phenomena, employing wall functions in the near-wall region. MSES [Drela (1993)] incorporates a streamline based Euler discretisation method for the inviscid flow field, coupled with a two-equation integral boundary-layer formulation and the lag entrainment method of Green et al (1973) determining the displacement thickness.

The key findings from the investigations are:

• As the angle of attack increases, CFX predictions of the flow field deviate progressively from both the MSES predictions and experimental findings. This results from an inability to adequately define the confluent shear layers and the component wakes of the high lift system. Consequently, in the CFX predictions the viscous flow displaces the inviscid freestream by a much greater extent from the aerofoil surface's reducing the amount of lift that can be generated by the high lift system, whilst increasing the profile drag. The variance between the CFX predictions and the experimental trends is largely attributed to the inability of computational method to account for laminar-to-turbulent boundary-layer transition and the inability of the k-ε turbulence model to account for the effects of high flow curvature in the turbulent boundary layers and wakes.

• Improvements in the predicted flow characteristics arise when estimating the effects of transition within the calculations. In so doing, the MSES results show good agreement with experimental findings for the integrated forces on the high lift system, up to stall. Notwithstanding this, MSES predicts a 6% lower value of C_{Nmax} than the

experiment, occurring prematurely at an angle of attack of 26° rather than the experimentally determined value of $\alpha=27°$. The ability of the MSES flow solver to adequately represent the experimental trends for the flow field around the high lift system is owing to the way in which the flow field is modelled. The inclusion of the lag-entrainment physics enables a first-order guess to be made for the effects of streamline curvature on the turbulence structure within the boundary layer layers, and hence the entrainment of the high momentum potential flow into the retarded shear layers above the high lift system component upper surfaces.

- Better estimates of the flow characteristics may be expected with improved turbulence and transition prediction methods, i.e., integrating up to the wall or utilising DNS techniques to predict transition. However, the generality and storage requirements of such techniques may be somewhat prohibitive for complex high lift geometries, certainly in terms of the need for rapid calculation methods for industry.

6. Three-dimensional flat plate 'local' AJVG model

6.1 Introduction

The purpose of the flat plate 'local' AJVG model is to determine a near-optimum array of AJVGs via sensitivity studies, to install on the three-element high lift system. The 'local' model defines an infinite array of either co-rotating or counter-rotating rectangular AJVGs that are embedded within the aerodynamic surface. By careful implementation of the 'local' model boundary conditions, a flow field was defined that 'locally' represented the high lift aerofoil system, as it approached stall. This 'local' model was then used to assess the effectiveness of the AJVGs (located at $x/c=0.14$) at suppressing boundary-layer separation on the top surface of the mainfoil.

Throughout this research programme, the performance of the AJVG arrays was assessed by the elevation in the level of skin friction enhancement downstream of the air-jet arrays. Parameters that were altered within the sensitivity study were based upon the air-jet spacing, jet-to-freestream velocity ratio and rotational sense of the vortex array. The pitch and skew angles (ϕ and ψ) of the AJVGs were fixed at respective angles of 45° and 60° (see sketch on Figure 4.2) in keeping with the suggested angles identified by Rao (1987), Compton & Johnston (1992) and Selby et al (1992).

No direct comparisons are made between predicted and experimental results for the 'local' numerical model in this research. It should be noted, that the 'local' computational model is based upon the validated approaches employed by Henry & Pearcey (1994) and Lewington et al (2000).

6.2 Initial prediction of the flat plate 'local' AJVG model flow field

The convergence criteria for the 'local' model solutions are essentially the same as those in the 2-D high lift system calculations (see Section 5.1.1). In each case, the solution is said to have converged once the mass source residual has reduced by at

least three orders of magnitude of the mass flow at the solution domain inlet, i.e. the error in continuity is reduced to 0.1% of the inlet mass flow rate, or less. On this basis, convergence was achieved within 2000 iterations in all computations.

Grid dependence studies were conducted for a co-rotating vortex array with a jet spacing, s ≈ 0.102c and a jet-to-freestream velocity ratio, V_R =2. Studies by Henry & Pearcey (1994) and Küpper (1999) have indicated that the accurate definition of the swirling flow field downstream of the AJVG is most dependent upon the spanwise cross-stream node distribution (NK), i.e., the grid density in the cross-stream direction is fine enough to capture the detail of the weaker convective flux in the cross flow plane. Reliance on the law of the wall in the calculations dictates that the node adjacent to the surface lies outside the viscous sub-layer within the log-law region. Above the viscous sub-layer, the cell density normal to the surface (NJ) is fine enough to capture the detail of the swirling vortical flow field. Results obtained with a grid density normal to the flat plate surface of NJ > 25 cells showed no further improvement in the predictions of the swirling flow. The streamwise cell distribution (NI) was set at 74 to maintain an acceptable cell aspect ratio in the streamwise plane normal to the surface.

AJVGs delay the onset of boundary-layer separation by enhancing the level of mixing between the high momentum freestream flow and the retarded shear layers close to the wall. By convecting the high momentum fluid towards the aerodynamic surface, whilst convecting the low momentum fluid into the freestream, the AJVGs generate a distinctive shear stress signature on the surface. On the downwash side of the vortex the local skin friction coefficient is increased and on the upwash side of the vortex the local skin friction is decreased. Monitoring the transverse skin friction distribution hence offers a suitable method for assessing the dependency of the numerical predictions on the grid density. Note the flow physics associated with the AJVGs will be covered in greater detail in the following Section 6.3. For the moment, attention is focussed on the computational modelling procedure.

The skin-friction enhancement, ΔC_f, is the difference between the predicted skin friction coefficient with the AJVGs active and inactive. The effects of varying NK on

the skin-friction enhancement 0.16c downstream of the AJVG, looking upstream with the AJVG centre at z/c=0, are shown on Figure 6.1 below.
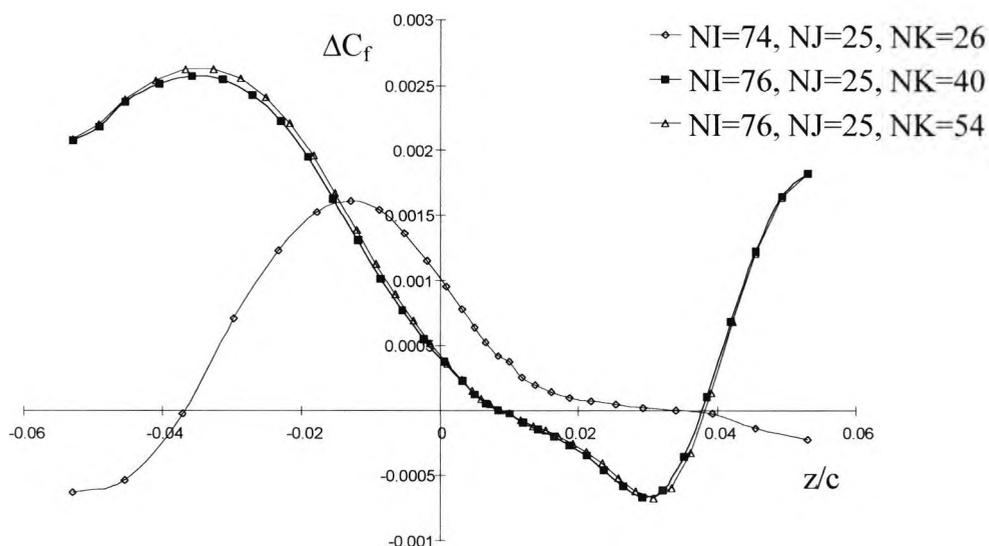
Figure 6.1: Skin friction enhancement 0.16c downstream of the AJVG array, looking upstream, on three grids of varying density, S=0.102c and V_R=2

Employing a transverse node distribution NK=26, results in the predicted skin-friction enhancement being concentrated over a smaller proportion of the spanwise section, with a value ΔC_f 0.001 lower than that predicted using the finer grids. Refinement above NK=40 yields virtually no improvement in the predicted skin friction enhancement. Subsequent predictions were evaluated employing a cell distribution of NI=74, NJ=25 and NK=40, as this grid density yields grid independent solutions with the lowest computer storage and CPU time requirements. Nevertheless, throughout this study, a range of AJVG spacings was tested, having implications for the grid density in the cross-stream direction (NK). The grid cell aspect ratio, the ratio of the cell height, width and thickness can influence the overall predicted results. To minimise the effects of changing cell aspect ratio on the flow field predictions, the density of the grid in the cross-stream direction is proportionately altered to maintain a constant cell aspect ratio when the jet spacing is increased or reduced.

6.3 Results and discussion of the 'local' AJVG flow field predictions

Computational studies on the 'local' AJVG model involved monitoring the following parameters at the locations depicted on Figure 6.2:

- Spanwise shear stress enhancement at ten chordwise locations (x/c=0 to 0.9)
- u/Ue, δ^*, θ and H properties, averaged across the span on a uniform grid, at three chordwise locations downstream of the AJVG (x/c=0.3, 0.6 and 0.9).
- Crossflow velocity vectors and velocity contours of constant axial velocity at three spanwise y-z planes downstream of the AJVG (x/c=0.3, 0.6 and 0.9).

Velocity contour plane 1 (V1)   (V2)   (V3)

Flow

AJVGs

0.9c
0.8c
0.7c
0.6c
0.5c
0.4c
0.3c
0.2c
0.1c
0c

Dimensions:

Domain height (mm) = 260
Domain width (mm) = 25.5 to 101.5
c (mm) = 500
δ at jet exit in the unblown case (mm) = 12
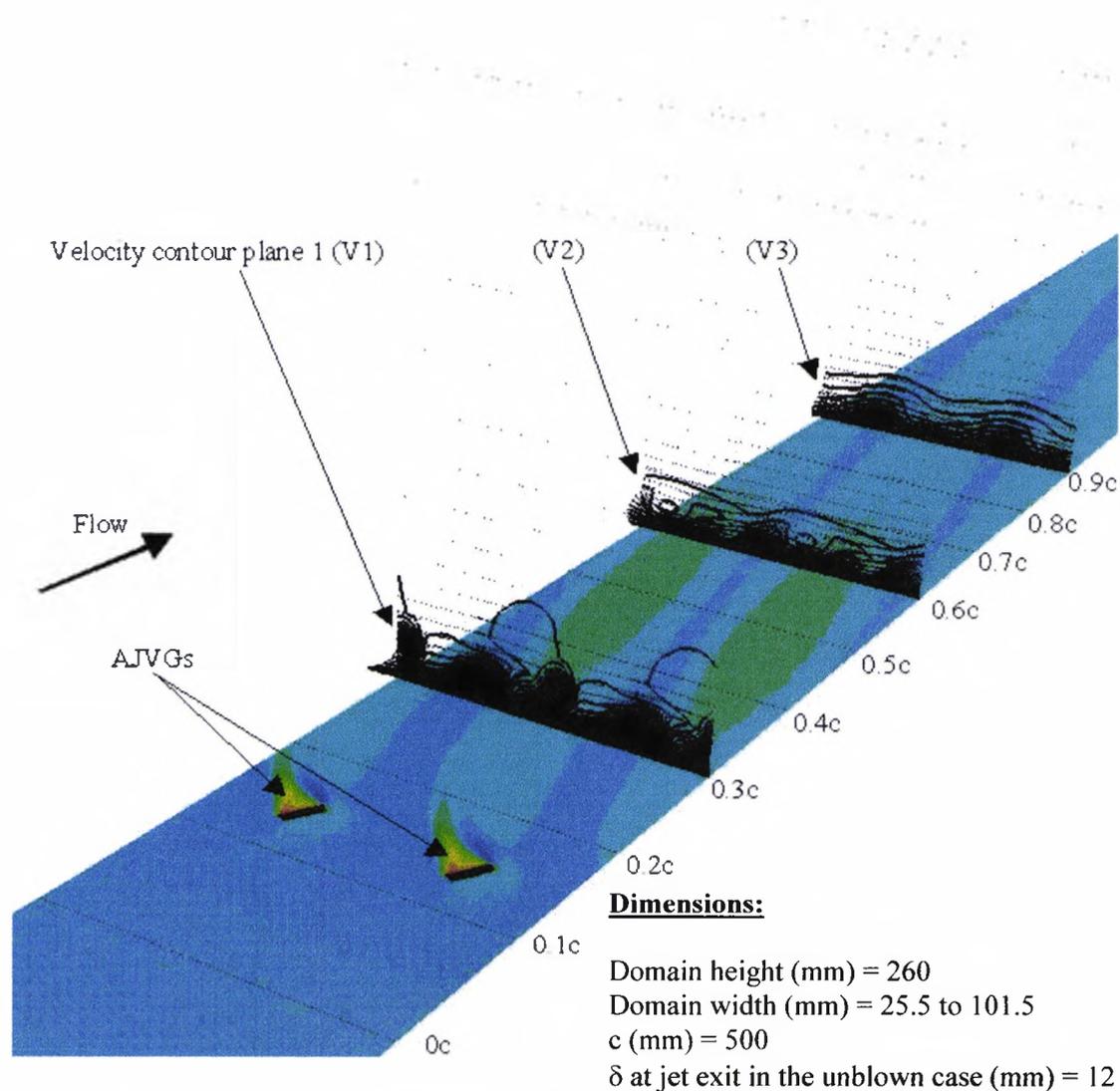
Figure 6.2: Data measurement locations for the 'local' AJVG model computations

Throughout the analysis of the results for the flat plate 'local' AJVG model, the velocities and wall shear stress predictions are made non-dimensional with the local freestream velocity at the boundary layer edge (U_e) and the freestream dynamic head ($\frac{1}{2}\rho_\infty U_\infty^2$) at entry to the computational domain respectively. All distances were normalised by the retracted chord length of the three-element high lift system. Figures 6.3-6.16 show the results of the 'local' model sensitivity study in a constant zero pressure gradient flow. The influence on these results, of imposing a pressure gradient analogous to that on an aerofoil approaching stall is illustrated on Figures 6.19-6.32.

Nominally zero pressure gradient flow

The performance of the air-jet array is judged primarily by the level of skin friction enhancement achieved downstream of the AJVG on the model surface. Because the transverse C_f distribution is periodic (see Figure 6.1) its capability is evaluated by integrating C_f in the z-direction and weighting the integrated value by the non-dimensional jet spacing (S) to obtain a figure of merit labelled $I\Delta C_f$. Figures 6.9-6.14 show the effects of model configuration, i.e., jet spacing, S, jet-to-freestream velocity ratio, V_R, and rotational sense of the vortex array, on the transverse $I\Delta C_f$ plotted versus axial distance along the model surface in a nominally zero pressure gradient flow. In each air-jet configuration, the graphs illustrate an increase in wall shear stress downstream of the AJVG installed at x/c=0.14. The figures also demonstrate that the rate of decay of $I\Delta C_f$ is heavily dependent upon the air-jet spacing.

Prior to discussing the effects of AJVG configuration on the skin friction enhancement it is useful to identify the mechanisms of flow control that are associated with AJVGs. Figures 6.3-6.8 show the global effects of employing the AJVGs on the local model flow field in both the co-rotating and counter-rotating air-jet configurations for S=0.106 and V_R=3. As will be shown later, this AJVG spacing and jet-to-freestream velocity ratio correspond to the configuration providing the best skin friction enhancement.

Figure 6.3 shows velocity vectors and contours of constant axial velocity in the crossflow plane, normal to the wall, at three chordwise locations downstream of the

AJVG array. The viewing planes are perpendicular to both the model surface and the oncoming freestream flow with the reader looking downstream from the AJVG. Figures 6.3a, 3c and 3e show in some detail the periodicity of the vortex array generated by the co-rotating AJVGs. On the right hand side of the vortex core there is evidence of the high momentum fluid being drawn towards the model surface. Conversely, on the left hand side of the vortex cores the velocity vectors demonstrate that the vortices promote the transport of the low momentum flow away from the model surface. The vectors also demonstrate that the AJVG spacing is sufficient to ensure that the low momentum fluid convected away from the model surface is not impeded by the neighbouring vortex. In line with the findings of Pearcey (1961), the predicted results for the co-rotating AJVG array show that as the vortex array flows downstream, interaction between neighbouring vortices has little effect on the core location above the model surface. However, the image vortices in the surface induce a spanwise motion to the vortex array, in this case from right to left looking downstream from the AJVG.

The influence of the interaction between neighbouring vortices in the counter-rotating configuration is demonstrated on Figures 6.3b, 3d and 3f. In this case, the flow between the adjacent vortices is away from the model surface. At x/c=0.3, the velocity vectors and velocity contour plots indicate strong interaction between the adjacent vortices, as the majority of the low momentum flow near the wall is convected away from the model surface. At subsequent downstream locations, the interaction between the neighbouring vortices and the image vortices in the wall force the pair to migrate from the model surface. As a consequence, the level mixing between the high momentum flow in the freestream and the low momentum flow within the retarded shear layers is significantly reduced.

The substantial effects of the enhanced mixing between the AJVG and its induced flow field and the consequent impression on the wall shear stress downstream of the AJVG in both the co-rotating and counter-rotating configuration, are shown on Figure 6.4. The shear stress footprints demonstrate that the in the regions where the high momentum freestream flow is directed towards the aerodynamic surface, the wall shear stress is elevated. On the other hand, when the vortices promote the transport of

low momentum flow away from the model surface, the wall shear stress is reduced. The confined region of low wall shear stress is developed over a relatively small percentage of the illustrated skin friction footprint.

In the co-rotating configuration (Figure 6.4a), the influence of the vortices is shown to persist beyond 0.9c, with the enhanced wall shear stress region expanding slightly as the vortex array moves downstream. The shear stress footprints demonstrate that utilising a co-rotating array of AJVGs would enable suppression of boundary layer growth over the majority of the aerodynamic test surface. The expansion of the region of elevated shear stress coincides with the growth of the vortices, and suggested by the velocity vector plots on Figure 6.3. Shear stress footprints for the counter-rotating array (Figure 6.4b) imply that the counter-rotating vortex do little to elevate the wall stress beyond a downstream location of x/c=0.5. However, the footprints show that, in close proximity to the AJVG, the skin friction enhancement is more substantial when utilising a counter-rotating air-jet configuration. For applications where flow control is required over only a small region of the aerodynamic surface, a counter-rotating AJVG array would be especially effective.

Further evidence of enhanced mixing between the freestream and the retarded flow within the shear layer is shown by the boundary layer profiles, u/U_e, and integral boundary layer property, δ^*, θ and H, plots (Figures 6.5-6.8). Activating the AJVGs results in the generation of a complex three-dimensional flow field downstream of the air-jet array (see Figure 2.6). The global effects of utilising the AJVGs expressed as two-dimensional quantities may be demonstrated by visualising their effects in the crossflow planes as we progress downstream of the AJVG.
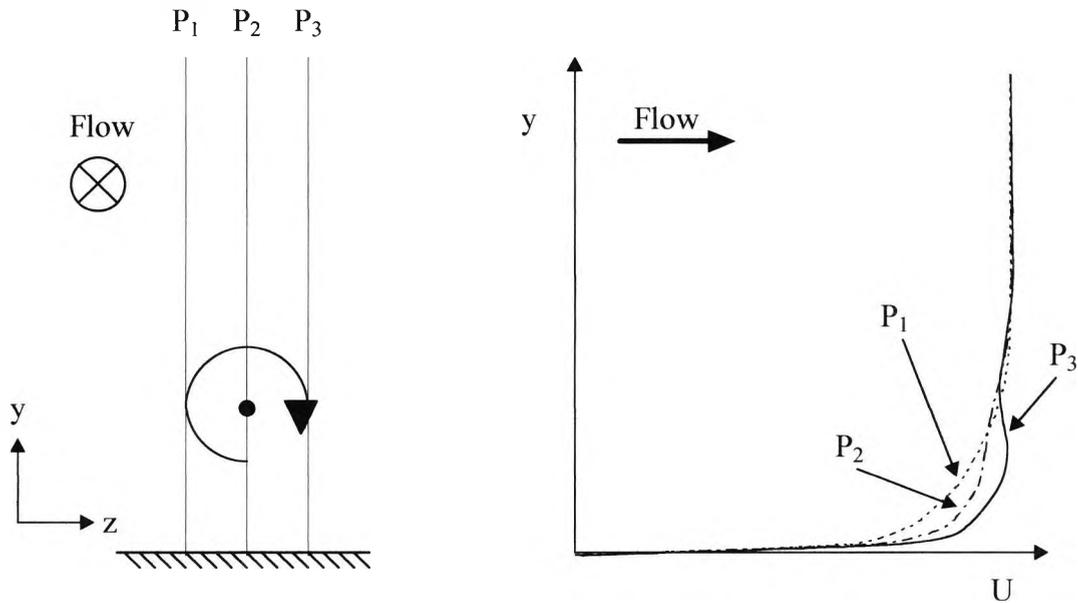
Sketch 6.1: Schematic of the velocity profile, in the freestream direction (U-velocity), across the vortex core.

Sketch 6.1, for example, demonstrates the behaviour of the velocity component in the direction of the freestream flow, across the vortex core. The sketch shows that on the downwash side of the vortex (P_3) the freestream flow is directed towards the model surface and the velocity profile is more than 'filled out'. Conversely, on the upwash side of the vortex (P_1), the low momentum flow near the wall is convected into the freestream, resulting in a deficit velocity profile. The work of Küpper (1999) demonstrates in more detail the velocity profiles observed in close proximity to the vortex core. Even with the air-jets active, Küpper (1999) demonstrates that the majority of the momentum in the 'local' model flow field remains in the freestream direction. It, therefore, makes sense to monitor the velocity field in the direction of the freestream flow to assess the effects of employing the AJVGs, in this case, the U-velocity component. Predictions for the 'local' model with the jets active and inactive are compared by evaluating the U-velocity profiles and the corresponding integral boundary parameters, δ^*, θ and H, that are determined from the axial velocity profiles. However, with the AJVGs active the U-velocity profile in the crossflow plane normal to the wall is three dimensional, as discussed above for Sketch 6.1. To reduce the data in the predictions with the AJVGs active, so that comparisons can be made with the

149

unblown case, the U-velocities are averaged across the model span, at 2.5mm height intervals above the model surface.

Results for the u/Ue-velocity profiles, 'averaged across the model span', utilising both co- and counter-rotating air-jet configurations, are depicted on Figures 6.5. Comparisons are made at three downstream locations (x/c=0.3, 0.6 and 0.9) with the AJVGs off and with the AJVGs on. The plots demonstrate that the u/U_e profile is filled-out near the wall, at all three chordwise locations when employing either a co-rotating or counter-rotating array of AJVGs. At x/c=0.3 the jet flux is visible at y/c≈0.03, as a region of high momentum fluid extending beyond u/U_e=1.

Analysis of the integral shear layer properties of δ^*, θ and H in Figures 6.6-6.8 show the effects of the increased mixing in the shear layers sponsored by the AJVGs. Generating either co-rotating or counter-rotating vortex arrays results in a reduction of δ* and θ by as much as 50% downstream of the AJVG. In each case, the reduction is greater when utilising a co-rotating air-jet configuration. Reducing δ^* and θ downstream of the AJVG array infers that the velocity profiles are 'filled out', increasing the velocity gradient at the wall, and as a consequence, yielding higher wall shear stresses.

The shape parameter plots (Figure 6.8) show that beyond a downstream location of x/c=0.5, δ^* and θ grow at approximately the same rate as the uncontrolled case, for both co-rotating and counter-rotating air-jet configurations. However, just downstream of the AJVG array (0.06c for co-rotating and 0.15c counter-rotating) there is a marked reduction in H, caused by the high momentum jet flux at the AJVG exit inducing local boundary-layer separation. Further evidence of the local effects of the high momentum jet flux is demonstrated by regions of very high and very low shear stress on the footprint plots depicted on Figure 6.4.

As mentioned above, the vortices impress a characteristic shear stress signature on the wall surface that is periodic in the mean. This signature can be integrated and expressed as a figure of merit IΔC_f to enable comparisons to be made between

150

different air-jet configurations. Comparisons of both co-rotating and counter-rotating air-jet configurations for jet spacings 0.051≤S≤0.203 and jet-to-freestream velocity ratios 1≤V_R≤4, in a nominally zero pressure gradient flow, are shown in Figures 6.9-6.16.

Figure 6.9 shows the results for the co-rotating array with a jet spacing of 0.051: as V_R increases from 1-2 there is little influence on IΔC$_f$ levels downstream of the AJVG (Figure 6.9a). This indicates that the vortices are too closely spaced which results in the vortex array limiting the amount of low momentum fluid that can be convected away from the surface. Employing V_Rs of 3 and 4 at S=0.051 yields large regions of enhanced skin friction beyond x/c=0.5. Analysis of the velocity vectors in the y-z plane along the chord (not included) indicate that the jets act as a form of tangential blowing and do not generate an array of vortices. As the purpose of AJVGs is to provide an effective flow control system with minimal power requirements, employing a jet spacing of 0.051, in terms of jet mass flux per unit span, is deemed prohibitively expensive.

Above a jet spacing of 0.051, the co-rotating arrays show a general increase in IΔC$_f$ with increasing V_R (Figure 6.9a-6.13a). At each velocity ratio tested, a 'blip' is apparent in the region of increasing IΔC$_f$ just downstream of the AJVG, which grows with increasing V_R. It is felt that this region represents the induced effect on the wall shear stress of the developing vortex arrays, as the AJVG, the freestream and the boundary layer flows combine. The greatest levels of skin friction enhancement downstream of the co-rotating AJVG array are demonstrated with the jets at S=0.106 and 0.127. These findings agree with those of Pearcey 1961 when studying the effect of VVG spacing on the vortex array characteristics. Pearcey demonstrated that above a critical VVG spacing (D/h>4) the performance of the array decays only slightly with increased spacing.

Predictions in the co-rotating configuration of IΔC$_f$ above a jet spacing of S=0.127 (Figure 6.13a), show that the extent of the skin friction enhancement, at all velocity

ratios, no longer increases with jet spacing. This is a result of the reduced interaction between adjacent vortices and image vortices as the jet spacing increases.

As discussed above the interactions between the adjacent and image vortices with the AJVGs in the counter-rotating configuration significantly influence the level of mixing between the high momentum flow in the freestream and the retarded shear layers at the wall. Figures 6.9b-6.13b showing the level of skin friction enhancement downstream of the counter-rotating AJVGs is highly dependent upon S. Between jet spacings of 0.051 and 0.106 increasing V_R has little influence on $I\Delta C_f$ along the chord (Figures 6.9b-6.11b). This is due to the neighbouring vortex and image vortex interactions that promote convection of the vortical array away from the aerodynamic surface. In turn, the array cannot promote as much mixing between the high momentum fluid in the freestream and retarded flow in the shear layers near the wall. Further evidence of the effects of vortex interaction are implied at the lower jet spacings $(0.051 \leq S \leq 0.076)$ in the counter-rotating configuration, where the level of skin friction enhancement diminishes at a much faster rate downstream of the AJVGs. It should be noted, that in the counter-rotating AJVG predictions there is no evidence of the 'blip' observed just downstream of the AJVG array in the co-rotating configuration. This is most likely a result of the imposition of symmetric boundary conditions on either side of the AJVG. As no flow can penetrate the symmetry plane the jet flow is forced to rapidly combine with the freestream and boundary layer flows to form a strong vortex pair in close proximity to the AJVG. This is demonstrated most forcefully in the counter-rotating configuration at S=0.051 and V_R=4 with $I\Delta C_f$ rising to 0.0055 just downstream of the AJVG (Figure 6.9b).

Figures 6.14 to 6.16 show the effect of jet spacing on the level of skin friction enhancement at three chordwise locations downstream of the AJVGs in both the co- and counter-rotating configurations. At x/c=0.3 (Figure 6.14), the potentially useful increase in surface skin friction is shown as being considerably larger when the AJVGs are configured to generate a co-rotating array of vortices. At each velocity ratio the peak values for $I\Delta C_f$ occur when employing $0.106 \leq S \leq 0.123$. In contrast, the level of skin friction enhancement remains relatively insensitive to S and V_R when utilising a counter-rotating AJVG configuration. Here the optimum performance may

be inferred by employing a jet spacing S=0.051 with V_R=4. However, flow control device power requirements, as discussed above, question the application of such an air-jet configuration. At x/c=0.6 and x/c=0.9, the co-rotating array of AJVGs demonstrate an increase in $I\Delta C_f$ with velocity ratio that is relatively insensitive to the increasing jet spacing (Figures 6.15 and 6.16). Again optimum S values are apparent with the peak $I\Delta C_f$ values occurring between 0.106 and 0.127 at V_RS of 3 and 4.

Adverse pressure gradient flow

To assess the effectiveness of utilising an AJVG array to suppress boundary layer growth, on a more realistic flow field, i.e., an aerofoil approaching stall, a representative adverse pressure gradient is imposed upon the 'local' model surface. Figures 6.17 and 6.18 show this sample adverse pressure gradient with the AJVGs turned off. The predictions show increasing growth of the test flow displacement thickness at a rate approximately twice that of the momentum deficit thickness. Predicted values of H and C_f show that the flow is approaching separation, i.e., H→2.5 and C_f→0 at x/c=0.7 and beyond.

As with the nominally zero pressure gradient flow results, prior to assessing the skin friction enhancement performance of the AJVG arrays, lets identify how the adverse pressure gradient influences the mechanisms of flow control. Figures 6.19-6.24 show the global effects of the adverse pressure gradient flow on the vortices generated by the AJVG array with S=0.076 and V_R=3. Once again, the chosen AJVG spacing and jet-to-freestream velocity ratio correspond with the configuration yielding the best skin friction enhancement (see later discussion).

Figure 6.19 shows the predicted velocity vectors and contours of constant axial velocity in the crossflow plane, normal to the wall, at three chordwise locations downstream of the AJVG array. The viewing planes are perpendicular to both the model surface and the oncoming freestream flow with the reader looking downstream from the AJVG.

In the co-rotating AJVG configuration (Figures 6.19a, 19c and 19e), the adverse pressure gradient is shown to heavily influence the development of the vortex array

153

downstream of the air-jets. The velocity vectors in the crossflow plane show that a large proportion of the flow leaves the solution domain in the positive y/c direction under the influence of the adverse pressure gradient. The result of the convection of the flow away from the model surface is that the vortices are significantly stretched in the direction normal to wall, during the early stages of their formation. Comparing the crossflow velocity vectors, at the same chordwise location, in a zero pressure gradient flow (Figure 6.3a), further illustrates the vortex stretching that is induced by the adverse pressure gradient. At subsequent downstream chordwise locations in the adverse pressure gradient flow, the velocity vectors in the crossflow plane for the co-rotating AJVG array (Figures 6.19c & 6.19e), show no evidence of presence of vortices in the flow field.

This phenomenon has not been observed in a number of experiments examining the effects of co-rotating AJVGs, operating in strong adverse pressure gradients [see Innes (1995), Oliver (1998) and Lewington et al (2000)] suggesting that the numerical 'local' AJVG model approach may not be valid for strong pressure gradient flows. In the experiments, co-rotating AJVG configurations are shown to be highly effective in delaying the onset of flow separation and reducing wake profile drag in very strong adverse pressure gradient flows. The author feels that the inability to adequately predict the co-rotating vortex flow field in strong pressure gradient flows, with the 'local' AJVG model, is attributable to the definition of the periodic boundary conditions on either side of the AJVGs. Unlike wall or inlet boundary conditions, no specific behaviour of the flow is defined at the periodic boundary. Instead, periodic boundaries translate the predicted flow characteristics to the solution domain boundary, in the direction of the periodicity. Periodic boundary conditions can therefore be defined 'numerically weak', in the sense that they do not drive the flow in a specific direction. As a result, convergence to a solution does not necessarily imply convergence to the correct solution but that the numerical constraints of satisfying continuity have been met. In this project, attempts were made to minimise the errors in predicting the adverse pressure gradient flow field by re-starting calculations from the converged cases in a nominally zero pressure gradient flow for the same air-jet configuration. The reasoning behind this approach is that by starting with a well-defined flow field it should be possible to assess the effects of the strong pressure

gradient. However, for the co-rotating AJVG configuration the results clearly indicate that the approach is not valid.

Further evidence of the importance of the boundary condition definition on either side of the AJVGs is shown in the results for the counter-rotating air-jet configuration (Figures 6.19b, 19d and 19f). Despite being subjected to the same strong adverse pressure gradient the 'local' model predictions show that the AJVGs are able to generate an array of vortices that persist downstream of the air-jets. As with the co-rotating results, the velocity vectors in the crossflow plane demonstrate that the vortices are stretched in the direction normal to the wall, due to the influence of the adverse pressure gradient, when compared to the results for the nominally zero pressure gradient flow, at the same chordwise location (see Figures 6.3b, 3d and 3f). However, the general trends observed in the nominally zero pressure gradient predictions (the formation of a strong vortex pair that convect away from the model surface as they flow downstream) appear to be replicated in the predictions for the adverse pressure gradient flow. The prediction of a persistent array of counter-rotating vortices, in the strong adverse pressure gradient flow, is the result of imposing symmetry boundary conditions on either side of the AJVG in the 'local' model. Numerically, symmetry boundaries act as slipping walls, so that flow cannot pass through and that the velocity normal to the boundary and the gradients of all other quantities are equal to zero. As a result, the jet flux and the freestream and boundary layer flows are forced to combine to form well-organised vortex arrays that are capable of withstanding the strong adverse pressure gradient. Results for the counter-rotating AJVG configurations highlight the importance of the 'local' model boundary condition definition on the physical relevance of the numerical solution. What is key is that without a better method of specifying the local model periodic boundary conditions, it is unlikely that the approach can be used to assess the effectiveness of the AJVG array ability to suppress boundary layer growth in strong adverse pressure gradient flows.

The trends identified in the crossflow velocity vector and velocity contour plots, in the adverse pressure gradient flow, are reinforced by the 'local' model wall shear stress footprints (see Figures 6.20a-20b). In the co-rotating AJVG configuration, the

influence of the vortices on the wall shear stress diminishes almost immediately, as a result of the inadequacy with periodic boundary condition implementation in strong pressure gradient flows. However, results for the counter-rotating air-jet configuration elevate the wall shear stress above that of the background level up until 0.3c. Beyond x/c=0.4, the interaction between neighbouring vortices forces the vortex pair away from the wall, limiting their ability to elevate the wall shear stress.

Predicted results obtained for the co-rotating AJVG array in a strong adverse pressure gradient have been shown to be of numerical artifice, in that they do not represent the 'real world' AJVG capability. Further discussion of the predicted results obtained with the 'local' AJVG model configured to generate a co-rotating array of vortices is of little relevance and is therefore discarded.

Figure 6.21 shows the U-velocity profiles, averaged across the 'local' model span, at three locations downstream of the AJVG array. As with the nominally zero pressure gradient predictions discussed above, U-velocities are averaged across the model span, at 2.5mm height intervals above the model surface. Results for the counter-rotating AJVG configuration, Figure 6.21, highlight the presence of the vortices as far downstream as x/c=0.9. The vortices can be identified by the inflection in the velocity profiles between 0.04<y/c<0.12 at x/c=0.6 and 0.04<y/c<0.18 at x/c=0.9. These inflections occur as the vortices promote mixing between the high momentum freestream flow and the low momentum fluid within the retarded shear layers. Near the model surface the velocity profile is filled out and by continuity a velocity deficit occurs at the core. At all three downstream locations, the counter-rotating vortices fill out the velocity profile, suppressing the likelihood of boundary layer separation.

Analysis of the average spanwise integral shear layer properties in Figure 6.22, 6.23 and 6.24 along the chord highlights the ability of the counter-rotating AJVGs to considerably reduce δ^* and θ, even in a strong pressure gradient (Figures 6.22 and 6.23). Generating a counter-rotating array of vortices is shown to reduce δ^* and θ by as much as 50% below the undisturbed values at x/c=0.9. Similarly the predicted reduction in H below 2.5 is indicative that the likelihood of flow separation is reduced when the counter-rotating AJVGs are utilised.

156

The effects of the adverse pressure gradient on the predicted level of skin friction enhancement downstream of the AJVG are shown on Figures 6.25-6.32. At jet spacings of S≤0.076 (Figure 6.25 & 6.26), significant enhancement in the predicted wall shear stress above the unblown case is demonstrated at jet-to-freestream velocity ratios V_R=2 and 3. As the jet spacing increases, Figures 6.27, 6.28 and 6.29, the level of skin friction enhancement is shown to diminish almost independently of jet-to-freestream velocity ratio. This reduction in IΔC_f is the result of a reduced level of interaction between the adjacent vortices as the spacing between the AJVGs increase. Consequently, the rate decay in the wall shear stress enhancement is much the same as is demonstrated for the co-rotating configurations.

The effects of jet spacing on the predicted skin friction enhancement at three chordwise locations downstream of the air-jets are shown on Figures 6.30-6.32. At all three locations, peaks in the IΔC_f curves, for the counter-rotating arrays, can be identified at a jet spacing close to S=0.076. Above a spacing of S=0.076, at x/c=0.3 and x/c=0.6, the performance of the vortex arrays quickly decays.

Results for the air-jets in the counter-rotating configuration at x/c=0.9 (Figure 6.32b), indicate that increasing V_R above 2 yields no significant improvement in the IΔC_f factor irrespective of the jet spacing. This is attributable to the fact that as V_R increases the rate of convection of the vortex system away from the surface increases. Hence, the extent of skin friction enhancement far downstream is limited when utilising a counter-rotating air-jet configuration.

6.4 Summary of 'local' air-jet vortex generator model results

The above discussion details the predicted results of the flow field characteristics downstream of either a co-rotating or counter-rotating AJVG array in both nominally zero and adverse pressure gradient flows. The effectiveness of the AJVG arrays was assessed by monitoring the skin friction enhancement above the uncontrolled flow level on the model surface (ΔC_f) and the shear layer properties u/U_e, δ^*, θ and H. Velocity vector/contour plots demonstrated the behaviour of the secondary motion of the generated vortices in three planes perpendicular to the freestream flow. Predictions were obtained utilising the finite volume block-structured flow solver (CFX4) employing a k-ε turbulence model with wall functions to predict the flow phenomena.

The periodic signature of the surface skin friction across the span enabled comparisons between AJVG configurations by integrating ΔC_f in the spanwise direction and normalising with the jet spacing to obtain a performance figure of merit $I\Delta C_f$. The shear layer properties are determined by averaging the streamwise velocity across the model span at 2.5mm height intervals above the model surface to enable comparison with the uncontrolled two-dimensional boundary layer profiles.

The key findings from the predictions are:
- Employing AJVGs with a jet-to-freestream velocity ratio $V_R \geq 1$ results in a significant enhancement of the surface skin friction downstream of the air-jet array. In a nominally zero pressure gradient flow, superior levels of skin friction enhancement are demonstrated when employing co-rotating, as opposed to counter-rotating, air-jet configurations. <u>Clear optimum performance of the air-jet arrays, in either co-rotating or counter-rotating configurations, is demonstrated when employing an air-jet spacing S=0.106 and V_R=3.</u>

- Analysis of the averaged boundary-layer u/U_e, δ^*, θ and H properties, across the model span, demonstrate the potential for the AJVGs to delay boundary layer separation. The heightened mixing between the high momentum freestream fluid and the retarded shear layers serves to fill out the velocity profile, thereby increasing the

158

skin friction at the wall. As a result, δ^* and θ growth are suppressed by up to 50% as far as 0.6c downstream of the AJVG array.

- In both zero pressure gradient and adverse pressure gradient flow regimes, viscous interactions between the adjacent vortices dictate the paths of the vortical arrays. In the co-rotating air-jet configuration, the vortices migrate across the span as the vortex system flows downstream. The height of the co-rotating vortex array remains relatively insensitive to the axial location of the array. Mutual interaction between adjacent vortices in the counter-rotating configuration promotes rapid convection of the vortex system away from the model surface. As a result, the co-rotating arrays demonstrate improved skin friction enhancement over a larger proportion of the model surface.

- Imposing an adverse pressure gradient on the model surface that is synonymous with an aerofoil approaching stall, has significant implications on the predicted performance of the AJVG arrays. Superior levels of skin friction enhancement are demonstrated when utilising a counter-rotating air-jet configuration. However, the effects on the predictions are felt to be related to the numerical boundary condition implementation, as opposed to a consequence of the 'real life' flow physics. Employing periodic boundary conditions, to simulate an infinite co-rotating array, results in the majority of the flow leaving the computational solution domain before a stable array of vortices can form. Conversely, the imposition of symmetric boundary conditions, on either side of the AJVG, promotes the formation of stable arrays that are capable of withstanding the strong adverse pressure gradient. <u>Optimum performance of the vortex arrays is demonstrated when employing an air-jet spacing of S=0.076 and V_R=3 and 4 with the AJVGs configured to generate a counter-rotating array of vortices.</u>

- Employing a 'local' AJVG model to predict trends associated with the flow field characteristics around complex geometries is not without its limits. As the severity of the adverse pressure gradient imposed on the 'local' model surface increases, the model boundary condition constraints give rise to what appear to be non-physical flow field solutions.

159

7. Predicted and measured results for the three-dimensional high lift system incorporating an array of AJVGs

7.1 Introduction

The purpose of the 3-D high lift system numerical model, incorporating the AJVGs, is to evaluate the performance of air-jet arrays on improving aerodynamics, prior to undertaking wind-tunnel testing. By combining the results of the 3-D 'local' flat plate model sensitivity studies and the 2-D high lift system, trends associated with the AJVG implementation can be evaluated and tailored to suit the experimental model; for example, manipulating the boundary conditions in the numerical model to assess the effectiveness of employing either co-rotating or counter-rotating AJVGs.

The numerical, i.e., the digital wind tunnel performance of the AJVGs, is assessed by investigating their effect on the following characteristics: generated normal force (C_N), wake profile drag (C_{Dp}), leading edge pitching moment (C_{Mle}), the streamwise boundary-layer properties (u/U_e, δ^*, θ and H) and surface skin friction (C_f). Normal force and leading-edge pitching moment coefficients are determined by integrating the chordwise surface pressure distributions, monitored at the same chordwise location of the pressure taps as on the experimental model. In the computations, the pressure at each chordwise position is taken as the average across the span at that location. Wake profile drag characteristics are determined by estimating the momentum deficit in the wake one chord length downstream of the high lift system trailing-edge. As with the 'local' AJVG model the shear layer profile information is determined by averaging the streamwise velocity profiles across the model span at 2.5mm intervals in the direction normal to the surface tangent. Figures 7.1(a) and (b) show the data measurement locations on the 3-D high lift system numerical model and the predicted flow fields obtained with the air-jets configured to produce both co-rotating and counter-rotating vortex arrays.

The analogue wind tunnel experimental results are obtained in City University's T2 low speed wind tunnel at U_∞=40ms^{-1} (M_∞=0.12) for a range of jet momentum

coefficients ($0 \leq C_\mu \leq 0.119$). The Reynolds number based on the retracted chord of 500mm is $Re_c=1.37 \times 10^6$. Thirteen AJVGs are installed across the span of 740mm, to produce an array of co-rotating vortices, spaced at the recommended S=0.106c apart, at a retracted chordwise location of x/c=0.14.

The convergence criteria for the 3-D high lift system model solutions are essentially the same as those stipulated in the 2-D high lift system computations (see Section 5.1). The solution is said to have converged once the mass source residual has reduced by at least three orders of magnitude of the mass flow at inlet. Some convergence difficulties were experienced, at angles of attack of $\alpha \geq 20°$, where the numerical grid is highly skewed and where the flow over the mainfoil is approaching separation. As yet, it has not been possible to obtain a converged solution for the 3-D high lift system incorporating an AJVG at $\alpha=25°$ or above. To obtain converged solutions at higher angles of attack for this complex three-dimensional flow field, requires the use, we believe of more sophisticated turbulence models on finer numerical grids [see results from the high lift CFD workshops, Ying (1996), Fejtek (1997) and Linblad & De Cock (1999)]. Such a study is beyond the scope and capabilities of the current project. In all other cases, convergence was achieved within 10,000 iterations on grids of approximately 800,000 control volumes.

Grid dependence studies were limited by the available computer storage capacity. As a result, the numerical grid for the high lift system incorporating the AJVG is generated by combining the grid densities utilised in the 2-D high lift system and the 3-D flat plate 'local' model studies (see Sections 5.1.2 and 6.2). Some local grid refinement was required close to the AJVG, to ensure orthogonality at the aerofoil surface and minimal skewing of the computational grid.

Velocity vector/contour and skin friction measurement locations
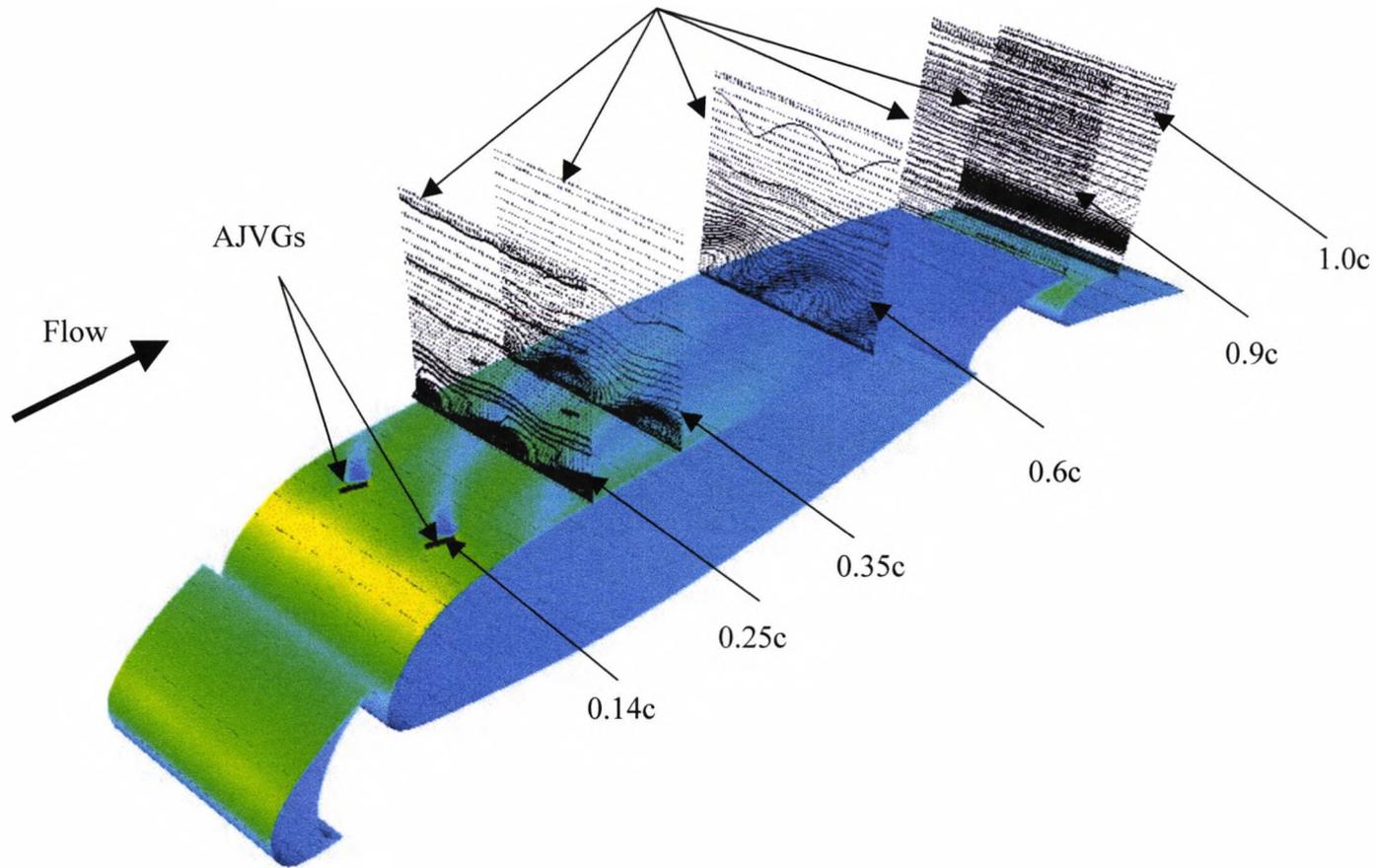
Figure 7.1(a): Data measurement locations for the numerical 3-D high lift system configured with a co-rotating array of AJVGs in the digital wind tunnel, $\alpha=20°$, $Re_c=1.37\times10^6$, $M_\infty=0.12$, $\phi=45°$, $\psi=60°$

Velocity vector/contour and skin friction measurement locations
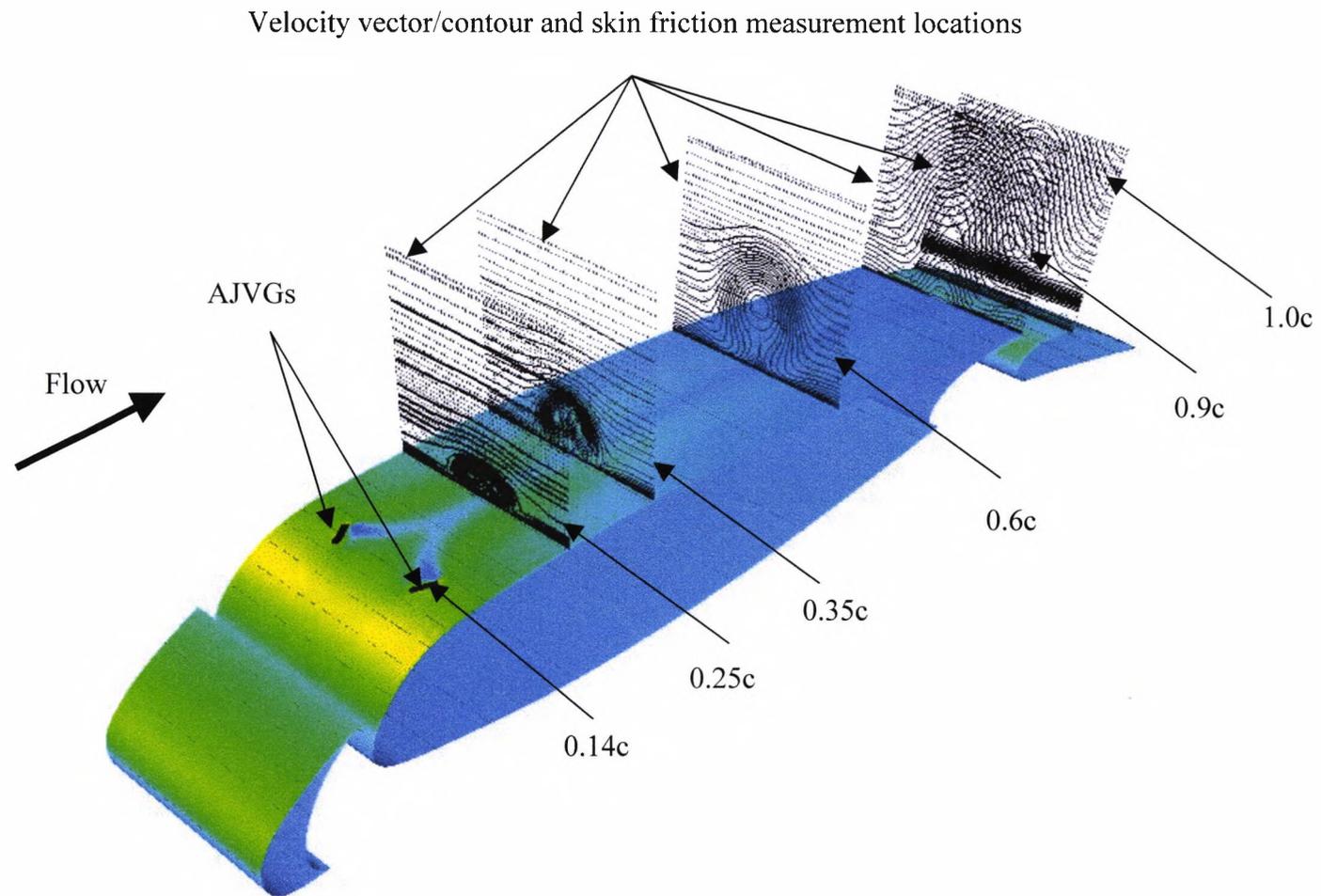
Figure 7.1(b): Data measurement locations for the numerical 3-D high lift system configured with a counter-rotating array of AJVGs in the digital wind tunnel, $\alpha=20°$, $Re_c=1.37\times10^6$, $M_\infty=0.12$, $\phi=45°$, $\psi=60°$

7.2 Results and discussion of the predicted and experimental three-dimensional high lift system flow field

Throughout these results and discussion, the velocities are made non-dimensional by the local freestream velocity at the boundary layer edge (U_e); while the pressures and wall shear stresses are made non-dimensional by the freestream dynamic head ($\frac{1}{2}\rho_\infty U_\infty^2$). All distances are normalised by the retracted chord length of c=500mm. Figures 7.1-7.19 show the results of the CFX-predicted flow field around the high lift system at angles of attack of 10° and 20° with blowing momentum coefficients in the range $0 \leq C_\mu \leq 0.072$. Wind tunnel experimental data, obtained with the high lift system at a range of angles of attack ($0° \leq \alpha \leq 36°$) and a range of jet momentum blowing coefficients ($0 \leq C_\mu \leq 0.119$) are shown on Figures 7.20-7.30.

CFX-predicted 3-D high lift system flow field results

Figure 7.1 shows the respective global effects of employing the co-rotating and counter-rotating AJVGs on the high lift system at $\alpha=20°$. The velocity vectors represent the flow field in the crossflow planes that are perpendicular to both the aerofoil surface and the streamwise flow and the contour plots represent lines of constant streamwise velocity. The predicted flow fields illustrated on Figure 7.1 are analogous to the predictions obtained using the 'local' flat plate AJVG model, in an adverse pressure gradient flow (see Figures 6.2, 6.19 and 6.12). In both sets of predictions, the jet flux, freestream and boundary layer flows, combine to produce vortical arrays downstream of the air-jets. As in the 'local' model predictions, the influence of the adverse pressure gradient and interactions between the neighbouring vortices affects the path of the vortical arrays.

In the co-rotating AJVG configuration (Figure 7.1a) the 3-D high lift system shear stress footprints and the velocity vectors/contour plots illustrate the spanwise periodicity of the flow field induced by the air-jets. Local regions of high shear stress are evident in very close proximity to the AJVG exit as a result of the high momentum jet flux. The shear stress footprints illustrate the spanwise translation of the vortices as they flow downstream under the influence of the image vortices in the aerofoil

surface. By approximately x/c=0.7, the shear stress signature on the mainfoil upper surface is constant and the velocity vector/contour plots at subsequent downstream locations show no evidence of the presence of the vortex array.

Predictions for the counter-rotating AJVG configuration (Figure 7.1b) show the individual vortices combining to form a pair that persist over the entire mainfoil upper surface and in the freestream above the flap. The shear stress footprints on the mainfoil upper surface also show the vortices influencing the near wall flow over the entire mainfoil upper surface to the trailing-edge. As with the flat plate 'local' AJVG model, the path of the vortex pair is governed primarily by the neighbouring vortex interactions and the adverse pressure gradient flow on the mainfoil upper surface.

The effects of employing AJVGs on the chordwise surface pressure distributions at $\alpha=10°$ and $20°$ are shown on Figures 7.2 and 7.3. The chordwise pressure distributions are determined by averaging the predicted surface pressure coefficient at 30 uniform intervals across the model span, at the x/c locations corresponding to the static pressure tap orifices on the experimental model. At both angles of attack, the AJVGs have been configured to generate arrays of either co-rotating (Figures 7.2a and 7.3a) or counter-rotating vortices (Figures 7.2b and 7.3b), utilising jet-to-freestream velocity ratios of $V_R=2$, 3 and 6. At $\alpha=10°$, the only notable differences in the surface pressure distributions, irrespective of the rotational sense of the vortex system, are apparent at peak suction on the mainfoil and just downstream of the AJVG array. Employing jet velocity ratios of 2 and 3 results in a slight reduction of the peak C_P around the mainfoil leading edge. The reduced suction yields slightly lower C_N values when compared to the corresponding cleanfoil high lift system predictions. The 'hump' regions of reduced C_P, observed at approximately x/c=0.2, are shown to grow significantly with increasing V_R. Following the arguments of Rao (1988) and Innes (1995), it is possible to define these 'humps' as the direct result of the locally induced vortex velocities. Flow passing underneath the jet flux is accelerated resulting in higher levels of suction at the mainfoil component surface.

At $\alpha=20°$, the predictions show that employing the AJVGs starts to be beneficial when utilising a jet-to-freestream velocity ratio of 6 and a counter-rotating AJVG

configuration (see Figure 7.3b). In this $V_R=6$, counter-rotating AJVG configuration, the predicted chordwise pressure distributions demonstrate pressure recovery at the flap trailing edge, increased suction on the mainfoil and flap upper surfaces and over-pressure on the mainfoil and flap lower surface. Predictions obtained with the AJVGs configured to generate an array of co-rotating array of vortices, demonstrate that C_P divergence at the flap trailing edge is increased with the AJVGs active. These predicted trends do not agree with the experimental wind tunnel observations (see Innes (1995) and later discussion) and are thought to be due to the inadequate definition of the flow field boundary conditions in strong adverse pressure gradient flows. As observed in the 'local' AJVG model predictions (see Chapter 6) the strength of the adverse pressure gradient negates the use of 'numerically weak' periodic boundary conditions on either side of the air-jets. Unlike symmetric boundary conditions that reflect the flow field characteristics at each grid point, periodic boundaries act as inter-grid-block boundaries through which flow can pass. As a result, the only driving forces on the flow arise from the inlet, outlet and adverse pressure gradient boundary conditions. Under these periodic boundary conditions, it is possible to converge to a numerical solution that satisfies continuity but is non-physical. Comparisons between predicted and experimental results for the high lift system incorporating the AJVG array are limited, as the computational model is unable to adequately replicate the experimentally measured flow field.

Figures 7.4 and 7.5 further demonstrate the contributions of the adverse pressure gradient and the boundary condition definition on the development of the predicted vortex array over the upper surface of the high lift system. The velocity vectors represent the secondary motion induced by the vortices in the crossflow planes normal to the aerofoil surface, at five chordwise locations downstream of the AJVGs. At $\alpha=10°$ (Figure 7.4) the predicted velocity vectors in the co-rotating AJVG configuration illustrate that the vortical array persists as far downstream as x/c=0.6. Further downstream at x/c=0.9 and 1.0, there is little evidence of the presence of the vortices in the flow field above the multi-component high lift system. At $\alpha=20°$ (Figure 7.5), the results for the co-rotating AJVG array illustrate that the vortices are only predicted to persist as far downstream as x/c=0.6. The velocity vectors on Figure 7.5c show that only 0.2c downstream of the air-jets, the vortices are elongated in the

direction normal to the model surface, when compared to the $\alpha=10°$ results. The elongation of the vortices is due to the increased severity of the adverse pressure gradient at $\alpha=20°$ and the inability of the code to adequately model periodic boundary conditions in the crossflow when severe pressure gradients are present in the flow field.

Conversely, the predicted velocity vectors for the counter-rotating AJVG configurations show little difference in the path and shape of the vortex pair, at each chordwise location for both $\alpha=10°$ and $20°$. Despite the increasing severity of the adverse pressure gradient when α is increased from $10°$ to $20°$, employing symmetric boundary conditions either side of the air-jets permits the formation of stable and persistent vortex arrays. These findings strengthen the arguments outlined in Chapter 6, that the inability to define a well-organised co-rotating vortex array lies with the 'numerical weakness' of the periodic boundaries.

The predicted streamwise velocity profiles at $\alpha=10°$ and $20°$ (Figures 7.6 & 7.7) imply in more detail how the vortices transfer momentum across the complex shear layers for both co-rotating and counter-rotating AJVG configurations with $V_R=6$. The velocity profiles are determined by averaging the streamwise velocity across the model span at 2.5mm height intervals normal to the aerofoil surface at each chordwise location (as depicted on Figure 7.1). At $\alpha=10°$ (Figure 7.6) the predictions with the AJVGs active in both configurations indicate that the vortices promote the 'filling out' of the velocity profiles in the near wall region. However, results for the counter-rotating air-jet configuration demonstrate that these beneficial effects are evident much further downstream in the mainfoil boundary layer and the mainfoil wake above the flap.

Velocity profile predictions at $\alpha=20°$ (Figure 7.7) further demonstrate the inability of the predicted co-rotating AJVG model configuration to suppress boundary layer separation. If anything, the velocity profiles indicate that activating the air-jets on this computational model only serve to promote separation at the mainfoil trailing edge (x/c=0.9). Employing a counter-rotating AJVG configuration at $\alpha=20°$ with $V_R=6$

(Figure 7.7b) yields a useful enhancement of mixing within the retarded shear layers over the high lift system upper surface. Despite the streamwise velocity deficit at the vortex core location, illustrated by the inflections in the velocity profiles, the velocity profiles are 'filled out' in the near wall region, inferring a useful enhancement in wall shear stress, particularly at the mainfoil trailing edge and above the flap.

The effects of employing the AJVGs on the integral shear layer property plots (δ^*, θ and H) are demonstrated at $\alpha=10°$ on Figures 7.8-7.10 and at $\alpha=20°$ on Figures 7.11-7.13. As with the 'local' AJVG flat plate model δ^* and θ are determined at each chordwise location by integrating the spanwise averaged velocity profiles such as those depicted on Figures 7.6 and 7.7.

Predictions of the chordwise displacement thickness growth at $\alpha=10°$ (Figure 7.8) show that employing a counter-rotating AJVG configuration with $V_R=6$ enables suppression of δ^* growth over the entire mainfoil upper surface. Below $V_R=6$ both air-jet configurations fail to usefully suppress δ^* growth when compared to the cleanfoil high lift system. In contrast, momentum thickness predictions at $\alpha=10°$ (Figure 7.9) show that in both air-jet configurations θ is greater than the cleanfoil predictions for all jet-to-freestream velocity ratios. As a consequence, the shape parameter (Figure 7.10) is reduced when utilising a counter-rotating AJVG configuration with $V_R=6$.

Predictions of δ^*, θ and H at $\alpha=20°$ (Figures 7.11-7.13) show that at all jet-to-freestream velocity ratios, the co-rotating AJVGs are unable to suppress boundary layer separation. Figure 7.12a demonstrates a small improvement in θ growth, at $x/c=0.9$ for $V_R\geq3$, when compared to the cleanfoil high lift system. This small θ reduction occurs at a point where the cleanfoil boundary layer is close to separation and the improvement is not significant enough to suppress flow separation (see Figure 7.13a). The only clear evidence of effective boundary layer control at $\alpha=20°$ is demonstrated when utilising the counter-rotating AJVG configuration with $V_R=6$ (Figures 7.11b, 7.12b and 7.13b). In this air-jet configuration, the rate of growth of δ^* and θ is suppressed enough to ensure that the retarded shear layers can withstand the strong adverse pressure gradient.

As discussed above, when the AJVGs promote shear layer mixing, they 'fill out' the velocity profiles in the near wall region, thus increasing the velocity gradient at the surface and hence increase the wall shear stress. Monitoring the wall shear stress on the aerofoil surface downstream of the AJVGs provides us with an effective method to assess the performance of the air-jet configuration. Figures 7.14 and 7.15 illustrate the predicted wall shear stress across the model span on the mainfoil upper surface at $\alpha=10°$ and $20°$ respectively. Data is presented for both co-rotating and counter-rotating AJVG configurations, at four chordwise locations, with $V_R=2$, 3 and 6. The wall shear stress is expressed as a skin-friction enhancement (ΔC_f) that is the difference between the predicted skin friction coefficient obtained at each location with the AJVGs active and inactive. Because the ΔC_f signature across the model span is periodic, the effectiveness of the AJVG can be evaluated at each chordwise location by integrating the ΔC_f profile in the spanwise direction and expressing the value as a figure of merit $I\Delta C_f$ (see Figure 7.16-7.17).

The spanwise skin friction enhancement plots (Figure 7.14 and 7.15) show that predicted shear stress signatures on the mainfoil upper surface are analogous with those observed in the 'local' flat plate model predictions (see Figure 6.1). Regions of high wall shear stress are evident on the downwash side of the vortices and lower wall shear stress on the upwash side of the vortices (Note the reader is looking upstream towards the AJVGs).

At $\alpha=10°$, the ΔC_f plots show that over the majority of the mainfoil span, employing the AJVGs in both configurations yields an increase in the skin friction coefficient above the uncontrolled flow case. Only at a jet velocity ratio, $V_R=2$, is ΔC_f across the model span notably lower than that of the uncontrolled flow case. The plots also indicate that in the relatively weak adverse pressure gradient at $\alpha=10°$, the rate of decay of peak ΔC_f on the mainfoil upper surface is similar for both co-rotating and counter-rotating AJVG configurations. However, the shear stress signatures imply that the paths of the vortex arrays on Figure 7.14 are quite different. In the co-rotating configuration (Figures7.14a, c, e and g) the predicted ΔC_f signature moves laterally

across the model span under the influence of the image vortices in the model surface; whereas, in the counter-rotating configuration, the ΔC_f signature is relatively stationary in its spanwise location, as the image and neighbouring vortex interactions promote convection of the vortices in the direction perpendicular to the aerofoil surface.

At $\alpha=20°$, Figure 7.15 shows that the increased severity of the adverse pressure gradient significantly inhibits the level of skin friction enhancement obtained by activating the AJVGs. In both co-rotating and counter-rotating air-jet configurations, useful ΔC_f enhancements are only achieved by employing a jet-to-freestream velocity ratio of 6. Below $V_R=6$, the results indicate that the air-jets are unable to elevate the wall shear stress, across the majority of the model span, above that of the unblown case.

In the co-rotating AJVG configuration, at subsequent chordwise locations beyond $x/c=0.35$, the skin friction enhancement across the span is much lower that observed in the $\alpha=10°$ predictions. As demonstrated by the velocity vector plots (Figures 7.5) the severity of the adverse pressure gradient at $\alpha=20°$ stretches the vortices in the direction normal to the high lift system surface, limiting the formation of a persistent vortex array. As previously discussed, the inability of the co-rotating AJVGs to generate a persistent vortex array is associated with the 'numerical weakness' of the periodic boundary condition defined in the numerical model and is not representative of the experimental flow field. These findings are further reinforced by the counter-rotating AJVG ΔC_f predictions at $V_R=6$. In this AJVG configuration, the ΔC_f enhancement across the span is shown to decay at approximately the same rate as the $\alpha=10°$ predictions. The imposition of the symmetric boundary conditions on either side of the air-jets, results in the formation of a persistent vortex array that can withstand the strong adverse pressure gradient.

Figures 7.16 and 7.17 show the integrated spanwise skin friction enhancement ($I\Delta C_f$) achieved with the AJVGs active, on the upper surface of the high lift system mainfoil as far along the chord as $x/c=0.9$. At $\alpha=10°$, Figure 7.16 shows that some skin friction

enhancement is achieved when employing jet-to-freestream velocity ratios of 3 or above. However, the chordwise IΔC_f distribution is elevated when V_R is increased from 3 to 6. At α=20°, where the severity of the adverse pressure gradient on the mainfoil upper surface is much greater, Figure 7.17 shows that potentially useful IΔC_f enhancements are only possibly when V_R=6.

Experimental flow field results

All experimental data were obtained with the AJVGs configured in a co-rotating array. Thirteen air-jets span the experimental model, pitched at 45° to the model surface and skewed at 60° to the oncoming freestream, with the jets spaced at the recommended 0.106c apart [see Pearcey 1961, Freestone (1985) and Rao (1988)]. Measurements were made of the surface static pressure distribution on the three components and the momentum deficit in the wake downstream of the high lift system. In contrast to the predicted results obtained with CFX, the experimental results indicate that the beneficial effects of activating the AJVGs at α=20° are relatively small, as at this angle of attack in the experiment the flow field around the multi-component high lift system is attached (see flap trailing-edge pressure coefficient plots on Figure 7.20). To assess the effects of blowing after the onset of flow separation from the flap trailing edge in the experiments (α=28.5° in the cleanfoil case) the pressure distributions around the multi-component high lift system are presented at α=30° as opposed to α=20°. Figures 7.18 and 7.19 show the effects of the AJVGs on the chord surface pressure distributions at respective angles of attack of 10° and 30°. At α=10°, there is marginal improvement in the top surface suction pressure distribution with the air-jets active. As with the CFX-predicted results, there is a slight 'bump' in the pressure distribution just downstream of the AJVG array. The 'bump' is associated with a local increase in the velocity of the flow, in close proximity to the AJVG exit, caused by the jet flux.

The results at α=30° (Figure 7.19) demonstrate that about the cleanfoil, the flow has separated over the entire flap upper surface and upstream of the trailing edge of the mainfoil (perhaps as far forward as x/c=0.6). Employing the air-jets, for all C_μs, $0.014 \leq C_\mu \leq 0.119$ results in recovery of the flow over the flap, substantial elevation in

C_P suction over the mainfoil, and under surface increase in positive C_P over the flap bottom. There is also evidence of increasing suction on the mainfoil upper surface with increasing C_μ. Note that the peak suction on the mainfoil does not increase further for $C_\mu \geq 0.057$.

The effects of the AJVGs on the levels of pressure recovery at the flap trailing-edge is shown on Figure 7.20 for $0 \leq C_\mu \leq 0.119$. At low blowing momentum coefficients ($C_\mu < 0.02$), the onset of stall angle, defined at the point where the flap trailing-edge C_P becomes positive, is delayed by 5°. Employing higher C_μ delays the onset of separation by as much as $\Delta\alpha = 7°$. Maintaining attached flow at these high angles of attack results in much thinner wakes downstream of the high lift system.

An example of the reduction in the wake size is demonstrated at $\alpha = 25°$ on Figure 7.21, for a range of C_μs ($0.0 \leq C_\mu \leq 0.095$). The plot shows the momentum deficit in the wake, one retracted chord length downstream of the high lift system model trailing edge. In the cleanfoil high lift system configuration, the wake has a width of approximately $0.15c$. At $y/c = 0.55$ there is a small region of negative momentum deficit measure in the wake that is most likely the result of the confluent slat and mainfoil wakes rapidly decelerating in the flap adverse pressure gradient leading to shear flow reversal in the high lift system wake. At lower jet momentum blowing coefficients ($0.014 \leq C_\mu \leq 0.042$) the momentum deficit in the wake is relatively unchanged when compared to the cleanfoil case. As the air-jet blowing momentum coefficient increases, the momentum deficit in the wake is further reduced yielding a wake profile drag coefficient (C_{Dp}) up to 30% lower than the cleanfoil measurement. Significantly, there is evidence of a large region of negative momentum deficit in the wake on the $C_\mu = 0.095$ curve between $0.55 < y/c < 0.6$. This region of negative momentum deficit at $C_\mu = 0.095$, is thought to be evidence of the high momentum air-jet flux in wake downstream of the multi-component high lift system. At $C_\mu = 0.95$, it is believed that the air-jet flux punches through the retarded shear layers into the high momentum freestream flow above the mainfoil, hence the vortex array forms above the retarded shear layers. Consequently, the vortex array is unable to convert the energy in high momentum jet flux into enhanced mixing within the retarded shears

172

layers above the mainfoil; so that the high momentum jet flux is still evident downstream of the multi-component high lift system. Similar regions of high momentum air-jet flux were identified in the shear layer studies above the flap upper surface in the experiments by Innes (1995).

The integrated high lift system performance characteristics C_N, C_{Dp} and C_{Mle} are shown on Figures 7.22-7.29. The normal force coefficient (C_N) and leading edge pitching-moment coefficient (C_{Mle}) are determined by integrating the chordwise surface pressure distributions around each component of the multi-element high lift system. Wake profile drag characteristics are determined by integrating the momentum deficit in the high lift system wake, one chord length downstream of the flap trailing edge. It should be noted that the C_{Dp} plots do not include the power requirements of the flow control devices, i.e., C_μ is not added to C_{Dp} to obtain the total drag on the high lift system.

Figure 7.22 shows the influence of the AJVGs on the normal force, wake profile drag and leading edge pitching moment characteristics of the high lift system for $0 \leq C_\mu \leq 0.119$. In the cleanfoil high lift system configuration, stall occurs at $\alpha=28°$, at which point there is divergence in the wake profile drag and leading-edge pitching moment coefficient curves. Activating the AJVGs is shown to yield extensions of the C_N, C_{Dp} and C_{Mle} curves beyond the cleanfoil stall angle attack. Below the cleanfoil stall angle of attack little difference the high lift system C_N and C_{Mle} curve slopes is evident with the jets active and inactive. Some reduction in C_{Dp} is illustrated at $C_\mu=0.057$, but the power requirements of the flow control devices offsets these C_{Dp} improvements.

At lower jet momentum blowing coefficients ($0.014 \leq C_\mu \leq 0.042$) the gradient of the normal force curve slope decreases progressively until at $\alpha=33°$, that is indicative of a long leading-edge separation bubble stall characteristic, Foster (1972). Beyond $\alpha=33°$, the measured C_N dramatically increases. This sudden C_N increase is felt to be the induced effects on the high lift system of the separating flow and the air-jet flux, once the flow over the high lift system has completely broken down (see later discussion of

Figure 7.24). At higher jet-momentum blowing coefficients ($C_\mu \geq 0.057$) the normal force generated by the high lift system increases with angle of attack, until stall occurs at approximately $\alpha = 34°$. Note that over blowing at $C_\mu > 0.057$ does not appear to yield any further increase in the normal force generated by the high lift system.

Figure 7.22 illustrates the effects of activating the AJVGs on the high lift system leading-edge pitching moment characteristics. Employing $0.014 \leq C_\mu \leq 0.042$ results in the C_{Mle} curves levelling off to a value of approximately -1.2 at $\alpha = 33°$ then becoming increasingly negative at stall. The decrease in C_{Mle} at $\alpha > 33°$, shown by the $C_\mu = 0.02$ curve, is attributed to the formation of the large spanwise vortex over the high lift system upper surface, that results in an increased loading on the mainfoil and flap components; and hence reduces the leading-edge pitching moment coefficient. Employing $C_\mu \geq 0.057$ results in an extension of the linear portion of the C_{Mle} curve until $\alpha = 34°$, at which point the leading-edge pitching moment coefficient increases. The increase in C_{Mle} corresponds to the reduced loading on the mainfoil and flap high lift system components, as the flow diverges from the component trailing edges.

Wake profile drag curves on Figure 7.22 indicate that by activating the AJVGs it is possible to suppress the large drag increases (drag divergence) that occur after stall on the cleanfoil high lift system. At the lowest jet momentum blowing coefficient ($C_\mu = 0.014$) the air-jets are unable to suppress drag divergence beyond the cleanfoil stall angle of attack. As C_μ increases, drag divergence is significantly reduced up until an angle of attack of 32° as the boundary layer growth is suppressed. At the highest jet momentum blowing coefficients ($C_\mu = 0.095$ & 0.119) the measured C_{Dp} is visibly reduced below the other measured data up until $\alpha \approx 34°$. The C_{Dp} reduction signifies the momentum addition measured in the wake, corresponding to the high momentum jet flux present in the flow field, downstream of the high lift system (see above discussion on Figure 7.21).

Figure 7.23 shows the total normal force generated on each of the three components of the high lift system and the total normal force generated by the high lift system. The plot shows that the majority of the extra loading generated when the AJVGs are active

is carried by the mainfoil component of the high lift system. By enhancing the mixing within the retarded shear layers above the mainfoil component the adverse effects of boundary layer confluence, increased momentum defect near the wall and hence increased displacement effects on the inviscid flow, are significantly suppressed. Figure 7.23 shows that by blowing at $C_\mu \geq 0.057$, the total normal force generated by the high lift system may be increased by as much as 25%. There is little enhancement of the normal force generated by slat when the AJVGs are active but the measured slat normal force continues to increase linearly with angle of attack up until stall. This is because as flow separation on the flap and mainfoil components is suppressed the slat benefits from the increased circulation around the high lift system. In particular, the slat benefits from the circulation effect defined by Smith (1972), where the slat trailing-edge is placed in a region of appreciably higher velocity and hence the circulation around the slat is increased.

At a jet momentum blowing coefficient of $C_\mu = 0.02$, the normal force curves on Figure 7.23 for the mainfoil and flap components show a sharp increase beyond $\alpha = 33°$. At the same time, there is a sharp decrease in the normal force generated by the slat. These sudden changes in the normal force curve characteristics are thought to be associated with a large spanwise region of re-circulating flow that forms as the boundary layer on the mainfoil upper surface separates. The chordwise pressure distribution plots on Figure 7.24 demonstrate how the region of re-circulating flow increases the normal force generated by the high lift system. The plot shows that the flow over the slat has broken down, as there is no suction peak, significantly reducing the normal force that the component can generate. However, the re-circulating flow above the high lift system mainfoil and flap components induces higher velocities over the majority of the component surfaces, increasing the level of suction.

The effect of blowing momentum coefficient, C_μ, on the incremental maximum normal force, ΔC_{Nmax}, generated by the high lift system with the AJVGs active (referenced to the unblown high lift system at the C_{Nmax}) is demonstrated on Figure 7.25. The plot demonstrates that ΔC_{Nmax} increases from 0 to 0.55 with increasing jet momentum blowing coefficient up until $C_\mu = 0.05$. At subsequent $C_\mu > 0.05$, the ΔC_{Nmax}

values do not vary significantly from C_{Nmax} 0.55 with increasing C_μ, indicating that no further suppression of boundary layer growth results from blowing at higher C_μs. Above $C_\mu=0.09$, ΔC_{Nmax} is shown to increase once more but at a slower rate than that measured for $C_\mu<0.05$. The curve infers that two mechanisms of flow control are at work: separation control and circulation enhancement. Separation control yields the greatest enhancement in ΔC_{Nmax} but the high momentum jet flux influences the normal force generated by the high lift system by inducing higher velocities above the mainfoil upper surface and hence increasing the level of circulation. Additionally, blowing at higher C_μ at a jet pitch angle $\phi=45°$ may result in generation of the vortex array far above the high lift system component surfaces in the freestream flow, as the jet flux punches through the retarded shear layers. As a result of the vortex arrays forming in the high momentum freestream flow; they are unable to significantly influence the mixing within the retarded shear layers near the mainfoil component surface. To enable enhanced mixing within the retarded shear layers, at high C_μ, it may be necessary to reduce the AJVG pitch angle below 45°.

Figure 7.26 shows the variation of incremental normal force per unit C_μ generated by the high lift system plotted against C_μ. The plot enables the effectiveness of the AJVGs to be assessed relative to the power requirements of the flow control system. The normal force enhancement increases almost linearly with increasing C_μ, until C_μ approaches 0.05. At higher C_μ the normal force performance gain per unit C_μ then reduces. In terms of lift generation for the best efficiency of momentum supply, Figure 7.26 demonstrates that C_μ needs to be no greater than 0.05.

The effects of employing the AJVGs on the wake profile drag and normal force/drag polars are shown on Figures 7.27 & 7.28. At $C_\mu \leq 0.042$ the benefits of employing the AJVGs do not become apparent until the flow in the uncontrolled case begins to breakdown, at which point activating the jets suppresses the large drag increases. At $C_\mu=0.057$, the measured wake profile drag is shown to be lower than the uncontrolled case over most of the measured angle of attack range. This reduction of the wake profile drag at $C_\mu=0.057$ is most probably due to the presence of the high momentum jet flux that persists in the wake, one chord length downstream of the high lift system

trailing-edge (as discussed on Figure 7.21). Integrating the momentum deficit across the wake when the high momentum jet flux is evident (see Figure 7.21 at $C_\mu = 0.095$), results in up to a 30% reduction of the measured profile drag, compared to the uncontrolled case. As a consequence, we see the dramatic increase in the high lift system C_N/C_{Dp} polar, particularly at low angles of attack, (Figure 7.28). At higher angles of attack and C_μ, the presence of the high momentum jet flux in the wake is manifested as an extension of the C_N/C_{Dp} polar to the right, i.e., providing lift potential where none existed without C_μ.

By taking into account the power requirements of the flow control devices, we can assess the effective drag of the high lift system with AJVGs active. The effective drag is determined by summing the measured wake profile drag and the jet momentum blowing coefficient, i.e., $C_{Def}=C_{Dp}+C_\mu$. Figure 7.29 shows the normal force per unit effective drag with the AJVGs active and inactive. The plot demonstrates that with the air-jets active, the C_N/C_{Def} performance over the majority of the angle of attack range is considerably lower than that of the uncontrolled high lift system. Once the flow has separated in the uncontrolled case, it is then possible to extend the high lift system-operating envelope by activating the AJVGs. Best normal enhancements with the minimum drag penalty are demonstrated when utilising $C_\mu=0.02$ up to $C_N=3.8$. Beyond this point, C_μ must be increased to extend the high lift system-operating envelope. With this in mind, it is possible to optimise the performance of the AJVG array by controlling C_μ. The green curve on Figure 7.29 gives some indication of how it may be possible to optimise the performance of the AJVG array by dynamically varying C_μ throughout the angle of attack range.

7.3 Summary of results for the high lift system with the air-jets active

The above discussion details the predicted and experimental results of the flow field around a three element high lift system incorporating an array of AJVGs located at x/c=0.14. Predictions of the flow phenomena were obtained with the finite volume flow solver CFX4, incorporating the k-ε turbulence model and utilising wall functions for expeditious computation. Experiments were conducted in City University's T2 low speed wind tunnel at a Reynolds number based on the retracted chord (c=500mm) of $Re_c=1.37\times10^6$ and a freestream Mach number of M=0.12. Throughout the experiments, a range of blowing momentum coefficients was employed with $0.014<C_\mu<0.119$.

Boundary conditions in the computations were made analogous with those walls in the T2 wind tunnel. On either side of the AJVG, periodic or symmetric boundary conditions were enforced to permit the simulation of an array of either co-rotating or counter-rotating AJVGs at jet V_RS of 2, 3 and 6. Results were obtained in the computations for the spanwise mean of the chordwise surface pressure distribution, the surface skin friction enhancement and the spanwise mean of the velocities in the crossflow plane normal to the aerofoil surface. From these measurements, the global performance parameters, C_N, C_f, u/U_e, δ^*, θ and H were determined. Results in the experiment were determined for the chordwise surface pressure distribution and the momentum deficit in the wake downstream of the high lift system. These results supplemented the extensive experimental database initiated by the earlier work of Innes (1995).

The key findings from the investigations are as follows:
• Below $V_R=6$ in the computations, little enhancement of the surface pressure and skin friction distributions are apparent at α=10° and 20°. At both these angles of attack, superior performance, in terms of delaying the onset of flow separation was observed when utilising a counter-rotating array of AJVGs. Unfortunately, due to excessive grid skewness and the presence of large regions of separated flow, convergence difficulties prohibited the analysis of angles of attack greater than 20°.

•   In the computations both co-rotating and counter-rotating air jet configurations increased the mixing within the complex shear layers above the high lift system mainfoil. The generated vortices filled out the u/U_c velocity profiles, demonstrating increased mixing in the confluent shear layers above the mainfoil and enhancing the surface skin friction distribution over the majority of the mainfoil upper surface. As a result, the displacement momentum thicknesses were reduced at the mainfoil trailing edge as well as the magnitude of the confluent boundary layer above the flap.

•   Utilising a near optimal array of AJVGs on the experimental high lift system yields an increase in C_{Nmax} of up to 25%, a linear extension of the leading edge pitching moment curve and a significant delay to the wake profile drag divergence. At all blowing momentum coefficients, the AJVGs are capable of restoring attached flow at angles of attack as high as $\alpha=30°$.

•   Analysis of a range of blowing momentum coefficients for the chosen AJVG geometries demonstrates that optimums exist in terms of the energy supplied to the flow control devices and the maximum attainable normal force. The results show that blowing above $C_\mu=0.057$ ($V_R=4.8$), yields no further enhancement of the normal force generated by this high lift system. However, as observed in the computations, blowing below $C_\mu=0.057$ does result in useful enhancement of the high lift system performance characteristics.

•   Employing the AJVGs yields considerable extension of the C_N/C_{Dp} envelope, particularly at high angles of attack. Nevertheless, it should be noted that the improvements in the wake profile drag values should be adjusted to account for the energy supplied to the flow control devices, i.e., the effective drag of the high lift system is the sum of the wake profile drag and the jet momentum blowing coefficient.

8. Concluding remarks of interactive test regime

The aim of this research was to develop an *interactive* computational and experimental test regime to analyse and optimise an array of air-jet vortex generators (AJVGs) installed in an unswept three-element high lift system. By combining computational results with those from carefully contrived wind tunnel experiments, it is demonstrated that the number of iterative experimental processes required to optimise the flow control devices can be reduced. The success of our *interactive* approach relies on the ability to break the geometrically complex flow field down into simple but meaningful computational and wind tunnel experiments. In this project, the problem is divided into the following four areas: (i) development of a two-dimensional numerical model to adequately represent the three-element high lift system flow field; (ii) development of a 'local' AJVG model, on which to optimise the performance of the vortex generator array, by means of sensitivity studies; (iii) development of a computational, three-dimensional, high lift system model to assess the performance of the optimised air-jet arrays; and (iv), validation of the high lift system computational models using wind tunnel experiments, with and without the AJVGs active.

Two numerical approaches were employed to predict the flow field characteristics. The first, a coupled viscous/inviscid method (VI), was the 2-D streamline based Euler solver, coupled to a two-equation integral boundary layer formulation, via the displacement thickness (MSES of MIT). Provision is made for boundary layer transition with the e^n method. The second, a full Navier-Stokes method (NS), was the finite volume block-structured flow solver, assuming fully turbulent flow and utilising the k-ε turbulence model with wall functions (CFX4 of AEA Technology). Tests with the AJVGs active conducted in areas (ii) and (iii) employed the NS method only.

Wind tunnel tests were conducted on the unswept, three-element high lift system of retracted chord length 500mm at angles of attack: $0°<\alpha<36°$, and jet momentum blowing coefficients $(0.0<C_\mu<0.12)$ in City University's T2 low speed wind tunnel $(Re_c=1.37\times10^6)$. The high lift system, configured in a regularly used take-off setting, was equipped with an array of 13 equi-spaced, co-rotating AJVGs across the span, located at x/c=0.14. Nominally two-dimensional flow conditions were ensured in the

experiments, up to and beyond stall, by air injection through two near tangential slots mounted in the model endplates at respective x/c locations of 0.16 and 0.6.

The key observations from the interactive test regime were:

• Prior to the existence of large regions of separated flow on the three-element high lift system, both VI and NS methods are capable of representing the experimentally observed flow field characteristics. Once substantial flow separation was established, the NS predictions were shown to deviate significantly from the MSES and experimental findings.

• In the computations with the AJVGs active, the NS solver adequately represented the experimentally observed trends in flows where the adverse pressure gradients were weak. Once the severity of the adverse pressure gradient increased, weaknesses in numerical boundary conditions, on either side of the AJVGs, were identified. The inability to adequately define the secondary flows induced by the co-rotating air-jets resulted in the generation of vortices that decayed rapidly downstream.

• Experiments on the three-element high lift system demonstrated the potential of employing the AJVGs to delay the onset of flow separation by up to $\Delta\alpha=7°$, to increase the maximum normal force by 25% above the uncontrolled case; and to delay drag rise to higher angles of attack. The best enhancement of the flow field characteristics was determined with $C_\mu=0.057$, but useful flow control was achieved at values of C_μ as low as 0.014.

In conclusion, employing relatively simple numerical models to analyse and optimise AJVG flow fields, prior to implementation on more complex geometries, has been demonstrated as an effective process. Further improvements in the predictive capabilities of computational models will arise when more adequate provision is made for boundary-layer transition; and if better turbulence modelling techniques can be employed to represent the confluent boundary layers and near-wall flows above the wing component surfaces.

9. Recommendations for future work

The enticing prospect from this research is the suitability of 'air-jet technology' to provide useful performance gains, in terms of lift generation and drag reduction for real world aerofoils and wings. By providing versatile incremental growth of the lift/drag envelope per unit wing area, it is conceivable that we may design a wing for a given lift performance with a reduced starting wing area.

Useful progress has been made through this research to optimise the arrangement of flow control devices for implementation on more complex aerodynamic systems by making use of well-defined simple numerical models. Further progress in the development of efficient AJVG flow control devices may be expected if the current approach is extended to include the following recommendations:

- Reflect the truly interactive nature of this project by feeding the lessons learned from the wind tunnel tests and MSES implementation back into the full Navier-Stokes calculations. Examples would be the implementation of alternative turbulence modelling techniques or even alternative flow solvers.

- Extend the 'local' AJVG flat plate model to include an array of several air-jets to eliminate uncertainties associated with the 'numerically weak' periodic boundary condition definition; on either side of the AJVGs, in weak and strong adverse pressure gradient flows.

- Implement more sophisticated numerical approaches (Direct numerical simulation) to predict the 'local' flow field phenomena such as transition to provide better boundary conditions for the RANS solutions.

- Assess the impact on performance of reducing the energy supplied to the flow control devices by pulsing the AJVGs or reducing the jet exit area, thereby minimising the jet mass flux.

10. References

Adair, D. and Horne, W. C., "Turbulent separated flow over and downstream of a two-element airfoil", Experiments in Fluids, Vol. 7, 1989, pp. 531-541.

AGARD-CP-515, Proceedings of the 71st AGARD FDP Symposium on "High Lift System Aerodynamics", Banff, Alberta, 1992.

Akanni, S. D. and Henry, F. S., "Numerical calculations of airjet vortex generators in turbulent boundary layers", CEAS European Forum on 'High Lift & Separation Control', Paper 16, 1995.

Alderton, J. H.and Wilkes, N. S., "Some applications of new finite difference schemes for fluid flow problems", AEA Industrial Technology, Harwell Lab., Oxfordshire, UK, AERE-R 13234, 1988.

Anderson, W. K. and Bonhaus, D. L., "Navier-Stokes computations and experimental comparisons for multi-element airfoil configurations", AIAA-93-0645, 1993.

Anerson, J. D. Jr., "Computational fluid dynamics", 1st ed., McGraw Hill, 1995.

Arnal, D., Casalis, G,. Reneaux, J. and Cousteix, J., "Laminar-turbulent transition in subsonic boundary layers: research and applications in France", AIAA-97-1905, 1997.

Back, R. F. and Wedderspoon, J. R., "The A320 wing - Designing for commercial success", Aerospace Journal, January 1986, pp. 12-19.

Baldwin, B. and Barth, T., "A one-equation turbulence transport model for high Reynolds number wall-bounded flows", AIAA-91-0610, January 1991.

Baldwin, B. And Lomax, H., "Thin layer approximation and algebraic model for separated turbulent flows", AIAA-88-0520, 1988.

Barbieux, J., "Contribution à l'étudede l'effet de paroi en écoulment plan incompressible", Publ. Sci. Tech. Min. Air France 304, 1955

Bartsch, P., Nitsche, W. and Britsch, M., "Navier-Stokes computations of turbulent flow around high-lift configurations", AGARD-CP-515, Paper 6, 1992.

Batchelor, G. K., "Interference on wings, bodies and airscrews in a closed tunnel of octagonal section", Report ACA-5, Australia, 1944.

Bhateley, I. C. and Bradley, R. G., "A simplified mathematical model for the analysis of multi-element airfoils near stall", AGARD-CP-102, Paper 12, 1972.

Boussinesq, J., "Theory de l'ecolement tourbillant", Mem. Pre. Par. Div. Sav. XXIII, Paris (1877).

Bradshaw, P., Ferriss, D. H. and Atwell, N. P., "Calculation of boundary-layer development using the turbulent energy equation", Journal of Fluid Mechanics, Vol.28, Part 3, 1967, pp.593-616.

Bradshaw, P., "Effects of streamline curvature on turbulent flow", AGARDograph 169, 1973.

Brune, G. W. and Manke, J. W., "Upgraded viscous flow analysis of multielement airfoils", AIAA-78-1224, 1978.

Brune, G. W. And Sikavi, D. A., "Experimental investigation of the confluent boundary layer of a multielement low speed airfoil", AIAA-83-0566, 1983.

Callaghan, J. G. and Beatty, T. D., "A theoretical method for the analysis and design of multielement airfoils", J. Aircraft, Vol. 9, No. 12, 1972, pp. 844-848.

Cebeci, T. And Smith, A. M. O., "A finite difference solution of the incompressible boundary-layer equations by an eddy-viscosity concept", Computation of Turbulent Boundary Layers, AFOSR-IFP-Stanford Conference, Vol. 1, Stanford University Press, Stanford, California, 1968, pp. 346-356.

CFX 4 User Manual, "CFX 4 Release 4.2", CFDS, AEA Industrial Technology, Harwell Lab., Oxfordshire, UK, December 1997.

Chin, V., Peters, D., Spaid, F. and McGhee, R., "Flow measurements about a multi-element airfoil at high Reynolds numbers", AIAA-93-3137, 1993.

Clarke, D. K., Hassam, H.A. and Salas, M. D., "Euler calculations for multi-element airfoils using Cartesian grids", AIAA-85-0291, 1985.

Compton, D. A. and Johnston, J. P., "Streamwise vortex production by pitched and skewed jets in a turbulent boundary layer", AIAA Journal, Vol. 30, No. 3, March 1992.

Drela, M., "Newton solution of coupled viscous/inviscid multielement airfoil flows", AIAA-90-1470, 1990.

Elfstrom, G. M., Kostopoulos, C., Peake, D. J. and Fisher, D. F., "The obstacle block as a device to measure turbulent skin friction in compressible flow", AIAA-82-0589, 1982.

Eriksson, L. E., "Generation of boundary-conforming grids around wing-body configurations using transfinite interpolation", AIAA Journal, Vol. 20, No. 10, 1982, pp.1313-1320.

Falkner, V. M., and Skan, S.W., "Some approximate solutions of the boundary layer equations", Phil. Mag., 12, p. 865; ARC R & M 1314 (1930).

Fejtek, I., "Summary of code validation results for a multiple element airfoil test case", AIAA-97-1932, June-July 1997.

Ferziger, J. H. and Peric, M., "Computational methods for fluid dynamics", Springer Verlag, Berlin 1996.

Foster, D.N., Irwin, H.P.A.H. and Williams, B.R., "The two-dimensional flow around a slotted flap", ARC R&M 3681, 1970.

Foster, D.N., "The flow around wing sections with high lift devices", AIAA-71-0096, 1971.

Foster, D.N., "The low-speed stalling of wings with high lift devices", AGARD-CP-102, Paper 11, 1972.

Freestone, M. M., "Preliminary tests at low speed on vorticity produced by air-jet vortex generators", RM 85/1 City University, London, 1985.

Freitas, C. J., "Perspective: Selected benchmarks from commercial CFD codes", Transactions of the ASME, Journal of Fluids Engineering, Vol. 117, pp. 208-218, June 1995.

Garner, H. C., Rogers, E. W. E., Acum, W. E. A. and Maskell, E. C., "Subsonic wind tunnel wall corrections", AGARDograph 109, October 1966.

Glauert, H., "Wind tunnel interference on wings, bodies and airscrews", ARC R & M 1566, 1933.

Gleyzes, C., Cousteix, Jr. and Bonnet, J. L., "Theoretical and experimental study of low Reynolds number transitional separation bubbles", Presented at the conference on 'Low Reynolds Number Airfoil Aerodynamics', University of Notre Dame, Notre Dame, IN, 1985.

Godin, P., Zingg, D. W. and Nelson, T. E., "High lift aerodynamic computations with one- and two-equation turbulence models", AIAA Journal, Vol. 35, No. 2, February 1997.

Goldstein, S., "Two-dimensional wind tunnel interference", ARC R & M 1902, 1942.

Goradia, S. H., and Lyman, V., "Laminar stall prediction and estimation of C_{Lmax}", Journal of Aircraft, Vol.11, No. 9, September 1974.

Gordon, W. J. and Hall, C. A., "Construction of curvilinear co-ordinate systems and applications to mesh generation", Int. Journal for Numerical Methods in Engineering, Vol. 7, 1973, pp.461-477.

Green, J. E., Weeks, D. J. And Brooman, J. W. F., "Predictions of turbulent boundary layers and wakes in compressible flow by a lag-entrainment method", RAE TR 72231, January 1973.

Hall, I.M. and Suddhoo, A., "Inviscid compressible flow past a multi-element aerofoil", AGARD-CP-365, Paper 5, 1984.

Handley Page, F., "The Handley Page wing", Aeronautical Journal, June 1921, p263.

Henry, F. S. and Pearcey, H. H., "Numerical model of boundary layer control using airjet generated vortices", AIAA Journal, Vol. 32, No. 12, 1994, pp. 2415-2425.

Hess, J.L. and Smith, A.M.O., "Calculation of potential flow about arbitrary bodies", Progress in Aeronautical Sciences, Vol. 8, Pergamon Press, New York, 1966.

Innes, F., "An experimental investigation into the use of vortex generators to improve the performance of a high lift system", PhD Thesis, City University, 1995.

Innes, F., Pearcey, H. H. and Sykes, D. M., "Improvements in the performance of a three element high lift system by the application of airjet vortex generators", Aeronautical Journal, August/September 1995, pp. 265-274.

Jacob, K. and Steinbach, D., "A method for prediction of lift for multi-element airfoil systems with separation", AGARD-CP-143, Paper 12, 1974.

Jasper, D. W., Agrawal, S. and Robinson, B. A., "Navier-Stokes calculations of multi-element airfoils using a chimera-based solver", AGARD-CP-515, Paper 8, 1993.

Johnston, J. P. and Nishi, M., "Vortex generator jets - a means for passive and active control of boundary layer separation", AIAA-89-0564, 1989.

Jones, B. M., "Measurement of profile drag by the pitot-traverse method", Report & Memorandum of the Aeronautical Research Council, London 1936.

King, D.A. and Williams, B.R., "Developments in computational methods for high lift aerodynamics", Aeronautical Journal, Aug/Sept, 1988, pp. 265-289.

Küpper, C., "A study of the application of air-jet vortex generators to intake ducts", PhD Thesis, City University, London, 1999.

Lachmann, G. V., "Die unterteilte Profilform", Flugsport Vol 1, 1921, pp207-208.

Launder, B. E. and Spalding, D. B., "The numerical computation of turbulent flow", Computational Methods in Applied Mechanics and Engineering, Vol. 3, 1974, pp. 269-289.

Launder, B. E., Reece, G. J. and Rodi, W., "Progress in the development of Reynolds stress turbulent closure", Journal of Fluid Mechanics, Vol. 86, 1975, pp.537-566.

Le Balleur, J. C., "Strong matching method for computing transonic viscous flows including wakes and separations on lifting aerofoils", La Recherche Aérospatiale, English Ed., No. 1981-1983, pp. 21-45.

Leonard, B. P., "A stable and accurate convective modelling procedure based on quadratic upstream interpolation", Computational Methods in Applied Mechanical Engineering, Vol. 19, 1979, pp.59-98.

Lewington, N. P., Henry, F. S., Peake, D. J. and Singh, C., "Numerical and experimental investigations of air-jet vortex generators in streamwise pressure gradients", Aerodynamics Conference, Royal Aeronautical Society, Paper 18, 2000.

Lewington, N. P., Peake, D. J., Henry, F. S., Kokkalis, A. and Perry, J. "The application of air-jet vortex generators to control the flow on helicopter rotor blades", 26th European Rotorcraft Forum, The Hague, Paper 39, 2000.

Lindblad, I. A. A. and De Cock, K. M. J., "CFD prediction of maximum lift of a 2D high lift configuration", AIAA-99-3180, 1999.

Liandrat, J., Aupoix, B. and Cousteix, J., "Calculation of longitudinal vortices imbedded in a turbulent boundary layer", Turbulent Shear Flows 5, Springer-Verlag, Berlin Heidelberg, 1987.

Ljunström, B. L. G., "Experimental high lift optimization of multiple element airfoils", AGARD-CP-143, Paper 13, 1974.

Lock, C. N. H., "The interference of a wind tunnel on a symmetrical body", ARC R & M 1275, 1929.

Lock, R. C. and Williams, B. R., "Viscous-inviscid interactions in external aerodynamics", Progress in Aerospace Sciences, Vol. 24, 1987, pp. 51-171.

Lorentzen, L. and Lindblad, I. A. A., "Application of two-equation and EARSM turbulence models to high lift aerodynamics", AIAA-99-3181, 1999.

McRae, D. M., "Aerodynamics of mechanical high-lift devices", AGARD-LS-43, Paper 1, 1971.

Menter, F. R., "Zonal two-equation k-ω turbulence models for aerodynamic flows", AIAA Journal, Vol. 30, No. 8, August 1992, pp. 2066-2072.

Metha, R. D., Shabaka, I. M. M. A. and Bradshaw, P., "Longitudinal vortices imbedded in turbulent boundary layers", AIAA-83-0378, January 1983.

Moir, I. R. M., "Measurements on a two-dimensional aerofoil with high-lift devices", AGARD-AR-303 (Case No. A2), August 1994.

Nakayama, A., Kreplin, H. P. and Morgan, H. L., "Experimental investigation of flowfield about a multi-element airfoil", AIAA Journal, Vol. 28, No. 1, 1990.

Nash, J. F. And Hicks, S. G., "An integral method including the effects of upstream history on the turbulent shear stress", Computation of Turbulent Boundary Layers, AFOSR-IFP-Stanford Conference, Stanford University Press, Stanford, California, 1968.

Nelson, T. E., Godin, P., De Rango, S. and Zingg, D. W., "Flow computations for a three-element airfoil system", Canadian Aeronautics and Space Journal, Vol. 45, No. 2, June 1999.

Nituch, M. J., "The use of congruent obstacle blocks for the indirect measurement of turbulent skin friction on smooth surfaces", M. Eng. Thesis, Carleton Univ., Ottawa, Canada, 1972.

Oliver, A. G., "Air jet vortex generators for wind turbines", PhD Thesis, City University, London, July 1999.

Oskam, B., "Transonic panel method for the full potential equation applied to multi-component aerofoils", AIAA-83-1855, 1983.

Patanker, S. V., and Spalding, D. B., "A calculation procedure for heat, mass and momentum transfer in three-dimensional parabolic flows", Int. J. Heat Mass Transfer, Vol. 15, 1972, pp. 1787-1806.

Pauley, W. R. and Eaton, J. K., "Experimental study of the development of longitudinal vortex pairs imbedded in a turbulent boundary layer", AIAA Journal, Vol. 26, No. 7, July 1988, pp. 816-823.

Peake, D. J., Henry, F. S. and Pearcey, H. H., "Viscous flow control with air-jet vortex generators", AIAA-99-3175, 1999.

Pearcey, H. H., "Shock induced separation and its prevention", Boundary Layer & Flow Control, Vol. 2, Pergammon Press, New York, 1961, pp. 1170-1344.

Pearcey, H. H., Rao, K. and Sykes, D. M., "Inclined airjets used as vortex generators to suppress shock-induced separation", AGARD-CP-534, Paper 40, 1993.

Rao, K., "Use of air-jet vortex generators to control shock induced boundary layer separation", PhD Thesis, City University, London, 1988.

Rhie, C. M. and Chow, W. L. A., "Numerical study of the turbulent flow past an airfoil with trailing edge separation", AIAA Journal, Vol. 21, 1983, pp.1525-1532.

Rogers, S. E., Wiltberger, N. L. and Kwak, D., "Efficient simulation of incompressible viscous flow over multi-element airfoils", AIAA-92-0405, 1992.

Rogers, S. E., Menter, F., Durbin, P. A. and Mansour, N. N., "A comparison of turbulence models in computing multi-element flows", AIAA-94-0291, 1994.

Rotta, J., "Turbulent boundary layer calculation with the integral dissipation method", Computation of Turbulent Boundary Layers, AFOSR-IFP-Stanford Conference, Vol. 1, Stanford University Press, Stanford, California, 1968, pp. 171-181.

Sankaran, L. and Russell, D. A., "A numerical study of longitudinal vortex interaction with a boundary layer", AIAA-90-1630, 1990.

Schlichting, H., "Boundary layer theory", 7th Edition, McGraw Hill, 1979.

Selby, G. V., Lin, J. C. and Howard, F. G., "Control of low-speed turbulent separated flow using jet vortex generators", Experiments in Fluids, Vol. 12, 1992, pp. 394-400.

Shabaka, I. M. M. A., Metha, R. D. and Bradshaw, P. "Longitudinal vortices imbedded in turbulent boundary layers. Part 1. Single vortex", Journal of Fluid Mechanics, Vol. 155, 1985, pp. 37-57.

Shevell, R. G., "Fundamentals of flight", Prentice Hall, 1989.

Smith, A.M.O., "Transition, pressure gradient, and stability theory", Proceedings of the 9th International Congress of Applied Mechanics, Vol. 4, 1956, p 234.

Smith, A.M.O., "Aerodynamics of high-lift airfoil systems", AGARD-CP-102, Paper 10, 1972.

Smits, A. J., Young, S. B. T. and Bradshaw, P., "The effect of short regions of high surface curvature on turbulent boundary layers", Journal of Fluid Mechanics, Vol. 94, part 2, 1979, pp. 209-242.

Spalart, P. R. and Allmaras, S. R., "A one-equation turbulence model for aerodynamic flows", AIAA-92-0439, 1992.

Stevens, W. A, Goradia, S. H. And Braden, J. A., "Mathematical model for the two-dimensional multi-component aerofoils in viscous flow", NASA CR-1843, 1971.

Taylor, G. I., "The force acting on a body placed in a curved and converging stream of fluid", ARC R & M 1166, 1928.

Tennekes, H. and Lumley, J. L., "A first course in turbulence", MIT-Press, Cambridge, Mass., 1972.

Thomas, F. O., Nelson, R. C. and Liu, X., "Experimental investigation of the confluent boundary layer on a high lift system", AIAA Journal, Vol. 38, No. 6, June 2000.

Thompson, J. S., "Present methods of applying blockage corrections in a closed rectangular high speed wind tunnel", ARC Report 11, 385, 1948 (Unpublished).

Thwaites, B., "Incompressible aerodynamics", Fluid motion memoirs, Clarenden Press, Oxford, 1960.

Truckenbrodt, E., "Ein quadraturverfahren zur berechnung der laminaren ana turbulenten reibungsschicht bei ebener und rotationssymmertrischer strömung", NASA TM 1379, 1955.

Valarezo, W. O. and Mavriplis, D. J., "Navier-Stokes applications to high-lift airfoil analysis", AIAA-93-3534, 1993.

Van Doormal, J. P. and Raithby, G. D., "Enhancements of the SIMPLE method for predicting incompressible fluid flows", Numerical Heat Transfer, Vol. 7, 1984,

Wallis, R. A., "The use of airjets for boundary layer control", Aeronautical Research Laboratories, Australia, Aero. note no. 110, 1952.

Wallis, R. A., "A preliminary note on a modified type of air jet for boundary layer control", Aeronautical Research Council, CP No. 513, 1960.

Westphal, R. V., Eaton, J. K. and Pauley, W. R., "Interaction between a vortex and a turbulent boundary layer in a streamwise pressure gradient", Turbulent Shear Flows 5, Springer-Verlag, New York, 1987, pp. 266-277.

Whitfield, D. L., "Integral solution of compressible turbulent boundary layers using improved velocity profiles", USAF Arnold Air Force Station, AEDC-TR-78-42, 1978.

Wilcox, D. C., "Multiscale model for turbulent flows", AIAA Journal, Vol. 26, No. 11, 1988, pp. 1311-1320.

Woodward, D. S. and Lean, D. E., "Where is high-lift today?-A review of past UK research programme", AGARD-CP-515, Paper 1, 1993.

Ying, S. X., "High lift: Challenges and directions for CFD", Proceedings of the Northwestern Polytechnical University/AIAA Atmospheric Flight Mechanics Conference, Northwestern Polytechnical University, Xian, PRC, 1996, pp. 164-177.

Ying, S. X., Spaid, F. W., McGinley, C. B. and Rumsey, C. L., "Investigation of confluent boundary layers in high-lift flows", AIAA-98-2622, 1998.

Young, A. D., "Boundary layers", BSP Professional publications, 1989.

Zhang, X., "Interaction between a turbulent boundary layer and elliptic and rectangular jets", 2nd International Conference on Turbulence Modelling, Florence, Italy, June 1993.

Zhang, X., "Computational analysis of co- and contra-rotating streamwise vortices in a turbulent boundary layer", AIAA-93-3035, 1993.

Appendix A: Two-dimensional high lift system results

Figures 5.7 to 5.25 inclusive
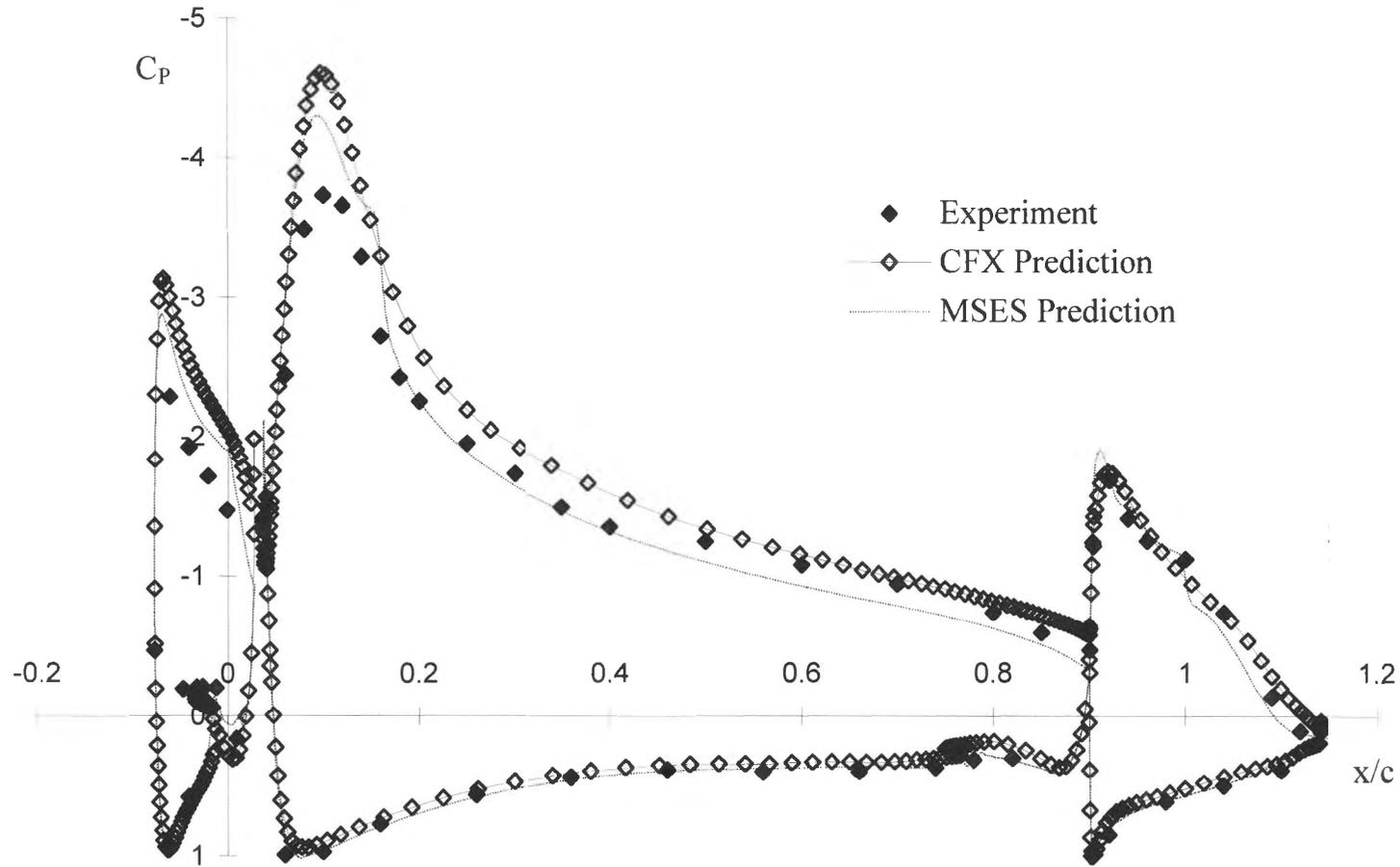
Figure 5.7: Predicted and experimental chordwise surface pressure distributions at $\alpha=10°$, $C_\mu=0$, $Re_c=1.37\times10^6$, $M_\infty=0.13$
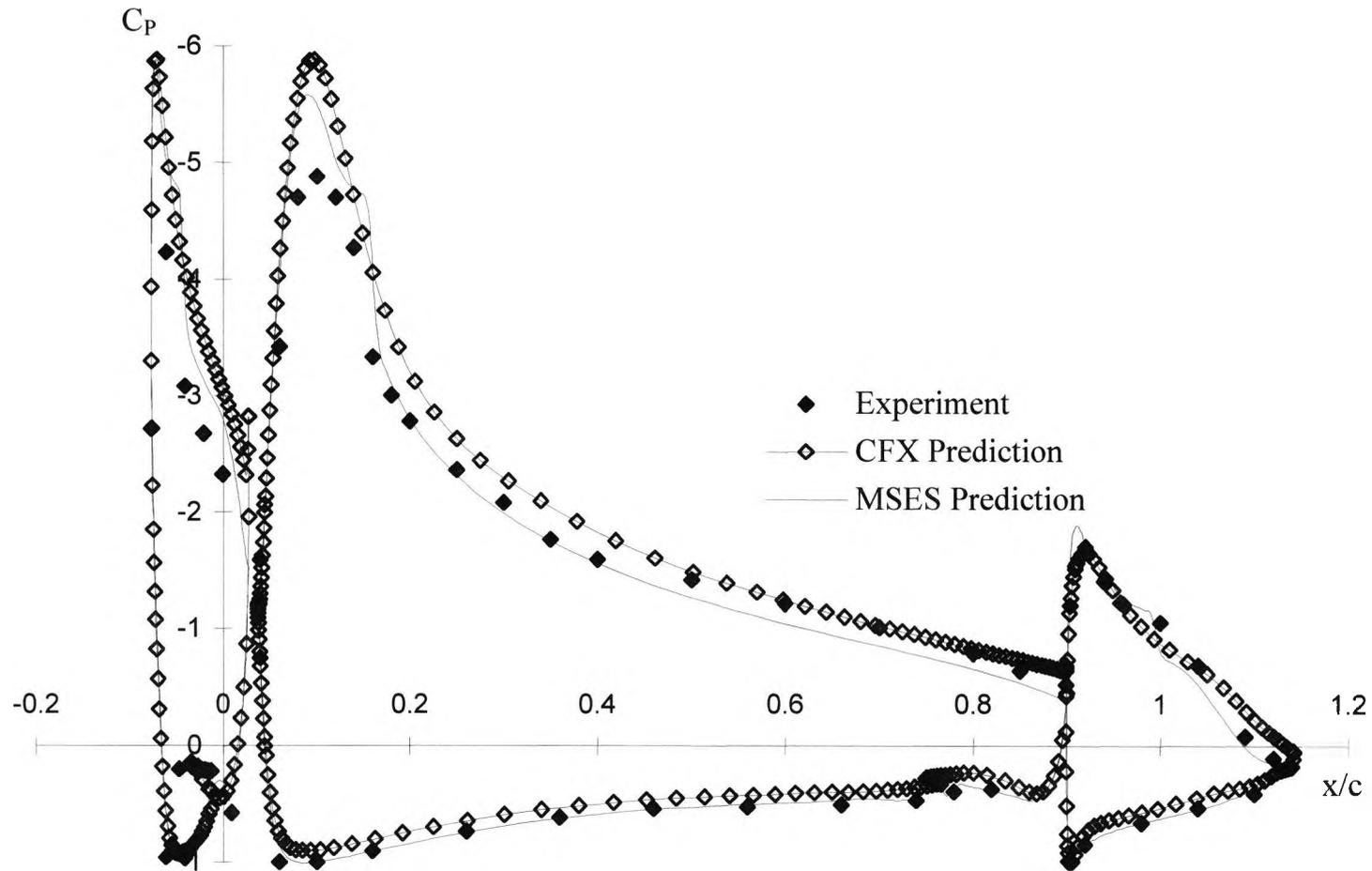
Figure 5.8: Predicted and experimental chordwise surface pressure distributions at $\alpha=15°$, $C_\mu=0$, $Re_c=1.37\times10^6$. $M_\infty=0.13$

Note: Change of CP scale on Figures 5.7, 5.8 and 5.9

- ◆ Experiment
- ◇ CFX Prediction
- MSES Prediction
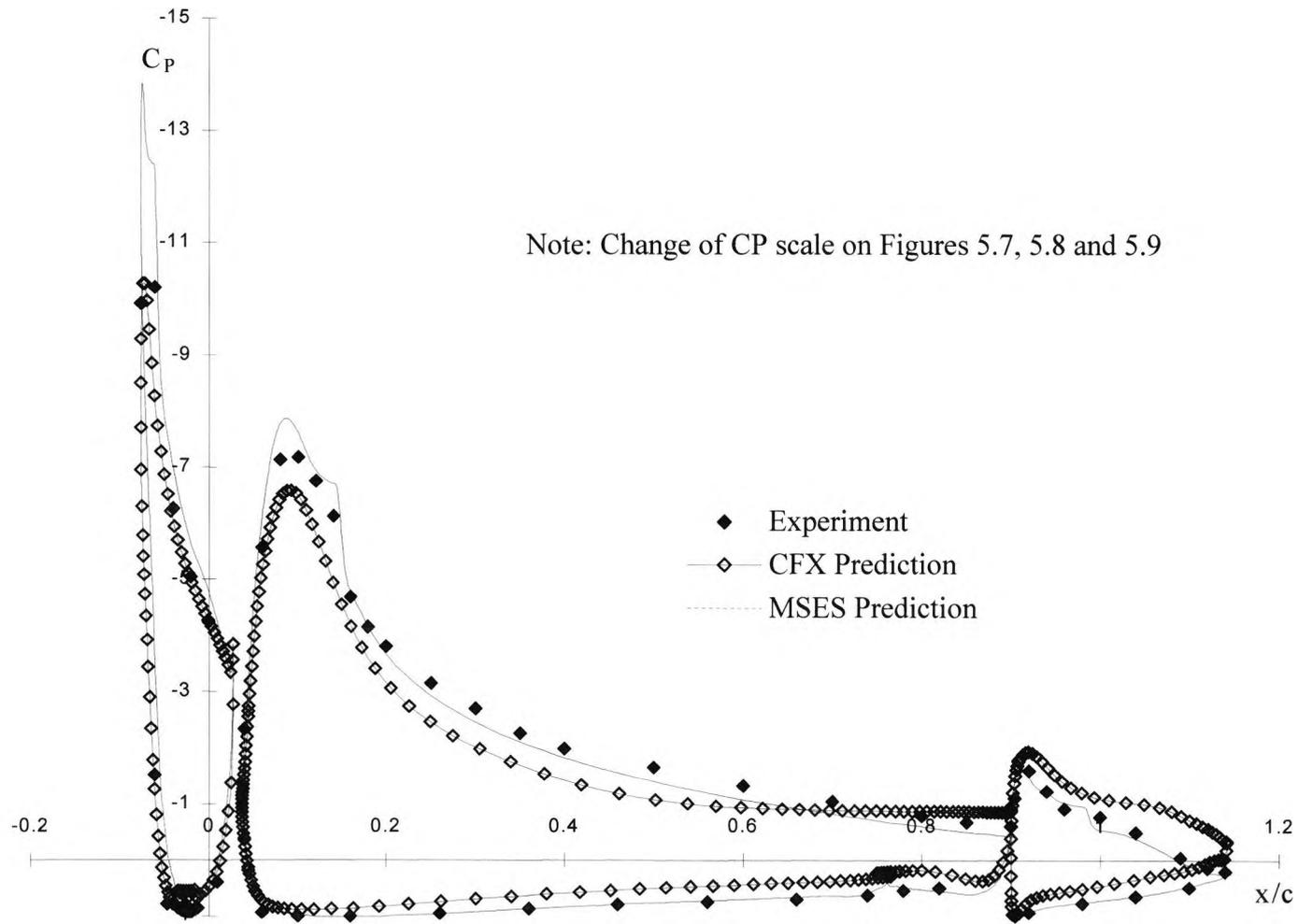
Figure 5.9: Predicted and experimental chordwise surface pressure distributions at $\alpha=25°$, $C_\mu=0$, $Re_c=1.37\times10^6$, $M_\infty=0.13$
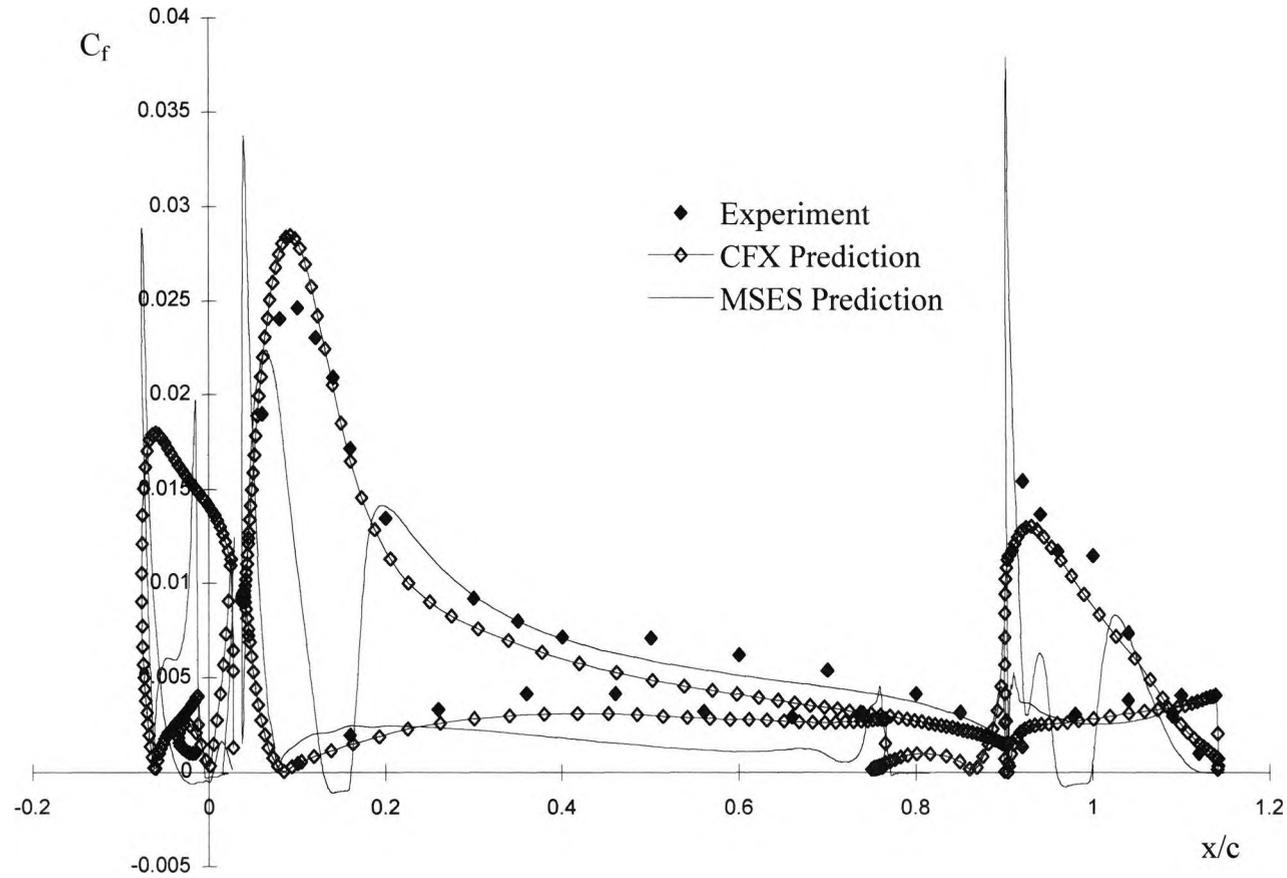
Figure 5.10: Predicted and experimental chordwise surface skin friction distributions at $\alpha=10°$, $C_\mu=0$, $Re_c=1.37\times10^6$, $M_\infty=0.13$
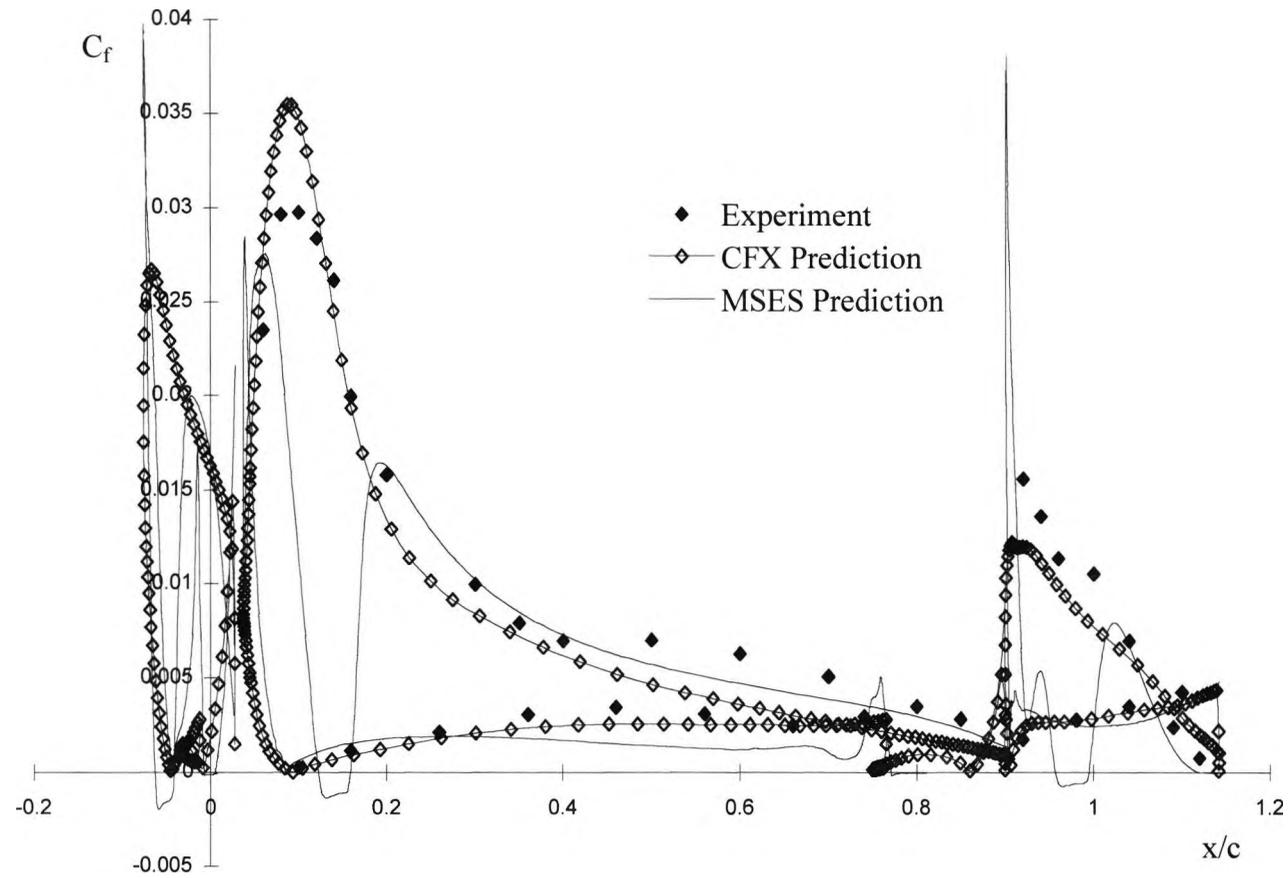
Figure 5.11: Predicted and experimental chordwise surface skin friction distributions at $\alpha=15°$, $C_\mu=0$, $Re_c=1.37\times10^6$, $M_\infty=0.13$
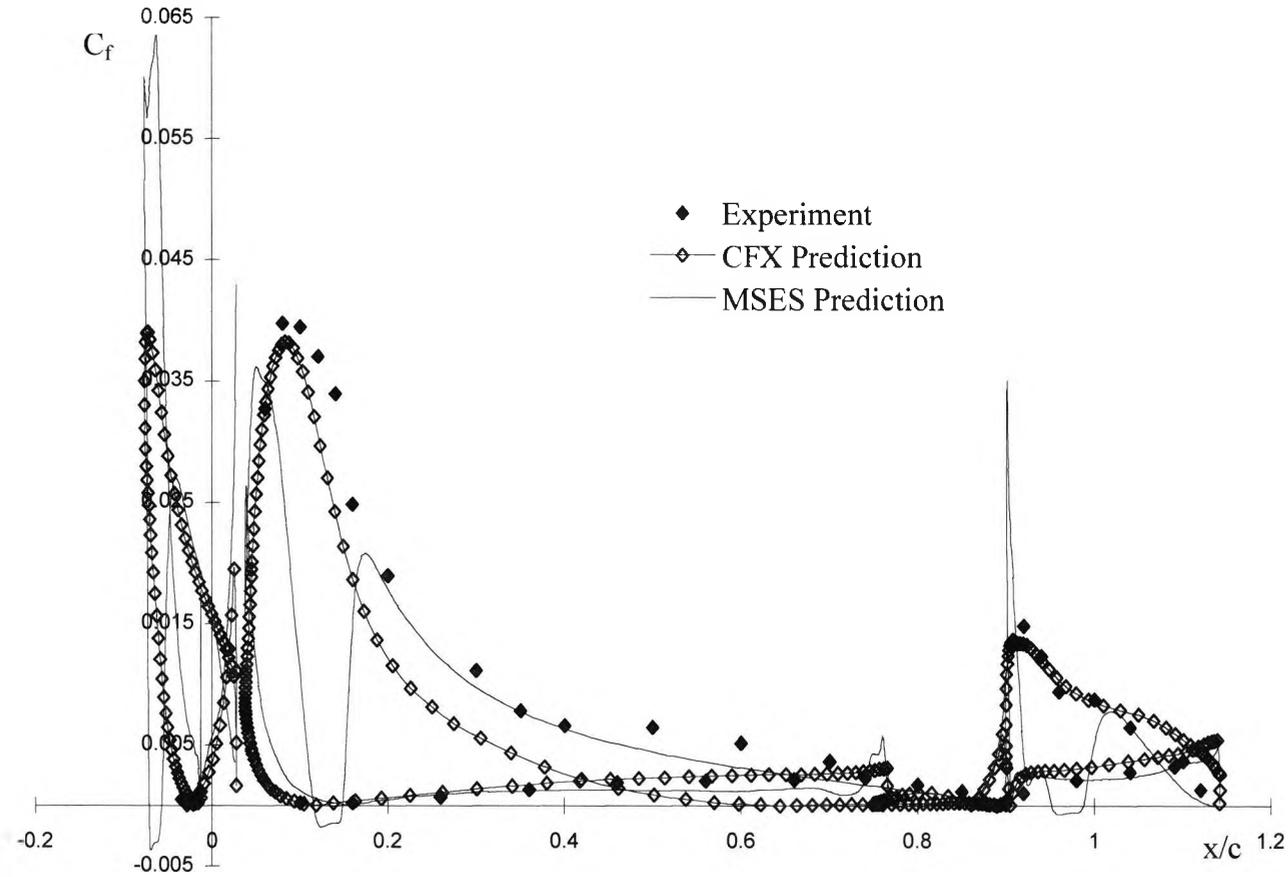
Figure 5.12: Predicted and experimental chordwise surface skin friction distributions at $\alpha=25°$, $C_\mu=0$, $Re_c=1.37\times10^6$, $M_\infty=0.13$
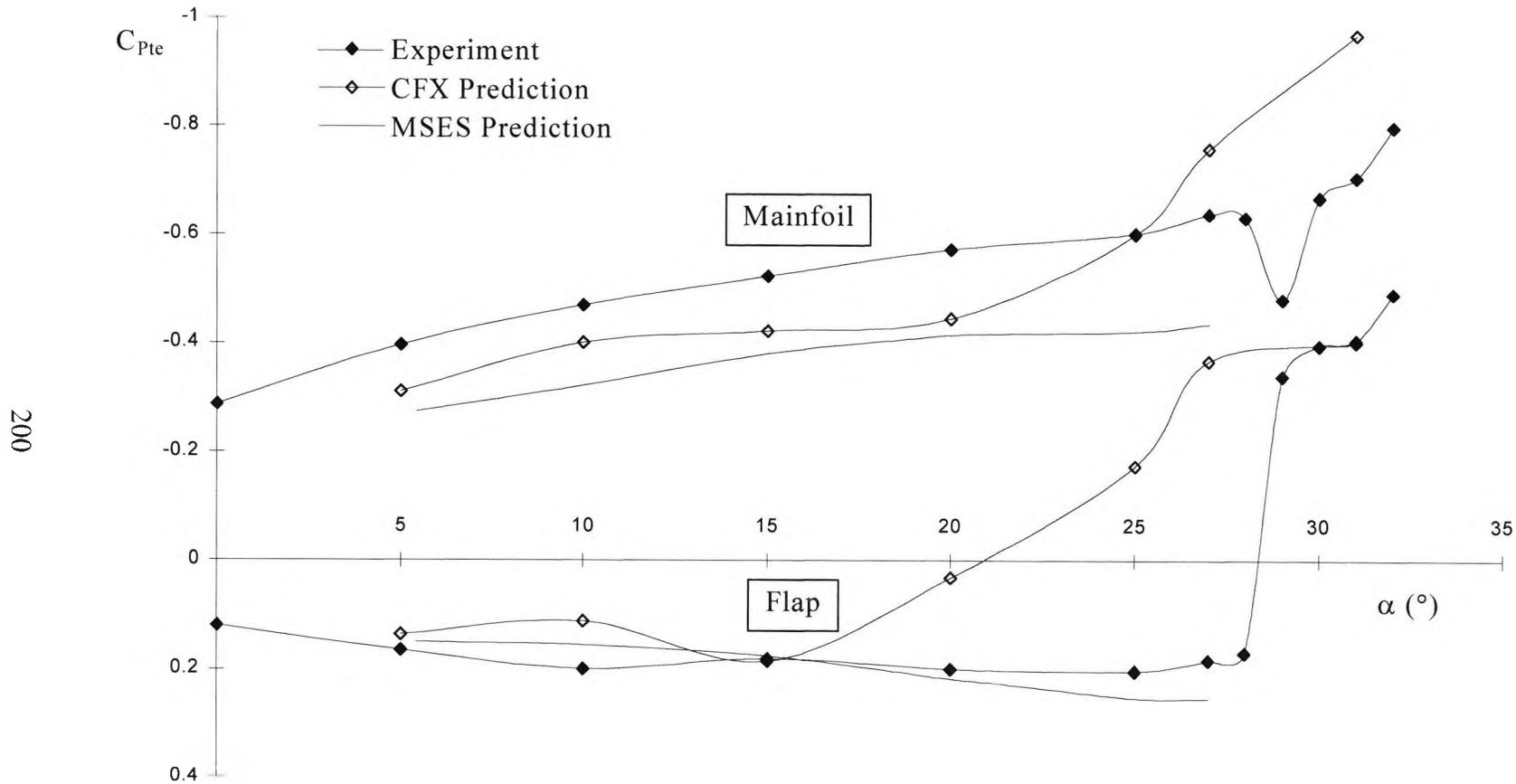
Figure 5.13: Predicted and experimental trailing edge pressure coefficient variation with angle of attack, C_μ =0, Re_c=1.37×10⁶, M_∞=0.13
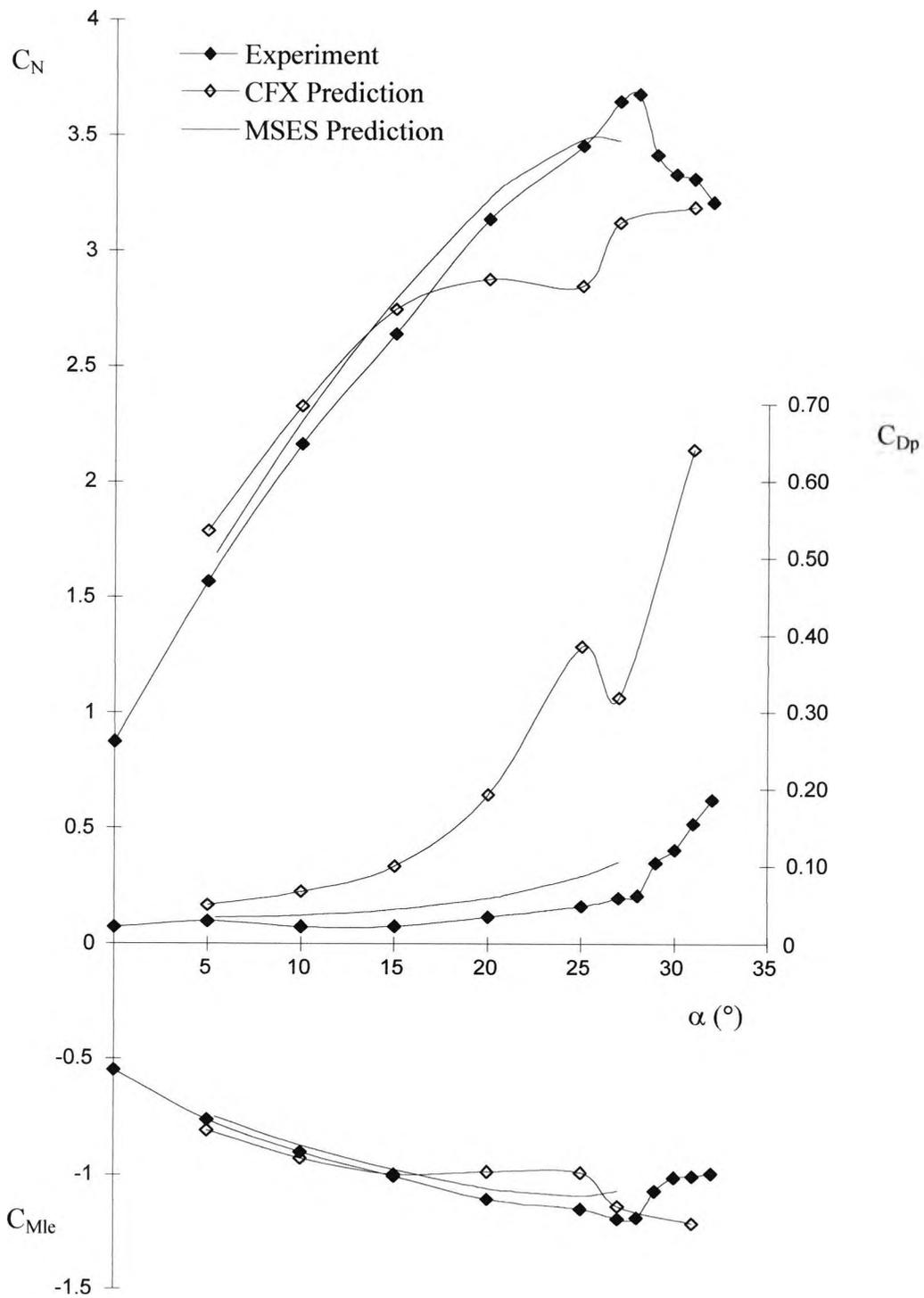
Figure 5.14: High lift system normal force, wake profile drag and leading-edge pitching moment coefficient variation with angle of attack, $C_\mu=0$, $Re_c=1.37\times10^6$, $M_\infty=0.13$

201
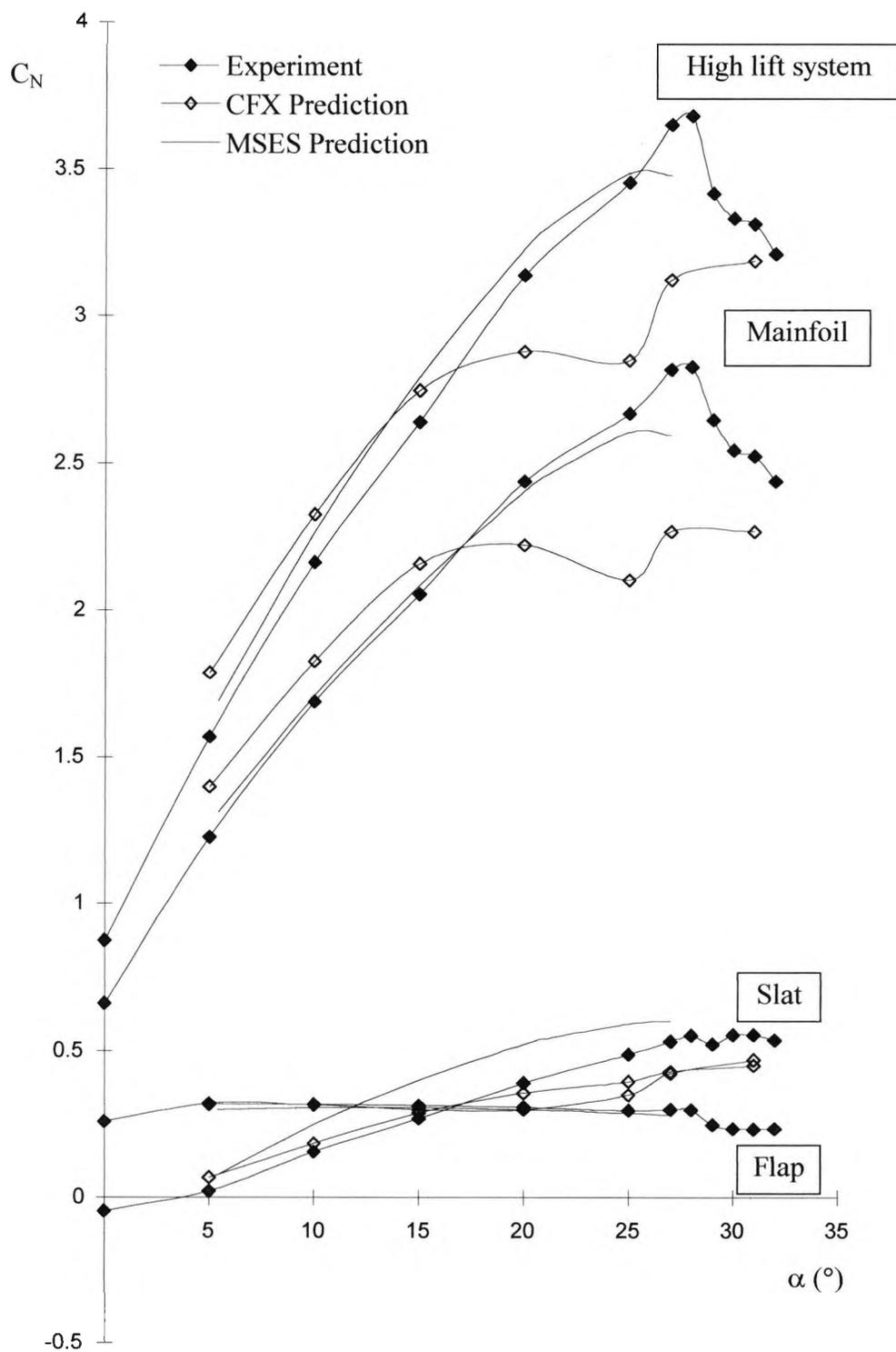
Figure 5.15: Predicted and experimental high lift system component normal force coefficient variation with angle of attack, $C_\mu = 0$, $Re_c = 1.37 \times 10^6$, $M_\infty = 0.13$
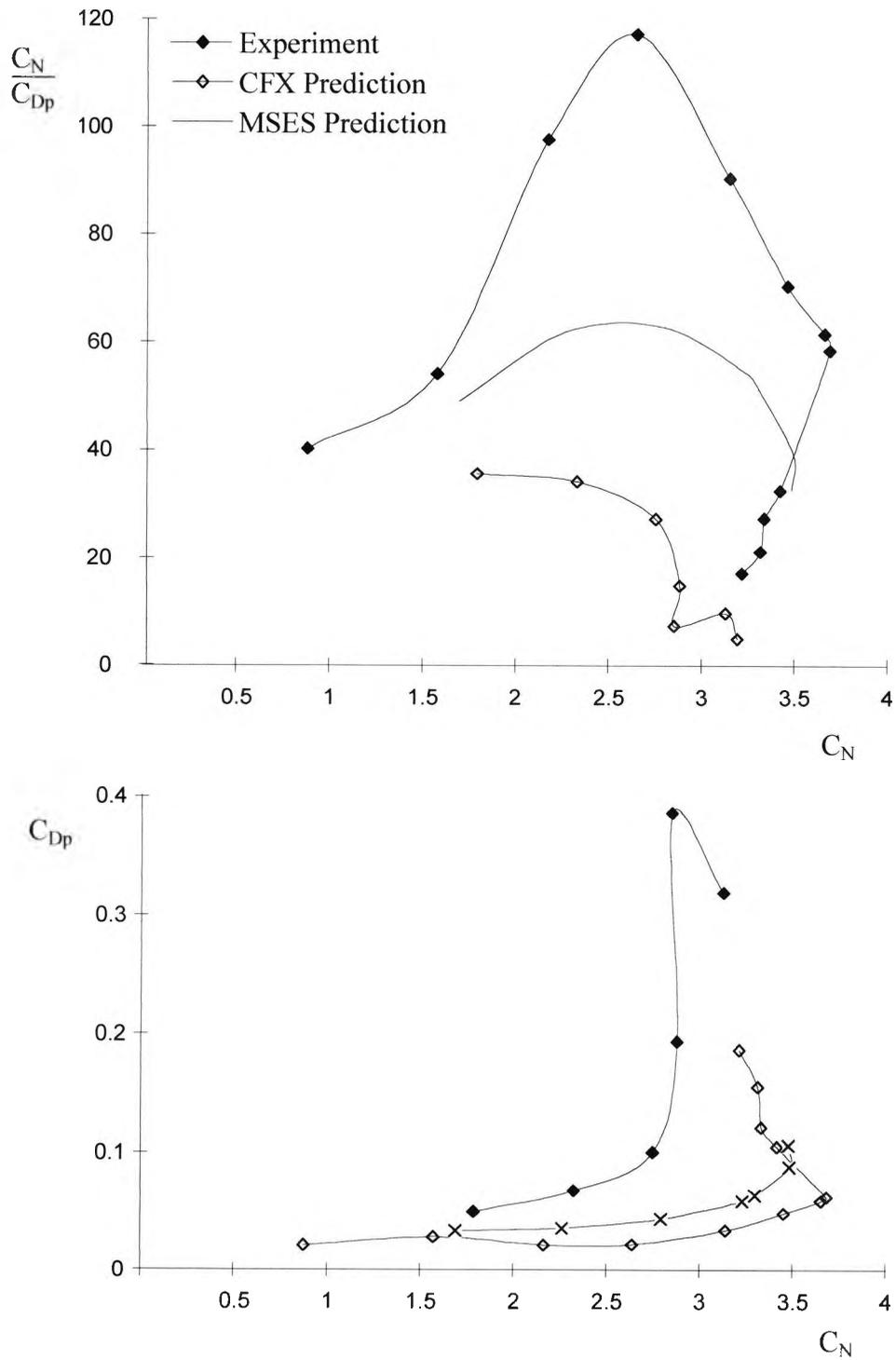
Figure 5.16: Predicted and experimental C_N/C_{Dp} and wake profile drag polars, $C_\mu =0$, $Re_c=1.37\times10^6$, $M_\infty=0.13$
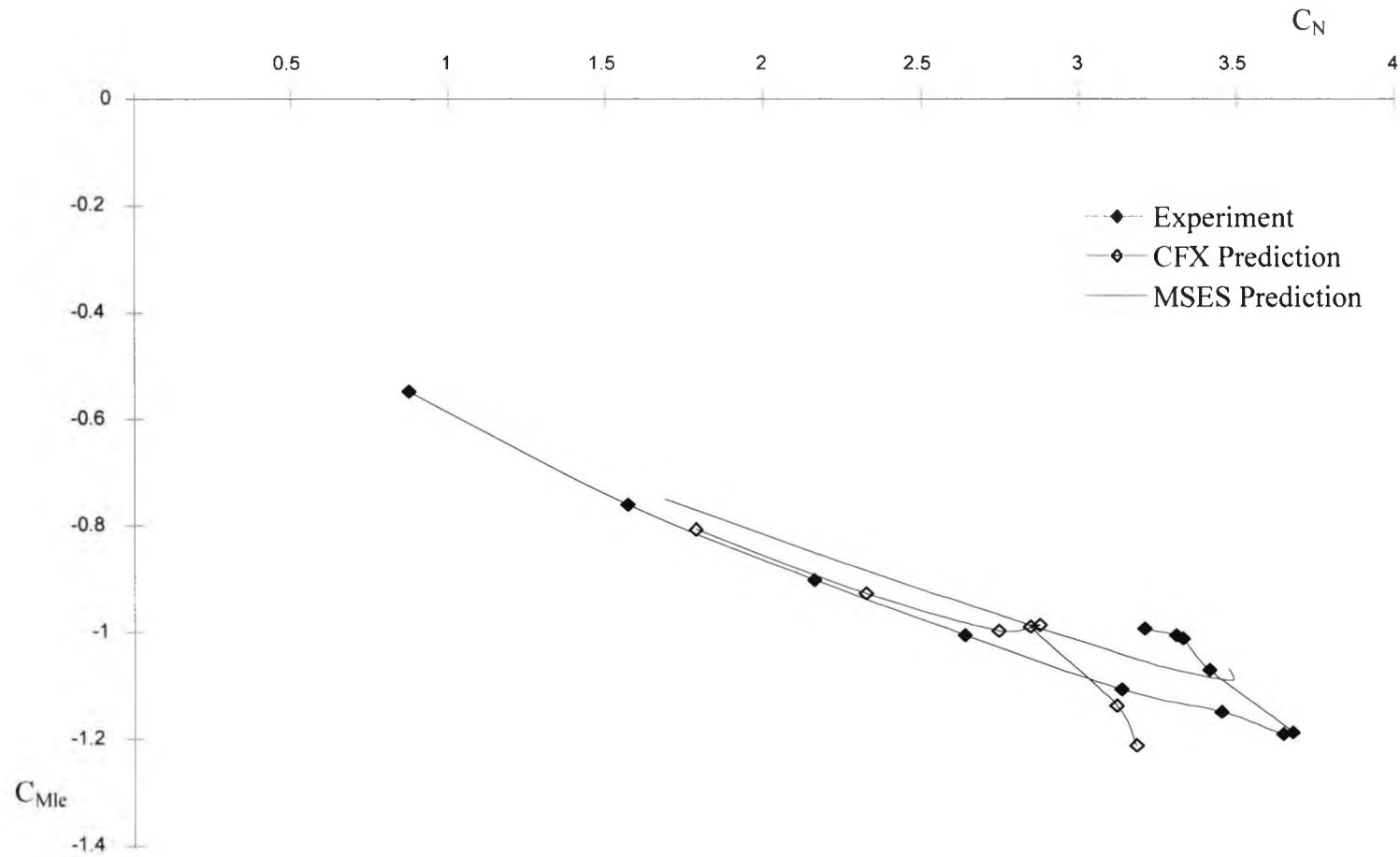
Figure 5.17: Predicted and experimental leading-edge pitching moment coefficient variation with C_N, $C_\mu = 0$, $Re_c = 1.37 \times 10^6$, $M_\infty = 0.13$
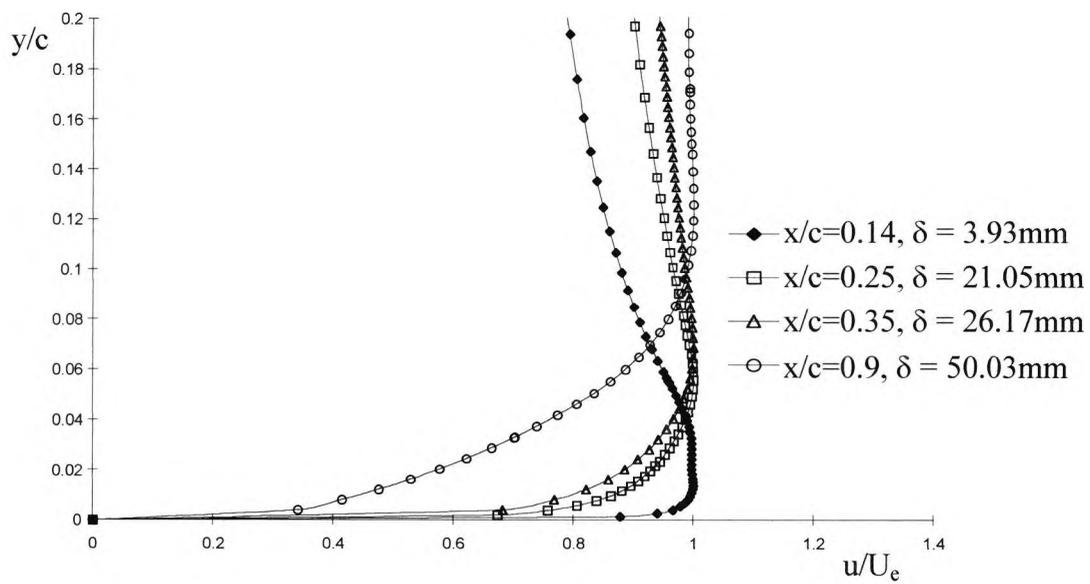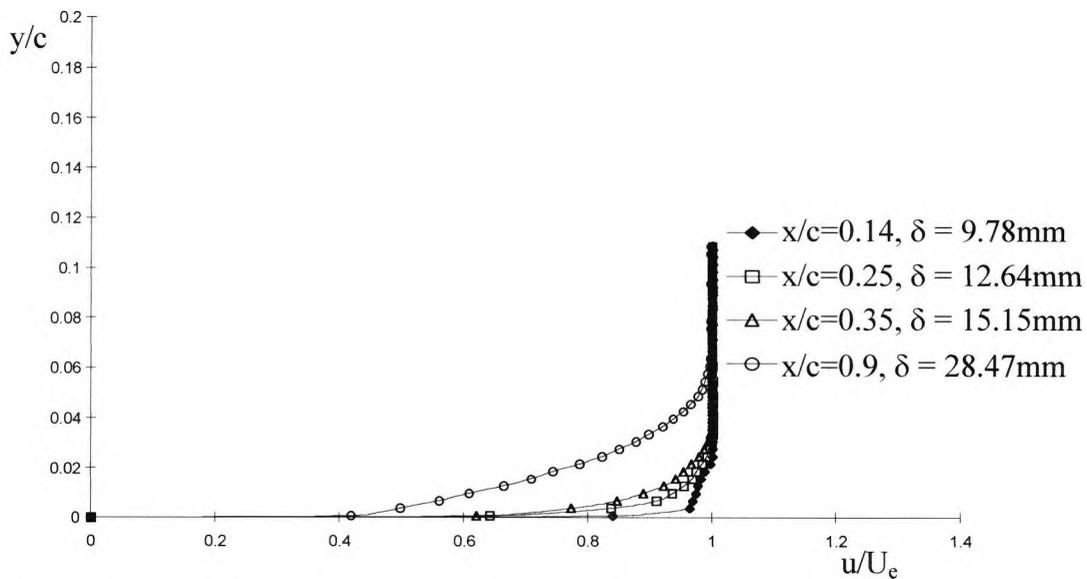
(a) Predicted CFX

(b) Experiment

Figure 5.18: Predicted and experimental shear layer profiles on the upper surface of the high lift system mainfoil at $\alpha=10°$, $C_\mu=0$, $Re_c=1.37\times10^6$, $M_\infty=0.13$
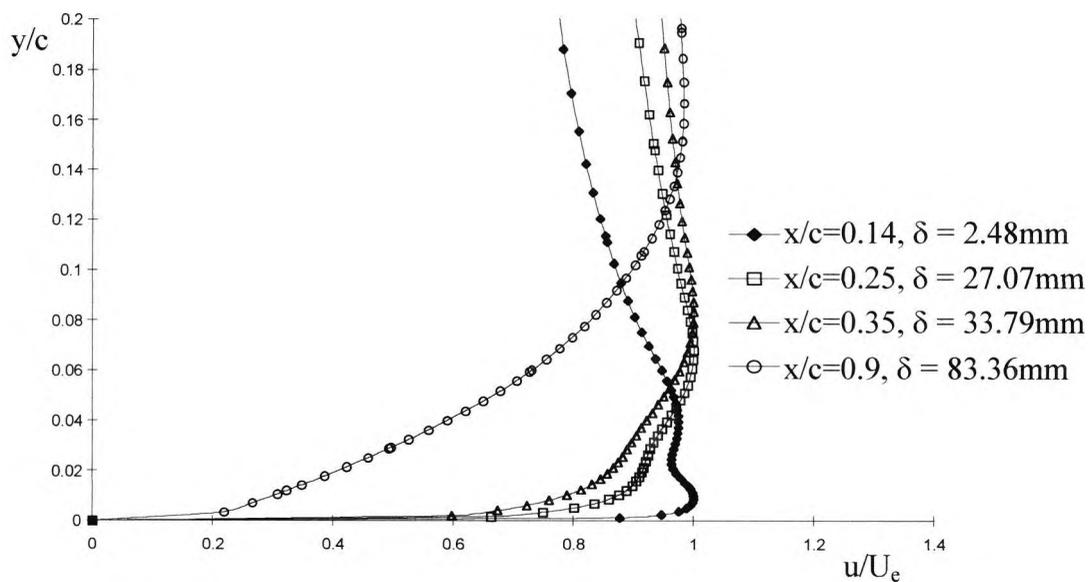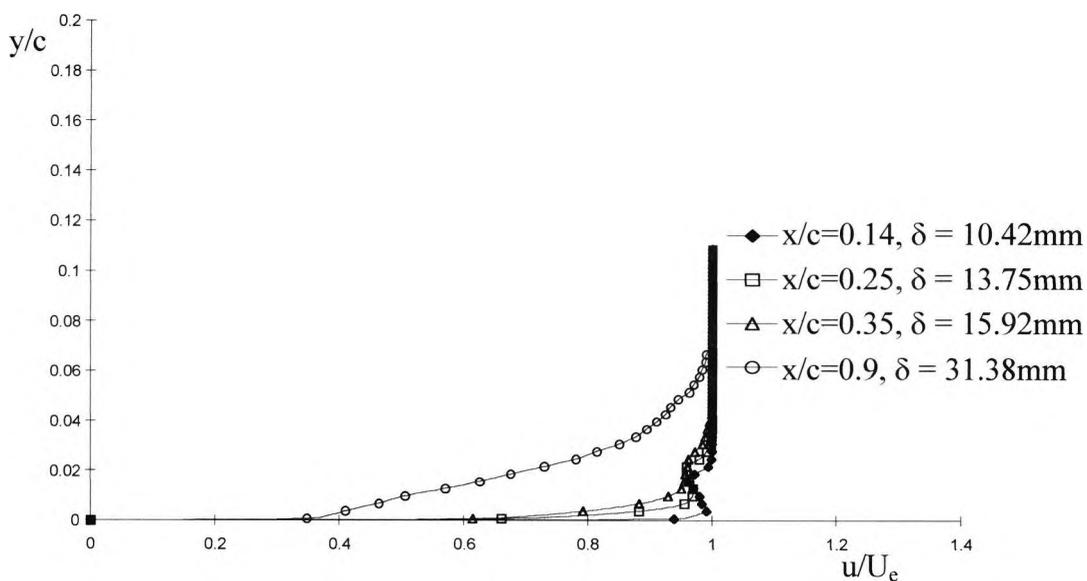
(a) Predicted CFX

(b) Experiment

Figure 5.19: Predicted and experimental shear layer profiles on the upper surface of the high lift system mainfoil at $\alpha=15°$, $C_\mu=0$, $Re_c=1.37\times10^6$, $M_\infty=0.13$
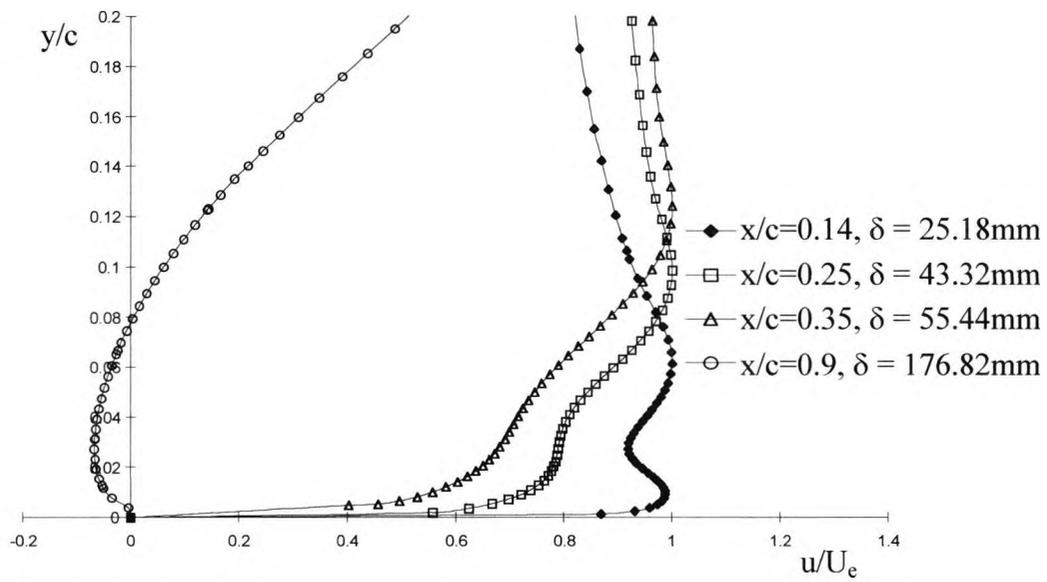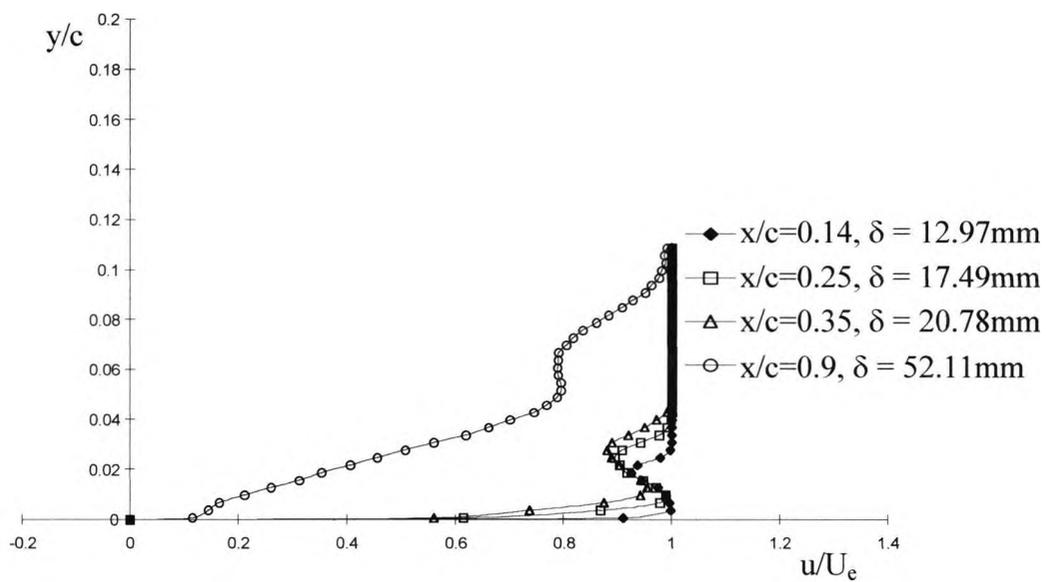
(a) Predicted CFX

(b) Experiment

Figure 5.20: Predicted and experimental shear layer profiles on the upper surface of the high lift system mainfoil at α=25°, C_μ =0, Re_c=1.37×10^6, M_∞=0.13

(a) Predicted CFX

(b) Experiment

Figure 5.21: Predicted and experimental shear layer profiles on the upper surface of the high lift system flap, x/c=1.0, C_μ =0, Re_c=1.37×10^6, M_∞=0.13

Note: c = retracted chord length
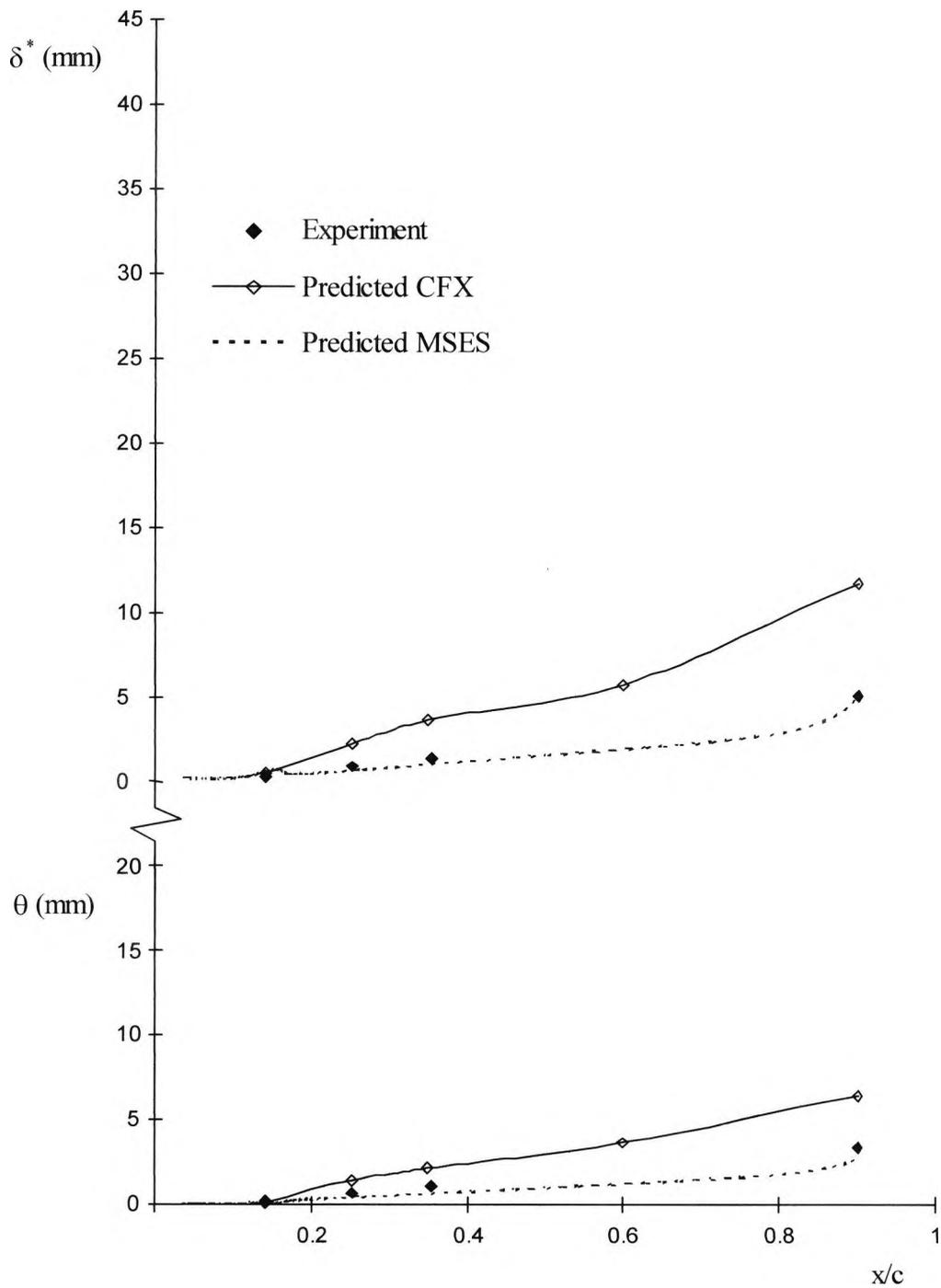
Figure 5.22: Predicted and experimental integral shear layer properties on the upper surface of the high lift system mainfoil at $\alpha=10°$, $C_\mu=0$, $Re_c=1.37\times10^6$, $M_\infty=0.13$
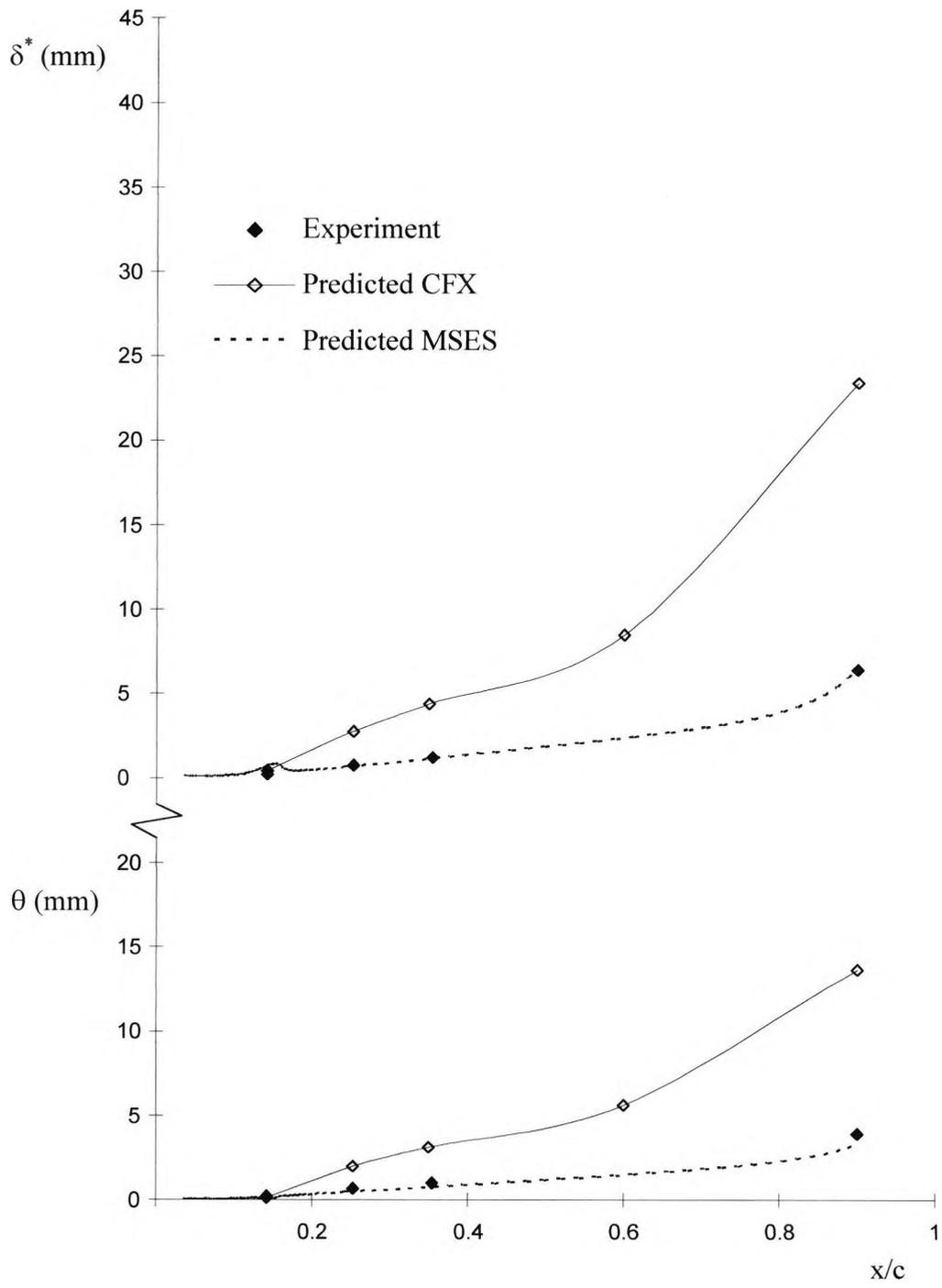
Figure 5.23: Predicted and experimental integral shear layer properties on the upper surface of the high lift system mainfoil at $\alpha=15°$, $C_\mu=0$, $Re_c=1.37\times10^6$, $M_\infty=0.13$
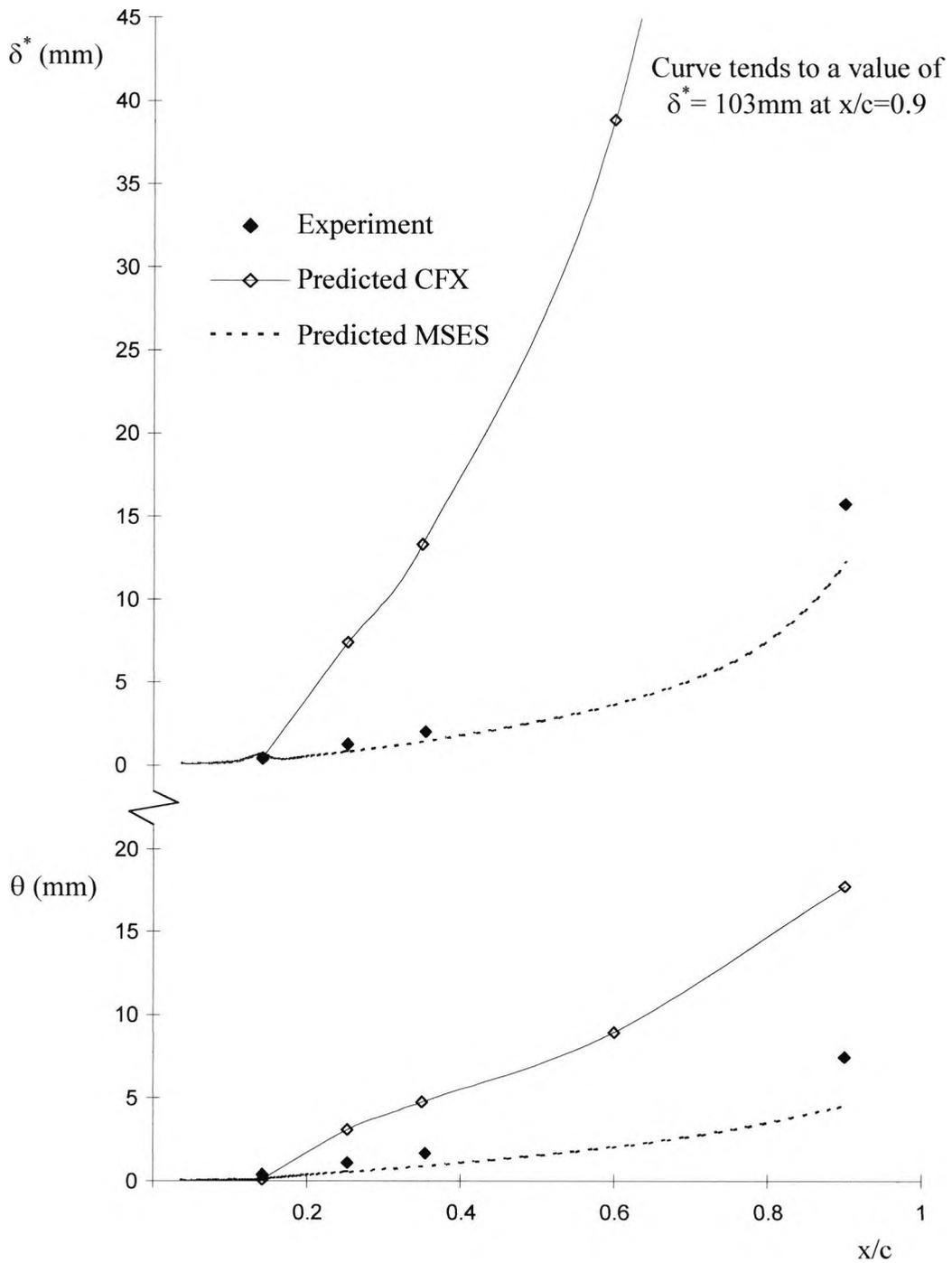
Figure 5.24: Predicted and experimental integral shear layer properties on the upper surface of the high lift system mainfoil at $\alpha=25°$, $C_\mu=0$, $Re_c=1.37\times10^6$, $M_\infty=0.13$
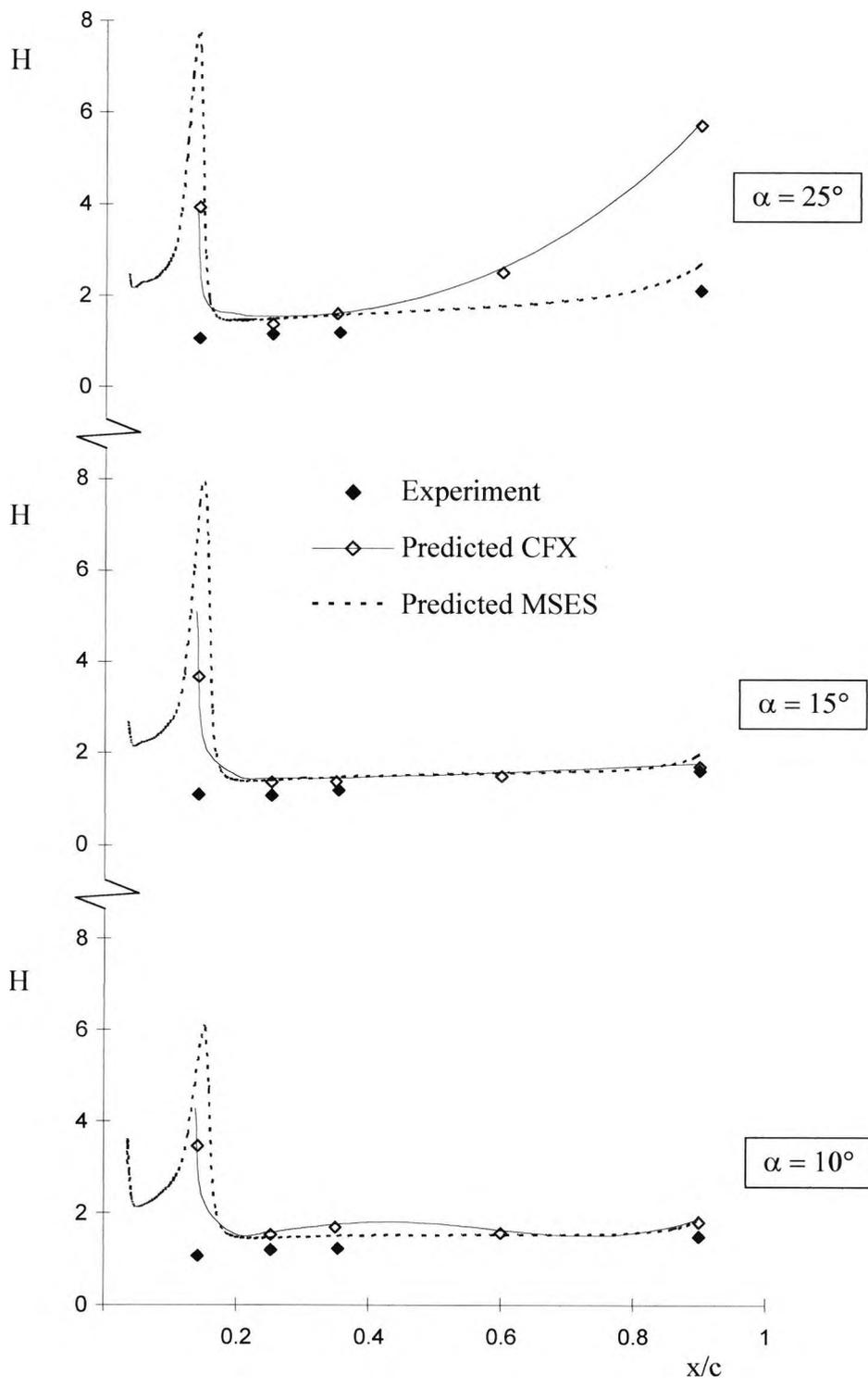
Figure 5.25: Predicted and experimental shape factor properties on the upper surface of the high lift system mainfoil, $C\mu = 0$, $Re_c = 1.37 \times 10^6$, $M_\infty = 0.13$

Appendix B: Flat plate 'local' air-jet vortex generator model results

Figures 6.3 to 6.32 inclusive
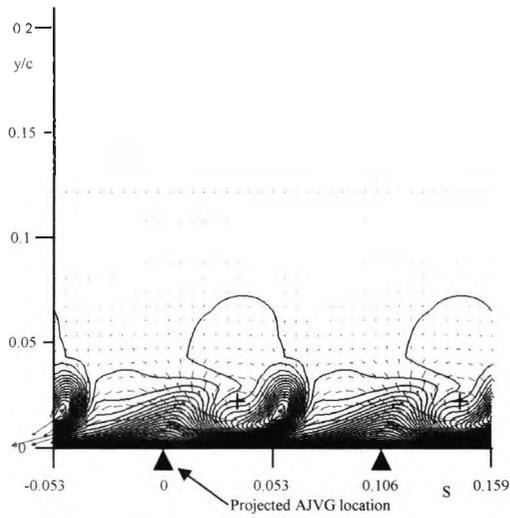
(a) Co-rotating array (x/c=0.3)
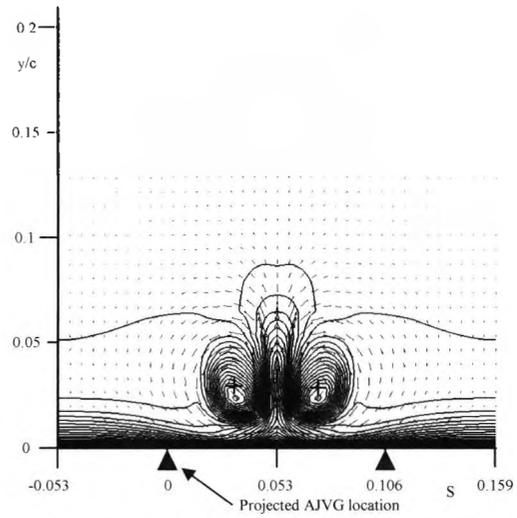
(b) Counter-rotating array (x/c=0.3)
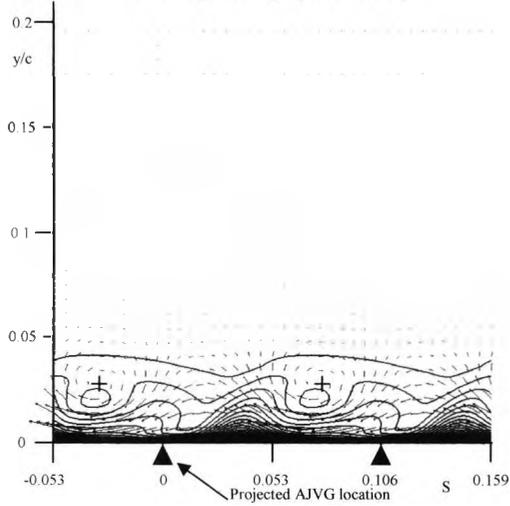
(c) Co-rotating array (x/c=0.6)
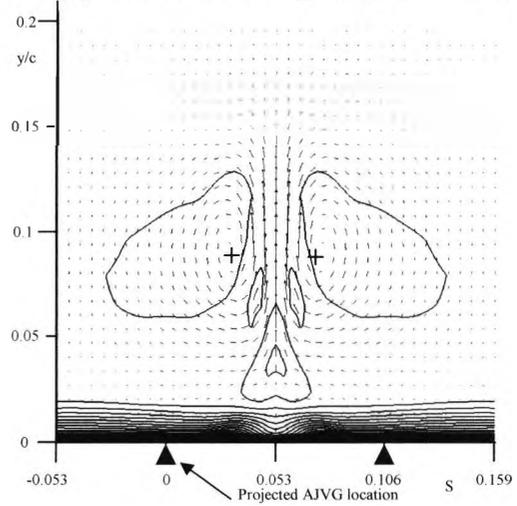
(d) Counter-rotating array (x/c=0.6)
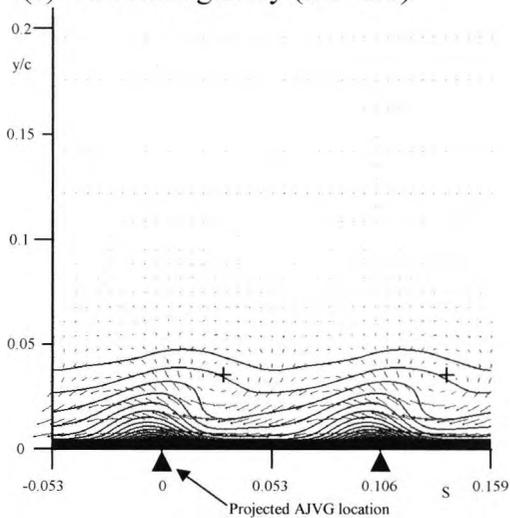
(e) Co-rotating array (x/c=0.9)
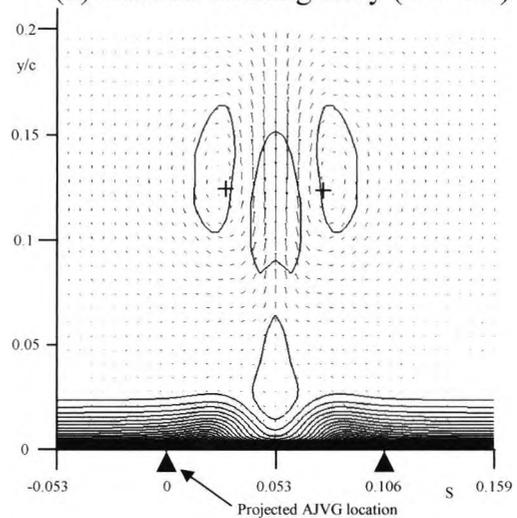
(f) Counter-rotating array (x/c=0.9)

Figure 6.3: Velocity contours and velocity vectors in the crossflow plane at three chordwise locations downstream of the AJVG array, installed at x/c=0.14, in a zero pressure gradient flow, $Re_c=1.37\times10^6$, $M_\infty=0.12$, S=0.106, $V_R=3$, $\phi=45°$, $\psi=60°$

213
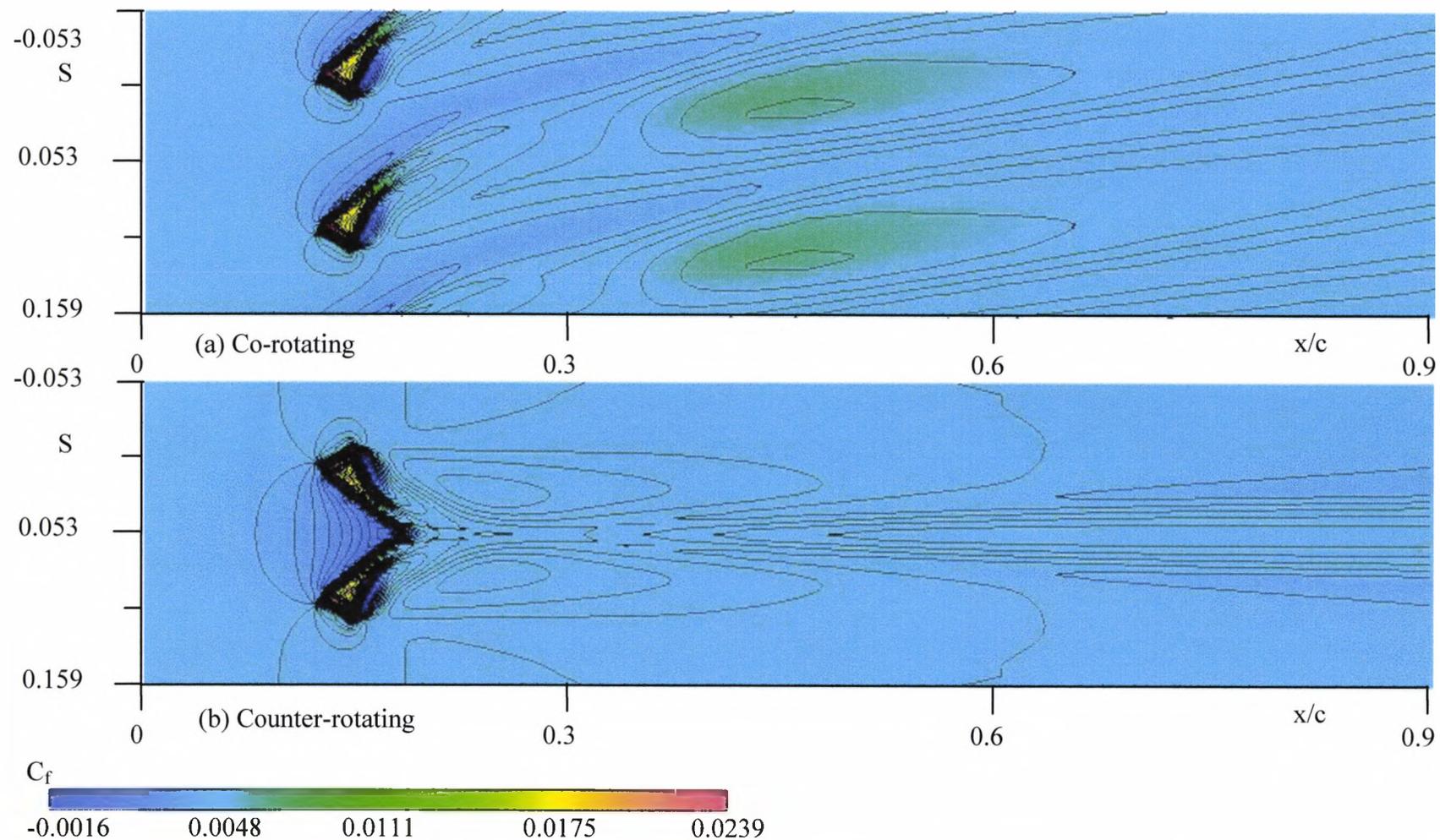
Figure 6.4: Shear stress footprints on the 'local' model surface in a zero pressure gradient flow, AJVGs installed at x/c=0.14, Re_c=1.37×10^{6}, M_∞=0.12, Jet spacing (S)=0.106, ϕ=45°, ψ=60°
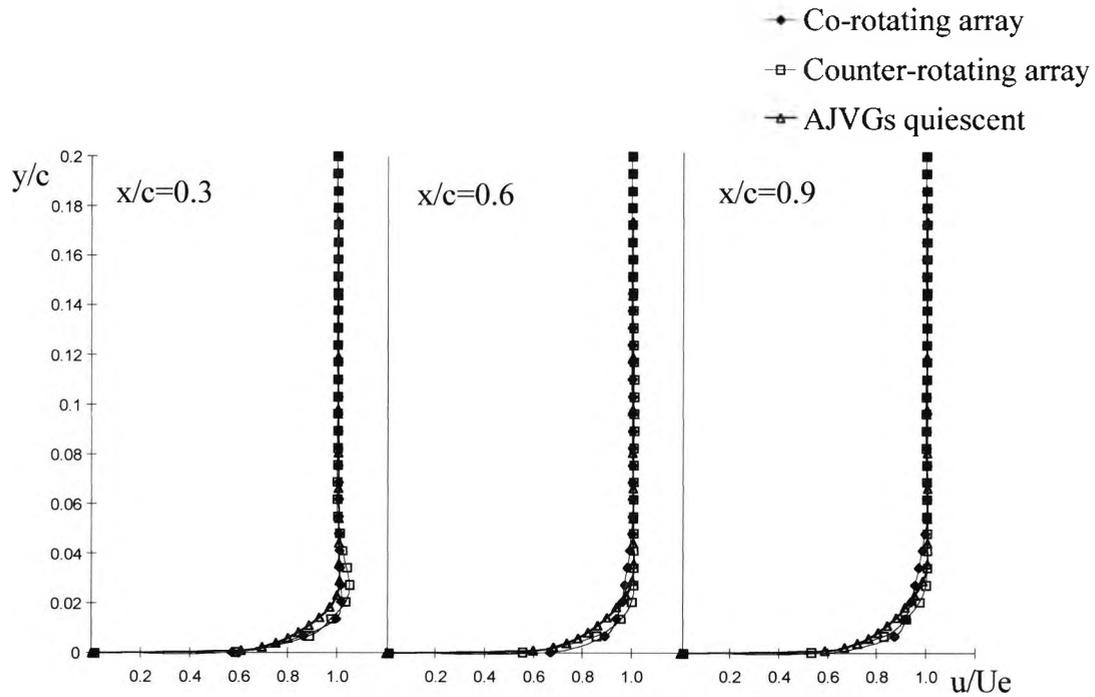
Figure 6.5: Comparison of the axial velocity profiles averaged across the model span, with the AJVGs active and inactive, installed at x/c=0.14, in a zero pressure gradient flow, Re_c=1.37×10^6, M_∞=0.12, S=0.106, V_R=3, ϕ=45°, ψ=60°
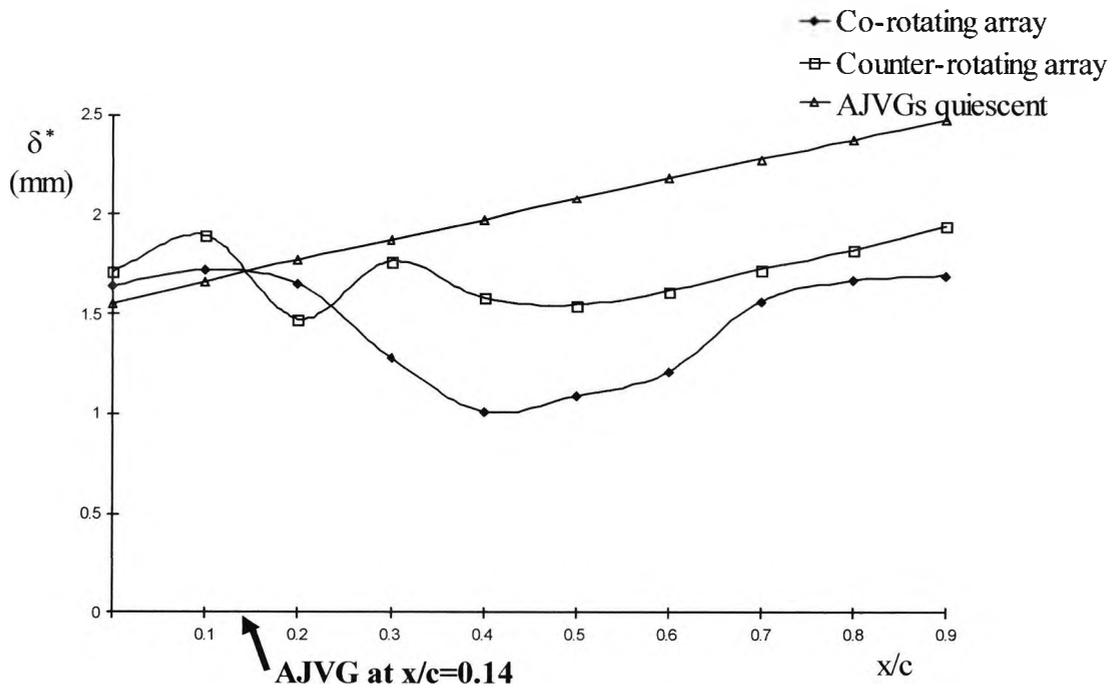
Figure 6.6: Comparison of the displacement thickness (δ^*) averaged across the model span, with the AJVGs active and inactive, installed at x/c=0.14, in a zero pressure gradient flow, Re_c=1.37×10^6, M_∞=0.12, S=0.106, V_R=3, ϕ=45°, ψ=60°

215
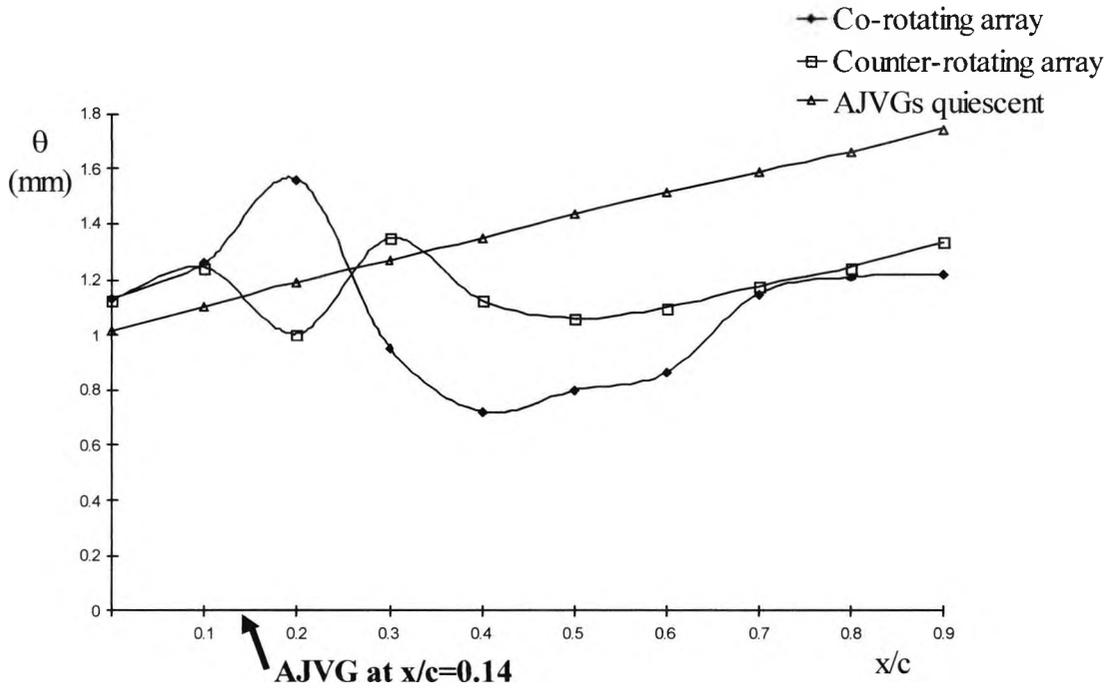
Figure 6.7: Comparison of the momentum thickness (θ) averaged across the model span, with the AJVGs active and inactive, installed at x/c=0.14, in a zero pressure gradient flow, Re_c=1.37×10^6, M_∞=0.12, S=0.106, V_R=3, ϕ=45°, ψ=60°
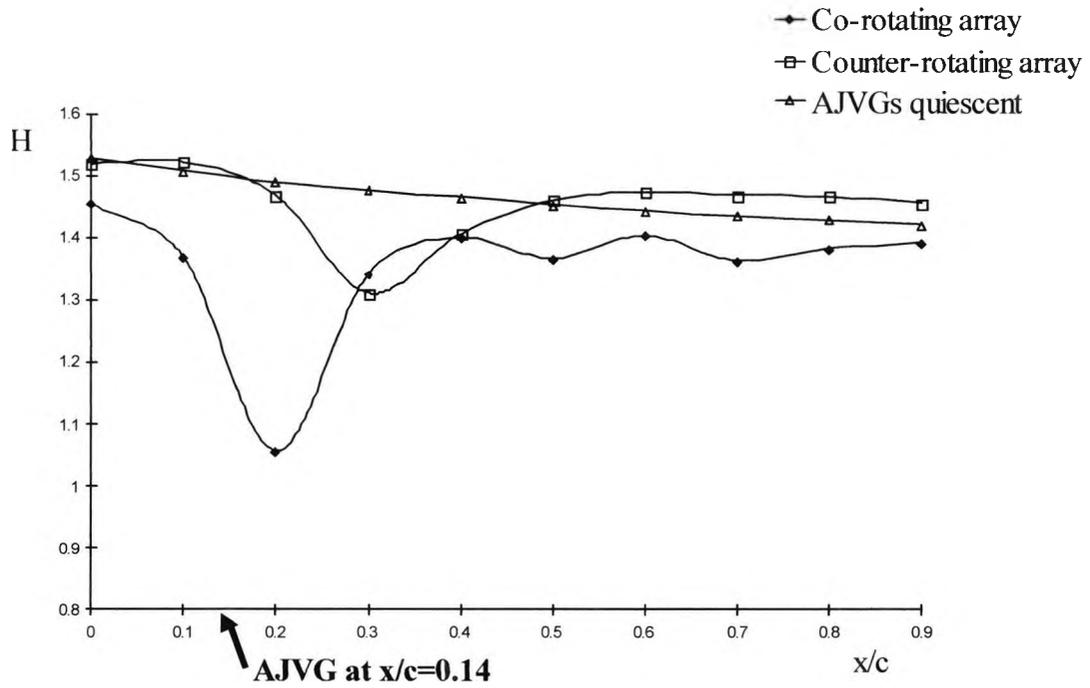
Figure 6.8: Comparison of the shape parameter (H) averaged across the model span, with the AJVGs active and inactive, installed at x/c=0.14, in a zero pressure gradient flow, Re_c=1.37×10^6, M_∞=0.12, S=0.106, V_R=3, ϕ=45°, ψ=60°

216

$$I\Delta C_f = \frac{1}{S} \int_0^S \Delta C_f d\left(\frac{z}{c}\right)$$
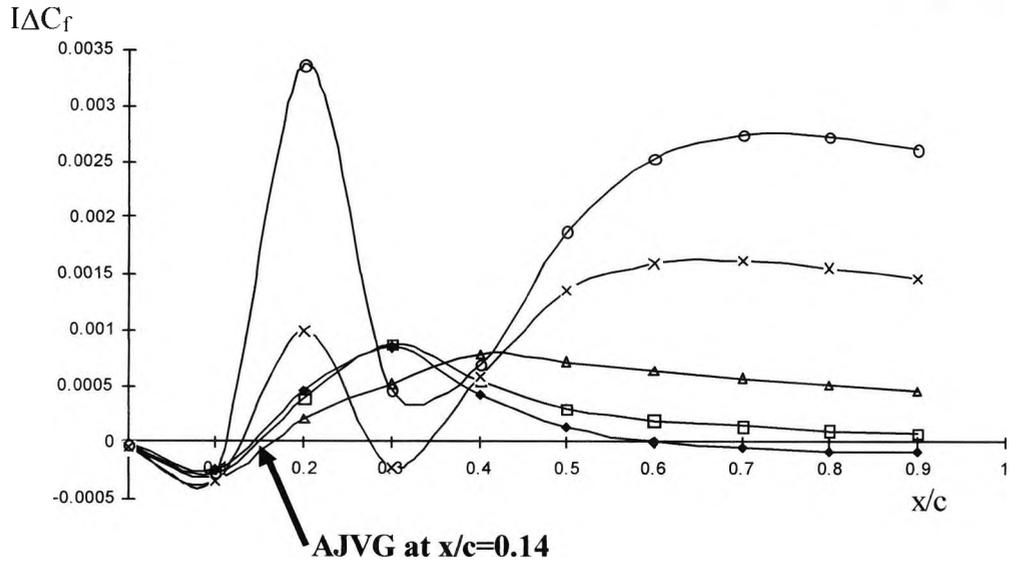
(a) Co-rotating AJVG array
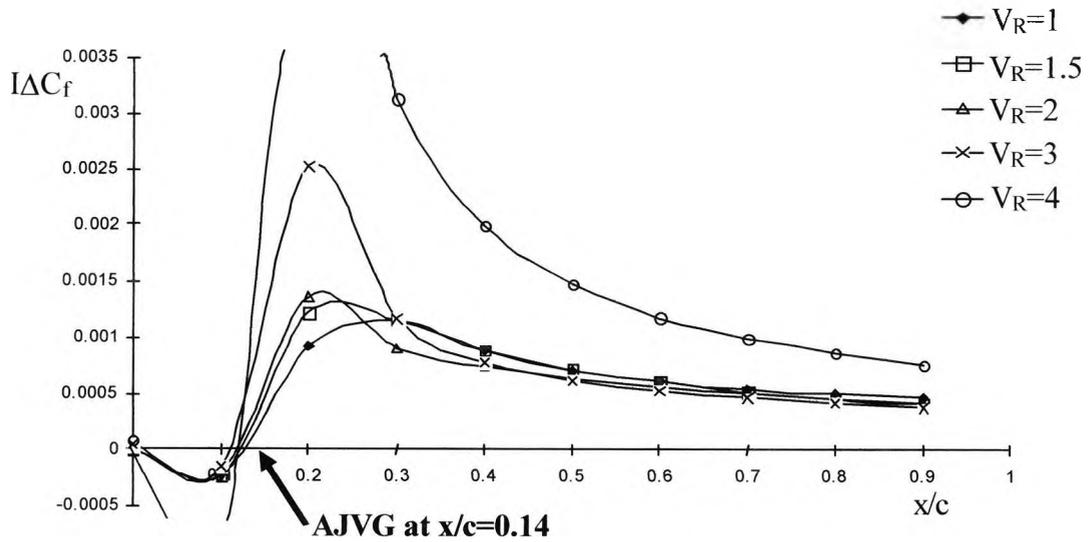
(b) Counter-rotating AJVG array

Figure 6.9: Axial variation of the integrated surface skin friction enhancement, $I\Delta C_f$, with increasing jet velocity ratio, in a zero pressure gradient flow, **Jet spacing (S)=0.051**, $Re_c=1.37\times10^6$, $M_\infty=0.12$, $\phi=45°$, $\psi=60°$

217

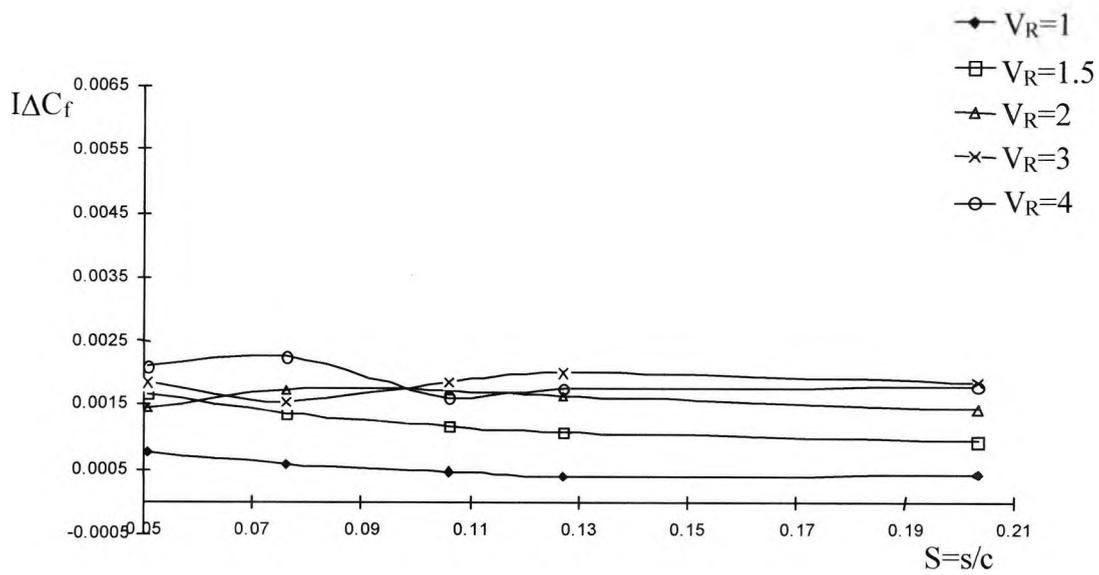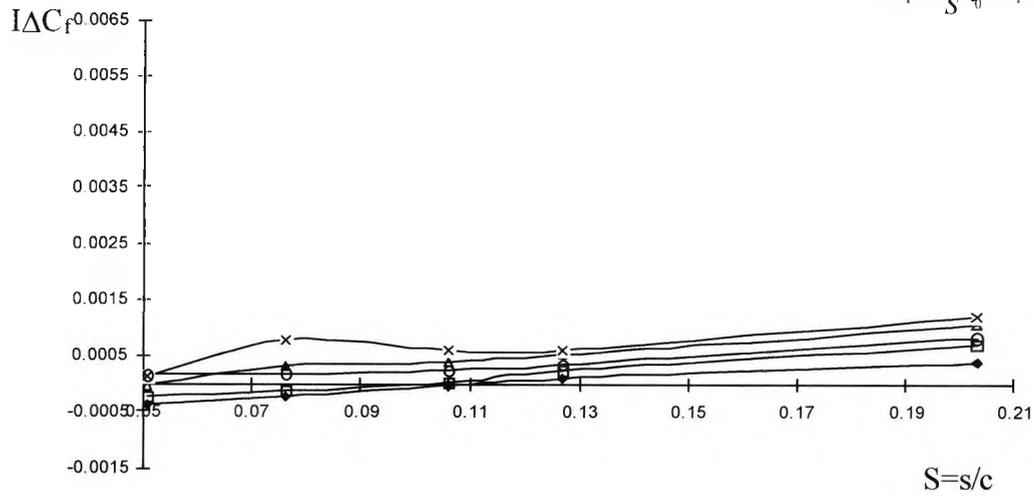$$I\Delta C_f = \frac{1}{S}\int_0^s \Delta C_f d\left(\frac{z}{c}\right)$$
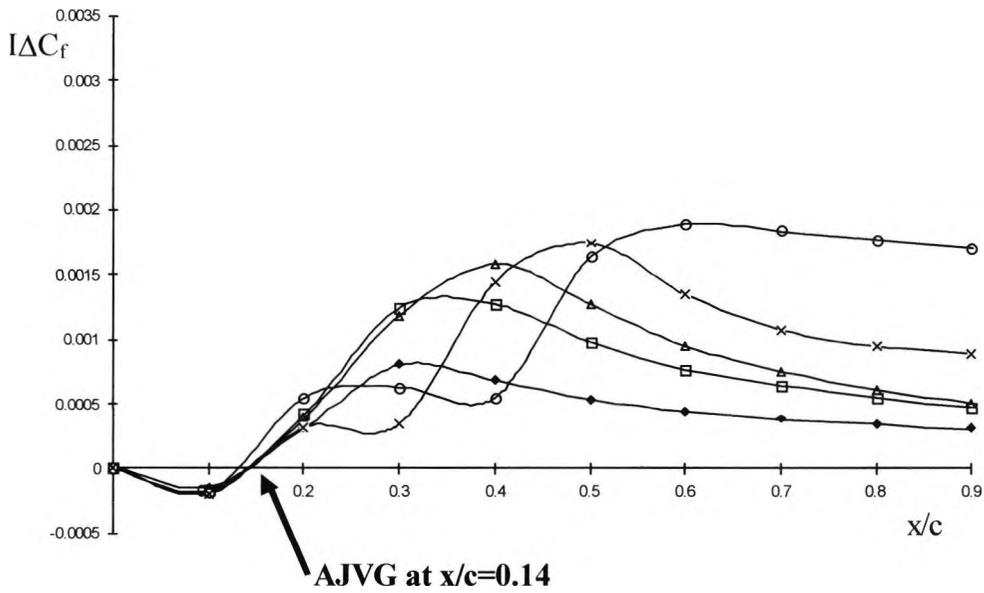
(a) Co-rotating AJVG array
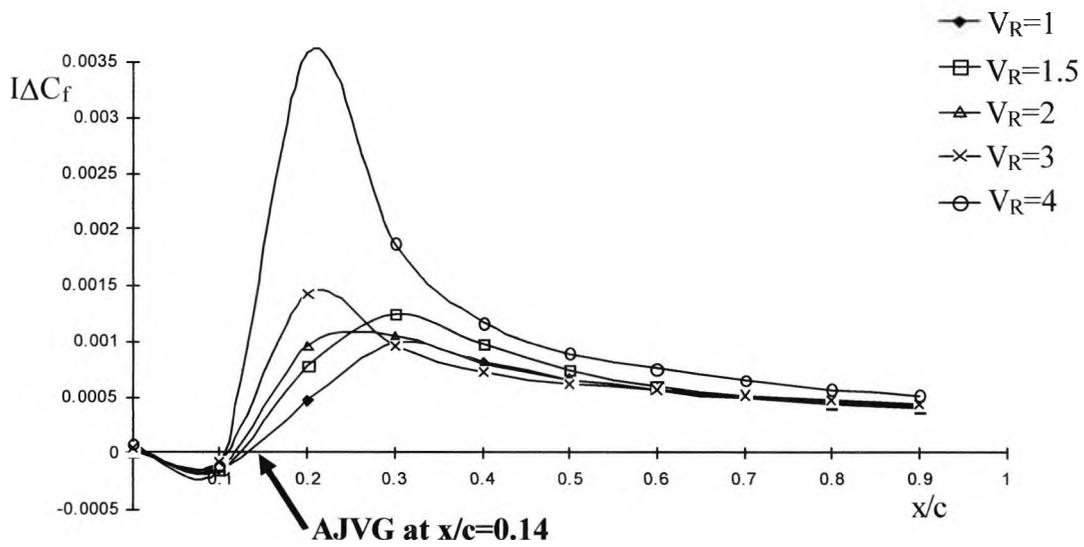
(b) Counter-rotating AJVG array

Figure 6.10: Axial variation of the integrated surface skin friction enhancement, $I\Delta C_f$, with increasing jet velocity ratio, in a zero pressure gradient flow, **Jet spacing (S)=0.076**, $Re_c=1.37\times10^6$, $M_\infty=0.12$, $\phi=45°$, $\psi=60°$

218

$$I\Delta C_f = \frac{1}{S}\int_0^s \Delta C_f d\left(\frac{z}{c}\right)$$
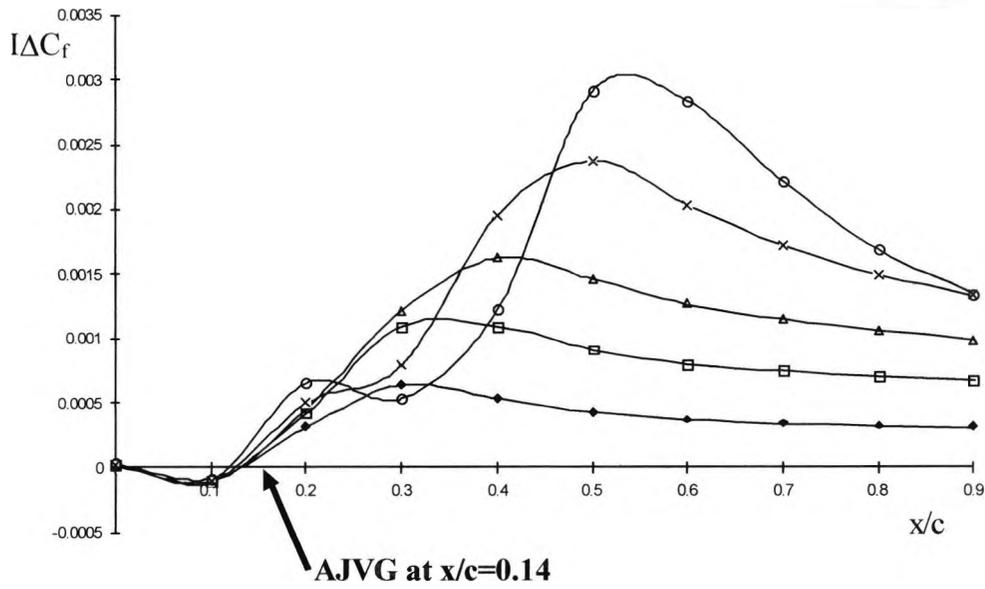
(a) Co-rotating AJVG array
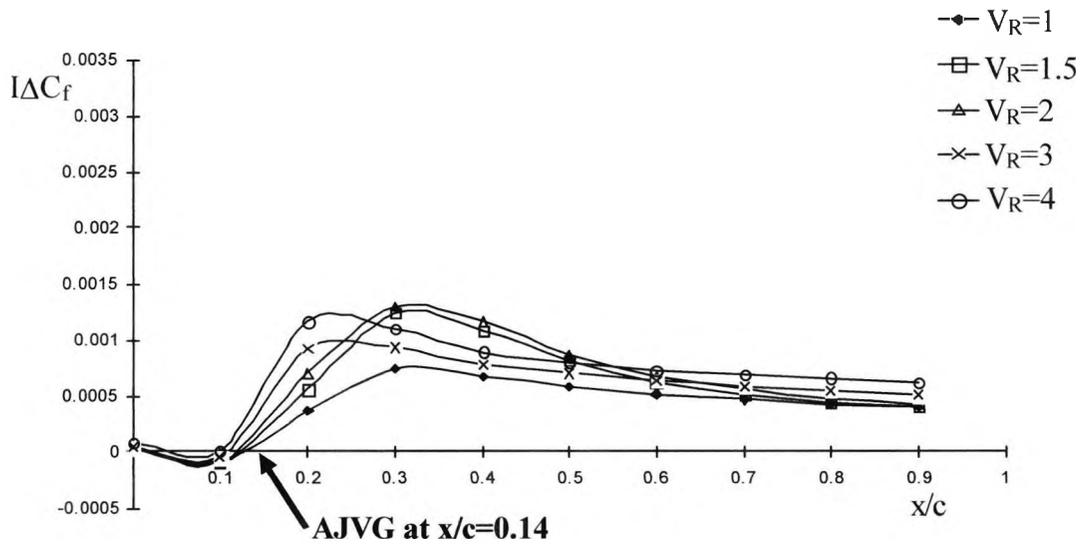
(b) Counter-rotating AJVG array

Figure 6.11: Axial variation of the integrated surface skin friction enhancement, $I\Delta C_f$, with increasing jet velocity ratio, in a zero pressure gradient flow, **Jet spacing (S)=0.106**, $Re_c=1.37\times10^6$, $M_\infty=0.12$, $\phi=45°$, $\psi=60°$

219

$$I\Delta C_f = \frac{1}{S}\int_0^s \Delta C_f \, d\left(\frac{z}{c}\right)$$
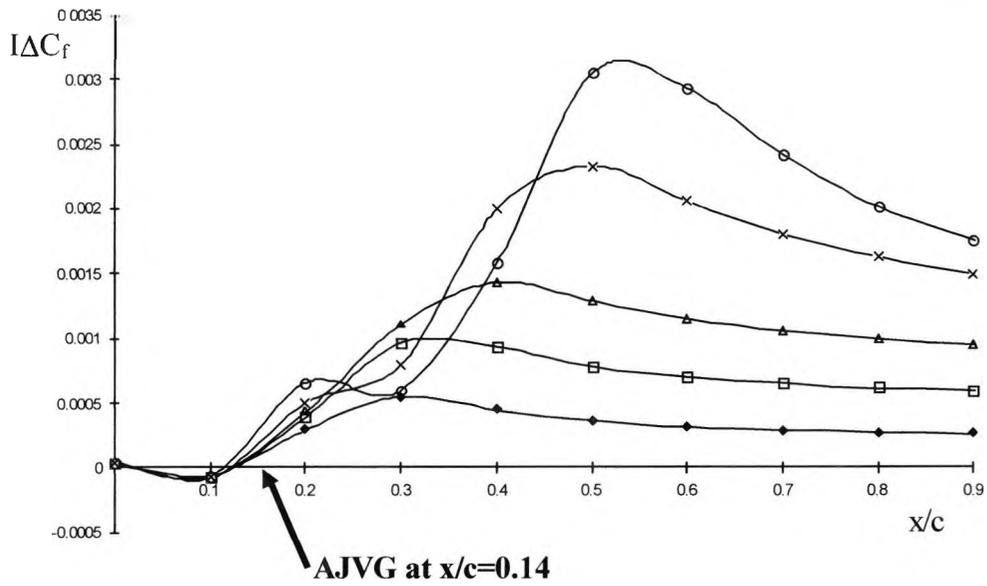
(a) Co-rotating AJVG array
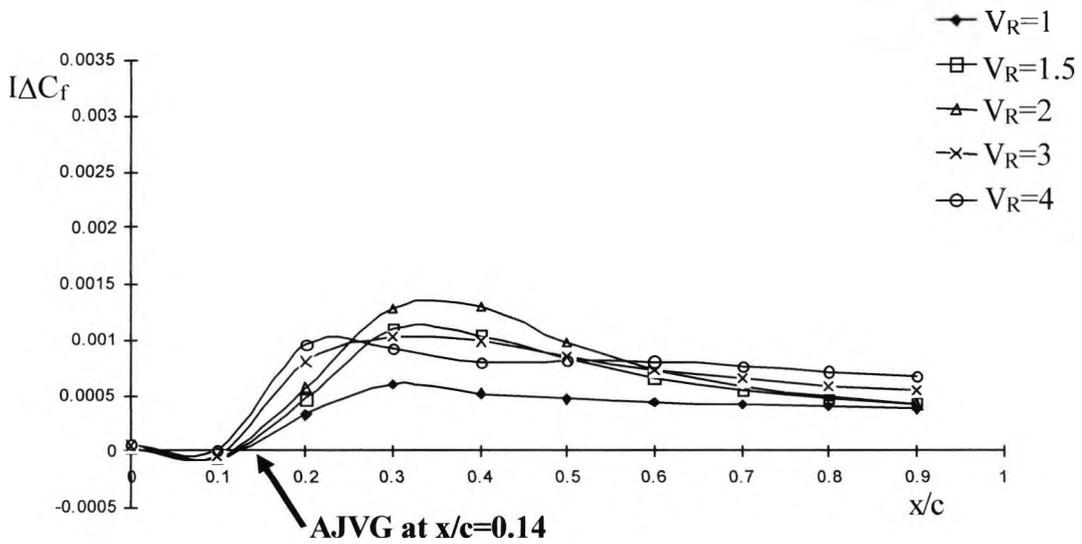
(b) Counter-rotating AJVG array

Figure 6.12: Axial variation of the integrated surface skin friction enhancement, $I\Delta C_f$, with increasing jet velocity ratio, in a zero pressure gradient flow, **Jet spacing (S)=0.127**, $Re_c=1.37\times10^6$, $M_\infty=0.12$, $\phi=45°$, $\psi=60°$

$$I\Delta C_f = \frac{1}{S} \int_0^s \Delta C_f d\left(\frac{z}{c}\right)$$
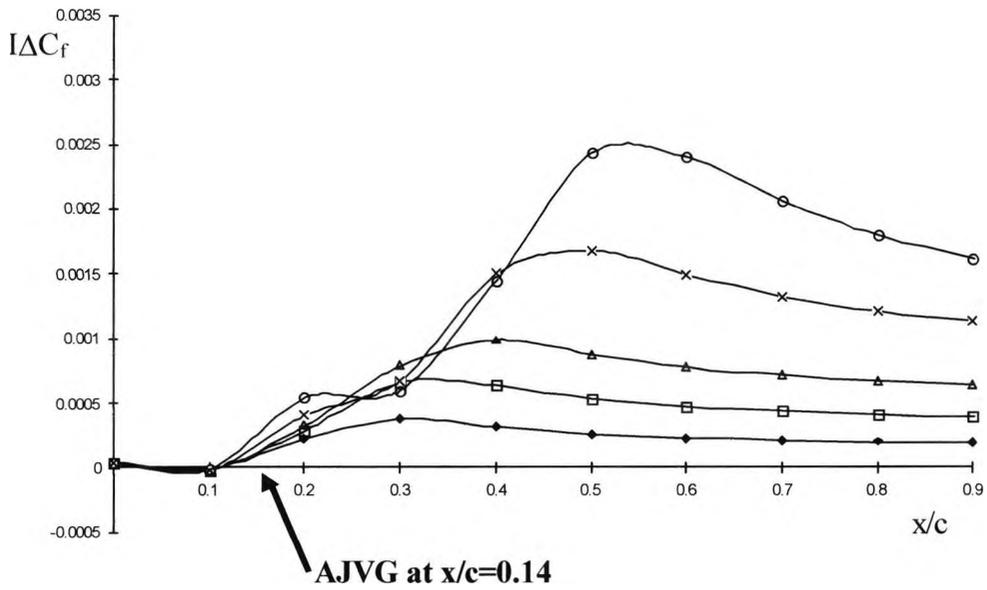
(a) Co-rotating AJVG array
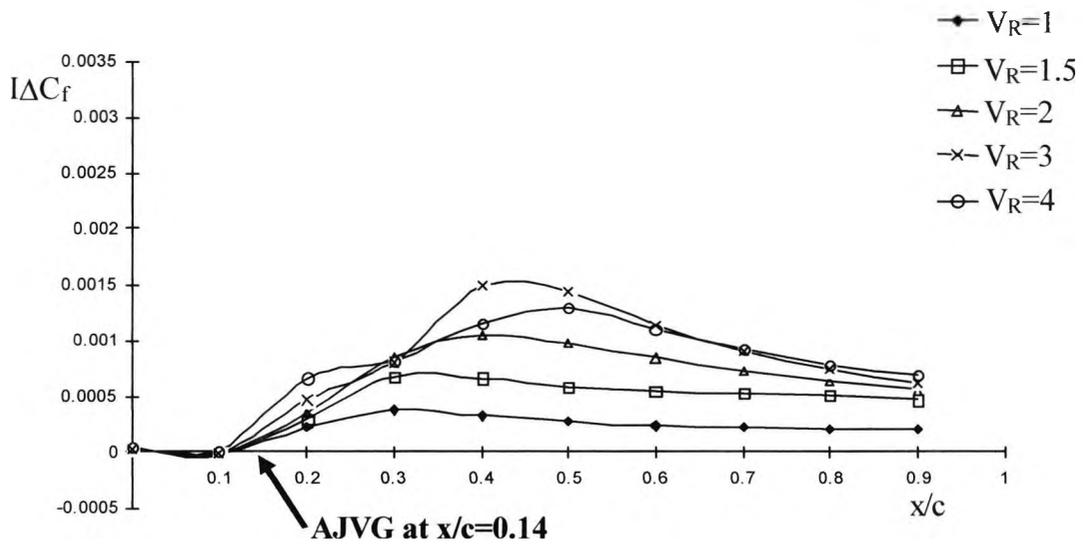
(b) Counter-rotating AJVG array

Figure 6.13: Axial variation of the integrated surface skin friction enhancement, $I\Delta C_f$, with increasing jet velocity ratio, in a zero pressure gradient flow, **Jet spacing (S)=0.203**, $Re_c=1.37\times10^6$, $M_\infty=0.12$, $\phi=45°$, $\psi=60°$

$$I\Delta C_f = \frac{1}{S} \int_0^s \Delta C_f d\left(\frac{z}{c}\right)$$
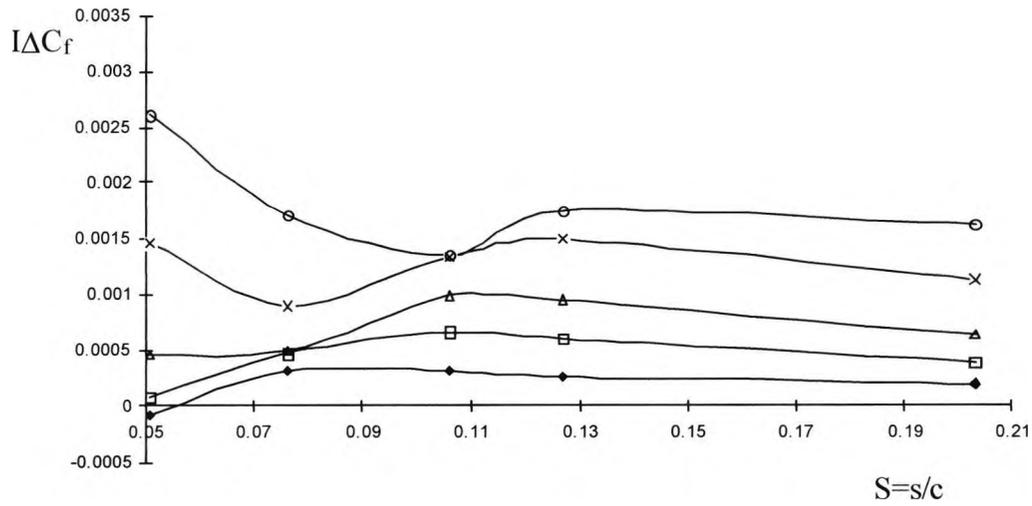
(a) Co-rotating AJVG array
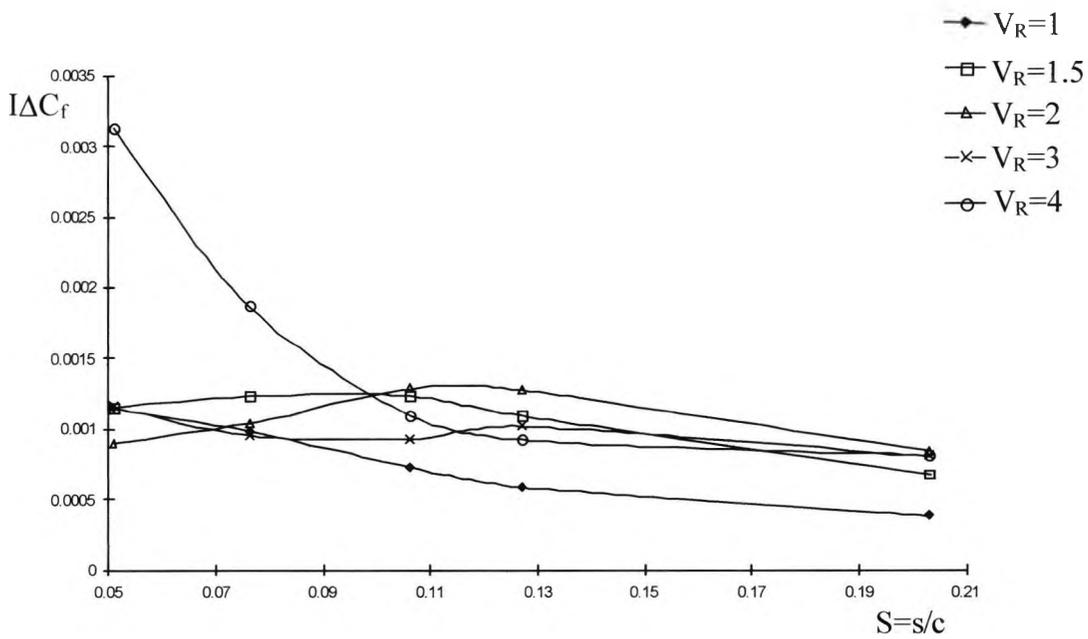
(b) Counter-rotating AJVG array

Figure 6.14: Variation of the integrated surface skin friction enhancement, IΔC_f, with jet spacing and jet velocity ratio, in a zero pressure gradient flow, **x/c=0.3**, Re$_c$=1.37×10^6, M$_\infty$=0.12, ϕ=45°, ψ=60°

$$I\Delta C_f = \frac{1}{S} \int_0^s \Delta C_f d\left(\frac{z}{c}\right)$$
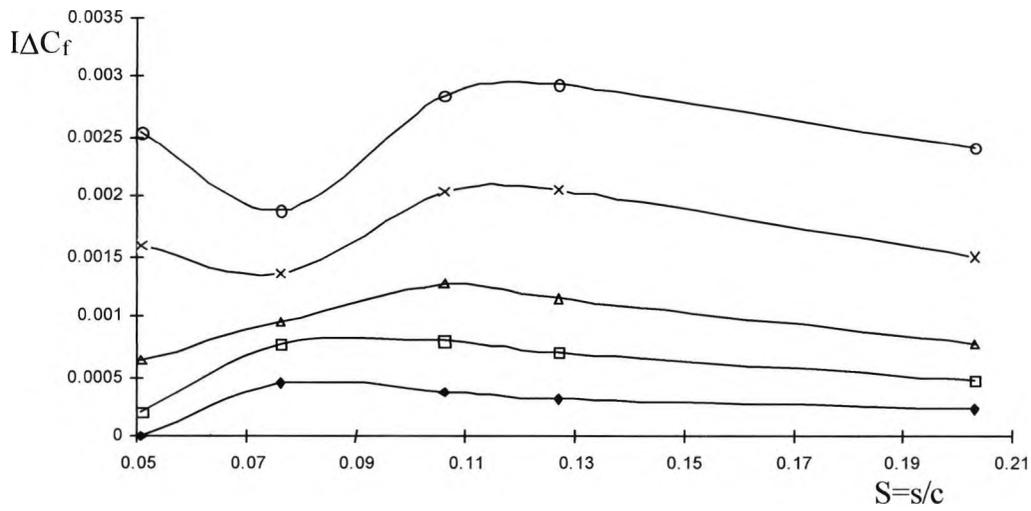
(a) Co-rotating AJVG array
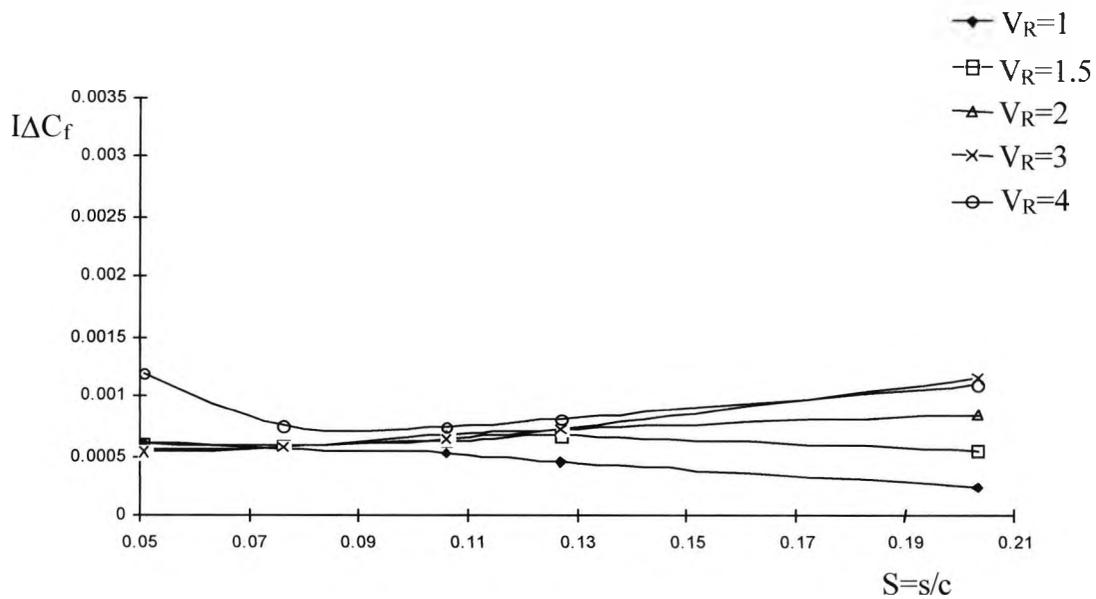
(b) Counter-rotating AJVG array

Figure 6.15: Variation of the integrated surface skin friction enhancement, $I\Delta C_f$, with jet spacing and jet velocity ratio, in a zero pressure gradient flow, **x/c=0.6**, $Re_c=1.37\times10^6$, $M_\infty=0.12$, $\phi=45°$, $\psi=60°$

$$I\Delta C_f = \frac{1}{S} \int_0^s \Delta C_f \, d\left(\frac{z}{c}\right)$$
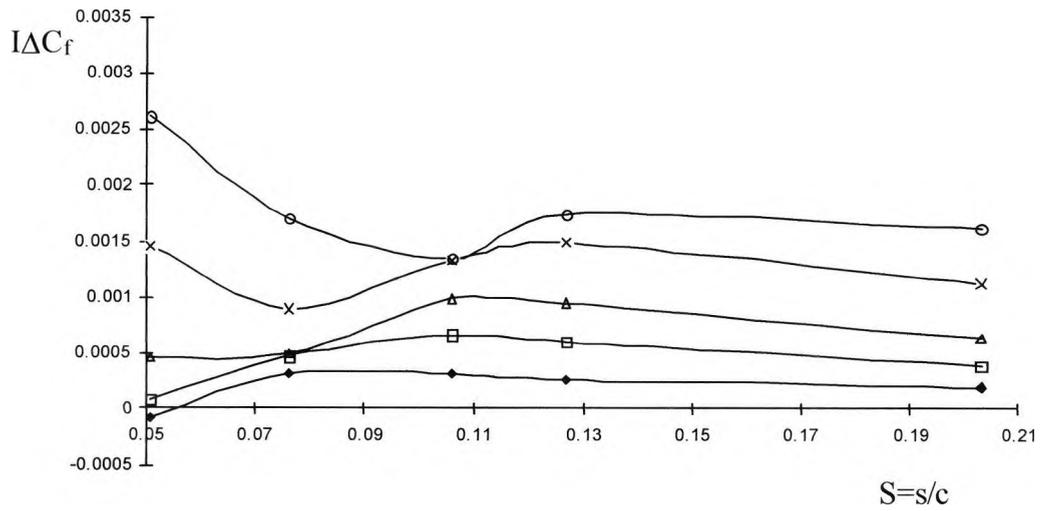
(a) Co-rotating AJVG array
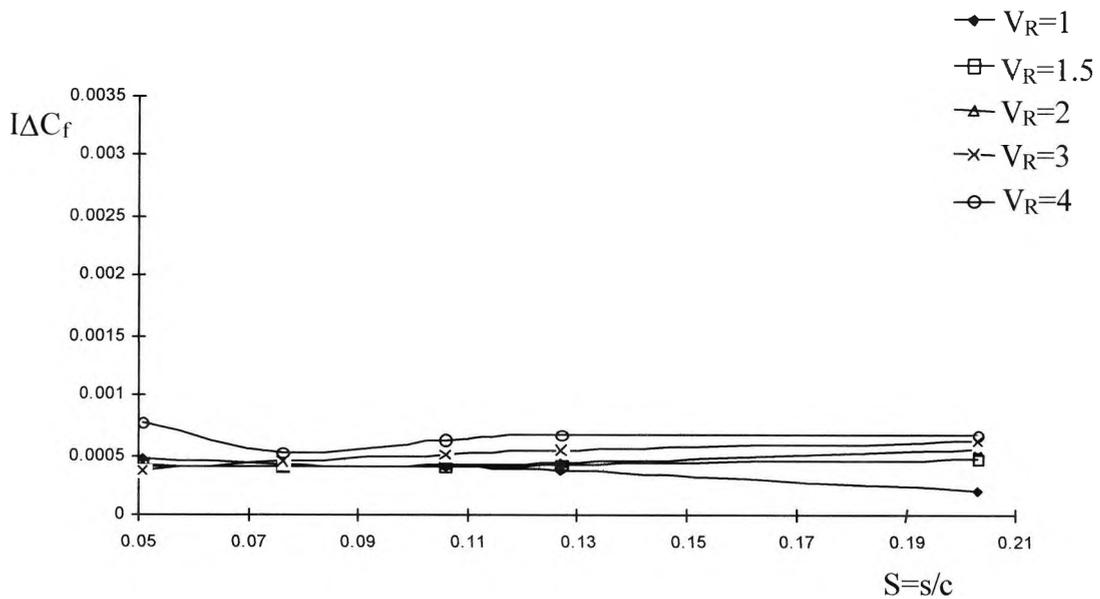
(b) Counter-rotating AJVG array

Figure 6.16: Variation of the integrated surface skin friction enhancement, $I\Delta C_f$, with jet spacing and jet velocity ratio, in a zero pressure gradient flow, **x/c=0.9**, $Re_c=1.37\times10^6$, $M_\infty=0.12$, $\phi=45°$, $\psi=60°$
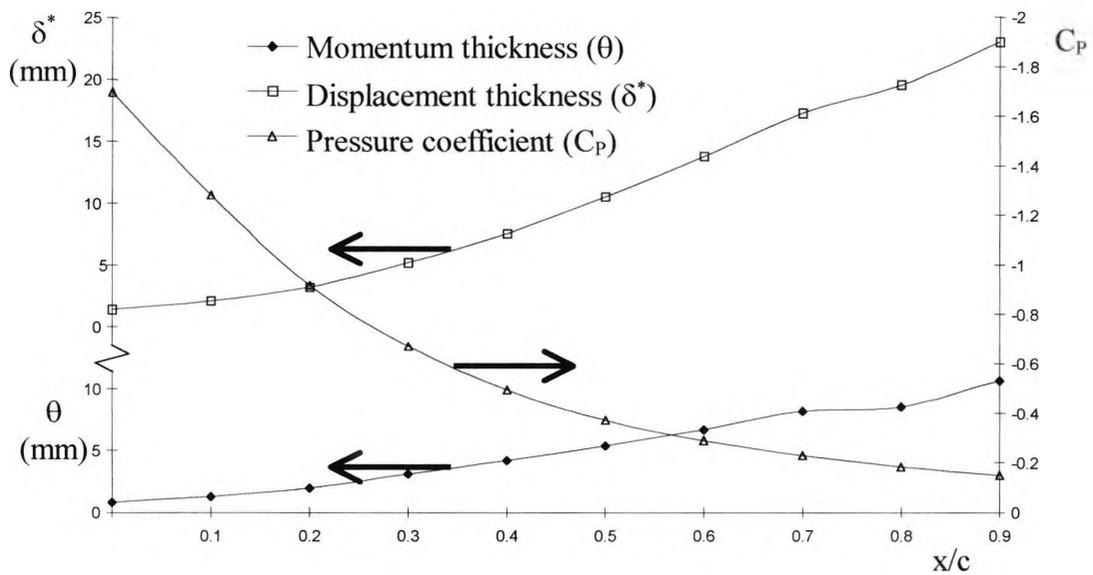
Figure 6.17: Local model flow with adverse pressure gradient: integral shear layer properties on the flat plate with the AJVGs inactive, $Re_c=1.37\times10^6$, $V_R=0$, $M_\infty=0.12$
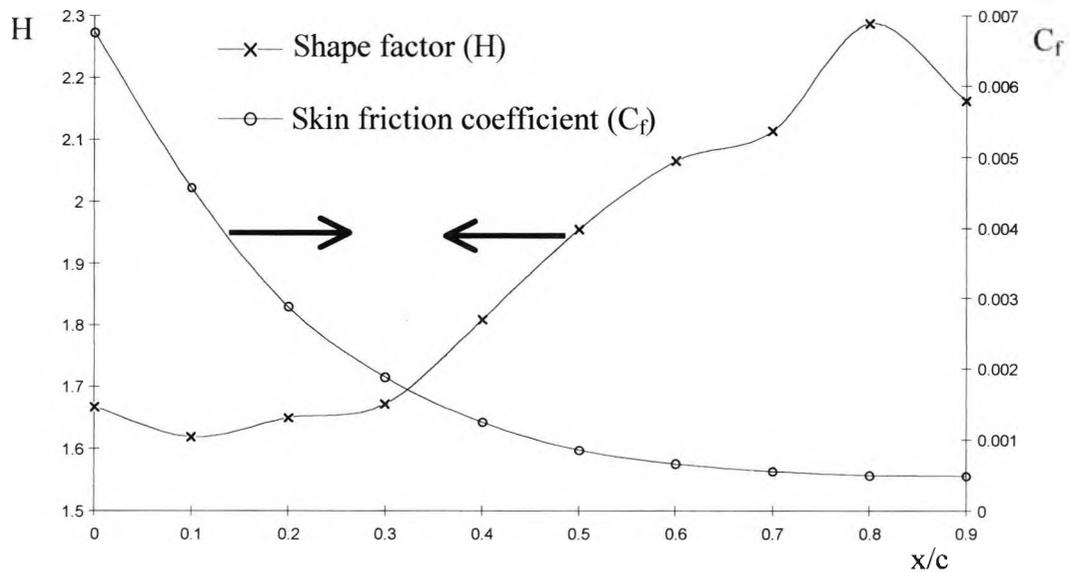
Figure 6.18: Local model flow with adverse pressure gradient: shape factor and surface skin friction distribution on the flat plate with the AJVGs inactive, $Re_c=1.37\times10^6$, $V_R=0$, $M_\infty=0.12$
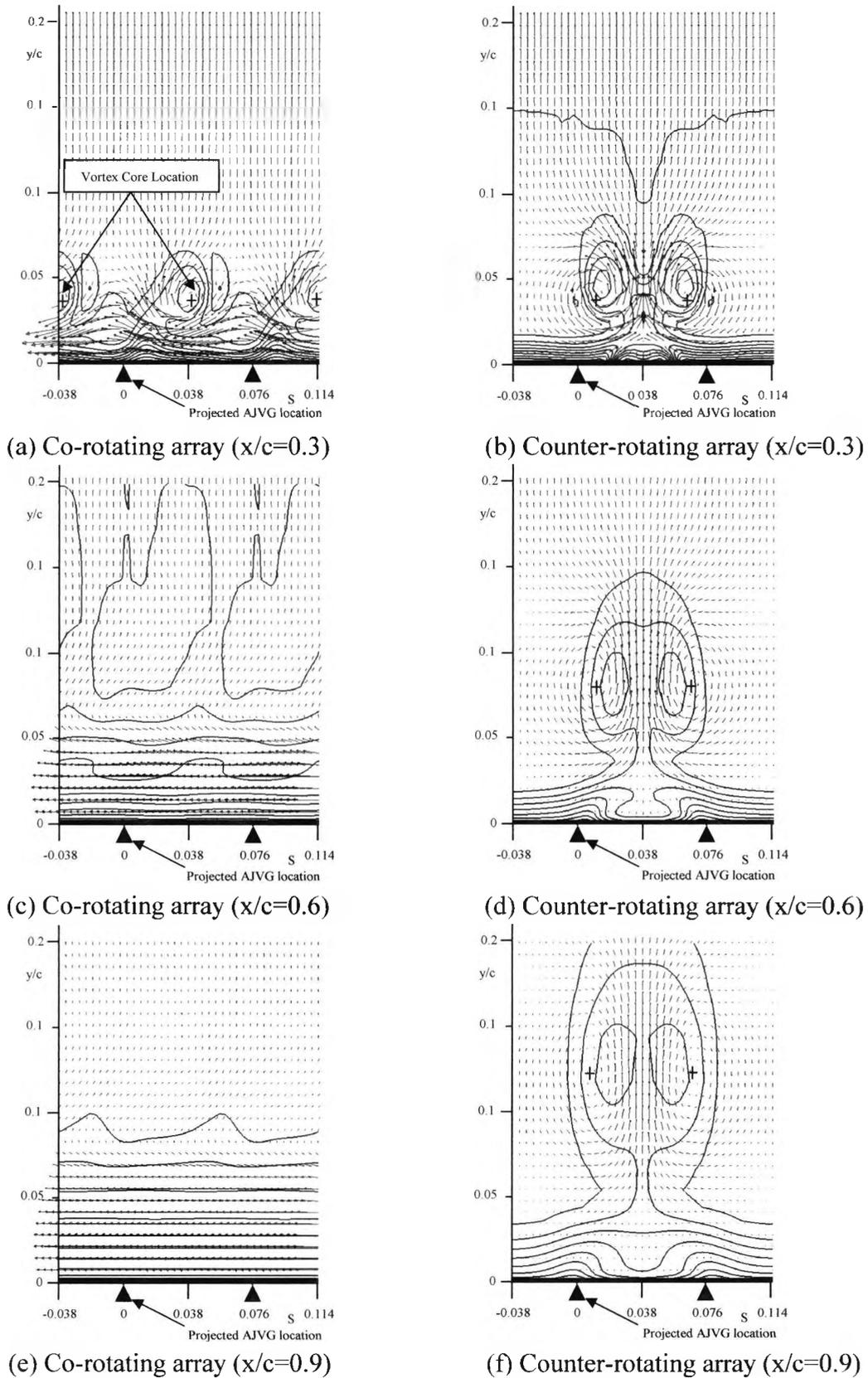
Figure 6.19: Velocity contours profiles and velocity vectors in the crossflow plane at three chordwise locations downstream of the AJVG array, installed at x/c=0.14, in an adverse pressure gradient flow, Re_c=1.37×10^6, M_∞=0.12, S=0.076, V_R=3, ϕ=45°, ψ=60°
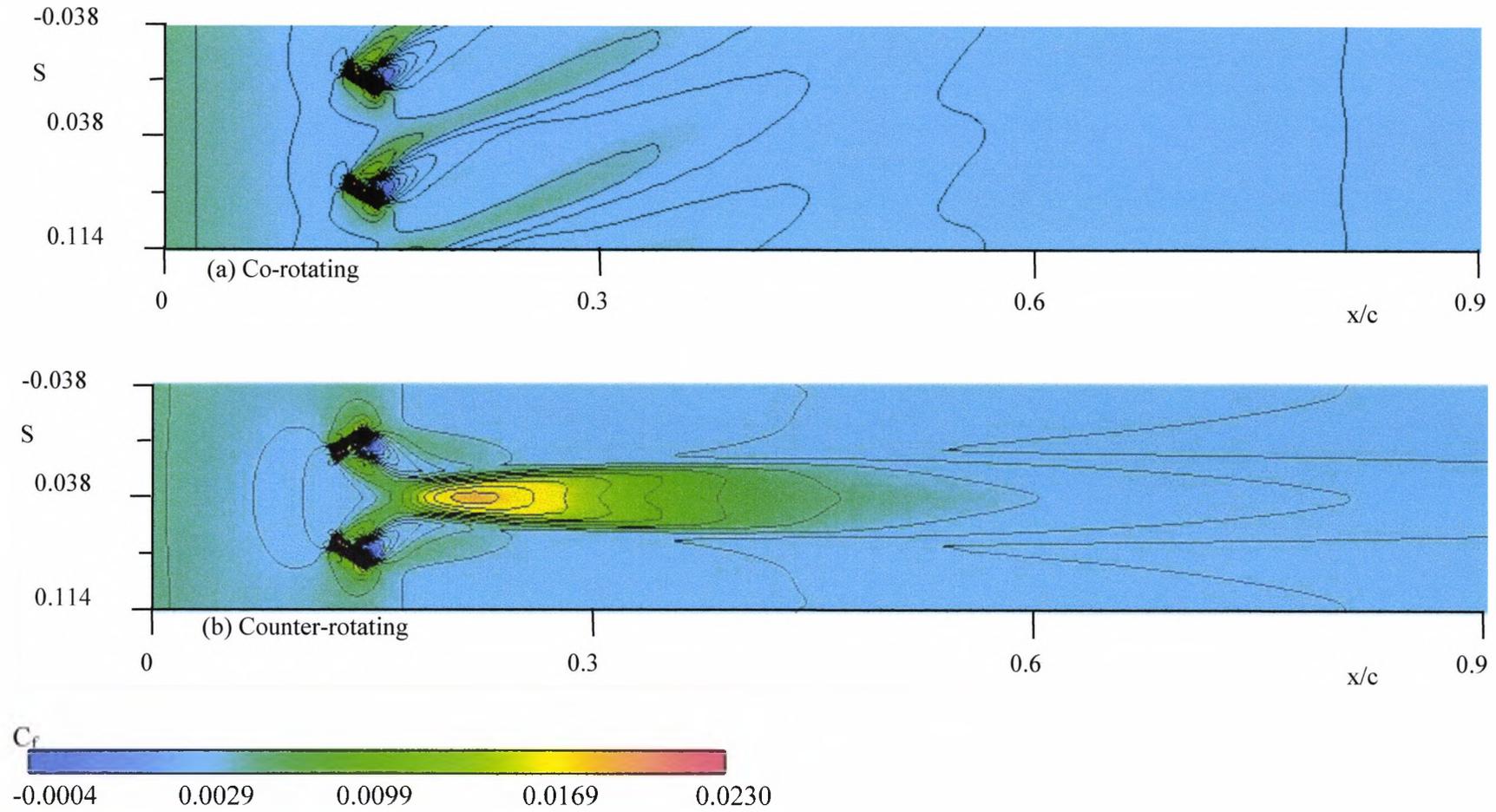
Figure 6.20: Shear stress footprints on the 'local' model surface in an adverse pressure gradient flow, AJVG installed at x/c=0.14, $Re_c=1.37\times10^6$, $M_\infty=0.12$, S=0.076, $V_R=3$, $\phi=45°$, $\psi=60°$
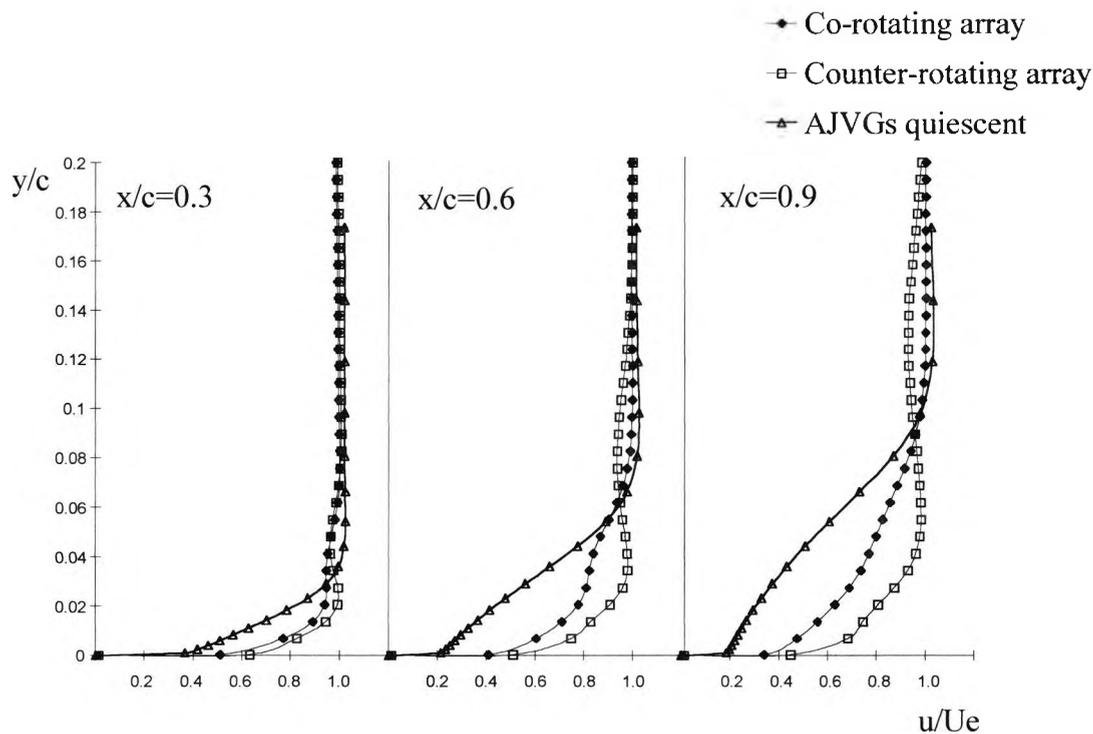
Figure 6.21: Comparison of the axial velocity profiles averaged across the model span, with the AJVGs active and inactive, in an adverse pressure gradient flow, $Re_c=1.37\times10^6$, $M_\infty=0.12$, S=0.076, $V_R=3$, $\phi=45°$, $\psi=60°$
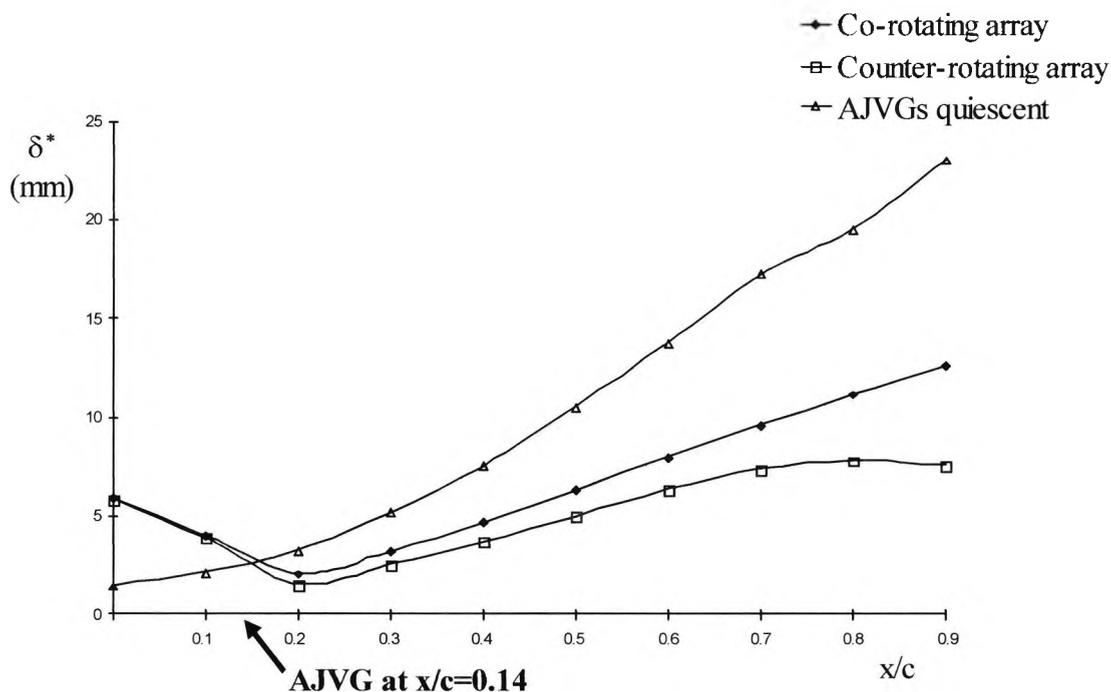
Figure 6.22: Comparison of the displacement thickness (δ^*) averaged across the model span, with the AJVGs active and inactive, in an adverse pressure gradient flow, $Re_c=1.37\times10^6$, $M_\infty=0.12$, S=0.076, $V_R=3$, $\phi=45°$, $\psi=60°$
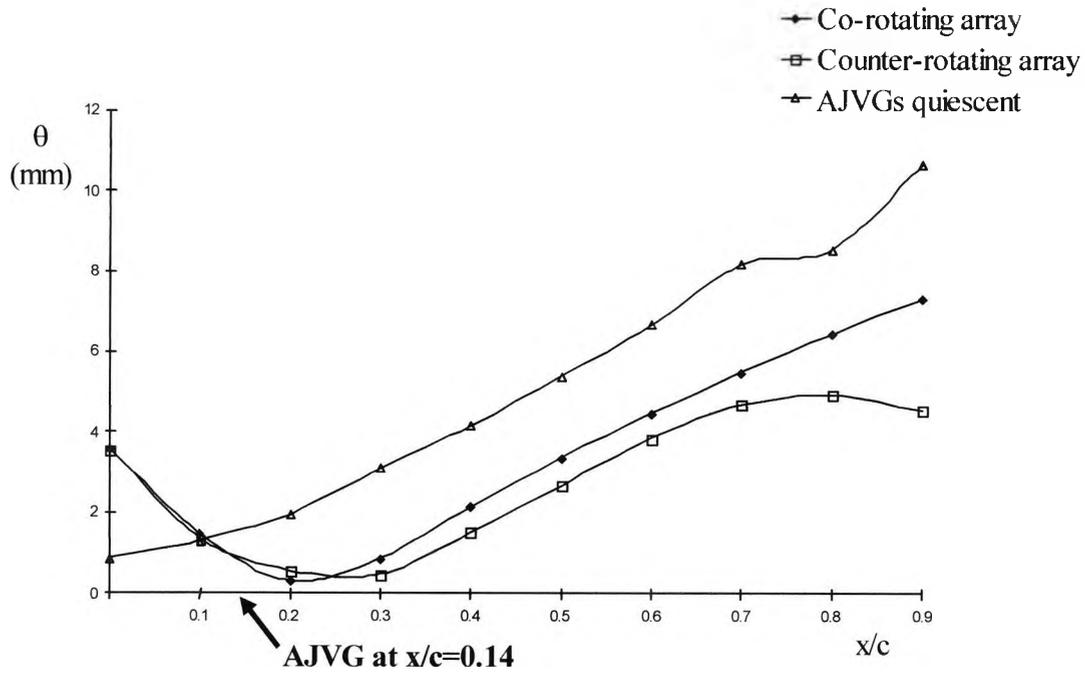
Figure 6.23: Comparison of the momentum thickness (θ) averaged across the model span, with the AJVGs active and inactive, in an adverse pressure gradient flow, $Re_c=1.37\times10^6$, $M_\infty=0.12$, S=0.076, $V_R=3$, $\phi=45°$, $\psi=60°$
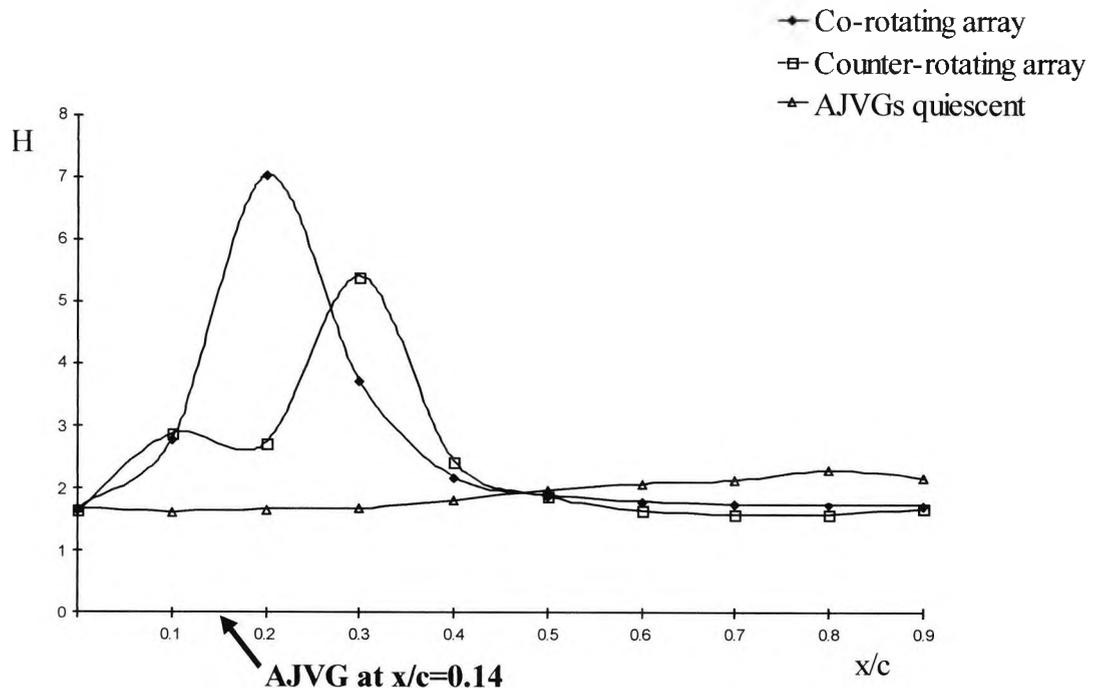
Figure 6.24: Comparison of the shape parameter (H) averaged across the model span, with the AJVGs active and inactive, in an adverse pressure gradient flow, $Re_c=1.37\times10^6$, $M_\infty=0.12$, S=0.076, $V_R=3$, $\phi=45°$, $\psi=60°$

$$I\Delta C_f = \frac{1}{S} \int_0^s \Delta C_f d\left(\frac{z}{c}\right)$$
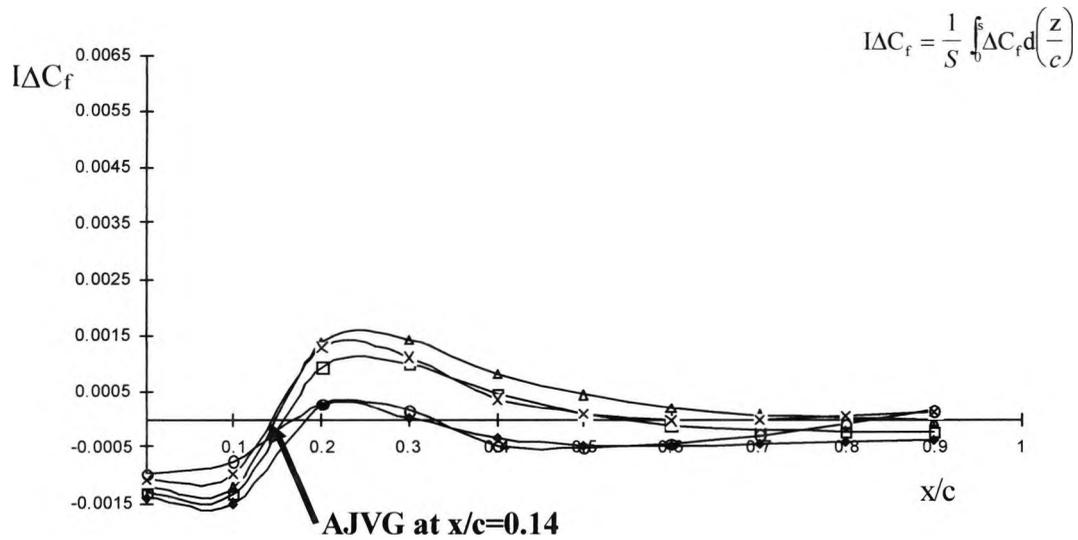
(a) Co-rotating AJVG array
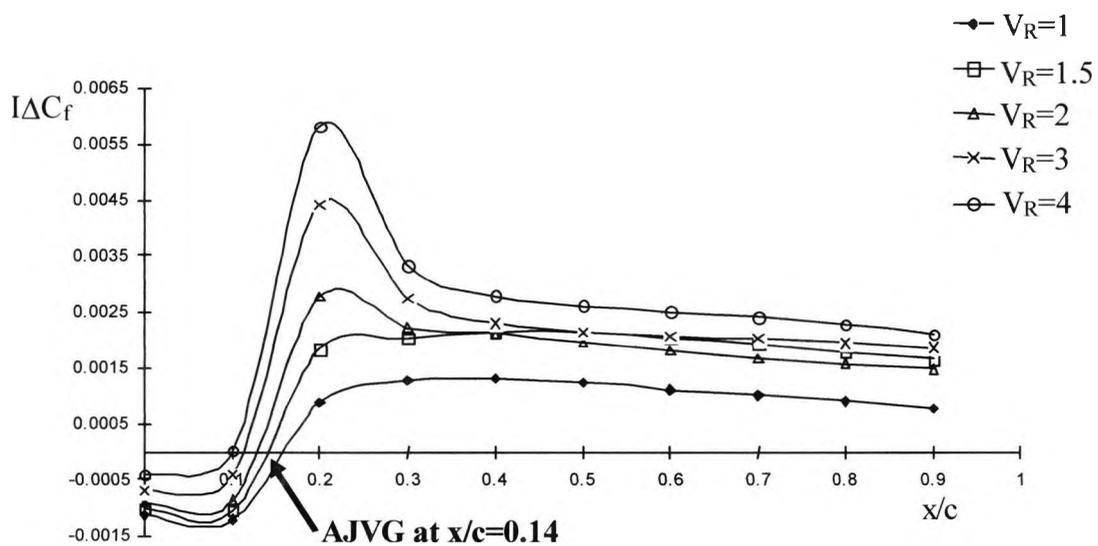
(b) Counter-rotating AJVG array

Figure 6.25: Axial variation of the integrated surface skin friction enhancement, $I\Delta C_f$, with increasing jet velocity ratio, in an adverse pressure gradient flow, **Jet spacing (S)=0.051**, $Re_c=1.37\times10^6$, $M_\infty=0.12$, $\phi=45°$, $\psi=60°$

$$IΔC_f = \frac{1}{S} \int_0^s ΔC_f d\left(\frac{z}{c}\right)$$
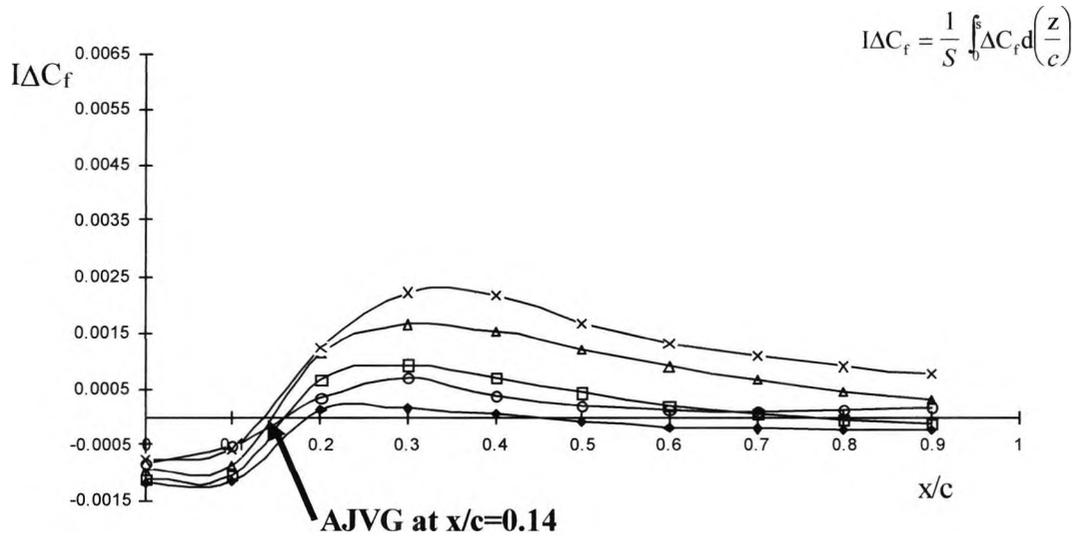
(a) Co-rotating AJVG array
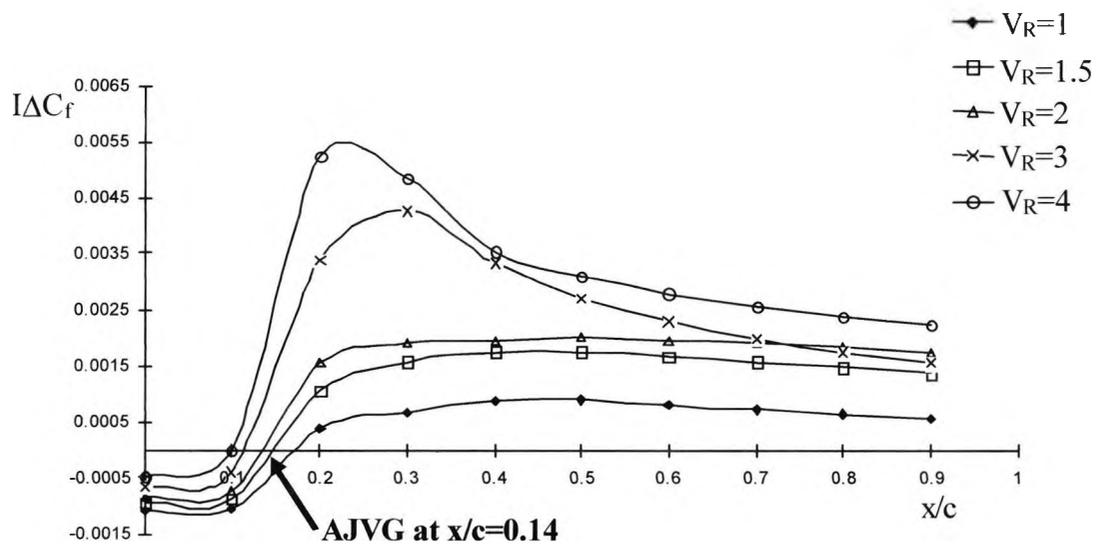
(b) Counter-rotating AJVG array

Figure 6.26: Axial variation of the integrated surface skin friction enhancement, $IΔC_f$, with increasing jet velocity ratio, in an adverse pressure gradient flow, **Jet spacing (S)=0.076**, $Re_c=1.37×10^6$, $M_∞=0.12$, $\phi=45°$, $\psi=60°$

$$I\Delta C_f = \frac{1}{S}\int_0^s \Delta C_f\, d\left(\frac{z}{c}\right)$$
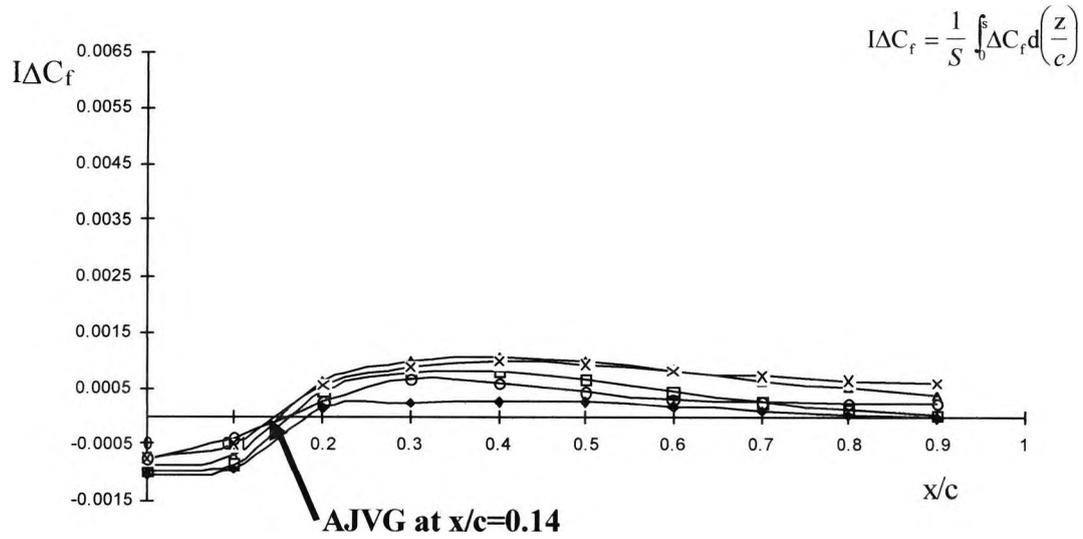
(a) Co-rotating AJVG array
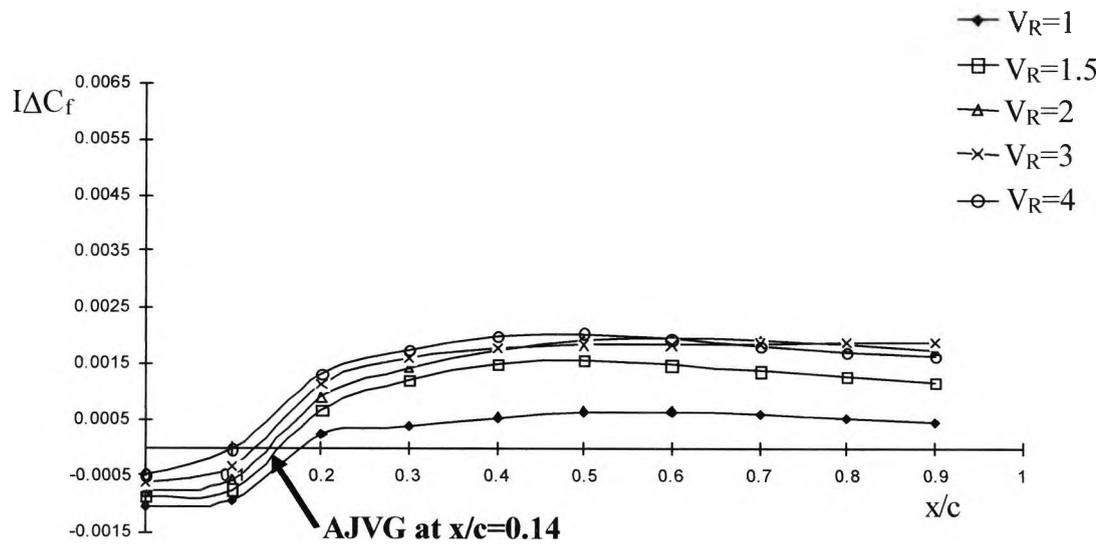
(b) Counter-rotating AJVG array

Figure 6.27: Axial variation of the integrated surface skin friction enhancement, $I\Delta C_f$, with increasing jet velocity ratio, in an adverse pressure gradient flow, **Jet spacing (S)=0.106**, $Re_c=1.37\times10^6$, $M_\infty=0.12$, $\phi=45°$, $\psi=60°$

$$I\Delta C_f = \frac{1}{S} \int_0^s \Delta C_f d\left(\frac{z}{c}\right)$$
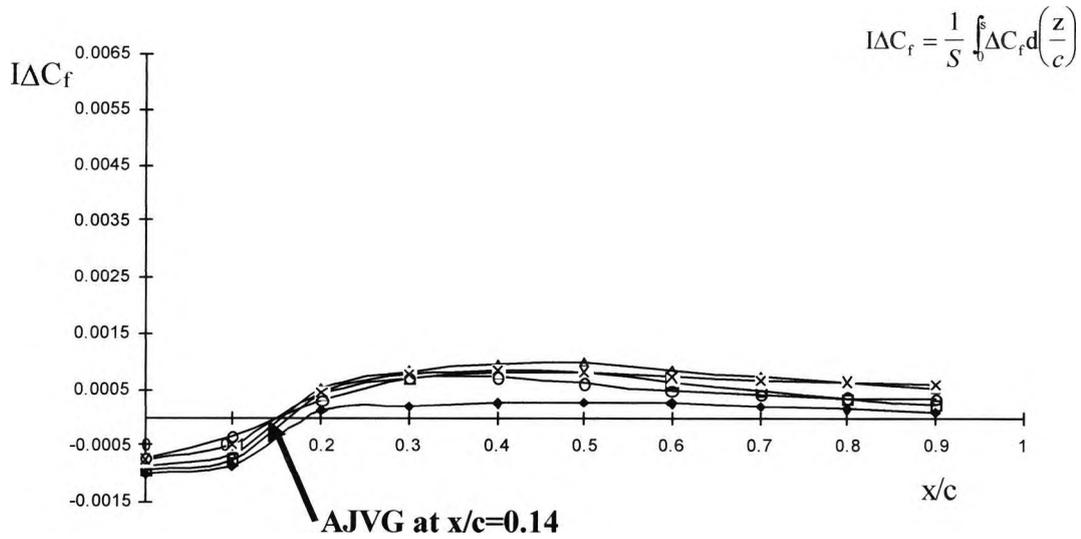
(a) Co-rotating AJVG array
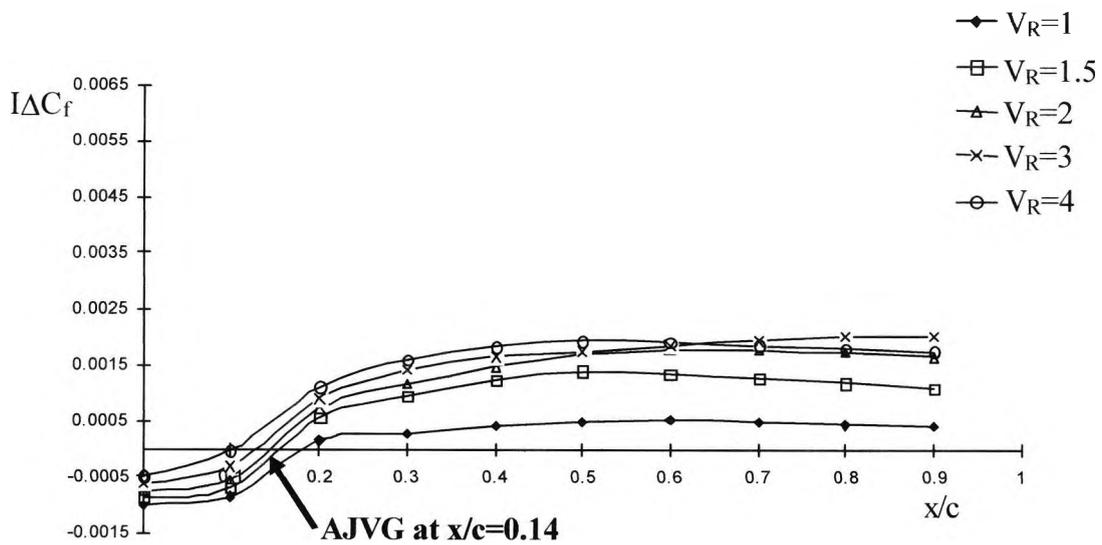
(b) Counter-rotating AJVG array

Figure 6.28: Axial variation of the integrated surface skin friction enhancement, $I\Delta C_f$, with increasing jet velocity ratio, in an adverse pressure gradient flow, **Jet spacing (S)=0.127**, $Re_c=1.37\times10^6$, $M_\infty=0.12$, $\phi=45°$, $\psi=60°$

$$I\Delta C_f = \frac{1}{S} \int_0^s \Delta C_f d\left(\frac{z}{c}\right)$$
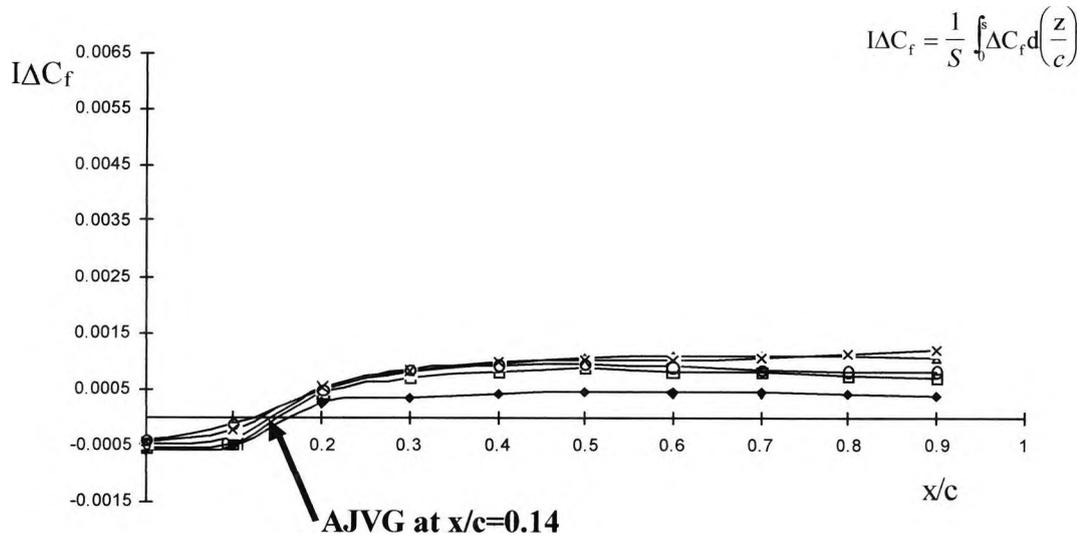
(a) Co-rotating AJVG array
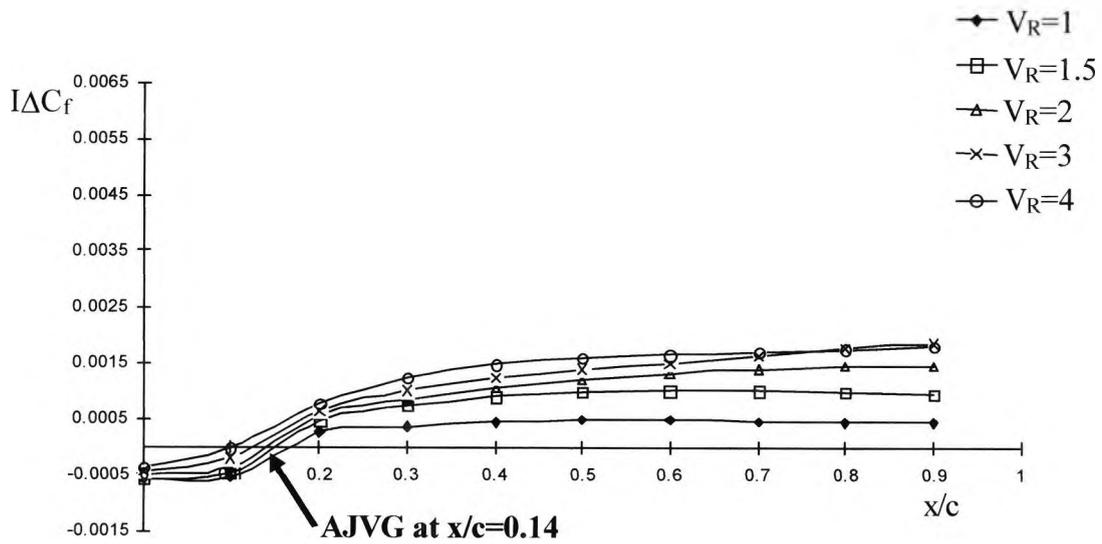
(b) Counter-rotating AJVG array

Figure 6.29: Axial variation of the integrated surface skin friction enhancement, $I\Delta C_f$, with increasing jet velocity ratio, in an adverse pressure gradient flow, **Jet spacing (S)=0.203**, $Re_c=1.37\times10^6$, $M_\infty=0.12$, $\phi=45°$, $\psi=60°$

$$I\Delta C_f = \frac{1}{S} \int_0^s \Delta C_f d\left(\frac{z}{c}\right)$$
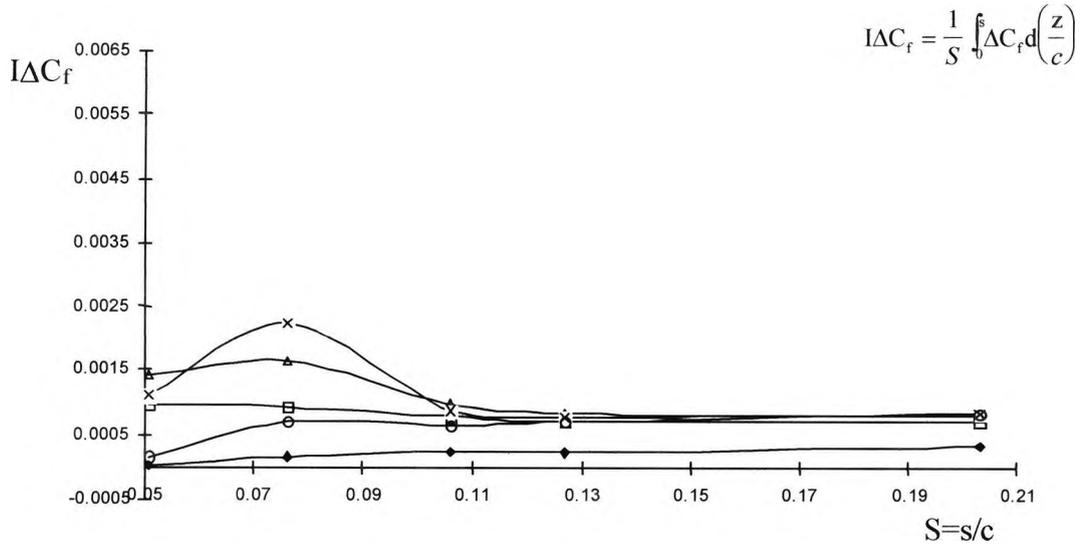
(a) Co-rotating AJVG array
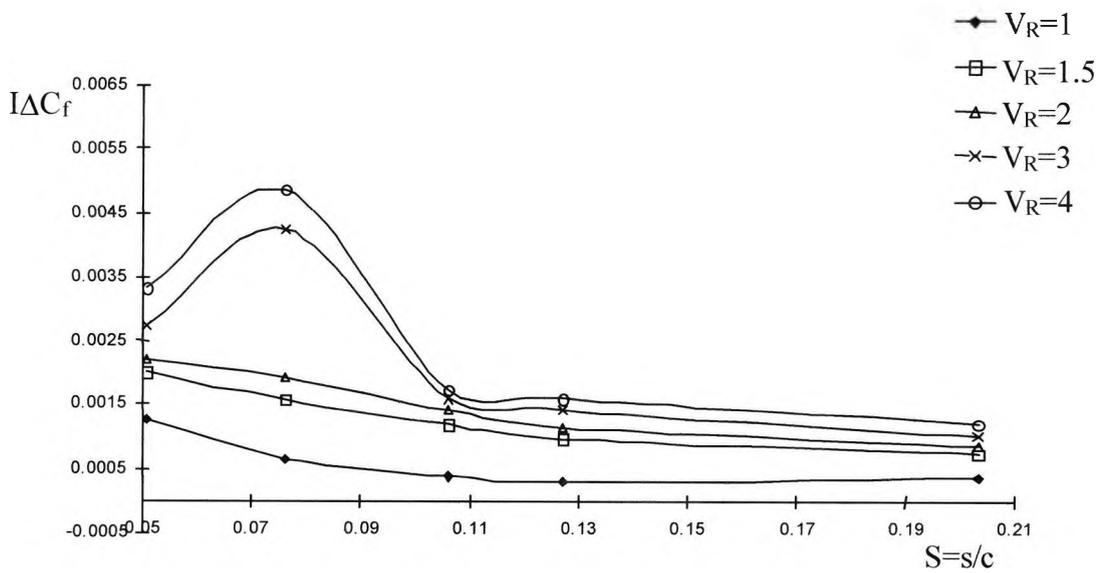
(b) Counter-rotating AJVG array

Figure 6.30: Variation of the integrated surface skin friction enhancement, $I\Delta C_f$, with jet spacing and jet velocity ratio, in an adverse pressure gradient flow, **x/c=0.3**, $Re_c = 1.37 \times 10^6$, $M_\infty = 0.12$, $\phi = 45°$, $\psi = 60°$

$$I\Delta C_f = \frac{1}{S} \int_0^s \Delta C_f d\left(\frac{z}{c}\right)$$

(a) Co-rotating AJVG array

(b) Counter-rotating AJVG array
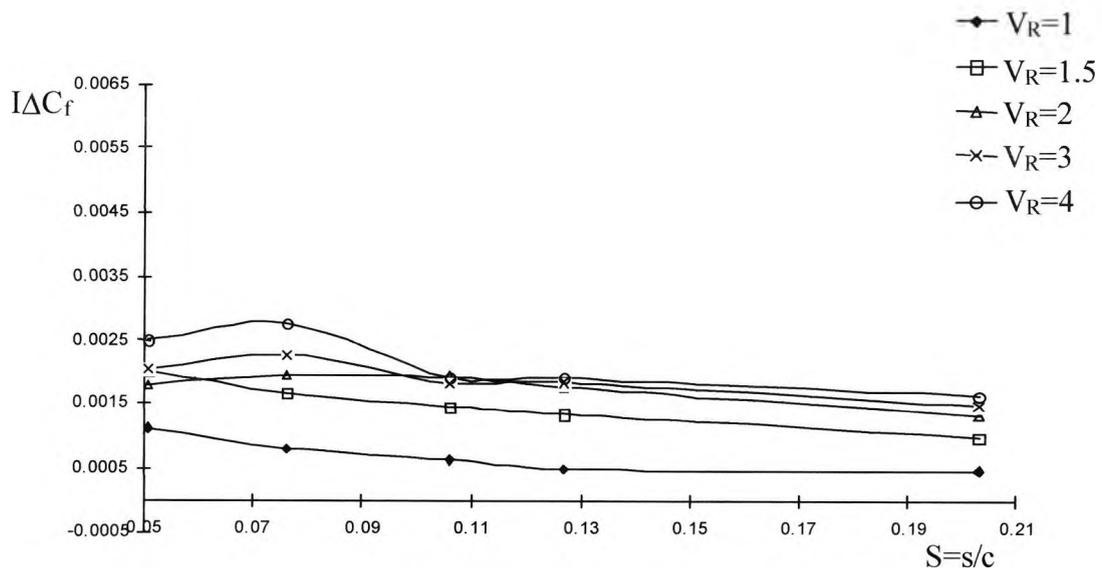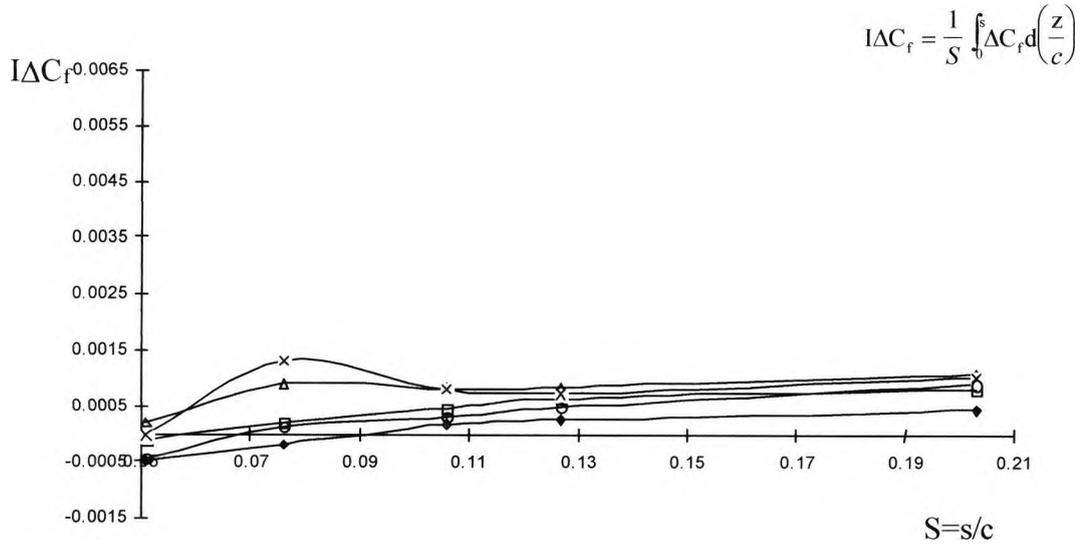
Figure 6.31: Variation of the integrated surface skin friction enhancement, $I\Delta C_f$, with jet spacing and jet velocity ratio, in an adverse pressure gradient flow, **x/c=0.6**, $Re_c=1.37\times10^6$, $M_\infty=0.12$, $\phi=45°$, $\psi=60°$

$$I\Delta C_f = \frac{1}{S} \int_0^s \Delta C_f d\left(\frac{z}{c}\right)$$

(a) Co-rotating AJVG array

(b) Counter-rotating AJVG array

Figure 6.32: Variation of the integrated surface skin friction enhancement, $I\Delta C_f$, with jet spacing and jet velocity ratio, in an adverse pressure gradient flow, **x/c=0.9**, $Re_c=1.37\times10^6$, $M_\infty=0.12$, $\phi=45°$, $\psi=60°$

Appendix C: Three-dimensional high lift system results incorporating an air-jet vortex generator array

Figures 7.2 to 7.29 inclusive
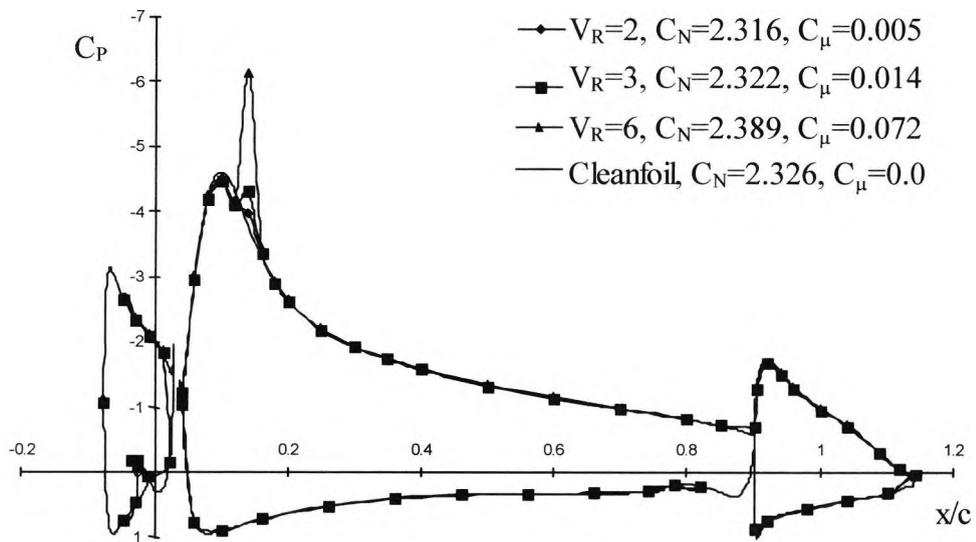
(a) Co-rotating AJVGs
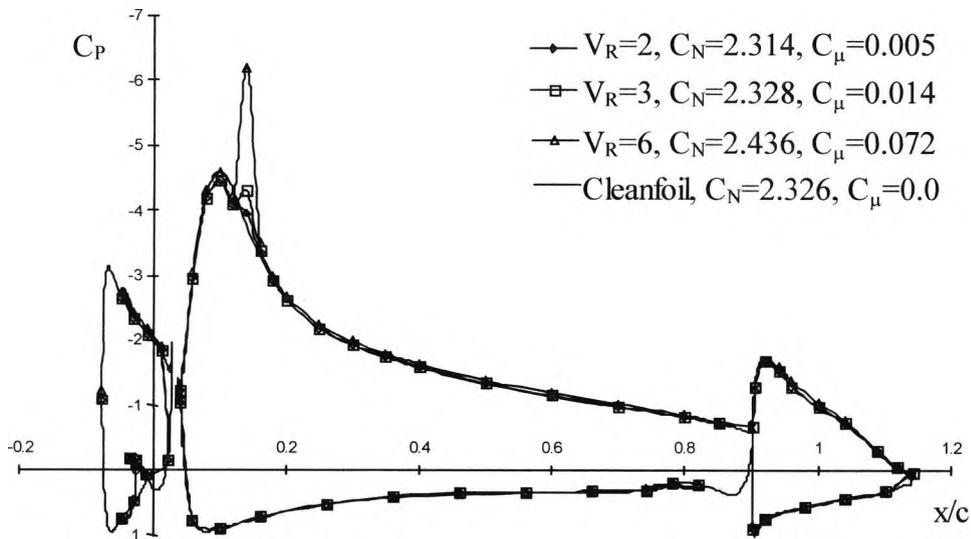
(b) Counter-rotating AJVGs

Figure 7.2: Predicted sensitivity of the CFX-determined chordwise surface pressure distribution to the jet-to-freestream velocity ratio (V_R), at an angle of attack of $\alpha=10°$ [Blowing at x/c=0.14, $Re_c=1.37\times10^6$, $M_\infty=0.12$, AJVG S =0.106, $\phi=45°$, $\psi=60°$]
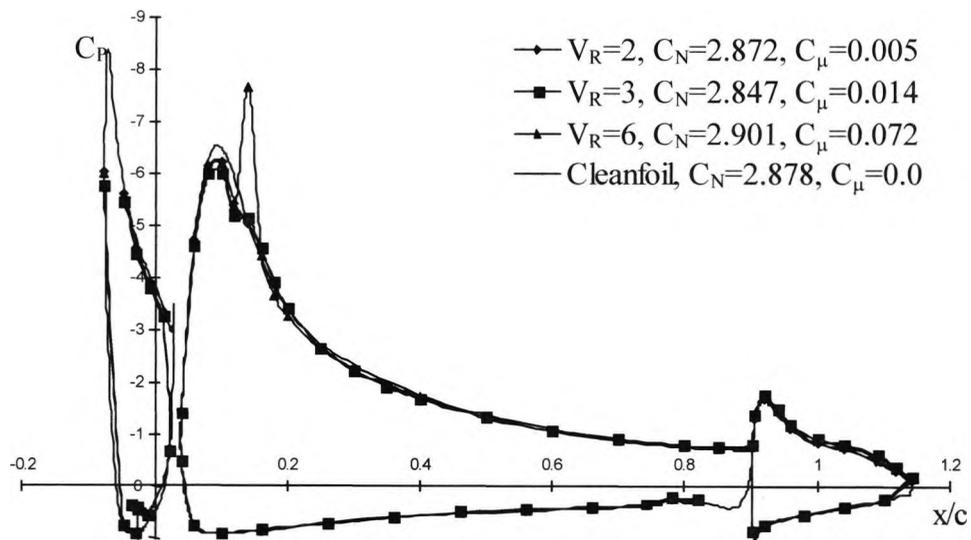
(a) Co-rotating AJVGs
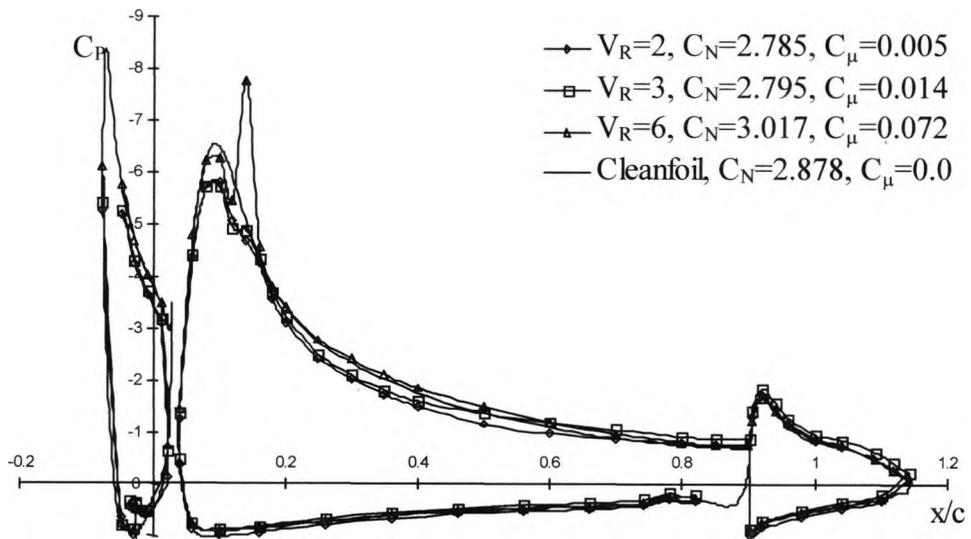
(b) Counter-rotating AJVGs

Figure 7.3: Predicted sensitivity of the CFX-determined chordwise surface pressure distribution to the jet-t- freestream velocity ratio (V_R), at an angle of attack of α=**20°** [Blowing at x/c=0.14, Re_c=1.37×10^6, M_∞=0.12, S=0.106, ϕ=45°, ψ=60°]
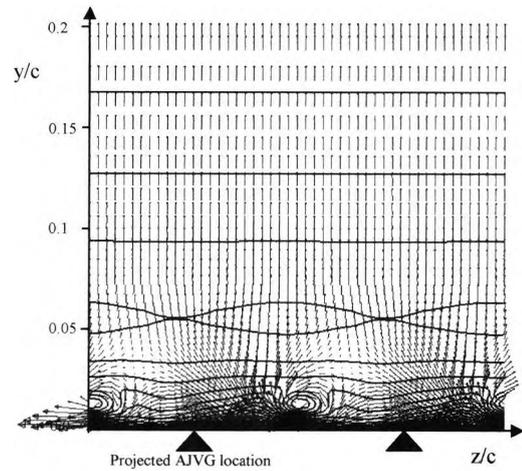
(a) Co-rotating array (x/c=0.25)
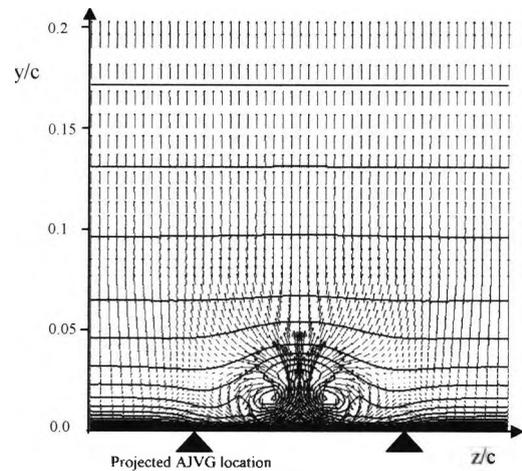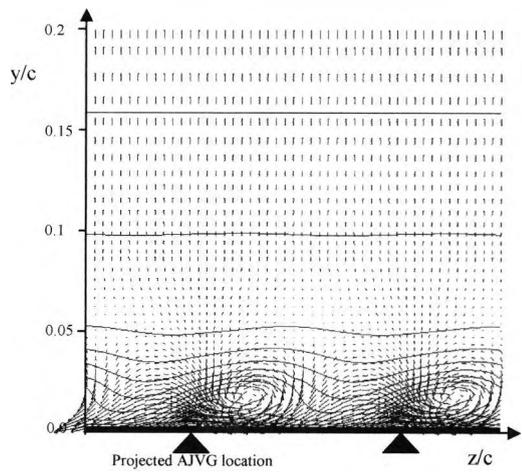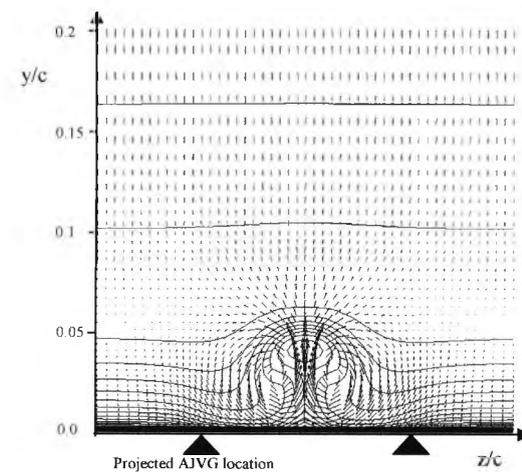
(b) Counter-rotating array (x/c=0.25)

(c) Co-rotating array (x/c=0.35)

(d) Counter-rotating array (x/c=0.35)
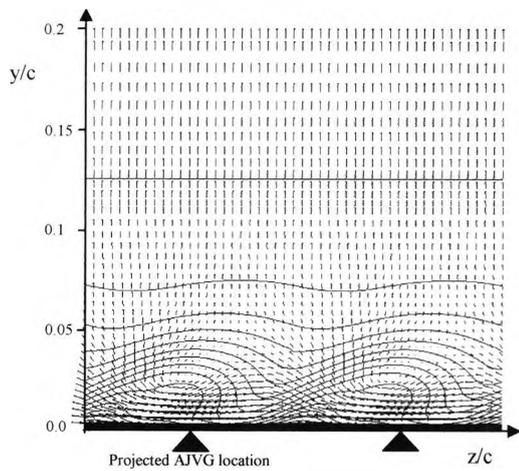
(e) Co-rotating array (x/c=0.6)
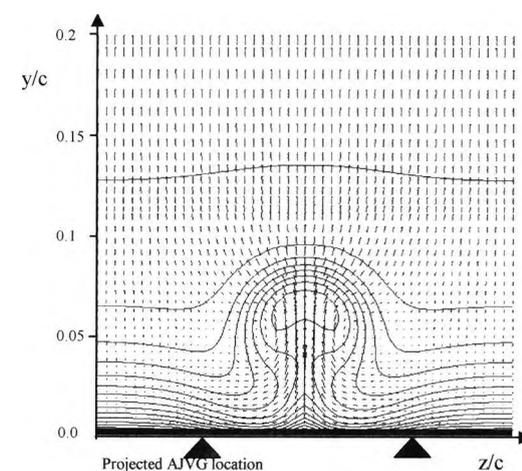
(f) Counter-rotating array (x/c=0.6)

Figure 7.4: Velocity contours and velocity vectors in the crossflow plane, normal to the aerofoil surface, at five chordwise locations at $\alpha=10°$ [Blowing at x/c=0.14, V_R=6, Re_c=1.3×10^6, M_∞=0.12, S=0.106, ϕ=45°, ψ=60°, C_μ=0.072]
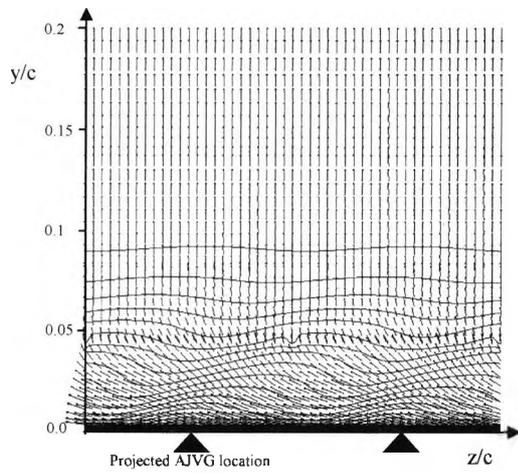
(g) Co-rotating array (x/c=0.9)
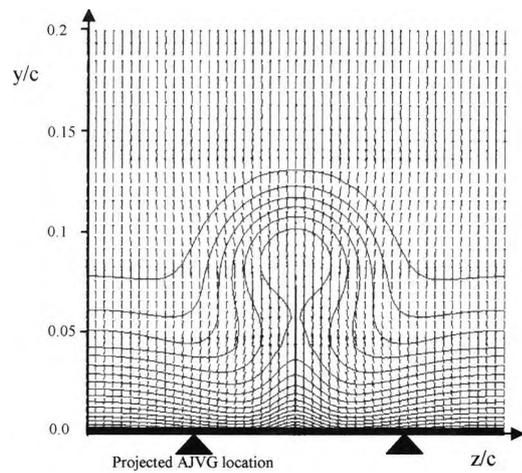
(h) Counter-rotating array (x/c=0.9)
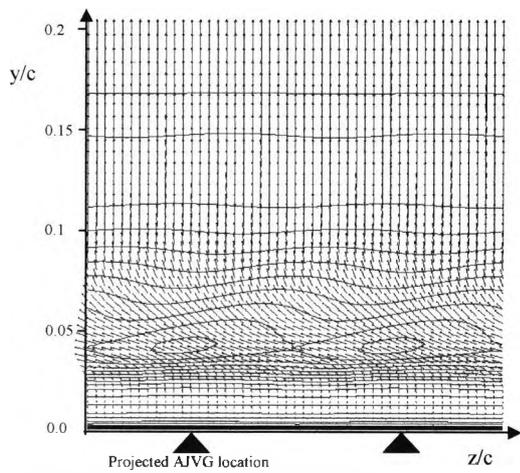
(i) Co-rotating array (x/c=1.0)
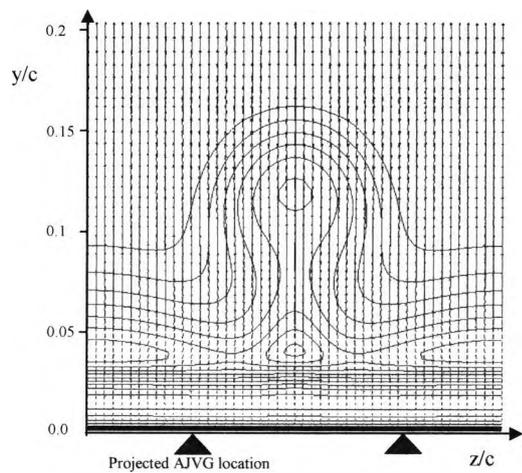
(j) Counter-rotating array (x/c=1.0)

Figure 7.4 (contd.): Velocity contours and velocity vectors in the crossflow plane, normal to the aerofoil surface, at five chordwise locations at $\alpha=10°$ [Blowing at x/c=0.14, V_R=6, Re_c=1.3×10^6, M_∞=0.12, S=0.106, ϕ=45°, ψ=60°, C_μ=0.072]

241
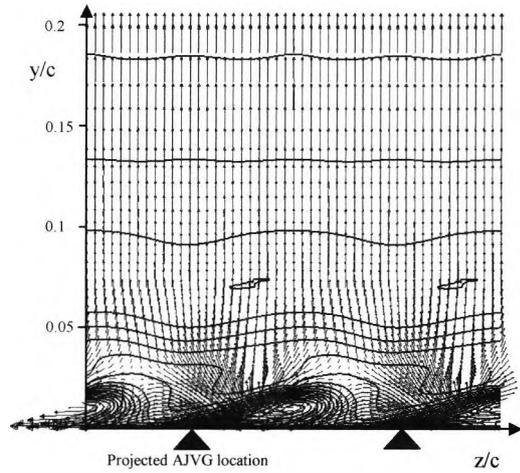
(a) Co-rotating array (x/c=0.25)
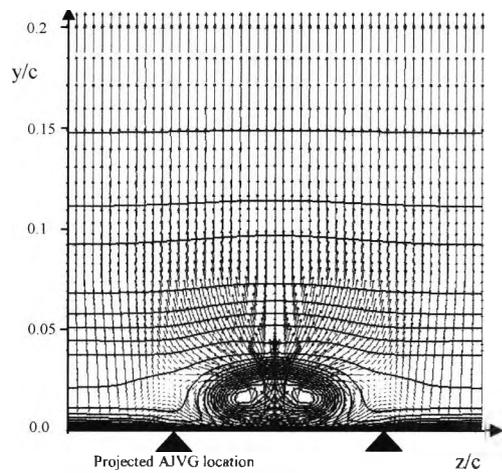
(b) Counter-rotating array (x/c=0.25)
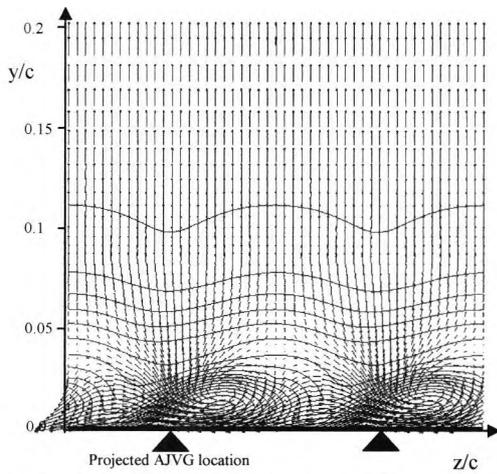
(c) Co-rotating array (x/c=0.35)
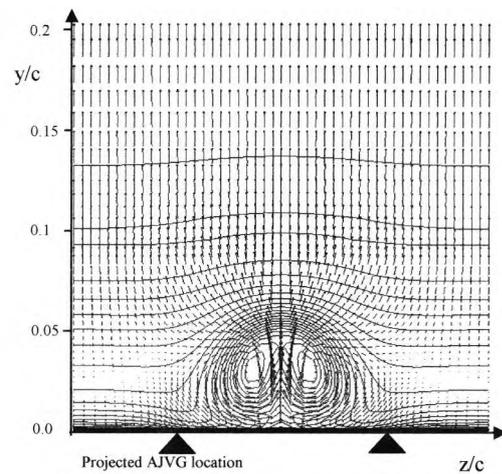
(d) Counter-rotating array (x/c=0.35)
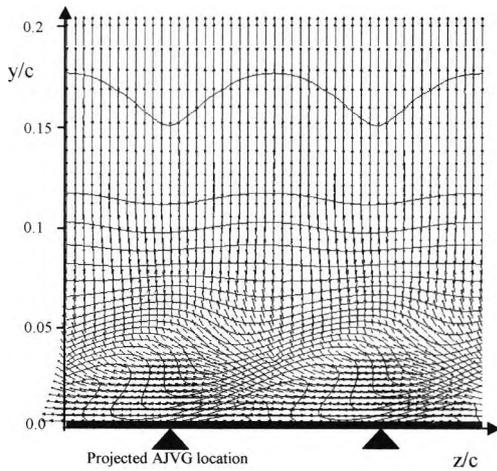
(e) Co-rotating array (x/c=0.6)
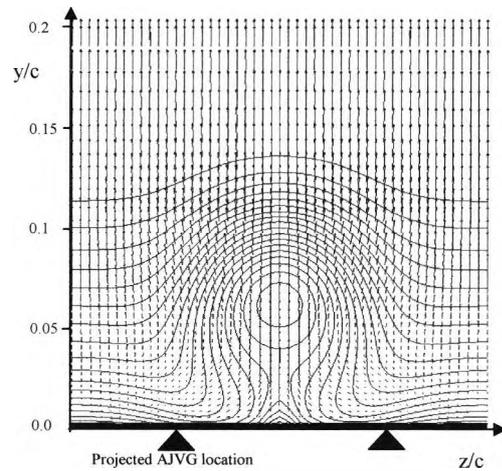
(f) Counter-rotating array (x/c=0.6)

Figure 7.5: Velocity contours and velocity vectors in the crossflow plane, normal to the aerofoil surface, at five chordwise locations at $\alpha=20°$ [Blowing at x/c=0.14, V_R=6, Re_c=1.3×10^6, M_∞=0.12, S=0.106, ϕ=45°, ψ=60°, C_μ=0.072]
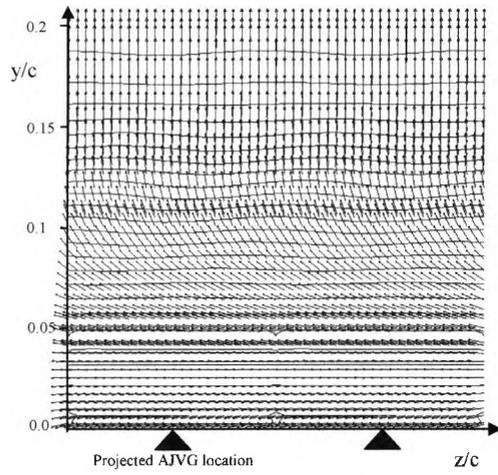
(g) Co-rotating array (x/c=0.9)
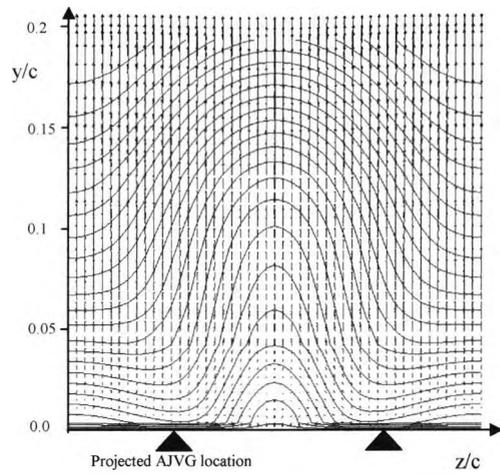
(h) Counter-rotating array (x/c=0.9)
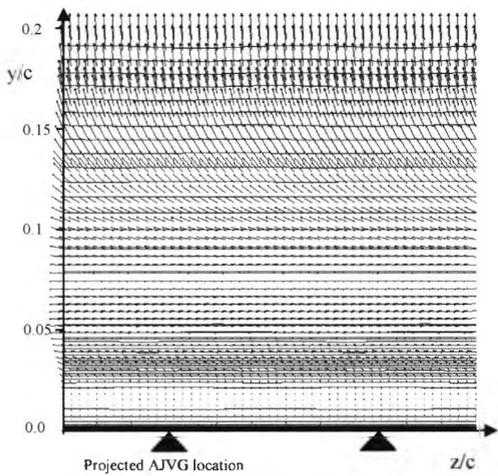
(i) Co-rotating array (x/c=1.0)
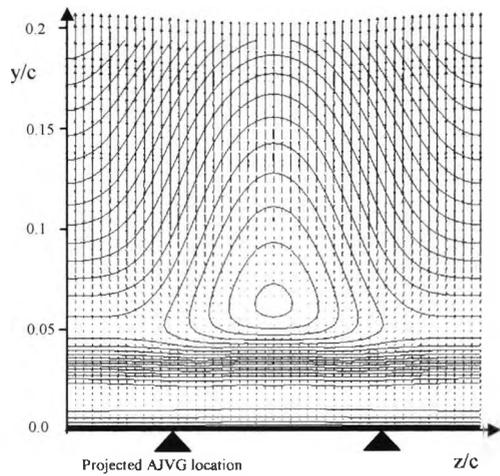
(j) Counter-rotating array (x/c=1.0)

Figure 7.5 (contd.): Velocity contours and velocity vectors in the crossflow plane, normal to the aerofoil surface, at five chordwise locations at $\alpha=20°$ [Blowing at x/c=0.14, V_R=6, Re_c=1.3×10^6, M_∞=0.12, S=0.106, ϕ=45°, ψ=60°, C_μ=0.072]
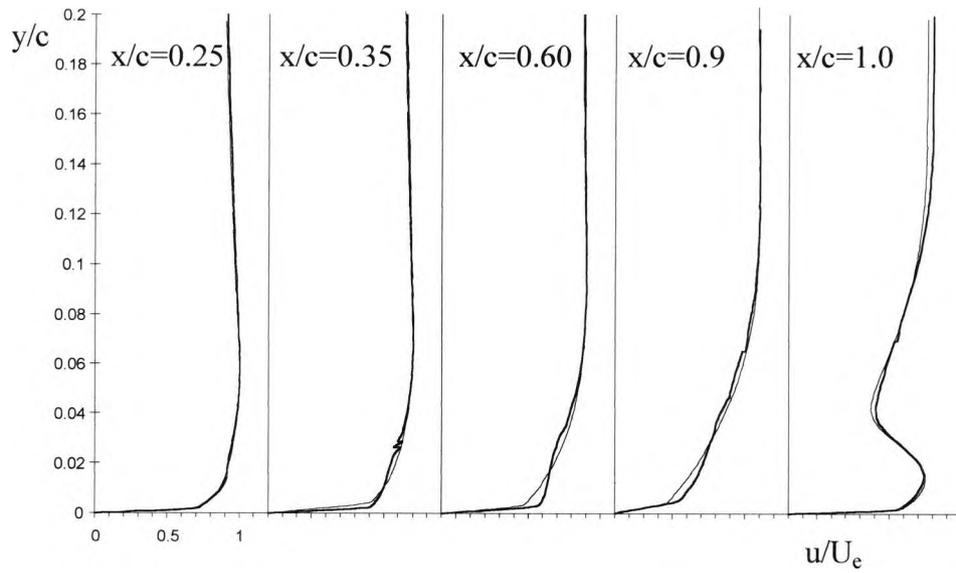
(a) Co-rotating AJVGs

—— AJVGs active, V_R=6
AJVGs quiescent, V_R=0
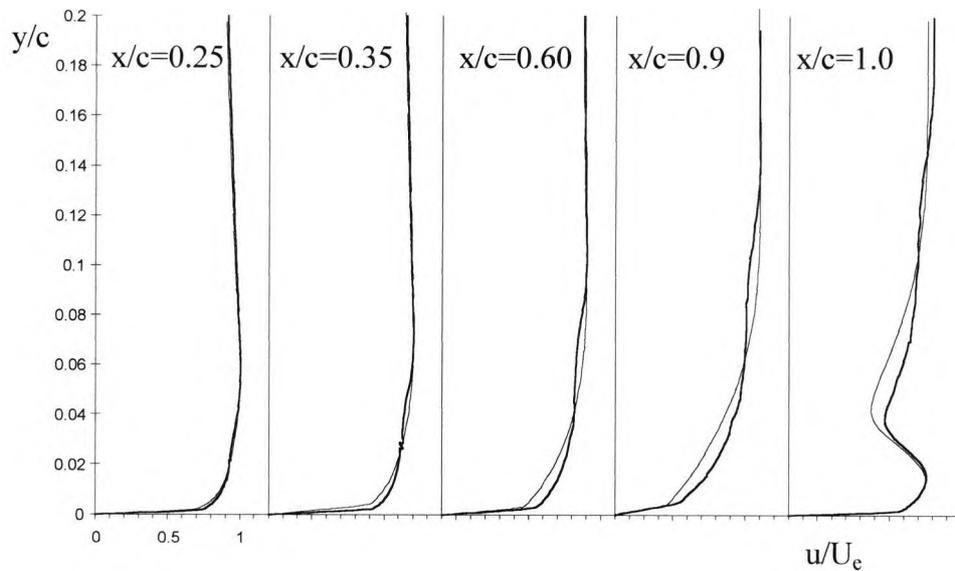
(b) Counter-rotating AJVGs

Figure 7.6: Comparison between the CFX-determined average spanwise axial velocity profiles, on the high lift system mainfoil upper surface, with varying V_R at α=**10°** [Blowing at x/c=0.14, Re_c=1.3×10^6, M_∞=0.12, S=0.106, ϕ=45°, ψ=60°, C_μ=0.072]
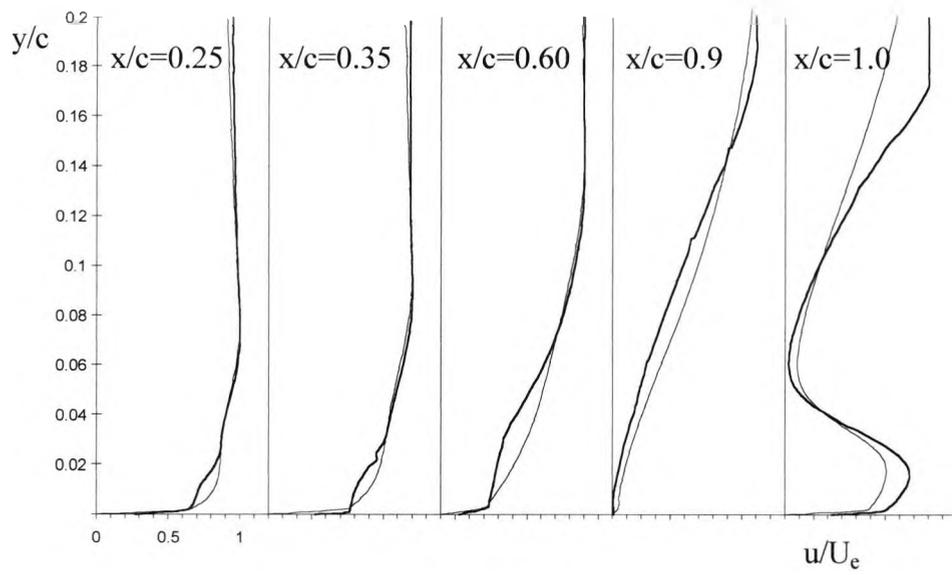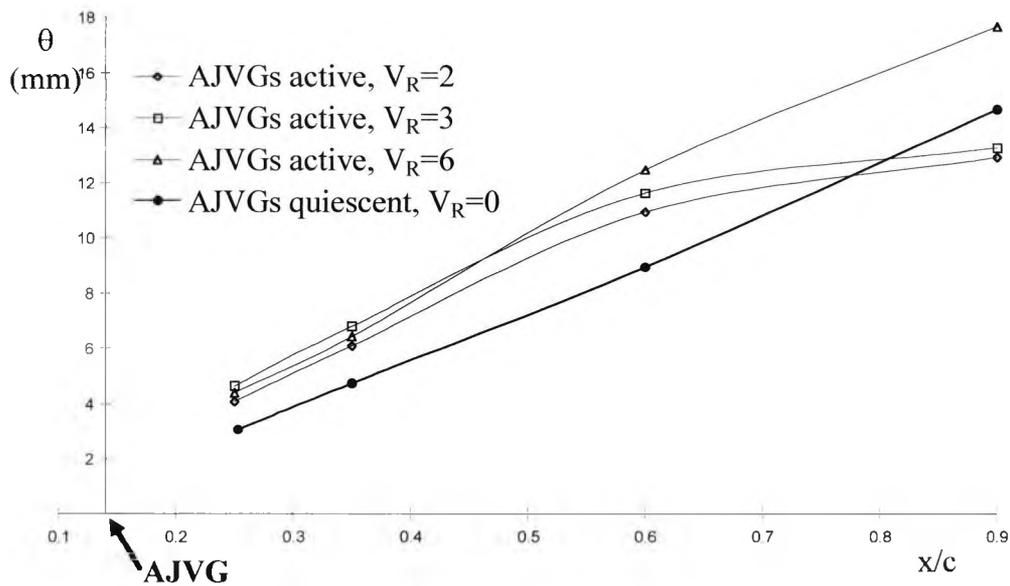
(a) Co-rotating AJVGs

AJVGs active, V_R=6

AJVGs quiescent, V_R=0
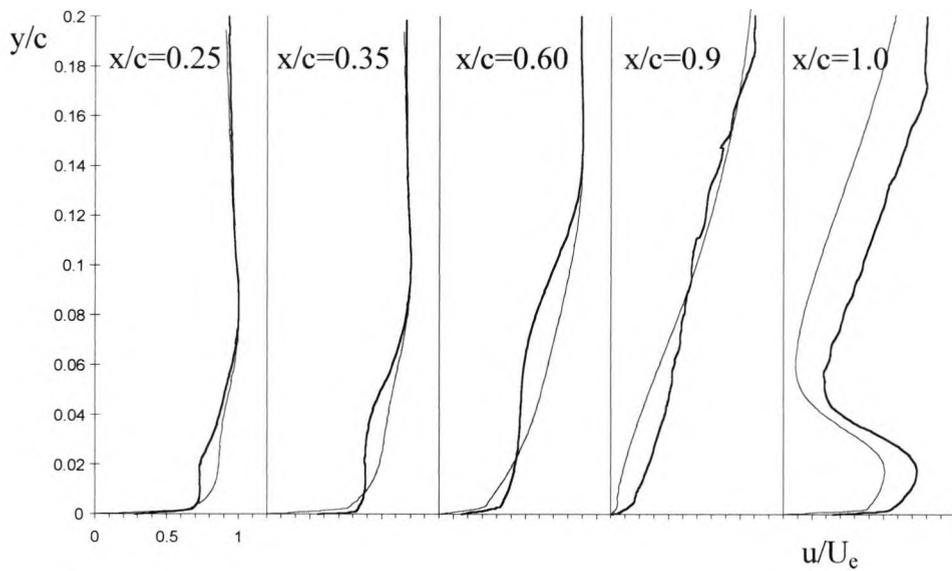
(b) Counter-rotating AJVGs

Figure 7.7: Comparison between the CFX-determined average spanwise axial velocity profiles, on the high lift system mainfoil upper surface, with varying V_R at α=**20°** [Blowing at x/c=0.14, Re_c=1.3×10^6, M_∞=0.12, S=0.106, ϕ=45°, ψ=60°, C_μ=0.072]
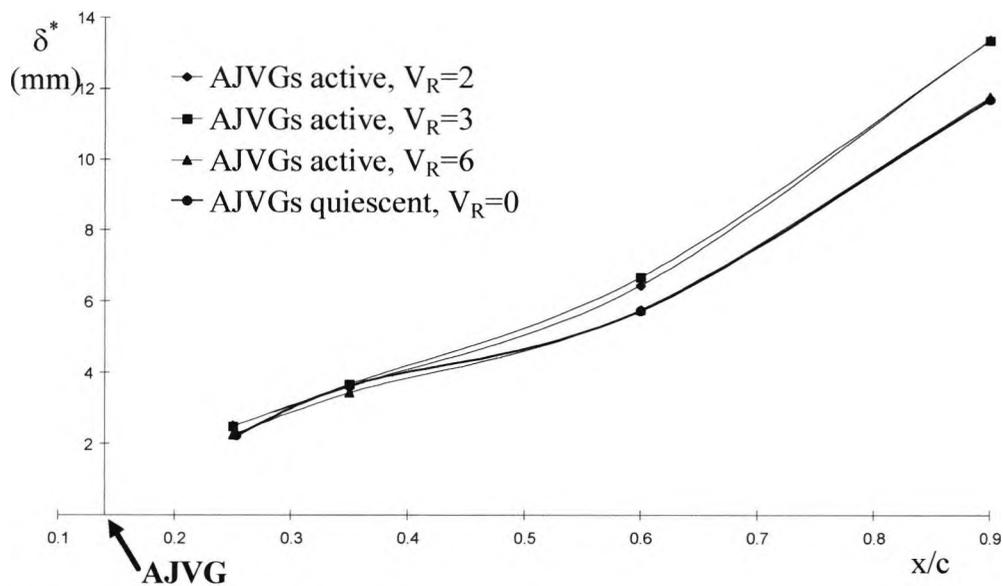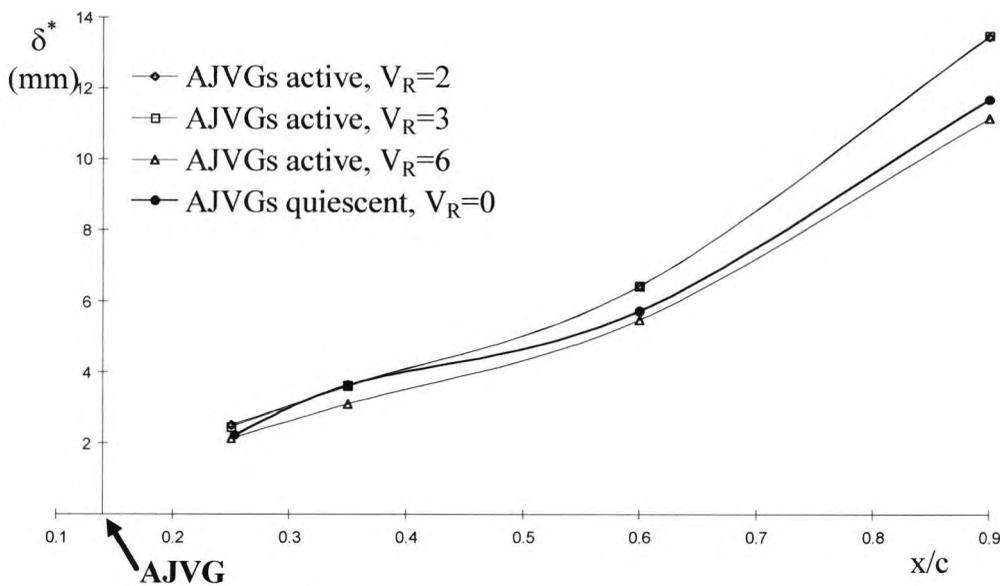
(a) Co-rotating AJVGs

(b) Counter-rotating AJVGs

Figure 7.8: Comparison of the CFX-determined average spanwise displacement thickness (δ^*), on the high lift system mainfoil upper surface, with varying V_R at an angle of attack at $\alpha=10°$ [Blowing at $x/c=0.14$, $Re_c=1.37\times10^6$, $M_\infty=0.12$, $S=0.106$, $\phi=45°$, $\psi=60°$, $C_\mu=0.072$]
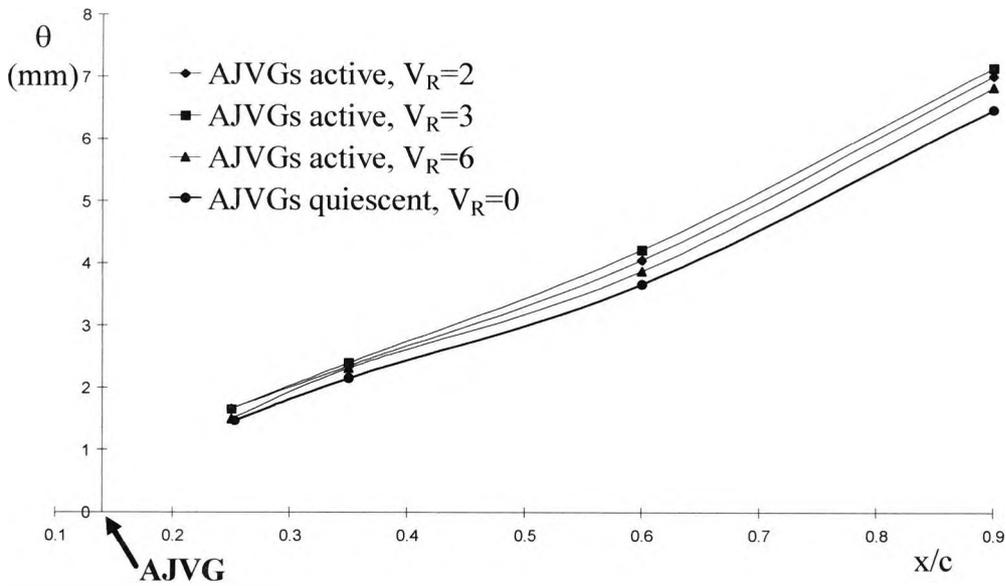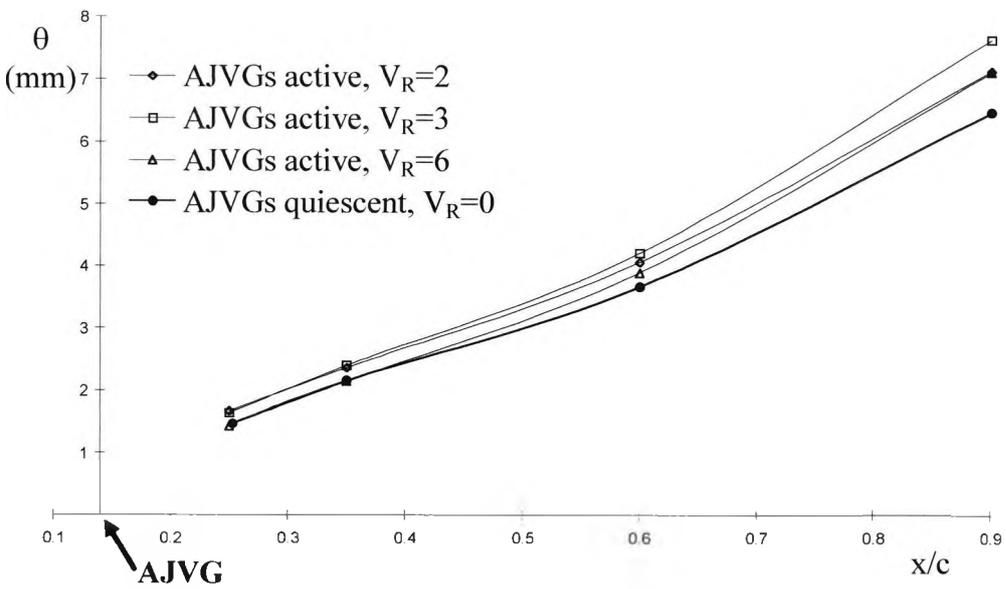
(a) Co-rotating AJVGs
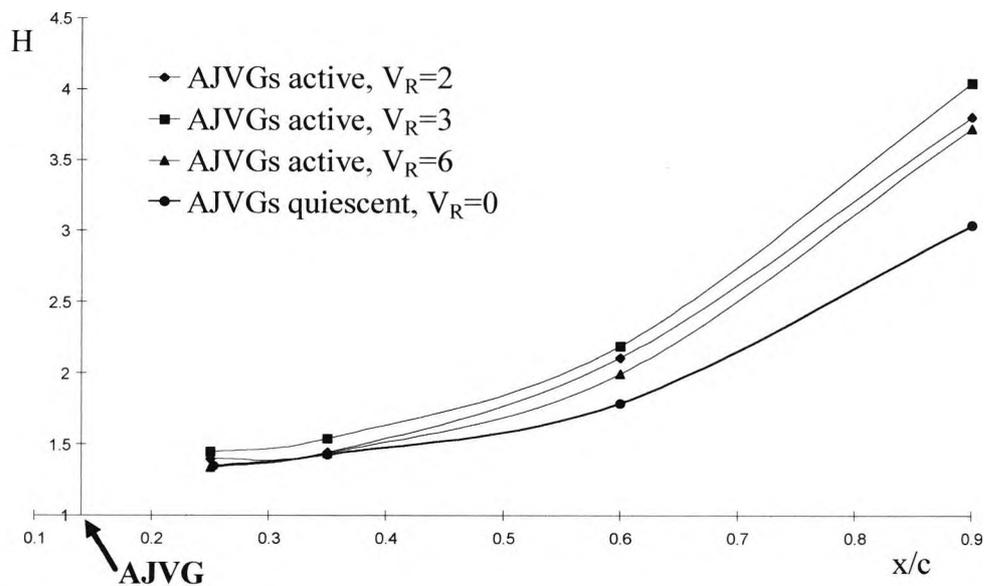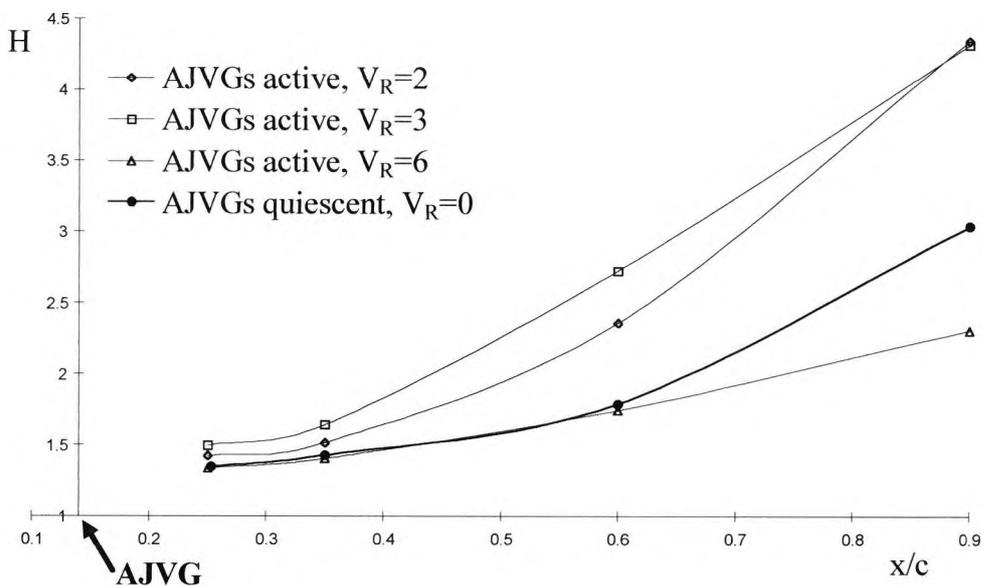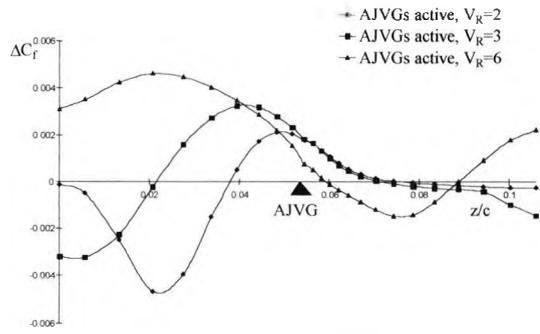

(b) Counter-rotating AJVGs

Figure 7.9: Comparison of the CFX-determined average spanwise momentum thickness (θ), on the high lift system mainfoil upper surface, with varying V_R at $\alpha=10°$ [Blowing at x/c=0.14, $Re_c=1.37\times10^6$, $M_\infty=0.12$, S=0.106, $\phi=45°$, $\psi=60°$, $C_\mu=0.072$]
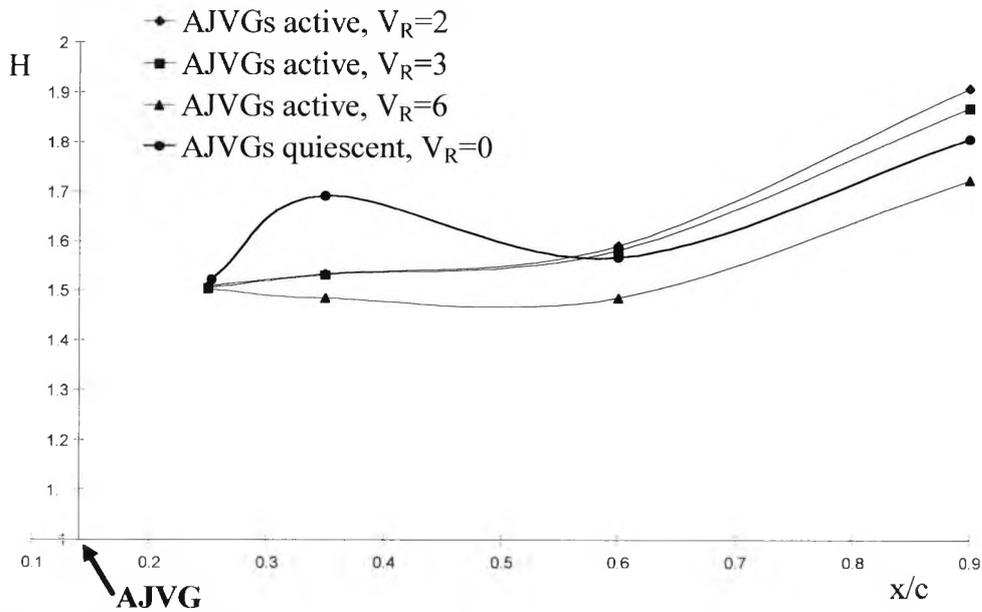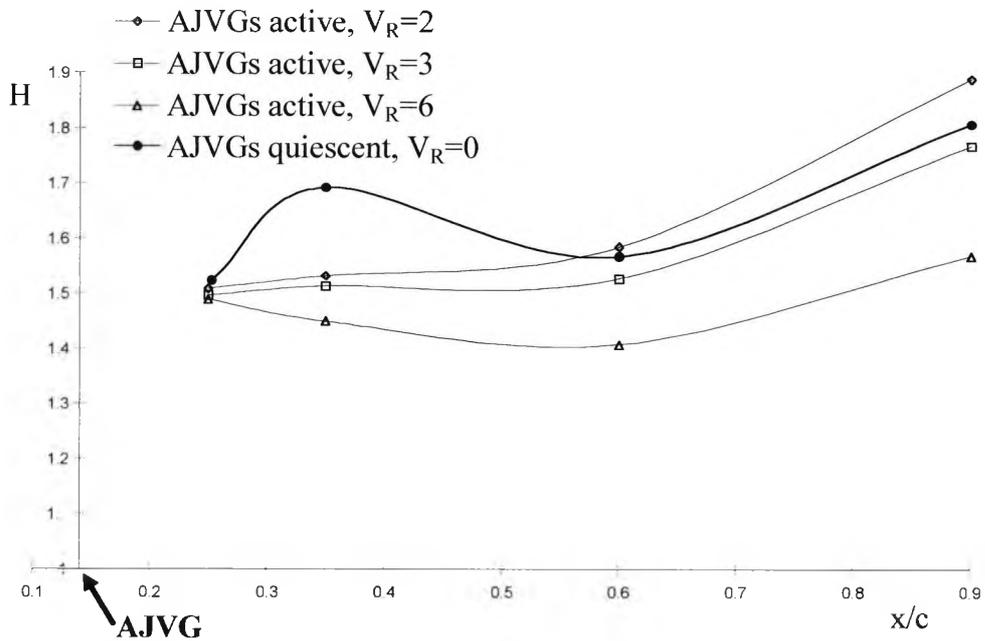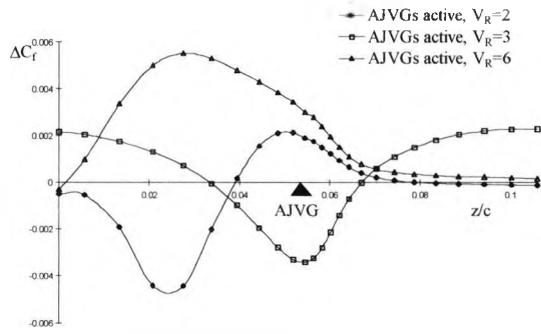
(a) Co-rotating AJVGs
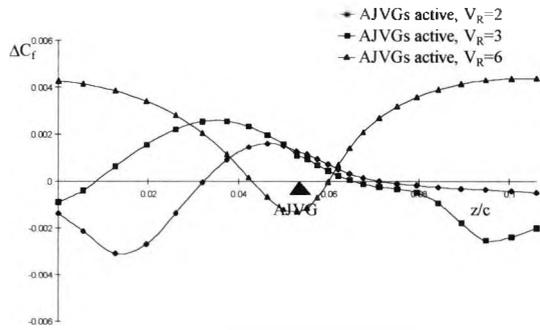

(b) Counter-rotating AJVGs

Figure 7.10: Comparison of the CFX-determined average spanwise shape parameter (**H**), on the high lift system mainfoil upper surface, with varying V_R at $\alpha=10°$ [Blowing at x/c=0.14, $Re_c=1.3\times10^6$, $M_\infty=0.12$, S=0.106, $\phi=45°$, $\psi=60°$, $C_\mu=0.072$]
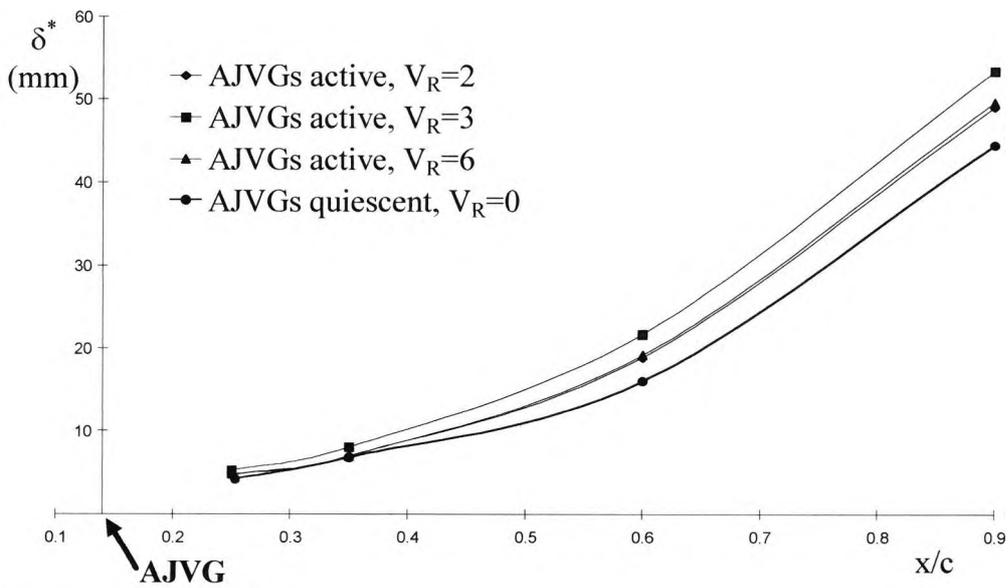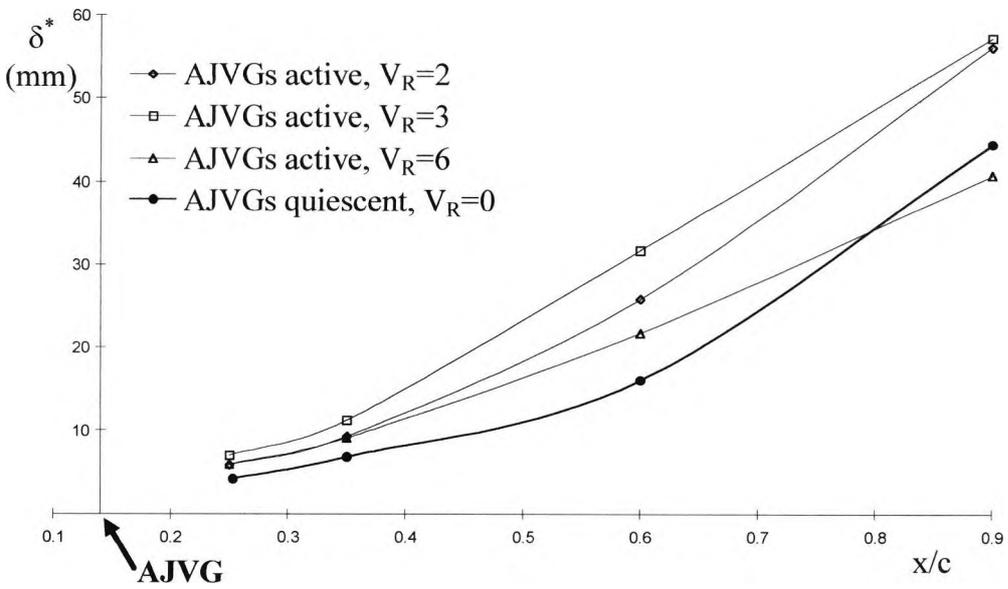
(a) Co-rotating AJVGs

(b) Counter-rotating AJVGs

Figure 7.11: Comparison of the CFX-determined average spanwise displacement thickness (δ^*), on the high lift system mainfoil upper surface, with varying V_R at $\alpha=20°$ [Blowing at x/c=0.14, $Re_c=1.37\times10^6$, $M_\infty=0.12$, S=0.106, $\phi=45°$, $\psi=60°$, $C_\mu=0.072$]
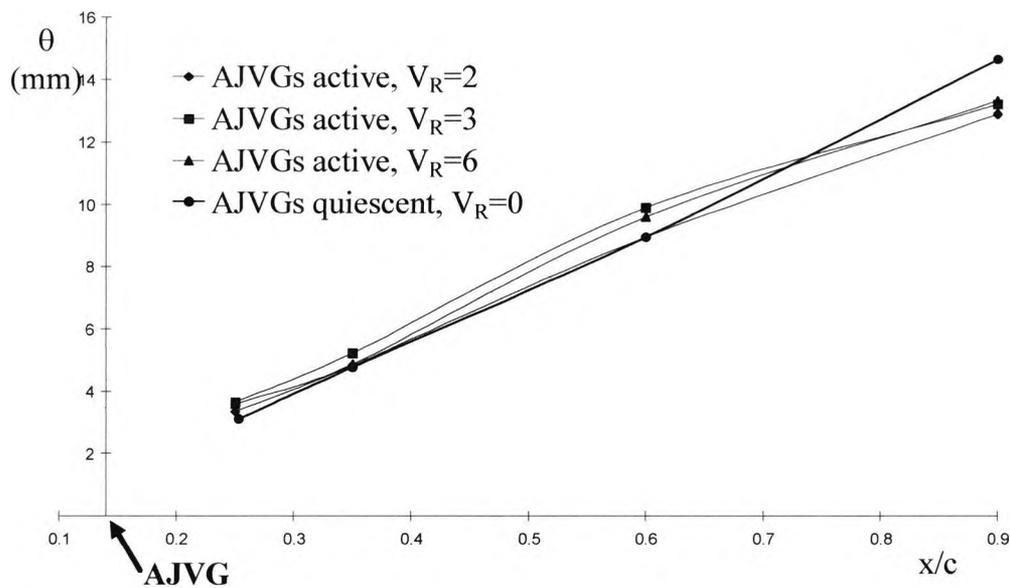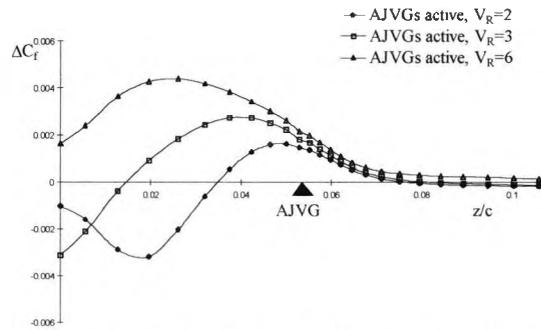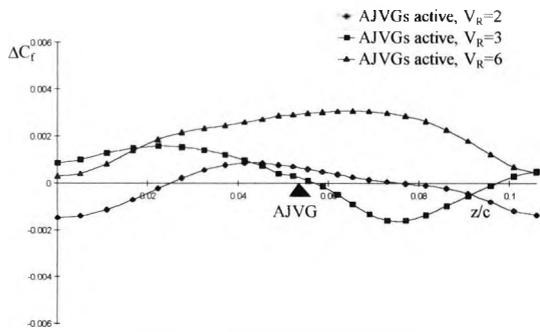
(a) Co-rotating AJVGs

(b) Counter-rotating AJVGs

Figure 7.12: Comparison of the CFX-determined average spanwise momentum thickness (θ), on the high lift system mainfoil upper surface, with varying V_R at $\alpha=20°$ [Blowing at x/c=0.14, $Re_c=1.37\times10^6$, $M_\infty=0.12$, S=0.106, $\phi=45°$, $\psi=60°$, $C_\mu=0.072$]

(a) Co-rotating AJVGs

(b) Counter-rotating AJVGs

Figure 7.13: Comparison of the CFX-determined average spanwise shape parameter (**H**), on the high lift system mainfoil upper surface, with varying V_R at α=**20°** [Blowing at x/c=0.14, Re_c=1.3×10^6, M_∞=0.12, S=0.106, ϕ=45°, ψ=60°, C_μ=0.072]
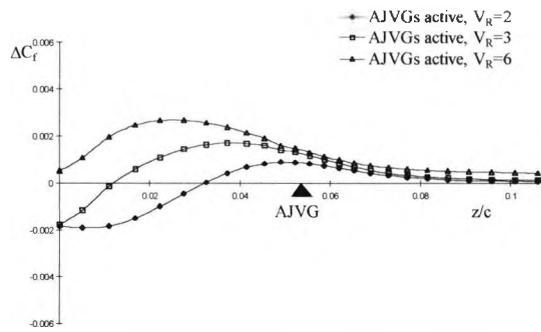
(a) Co-rotating AJVGs (x/c=0.25)

(b) Counter-rotating AJVGs (x/c=0.25)

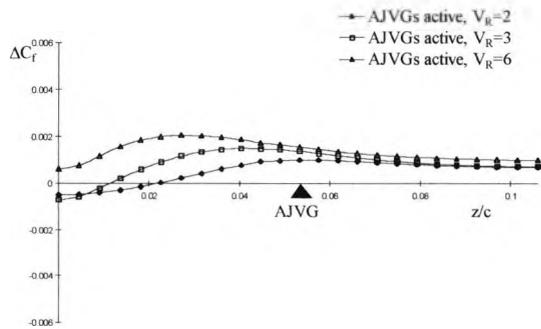(c) Co-rotating AJVGs (x/c=0.35)

(d) Counter-rotating AJVGs (x/c=0.35)

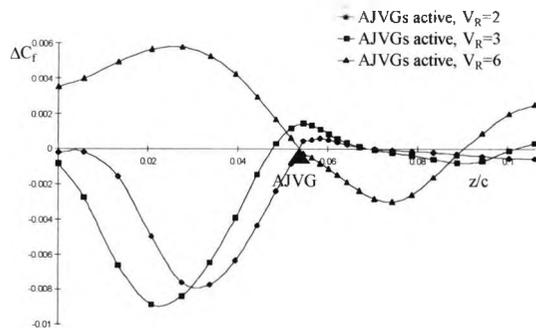(e) Co-rotating AJVGs (x/c=0.6)

(f) Counter-rotating AJVGs (x/c=0.6)
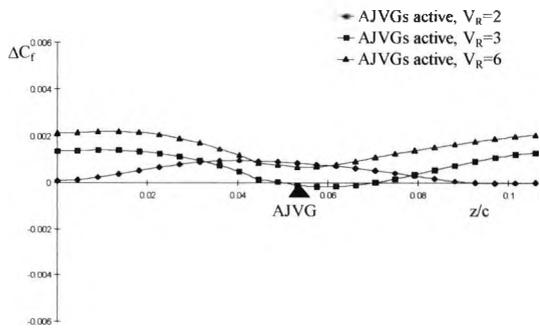
(g) Co-rotating AJVGs, (x/c=0.9)

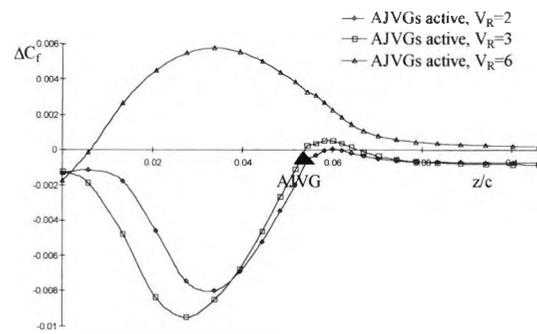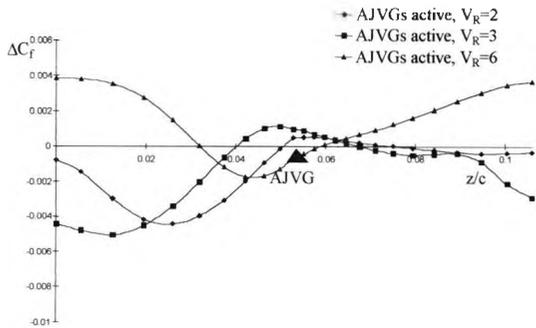(h) Counter-rotating AJVGs (x/c=0.9)

Figure 7.14: CFX-determined variation of the spanwise skin friction enhancement (ΔC_f), downstream of the AJVG array on the mainfoil upper surface, $\alpha=10°$ [Blowing at x/c=0.14, $Re_c=1.3\times10^6$, $M_\infty=0.12$, S=0.106, $\phi=45°$, $\psi=60°$]
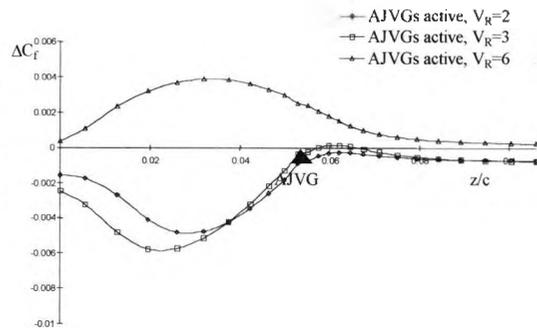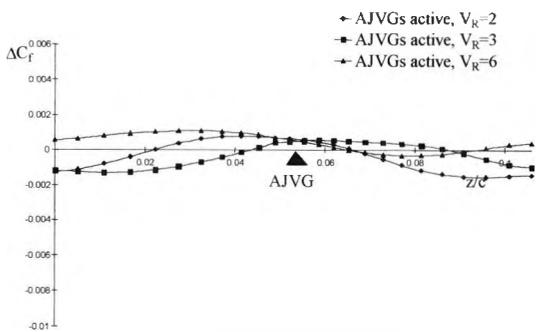
252

(a) Co-rotating AJVGs, x/c=0.25

(b) Counter-rotating AJVGs, x/c=0.25

(c) Co-rotating AJVGs, x/c=0.35

(d) Counter-rotating AJVGs, x/c=0.35

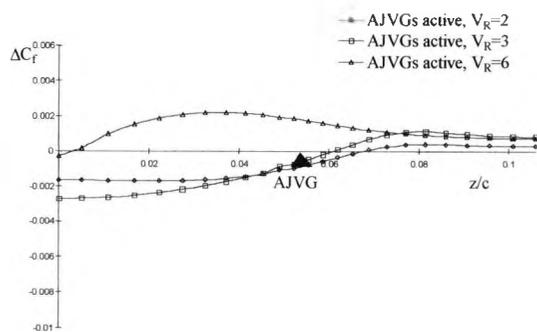(e) Co-rotating AJVGs, x/c=0.6

(f) Counter-rotating AJVGs, x/c=0.6
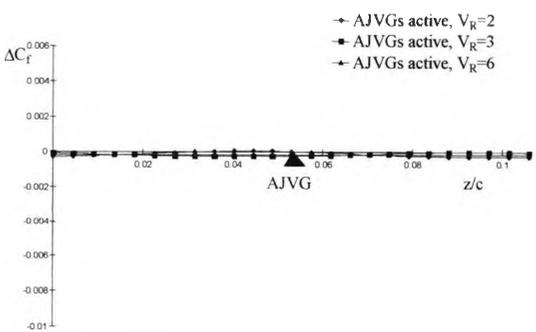
(g) Co-rotating AJVGs, x/c=0.9
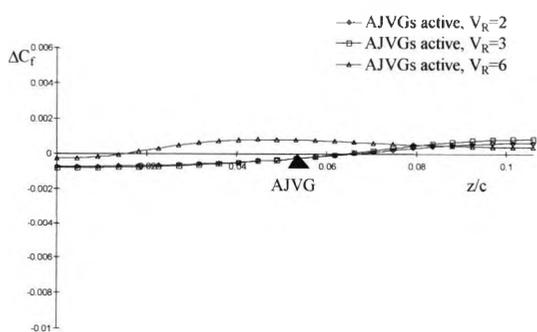
(h) Counter-rotating AJVGs, x/c=0.9

Figure 7.15: CFX-determined variation of the spanwise skin friction enhancement (ΔC_f), downstream of the AJVG array on the mainfoil upper surface, α=**20°** [Blowing at x/c=0.14, Re_c=1.3×10^6, M_∞=0.12, S=0.106, ϕ=45°, ψ=60°]

253

(a) Co-rotating AJVGs

$$I\Delta C_f = \frac{1}{S} \int_0^s \Delta C_f d\left(\frac{z}{c}\right)$$
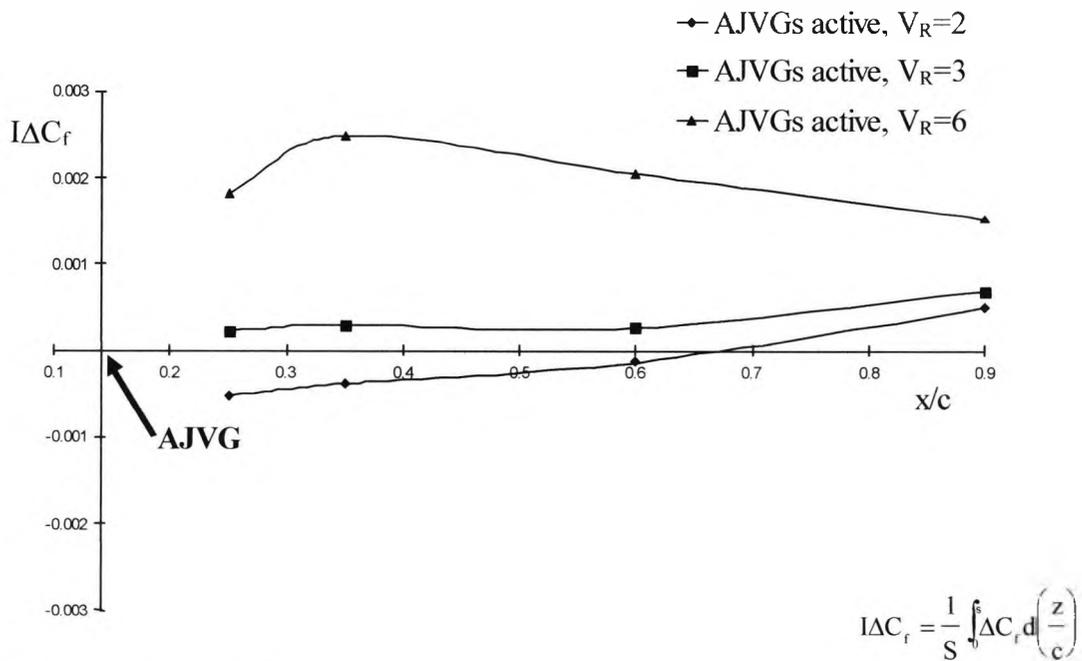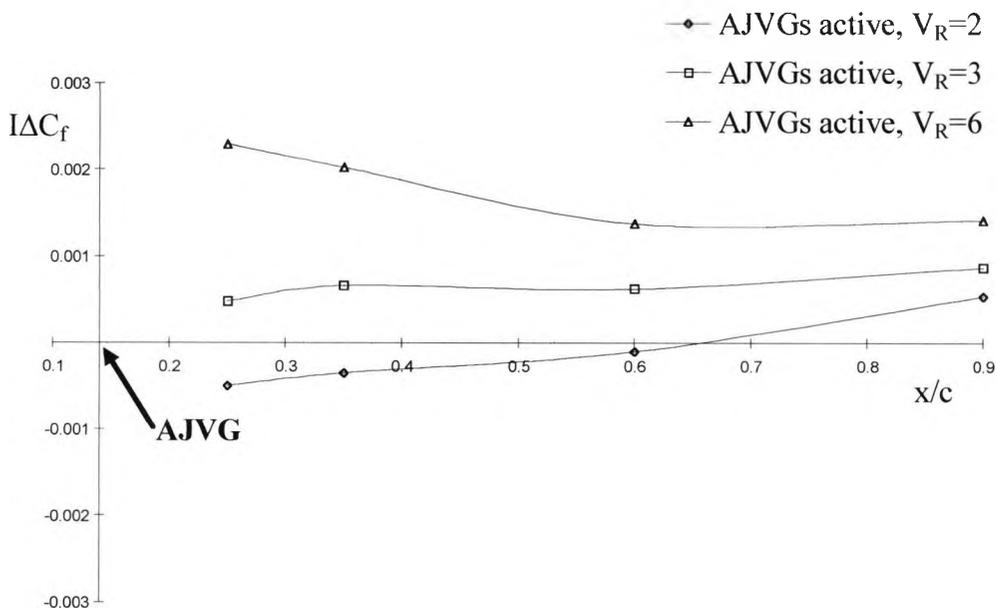
(b) Counter-rotating AJVGs

Figure 7.16: CFX-predicted axial variation of the integrated spanwise surface skin friction enhancement, expressed as a figure of merit ($I\Delta C_f$), with V_R, α=**10°** [Blowing at x/c=0.14, Re_c=1.3×10^6, M_∞=0.12, S=0.106, ϕ=45°, ψ=60°]

$$I\Delta C_f = \frac{1}{S}\int_0^s \Delta C_f d\left(\frac{z}{c}\right)$$
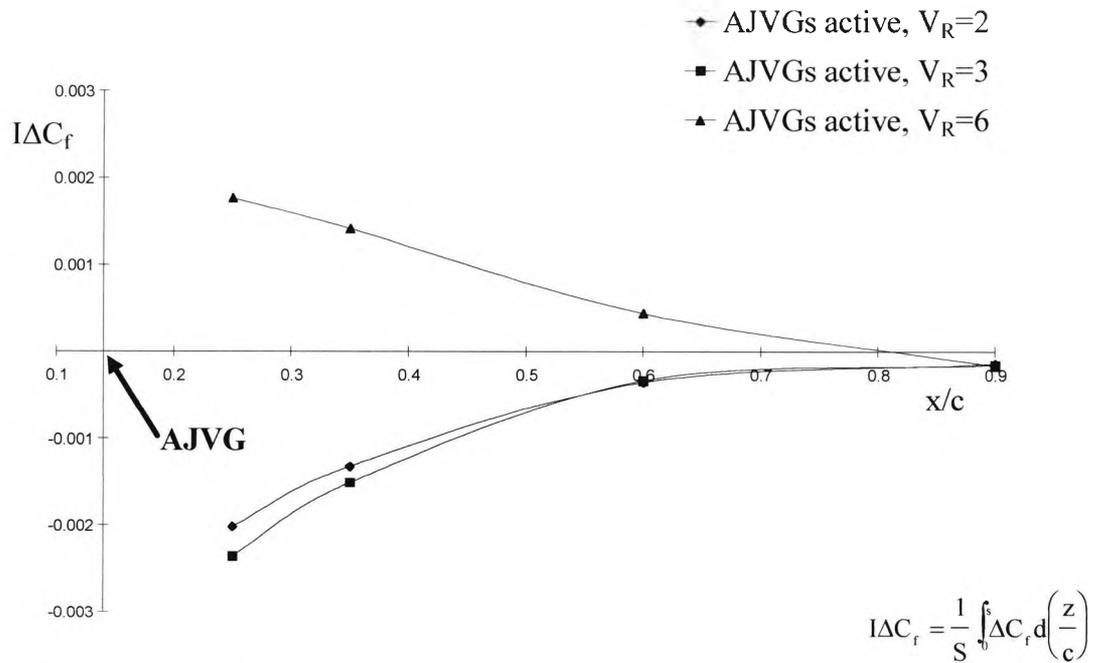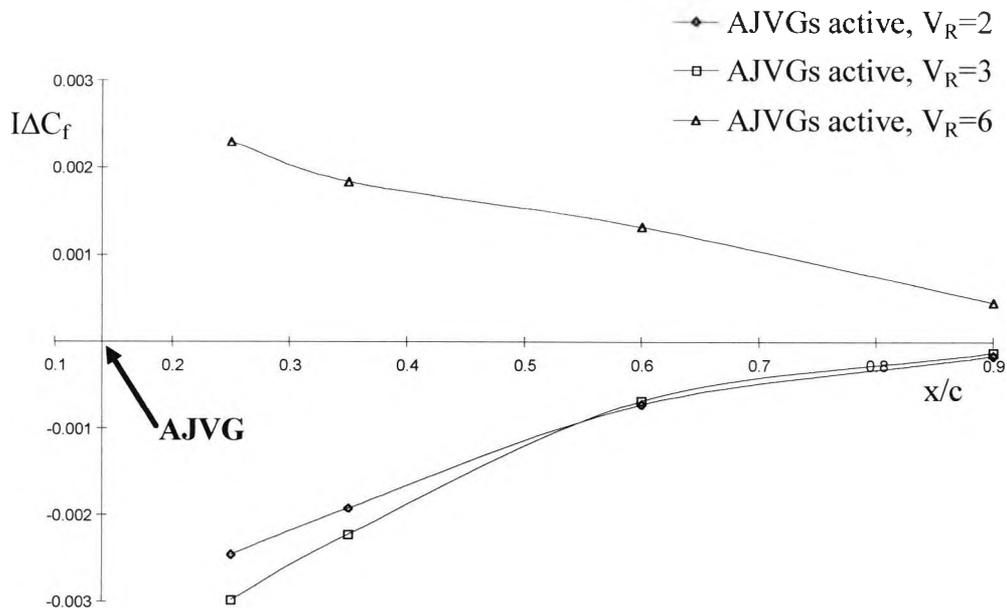
(a) Co-rotating AJVGs

(b) Counter-rotating AJVGs

Figure 7.17: CFX-predicted axial variation of the integrated spanwise surface skin friction enhancement $I\Delta C_f$ with V_R, $\alpha=\mathbf{20°}$ [Blowing at x/c=0.14, $Re_c=1.3\times10^6$, $M_\infty=0.12$, S=0.106, $\phi=45°$, $\psi=60°$]

255
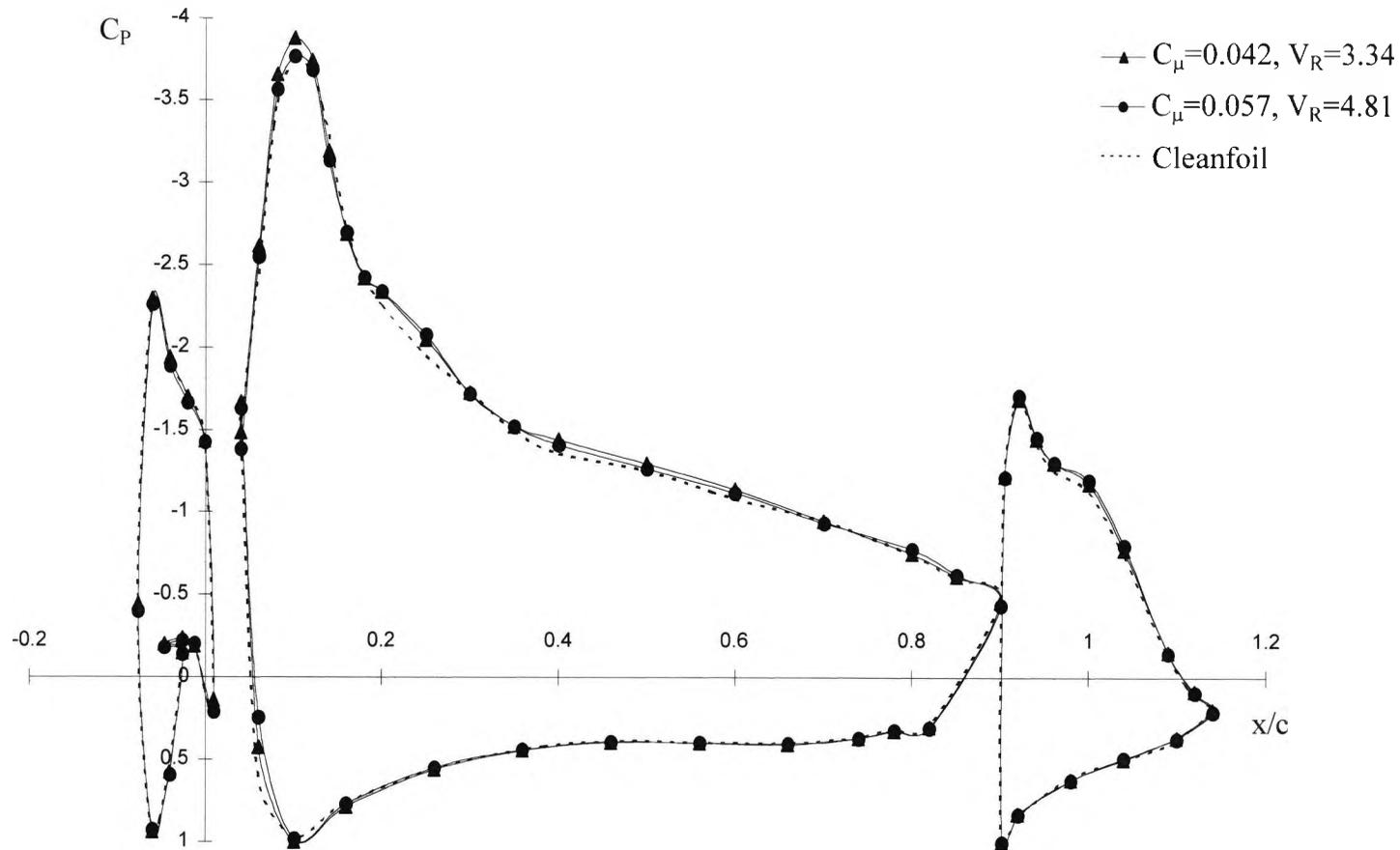
Figure 7.18: Sensitivity of experimental chordwise surface pressure distributions at tunnel centreline to jet blowing momentum coefficient C_μ, at $\alpha=\mathbf{10°}$ [Blowing at x/c=0.14, Re_c=1.37×10^6, M_∞=0.12, S=0.106, ϕ=45°, ψ=60°]
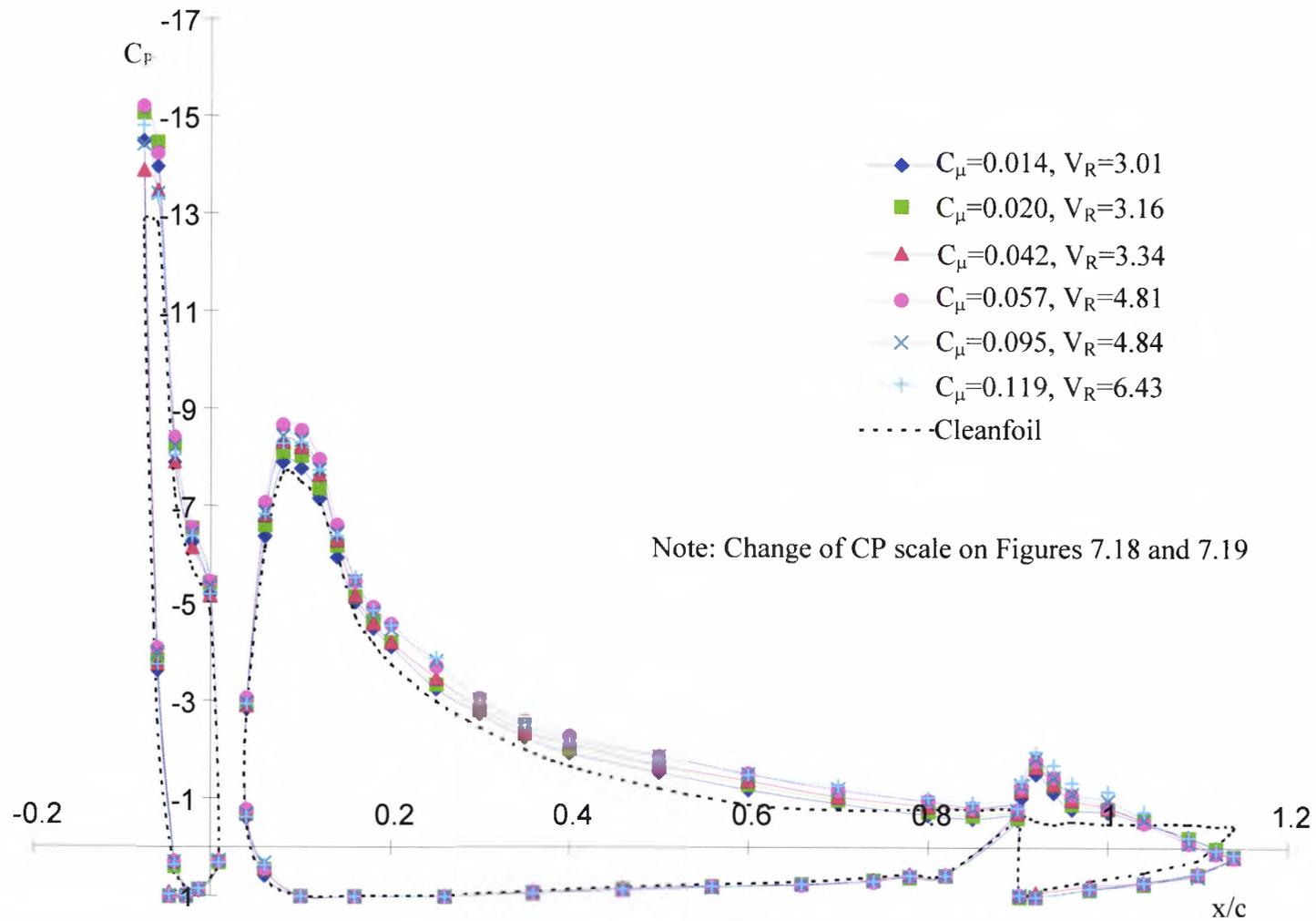
Figure 7.19: Sensitivity of experimental chordwise surface pressure distributions at tunnel centreline to C_μ, at $\alpha=30°$ [Blowing at x/c=0.14, $Re_c=1.37\times10^6$, $M_\infty=0.12$, S=0.106, $\phi=45°$, $\psi=60°$]
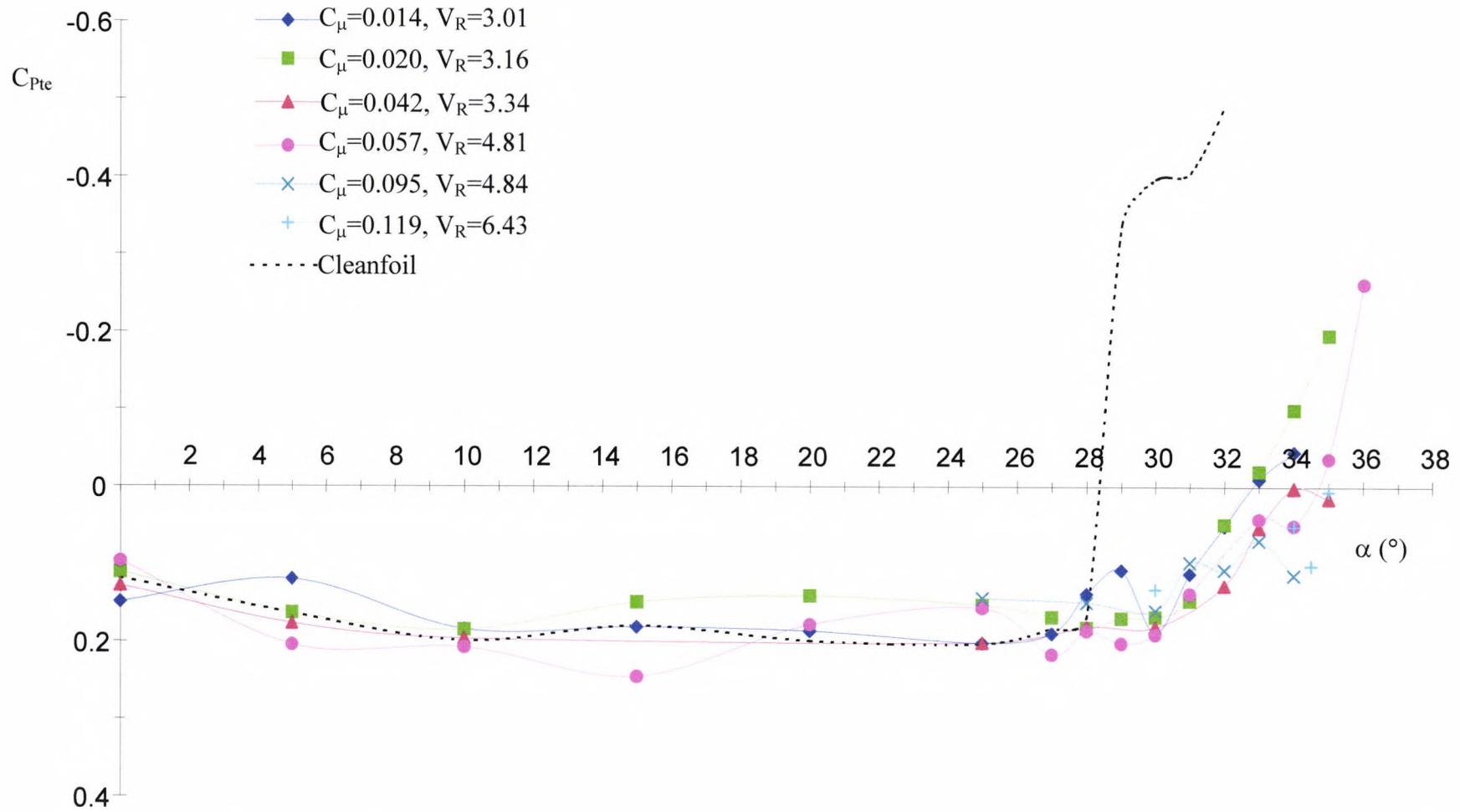
Figure 7.20: Experimentally measured mainfoil and high lift system trailing-edge pressure coefficient variation with angle of attack at varying C_μ [Blowing at x/c=0.14, Re_c=1.37×10^6, M_∞=0.12, S=0.106, ϕ=45°, ψ=60°]
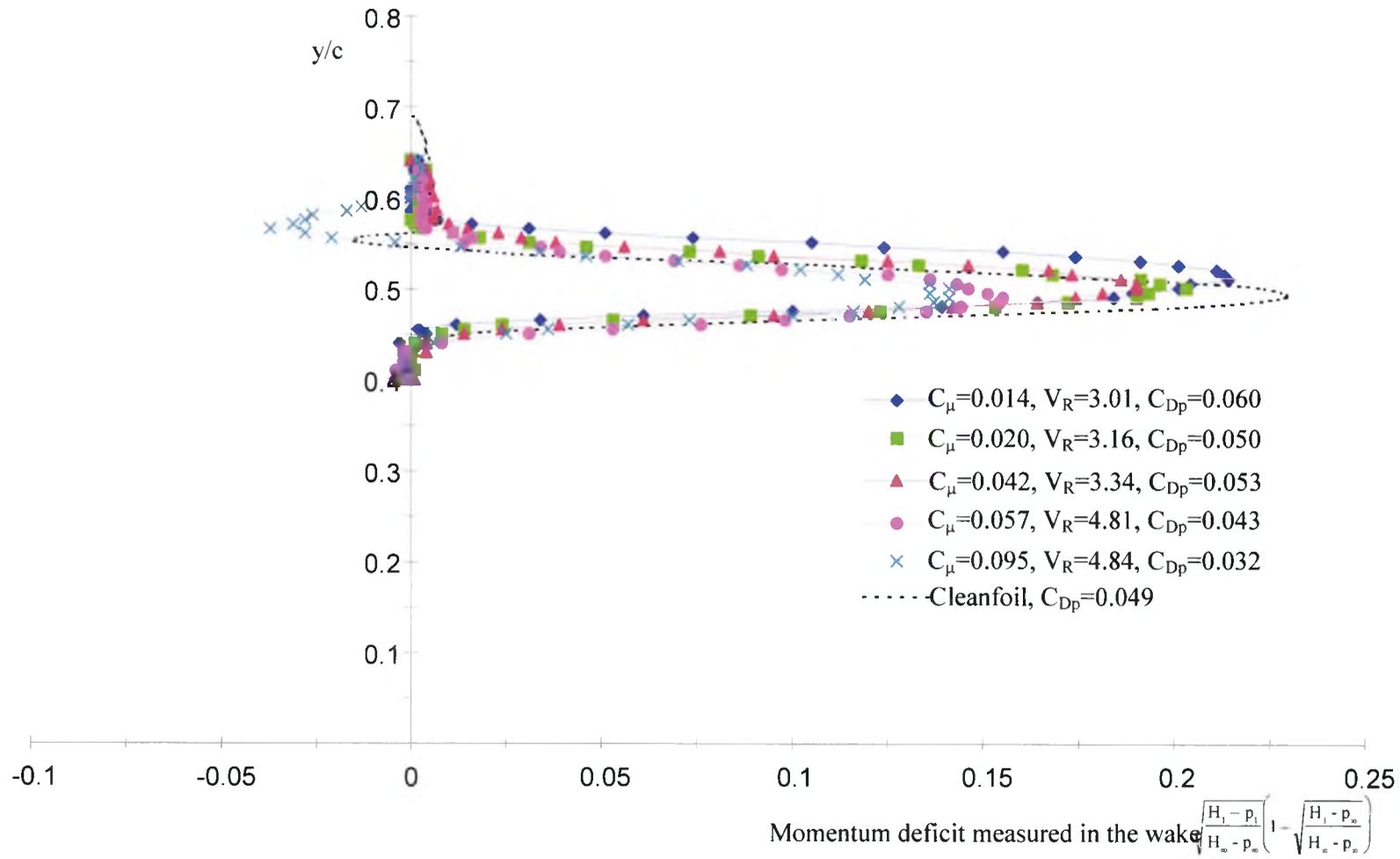
Figure 7.21: Experimental wake profiles measured one chord length downstream of the high lift system at $\alpha=25°$, at varying C_μ [Blowing at x/c=0.14, $Re_c=1.37\times10^6$, $M_\infty=0.12$, S=0.106, $\phi=45°$, $\psi=60°$]
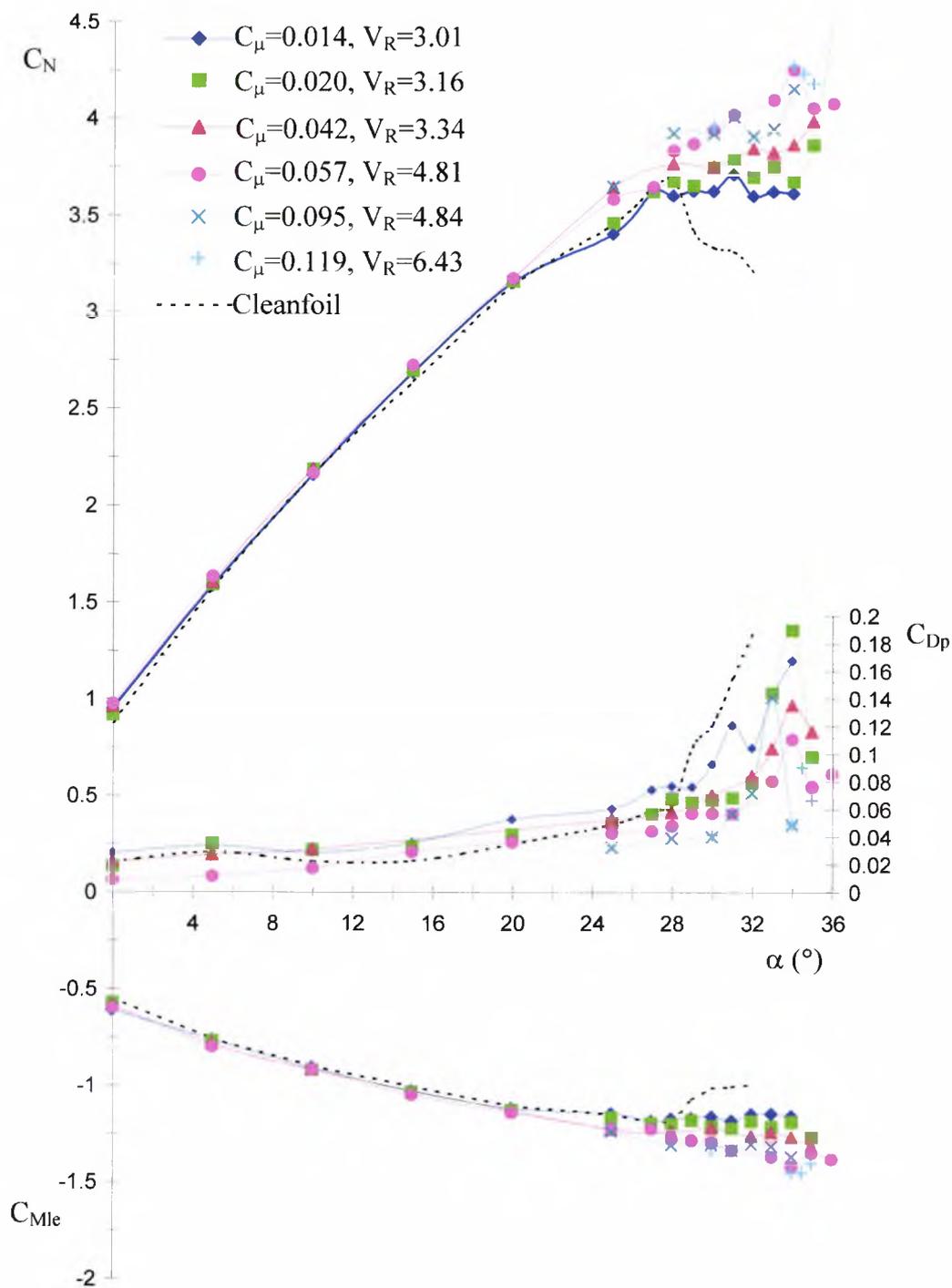
Figure 7.22: Experimentally determined normal force, wake profile drag and leading edge pitching moment variation with angle of attack at varying C_μ [Blowing at x/c=0.14, $Re_c=1.37\times10^6$, $M_\infty=0.12$, S=0.106, $\phi=45°$, $\psi=60°$]
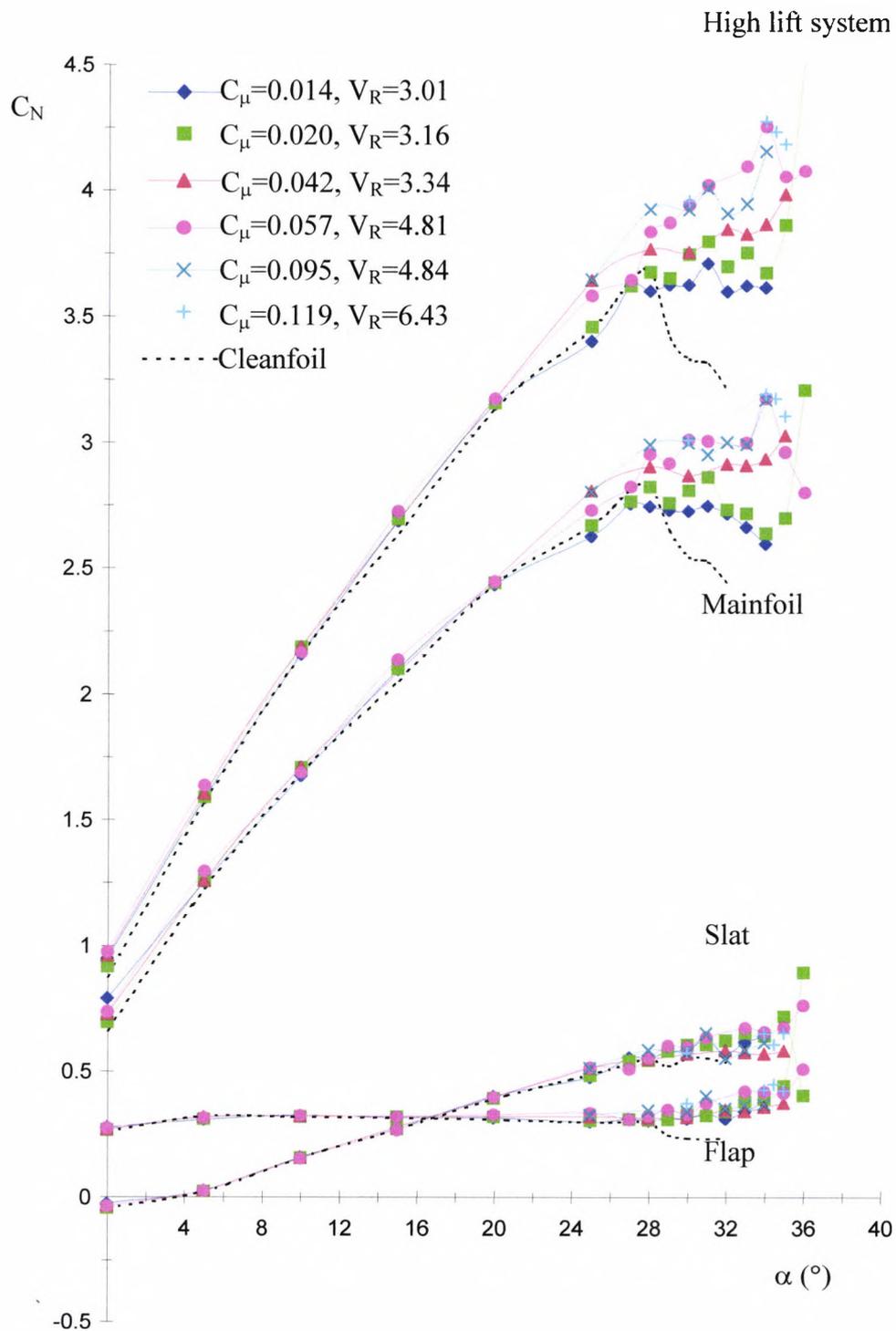
Figure 7.23: Experimentally determined normal force coefficients on each element of the high lift system at increasing angles of attack and varying C_μ [Blowing at x/c=0.14, Re_c=1.37×10^6, M_∞=0.12, S=0.106, ϕ=45°, ψ=60°]
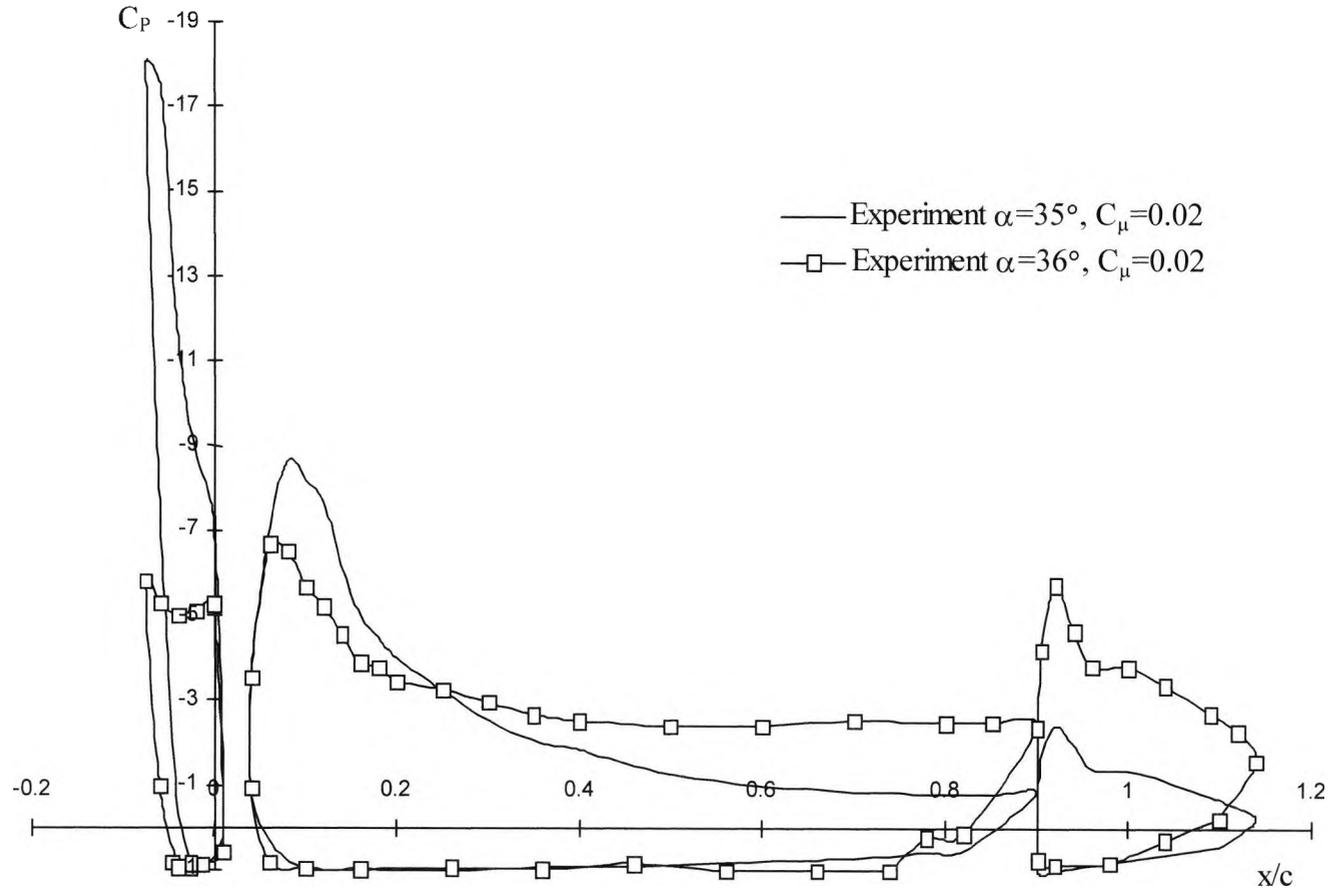
Figure 7.24: Experimentally determined surface pressure distribution around the high lift system at $\alpha=35°$ and $\alpha=36°$ and $C_\mu=0.020$ [Blowing at x/c=0.14, $Re_c=1.37\times10^6$, $M_\infty=0.12$, S=0.106, $\phi=45°$, $\psi=60°$]
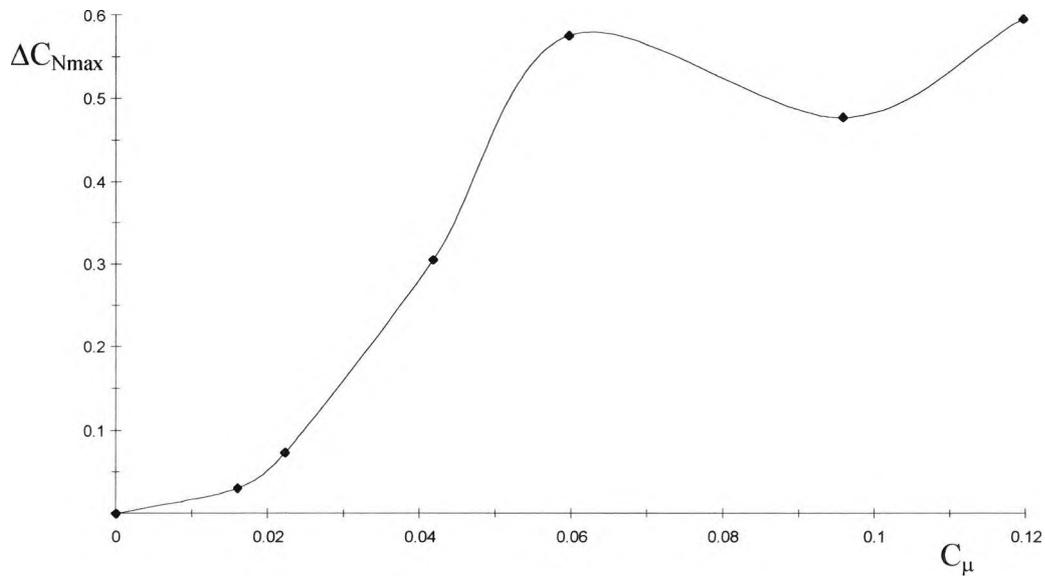
Figure 7.25: Experimentally determined variation of the high lift system maximum normal force increment with blowing momentum coefficient [Blowing at x/c=0.14, $Re_c=1.37\times10^6$, $M_\infty=0.12$, S=0.106, $\phi=45°$, $\psi=60°$]
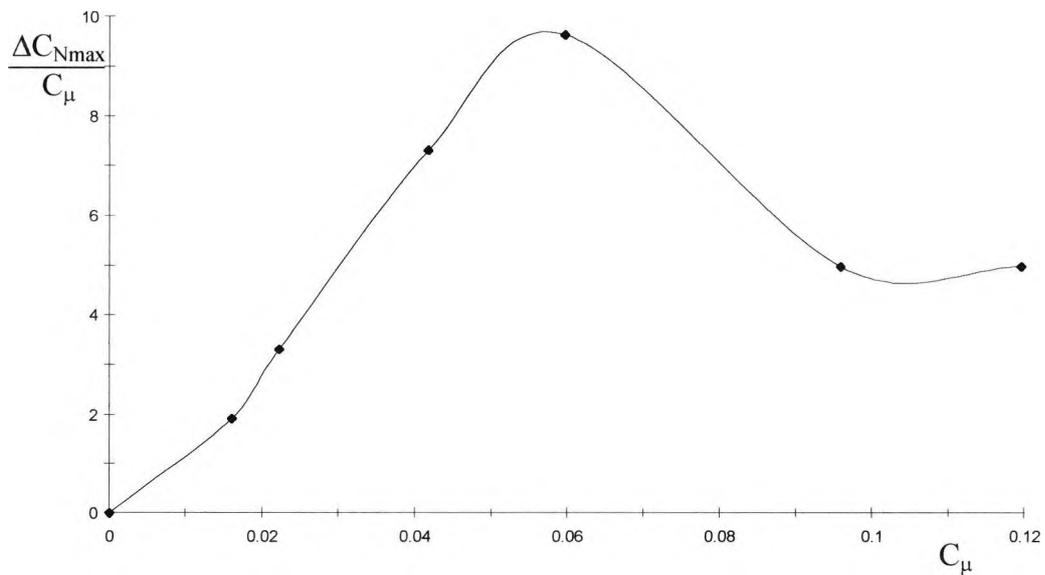
Figure 7.26: Experimentally determined variation of the high lift system maximum normal force increment per unit C_μ with blowing momentum coefficient [Blowing at x/c=0.14, $Re_c=1.37\times10^6$, $M_\infty=0.12$, S=0.106, $\phi=45°$, $\psi=60°$]

Figure 7.27: Experimentally determined wake profile drag polars for the high lift system at varying C_μ [Blowing at x/c=0.14, Re_c=1.37×10^6, M_∞=0.12, S=0.106, ϕ=45°, ψ=60°]
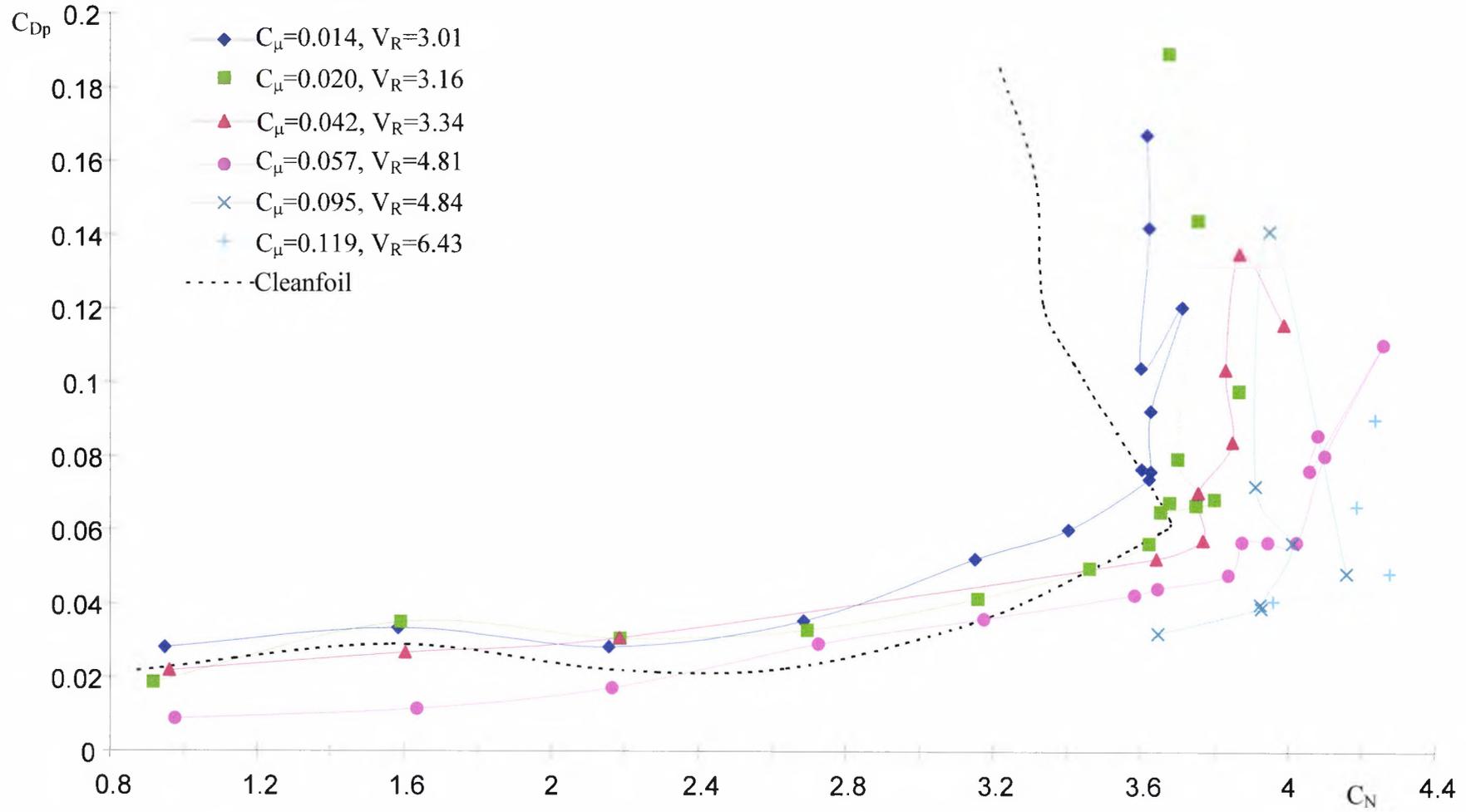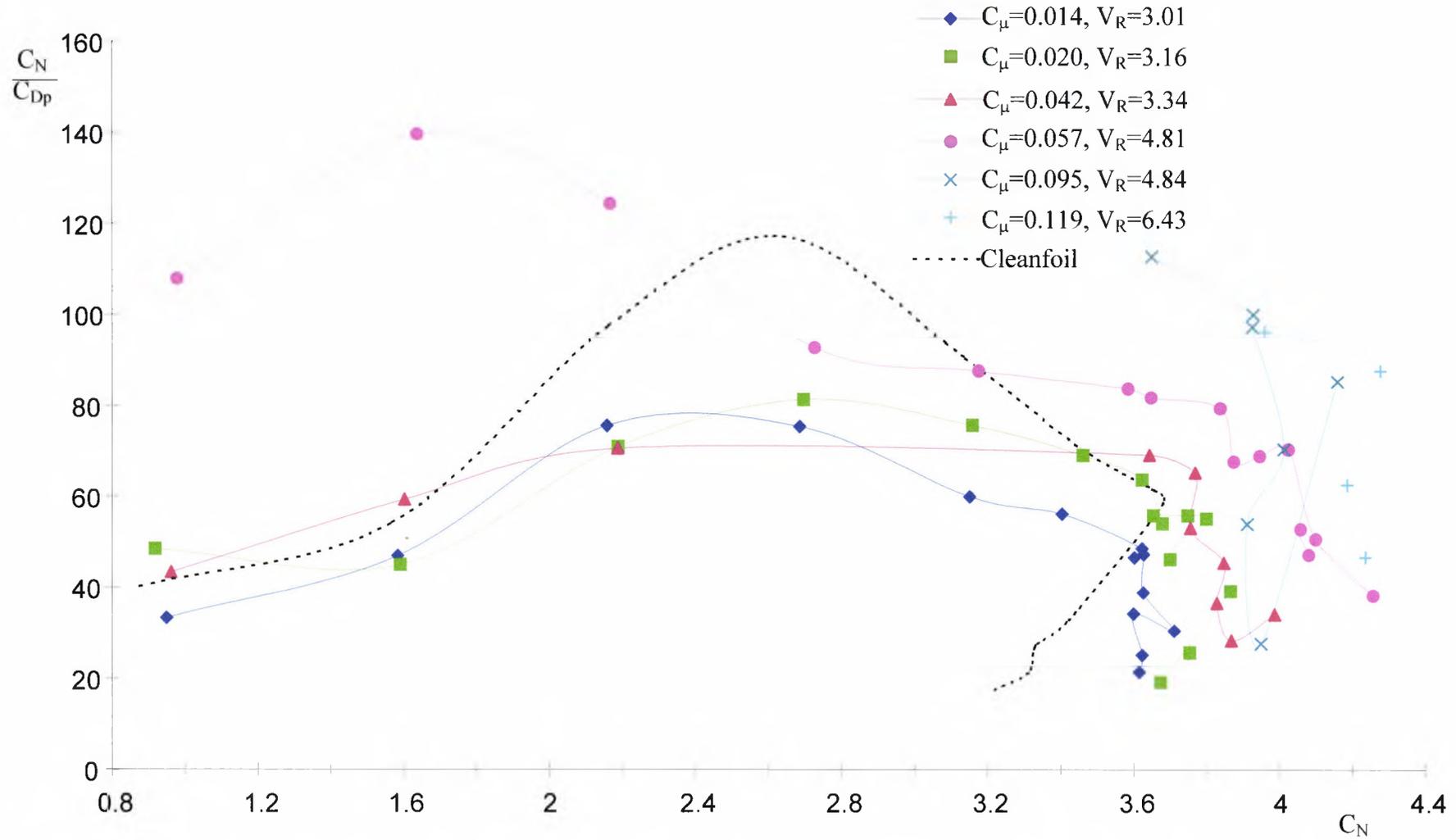
Figure 7.28: Experimentally determined normal force/drag polars for the high lift system at varying C_μ [Blowing at x/c=0.14, Re_c=1.37×10^6, M_∞=0.12, S=0.106, ϕ=45°, ψ=60°]
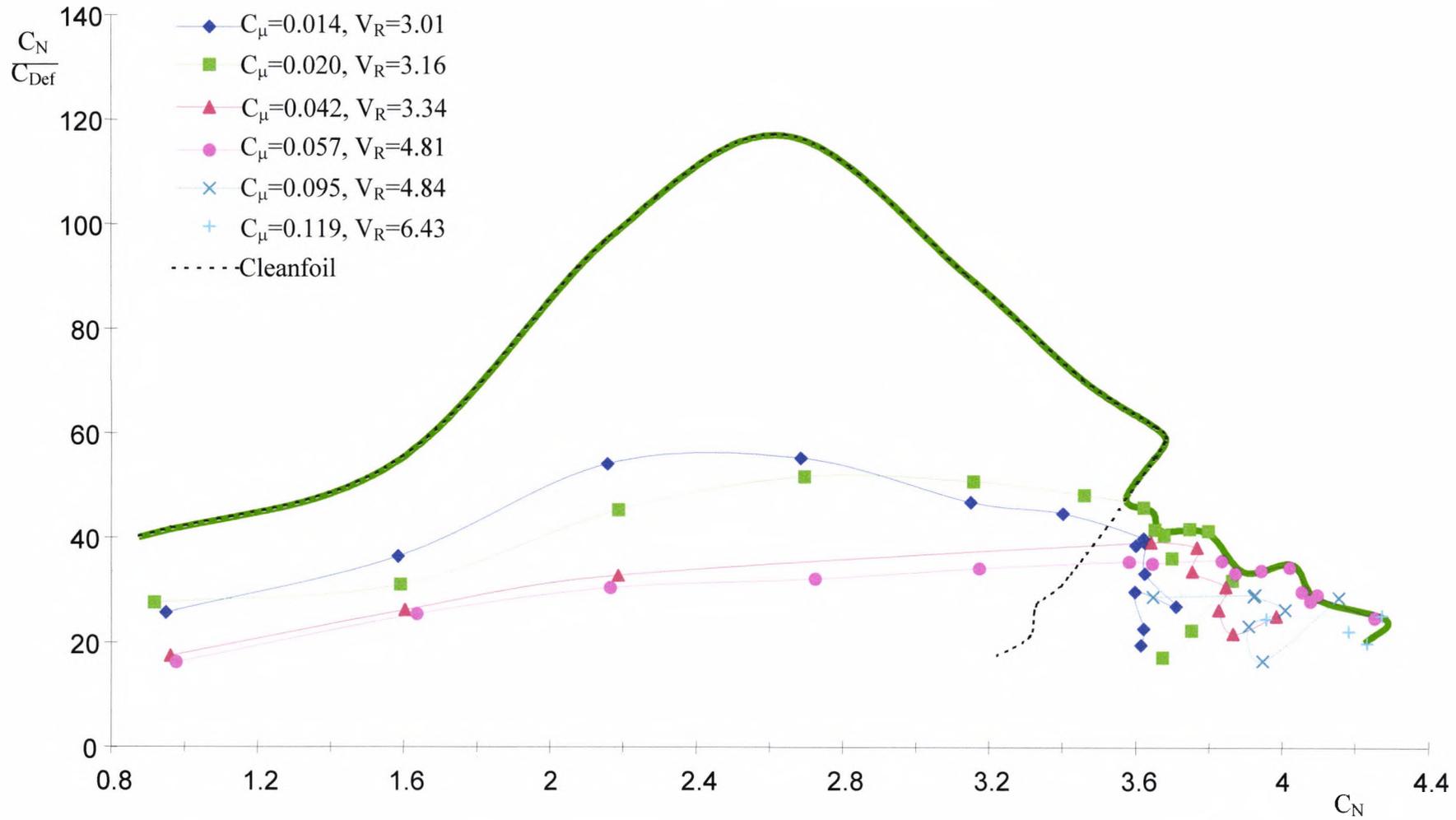
Figure 7.29: Experimentally determined normal force/effective drag polars for the high lift system at varying C_μ [Blowing at x/c=0.14, Re_c=1.37×10^6, M_∞=0.12, S=0.106, ϕ=45°, ψ=60°]

Appendix D: High lift system pressure orifice locations

Deployed slat coordinates

Orifice	x (mm)	Y (mm)
1	-14	-52
2	-24	-52
3	-32	-20
4	-24	-12
5	-14	-5
6	-4	1
7	6	7
8	11	9
9	0	0
10	-7	-8
11	-17	-31
12	-7	-51

Mainfoil coordinates

Orifice	x (mm)	y (mm)
1	370	-17
2	330	-23
3	280	-28
4	230	-33
5	180	-35
6	130	-33
7	80	-29
8	50	-25
9	30	-21
10	20	-14
11	20	0
12	30	14
13	40	22
14	50	28
15	60	31
16	70	33
17	80	34
18	90	35
19	100	35
20	125	36
21	150	37
22	175	36
23	200	36
24	250	33
25	300	30
26	350	25
27	400	19
28	425	15
29	450	11
30	410	10
31	390	5

Deployed flap coordinates

Orifice	x (mm)	y (mm)
1	550	-40
2	520	-33
3	490	-27
4	460	-21
5	451	-16
6	452	-8
7	460	-3
8	470	-2
9	480	-3
10	500	-7
11	520	-15
12	545	-28
13	560	-38
14	570	-44

Appendix E: Wall interference corrections to wind tunnel measurements and CFX predictions for comparison with MSES

In this section, the effects of wind tunnel wall interference on the measured high lift system force coefficients are evaluated. The inclusion of the free-air corrected wind tunnel measured data enables a like-to-like comparison with the MSES predictions that are calculated in free-air. Additionally, the CFX predictions are corrected for free-air, as the computational boundary conditions are synonymous with the experimental wind tunnel geometry.

Correction to dynamic pressure through wind tunnel blockage

Wind tunnel blockage occurs because the wind tunnel model and its wake occupy a certain volume within the wind tunnel finite stream. As a result, the streamline pattern around the model is distorted when compared with the corresponding free-air conditions. The magnitude of the flow distortion and its effect on measured tunnel velocities and pressures is related to the cross-sectional area of the model relative to the cross-sectional area of the wind tunnel working section geometry.

Interference on the measured variables can be said to arise from 'solid blockage' associated with the model itself and that due to the wake 'wake blockage' [see AGARDograph 109 (1966)]. In most cases, it is possible to assume that the two blockage components are independent of both each other and the model lift, so that the analysis for blockage corrections can be evaluated at zero lift. Separating these interference effects requires assumptions that the model is small compared with the wind tunnel (aerofoil chord $\leq 0.25\times$wind tunnel working section height), the lift is below C_{Lmax} and the model is mounted in the centre of the wind tunnel.

If the above assumptions are appropriate, then the flow about the model in a wind tunnel corresponds with the flow about the same model in free air, but at a corrected freestream velocity, so that:

$$U_{\infty_{AIR}} = U_{\infty_{WT}} + \Delta U \qquad\qquad (E.1)$$

where

$U_{\infty_{AIR}}$ = Free air freestream velocity

$U_{\infty_{WT}}$ = Wind tunnel freestream velocity

ΔU = Sum of the two velocity increments associated with solid and wake blockages estimated at 0.5c

For streamline flow, it is convenient to express the ratio $\Delta U / U_{\infty_{WT}}$ as the blockage factor ε_B, that is; the sum of the respective solid and wake blockage factors ε_S and ε_W.

Solid Blockage

Lock (1929) demonstrates that the solid blockage of the wind tunnel model can be determined by representing the aerofoil by an equivalent doublet and the effect of the wind tunnel walls by an infinite array of doublet images extending above and below the model and spaced at the tunnel height. The additional velocity induced at the model position can then be calculated and is equivalent to the velocity increment associated with solid blockage. For an aerofoil of chord c, maximum thickness t, spanning a rectangular wind tunnel of height h, Lock shows in <u>incompressible</u> flow that the solid blockage factor is:

$$\varepsilon_S = \frac{\Delta U_S}{U_{\infty_{WT}}} = \frac{\pi^2}{12}\left(\frac{c}{h}\right)^2\left(\frac{t}{c}\right)^2 \lambda_2 \qquad\qquad (E.2)$$

where

λ_2 = is a parameter related to the profile thickness

The later work of Thompson (1948) that takes into account compressibility and the profile thickness by empirical means suggests an equation for ε_S (that applies for t/c ratios ≈ 0.2) of the form:

$$\varepsilon_S = \frac{\pi}{6}\left[1 + 1.2\beta\left(\frac{t}{c}\right)\right]\frac{A}{\beta^3 h^2} \qquad\qquad (E.3)$$

where

A = aerofoil cross-sectional area

$\beta = \sqrt{1 - M_\infty^2}$

Eqn. E.3 again implies that the model forces are independent of the blockage distribution along the model chord; so that the model chord is small relative to the wind tunnel height. As c/h increases, the distortion of the aerofoil pressure distribution due to the presence of the wind tunnel walls must be taken into account. Although more advanced methods are available to deal with the lifting aerofoil [see Barbieux (1955)] it is relatively simple to deal with solid blockage as the angle of attack α increases. Batchelor (1944) shows that ε_S must be increased by an amount proportional to α^2 and defines the following relationship between the solid blockage factor at zero lift and angle of attack:

$$\varepsilon_S(\alpha) = \varepsilon_S\left(1 + 1.1\left(\frac{c}{h}\right)\alpha^2\right) \qquad \text{(E.4)}$$

Wake Blockage

Early attempts to account for the wake blockage of a two-dimensional aerofoil in incompressible flow were made by Glauert (1933) who suggested that the effect of wake-induced longitudinal velocity increment on the measured drag giving rise to the following wake-blockage factor is:

$$\varepsilon_W = \eta\left(\frac{t}{c}\right)\left(\frac{c}{h}\right) \qquad \text{(E.5)}$$

where

η t = effective wake width at a distance downstream of the model within the test section

Improvements to Eqn. E.5 have been suggested by using Prandtl's approach that represents the wake by an equivalent source situated at mid-chord on the aerofoil that is related to the measured body drag, D, (of strength $D/\rho U$) and a sink of equal

270

strength far downstream of the model. The implicit assumption is made here that the effect of compressibility on wake blockage can be ignored so that the appropriate wake blockage factor is defined as:

$$\varepsilon_W = \frac{1}{4}\left(\frac{c}{h}\right)C_{D_{WT}}$$

(E.6)

Correction to stream and model quantities

Estimation of wind tunnel blockage is based upon the assumption that the model behaves in the tunnel as it would in free air but at a slightly different speed (see Eqn. E.1). Defining Eqn. E.1 in terms of solid and wake blockage factors, we obtain:

$$U_{\infty_{AIR}} = U_{\infty_{WT}}\left(1 + \varepsilon_B\right) = U_{\infty_{WT}}\left(1 + \varepsilon_S + \varepsilon_W\right)$$

(E.7)

Once the blockage factor is known, it is possible to assess the corrections to the freestream static pressure and freestream dynamic head as

$$\Delta p_{\infty} = -\rho U_{\infty_{WT}}^2\, \varepsilon_B$$
$$\Delta\left(\frac{1}{2}\rho U_{\infty}^2\right) = \left(2 - M_{\infty}^2\right)\left(\frac{1}{2}\rho U_{\infty_{WT}}^2\right)\varepsilon_B$$

(E.8)

Additionally, the corrected freestream static pressure and dynamic head can be utilised to determine the non-dimensional normal force and leading edge pitching-moment coefficients for the wind tunnel model with the following expression:

$$C_{A_{AIR}} = C_{A_{WT}} + \Delta C_A = C_{A_{WT}}\left[1 - \left(2 - M_{\infty}^2\right)\varepsilon_B\right]$$

(E.9)

where

C_A = a typical non-dimensional coefficient, that is C_N or C_{Mle}

In order to assess the effects of blockage on the measured drag coefficient, an additional correction is required, because the images of the source defined to represent

271

the wake impose a longitudinal pressure gradient along the tunnel and a buoyancy force on the model (see AGARDograph 109, Section 5.4.4). The longitudinal pressure gradient may be regarded as linear along the length of the model so that the buoyancy force (D_g) is the product of the pressure gradient and the effective volume of the model (V_e); so that

$$D_g = -\left(\frac{dp}{dx}\right)V_e \qquad (E.10)$$

Glauert (1933) shows that V_e is related to the doublet strength (P) that defines the potential flow past the model by:

$$V_e = \frac{U_{\infty_{WT}}}{P} \qquad (E.11)$$

On the basis of linear theory, this pressure gradient may be written as:

$$\left(\frac{dp}{dx}\right) = -\rho U^2_{\infty_{WT}} \frac{\partial \varepsilon_W}{\partial x} \qquad (E.12)$$

Assuming ΔU_S denotes the solid blockage effect of a doublet strength P, Taylor (1928) demonstrates that the gradient $\dfrac{\partial U_{\varepsilon_W}}{\partial x}$ is related to a source strength Q precisely by $Q(\Delta U_S)/P$.

Combining the relationships of Glauert and Taylor above with the source strength used in the wake-blockage analysis, $(D/\rho U)$ yields the following expression for the longitudinal pressure gradient:

$$\left(\frac{dp}{dx}\right)_B = -\frac{DU_{\infty_{WT}}\varepsilon_S}{P} \qquad (E.13)$$

Substituting Eqns. E.11 and E.13 into Eqn. E.10, we may derive the following correction for the non-dimensional drag coefficient that accounts for buoyancy:

$$(\Delta C_D)_g = -C_D \varepsilon_S \qquad (E.14)$$

Finally, to obtain the full correction for the profile drag coefficient, we combine Eqn. E.9 with the additional buoyancy correction of Eqn. E.14 to get:

$$\Delta C_D = -\left[\varepsilon_S + \left(2 - M_\infty^2\right)\varepsilon_B\right] C_{D_{WT}} \qquad (E.15)$$

Correction to angle of attack through wall-induced upwash

As discussed above, the presence of wind tunnel walls in the experiments results in a distortion of the flow field around the wind tunnel model when compared to free air tests. As a result, the upwash induced by the tunnel walls must be interpreted as a correction to the measured angle of attack. The classical work of Glauert (1933) provides the basis on which two-dimensional wall interference is evaluated for thin aerofoils at small angles of attack with relatively small chord (c<0.4h). In Glauert's approach, the lifting aerofoil may be replaced by a single vortex at the model centre of pressure to obtain the flow field induced by the walls. However, when the angle of attack of the wind tunnel model is not small, conformal transformation of the equations of inviscid flow are required.

Goldstein (1942) considers the general two-dimensional problem of a thick cambered aerofoil at some angle of attack in a low-speed closed wind tunnel. He first derives the transformation of the aerofoil into a circle, then considers the velocity-potential field at large distances from the aerofoil, in a uniform free stream, as an algebraic power series of the ratio of model chord to wind tunnel height (c/h).

Goldstein defines a correction to the angle of attack to be the interference upwash angle at mid chord:

$$\Delta\alpha = \frac{\pi^2}{96}\left(\frac{c}{h}\right)^2 \left(2\alpha + D_2\right) + \frac{\pi^4}{92160}\left(\frac{c}{h}\right)^4 \left(-2\alpha + 20D_2 + 21D_4\right) \qquad (E.16)$$

where

$$D_n = \frac{4}{\pi} \int_0^\pi \frac{z_c}{c} \frac{\sin n\theta}{\sin \theta} d\theta$$

z_c = the ordinate of the camber line of the aerofoil and θ is the angular coordinate defined such that the distance from the leading edge is $x = \frac{1}{2} c(1 - \cos \theta)$.

In the current approach, wind tunnel interference is interpreted by representing the lifting aerofoil globally by a single vortex, so that the effects of camber can be neglected i.e., $D_n = 0$. By making use of the relationship below between angle of attack, lift coefficient and the two-dimensional lift curve slope in potential flow ($a_1 = 2\pi$):

$$C_{L_{AIR}} = a_1 (\alpha_{AIR}) \equiv (C_{L_{WT}} + \Delta C_L) = a_1 (\alpha_{WT} + \Delta\alpha) \tag{E.17}$$

Goldstein shows that Eqn E.16 can be reduced to:

$$\Delta\alpha = C_{L_{WT}} \left[\frac{\pi}{96} \left(\frac{c}{h} \right)^2 - \frac{41\pi^3}{92160} \left(\frac{c}{h} \right)^4 \right] \tag{E.18}$$

Corrected experimental wind tunnel data and wind tunnel CFX predictions

Utilising Eqns. E.3, E.4, and E.18 enables the effects of wind tunnel interference blockage effects to be interpreted for the wind tunnel CFX predictions and experimentally measured data. Upon calculating the interference effects, Eqns. E.9 and E.15 can be used to determine the corrections to the predicted and measured normal force coefficients, leading edge pitching moment coefficients and drag coefficients.

274

Table E.1: Measured and CFX predicted high lift system force coefficient data, determined in the wind tunnel and corrected for free-air

Experimentally measured data

α (°) (Expt wt)	C_N (Expt wt)	C_{Mle} (Expt wt)	C_{Dp} (Expt wt)	$\varepsilon_S(\alpha)$	ε_W	ε_B	Δα (°)	α (°) (Expt fa)	C_N (Expt fa)	C_{Mle} (Expt fa)	C_{Dp} (Expt fa)
0	0.876	-0.548	0.022	0.0123	0.0024	0.0147	0.30	0.30	0.85	-0.53	0.021
5	1.570	-0.761	0.029	0.0130	0.0032	0.0163	0.54	5.54	1.52	-0.74	0.028
10	2.163	-0.901	0.022	0.0152	0.0025	0.0177	0.75	10.75	2.09	-0.87	0.021
15	2.640	-1.005	0.023	0.0188	0.0025	0.0213	0.93	15.93	2.53	-0.96	0.021
20	3.138	-1.107	0.035	0.0238	0.0039	0.0277	1.14	21.14	2.97	-1.05	0.032
25	3.454	-1.149	0.049	0.0303	0.0055	0.0358	1.30	26.30	3.21	-1.07	0.044
27	3.649	-1.190	0.059	0.0333	0.0066	0.0399	1.39	28.39	3.36	-1.10	0.053
28	3.679	-1.187	0.063	0.0349	0.0070	0.0419	1.41	29.41	3.37	-1.09	0.055
29	3.416	-1.070	0.105	0.0365	0.0117	0.0482	1.32	30.32	3.09	-0.97	0.091
30	3.331	-1.011	0.122	0.0382	0.0136	0.0518	1.29	31.29	2.99	-0.91	0.105
31	3.312	-1.005	0.156	0.0399	0.0174	0.0573	1.29	32.29	2.93	-0.89	0.132
32	3.210	-0.993	0.187	0.0418	0.0208	0.0626	1.26	33.26	2.81	-0.87	0.156

CFX Predicted data

α (°) (CFX wt)	C_N (CFX wt)	C_{Mle} (CFX wt)	C_{Dp} (CFX wt)	$\varepsilon_S(\alpha)$	ε_W	ε_B	Δα (°)	α (°) CFX (fa)	C_N CFX (fa)	C_{Mle} CFX (fa)	C_{Dp} CFX (fa)
5	1.787	-0.808	0.050	0.0130	0.0056	0.0186	0.61	5.61	1.72	-0.78	0.048
10	2.326	-0.927	0.068	0.0152	0.0076	0.0228	0.80	10.80	2.22	-0.89	0.064
15	2.747	-0.997	0.101	0.0188	0.0112	0.0300	0.96	15.96	2.58	-0.94	0.093
20	2.878	-0.986	0.194	0.0238	0.0216	0.0455	1.02	21.02	2.62	-0.90	0.172
25	2.848	-0.989	0.386	0.0303	0.0431	0.0734	1.01	26.01	2.43	-0.84	0.318
27	3.122	-1.137	0.319	0.0333	0.0357	0.0689	1.14	28.14	2.69	-0.98	0.265
31	3.187	-1.211	0.642	0.0399	0.0716	0.1116	1.14	32.14	2.48	-0.94	0.474

Figures E.1 illustrates the wind tunnel interference effects on the integrated normal force, leading-edge pitching moment and wake profile drag polars for the experimentally measured data and CFX predictions. The plots demonstrate that the presence of the wind tunnel walls gives rise to a reduction in the effective high lift system angle of attack and the leading edge pitching moment coefficient and increases in the normal force and wake profile drag coefficients.

Figure E.2 shows a comparison between the corrected free-air wind tunnel measurements and CFX predictions and the free-air MSES predictions. Having corrected the wind tunnel measured data for wall interference effects there is a noticeable difference between the measured data and the MSES free-air predictions across the angle of attack range that is consistent with an angle of attack increase in the experiment. The reasons for the shift in the force coefficient curves are unknown but may be attributed to the global representation of the highly cambered high lift system with a single vortex in the wind tunnel wall interference calculations. Despite the difference between predicted and measured absolute force coefficients, Figure E.2 shows MSES is capable of identifying the experimental trends up to stall.
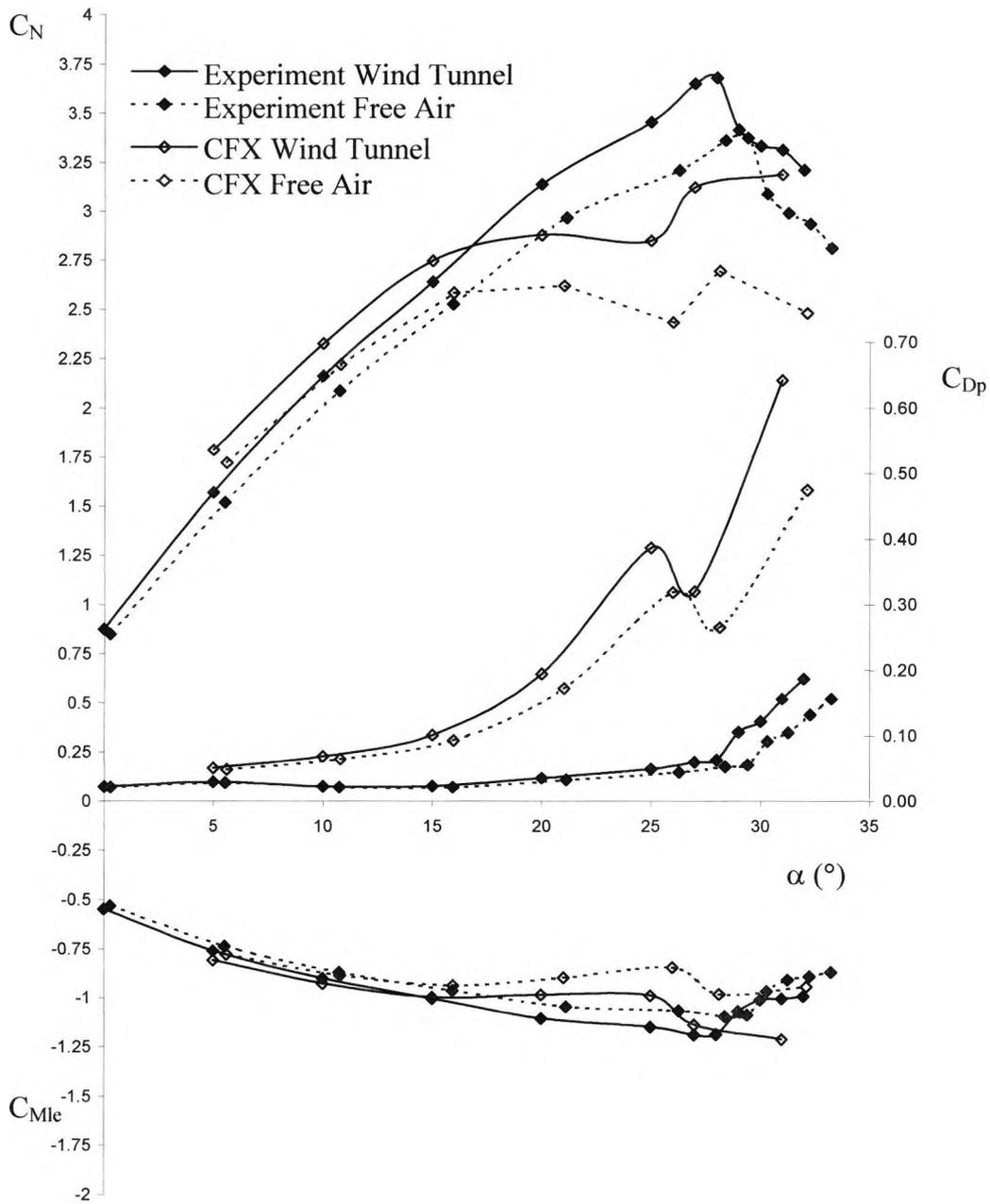
Figure E.1: Wind tunnel wall interference effects on the experimentally determined and CFX-predicted high lift system normal force, wake profile drag and leading-edge pitching moment coefficient variation with angle of attack, C_μ=0, Re_c=1.37×10^6, M_∞=0.13
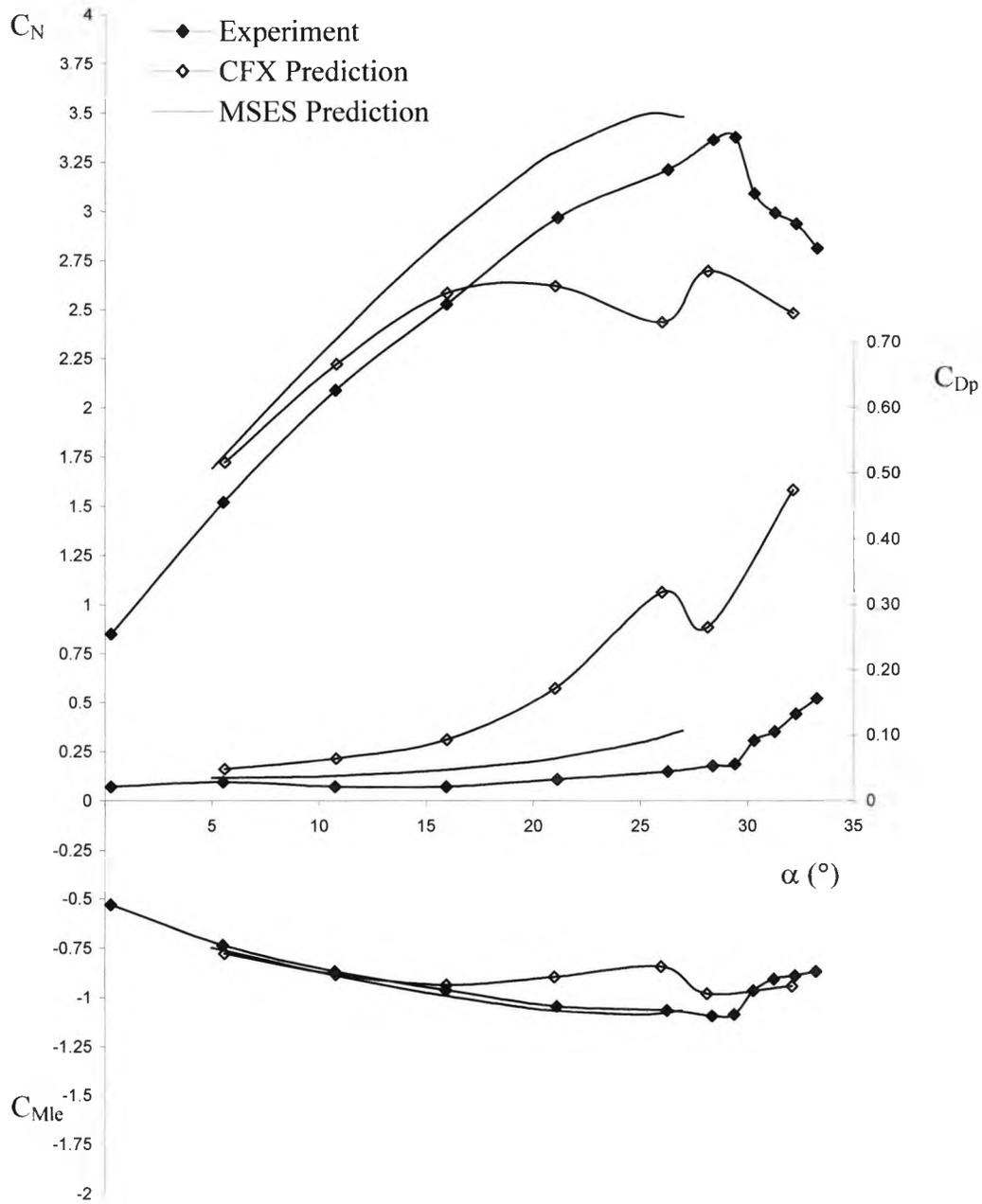
Figure E.2: Free-air high lift system normal force, wake profile drag and leading-edge pitching moment coefficient variation with angle of attack, C_μ=0, Re_c=1.37×10^6, M_∞=0.13